Self Injection and Radiation Production in Laser Wakefield Accelerators

Matthew Philip Tooley

Submitted in partial fulfillment of the requirements
for the degree of Doctor of Philosophy.
Department of Physics,
University of Strathclyde

April 2019

Declaration

This thesis is the result of the author's original research. It has been composed by the author and has not been previously submitted for examination which has led to the award of a degree.

Work from chapter 4 was published in Tooley *et al.*[1]

Matthew Philip Tooley

April 2019

---

[1] M. P. Tooley et al. *Phys. Rev. Lett.* **119**, p. 044801, 2017.

To “the whole village”, with my heartfelt thanks.

Abstract

The laser wakefield accelerator (LWFA) is a nascent electron acceleration technology characterised by extremely large (100s GV/m) accelerating fields and compact ($\sim$ cm) scale. Self-injection is a key mechanism in the production of electron beams from the laser wakefield accelerator (LWFA), where background plasma electrons spontaneously enter the accelerating field region. Self-injection is routinely exploited but a fully self-consistent model for the process is still lacking, as are reliable methods for the control of the self-injection process. In this thesis a model for control of self-injection using plasma density gradients or laser intensity evolution is presented. The model is validated using particle-in-cell (PIC) simulations and injection of sub-femtosecond electron bunches is demonstrated. This control is further exploited to demonstrate injection of a train of multiple electron bunches into the LWFA.

An additional characteristic of the LWFA is the strong transverse focusing fields, which cause electrons to undergo betatron motion and emit broadband XUV and X-ray radiation. The previously demonstrated bunching is investigated as a source of tuneable coherent emission. Analytic and numerical models demonstrate coherent enhancement at the bunching wavelength. Finally the stability of the scheme is considered with respect to energy and spatial bunch spreads and found to be viable for tuneable XUV radiation production with current state of the art LWFA bunch parameters.

Acknowledgements

There is an African proverb that wisely states “it takes a whole village to raise a child”, and, in the same way, this thesis is the product of the knowledge, experience and effort of many more people than just myself. I would therefore like to take the opportunity to highlight and thank some of the many people who have helped me produce this work.

First and foremost, I would like to express my sincere gratitude to my Supervisor, Prof. Dino Jaroszinski, for his guidance, encouragement and patience over the course of my studies. I thank Dr. Bernhard Ersfeld for the tremendous amount of time he spent with me, discussing and explaining crucial theoretical concepts, and Dr. Enrico Brunetti for sharing his expertise in numerical calculation and his radiation calculation code.

I owe a tremendous debt of gratitude to Drs. Adam Noble and Sam Yoffe, who are not merely colleagues but my close friends. Their input has been invaluable at every stage of the process, as both mentors and fellow researchers. Thank you both for dedicating so much time and energy to our discussions of theoretical physics, mathematics, scientific computing (sorry Adam!) and cricket (sorry Sam!).

Most importantly I must thank my family and friends for their love and support throughout my PhD. In particular my wonderful husband Scott, for listening to me talk endlessly about my work, and patiently assisting me with my grammar; my mum and dad, and my sister Rachel, who always take an interest in my work — in full knowledge, I suspect, that my answer will be unintelligible; and my climbing friends Jody, Ian, Alasdair and Will who have helped provide much needed escape and relaxation.

Finally, this thesis, like so many others, is built on a whole ecosystem of research software. So I give my thanks to the developers of EPOCH, FBPIC, Python, Numpy, Scipy and Matplotlib, without whose excellent code this work would have been impossible.

The Role of the Author

The self-injection model in chapter 4 was developed by the author in collaboration with Prof. Dino Jaroszynski, Dr. Bernhard Ersfeld, Dr. Sam Yoffe and Dr. Adam Noble. The numerical simulations and analysis were performed by the author, using existing PIC codes as described in the main text.

The scheme for coherent enhancement of radiation in chapter 5 was developed by the author with assistance from Prof. Dino Jaroszynski, Dr. Bernhard Ersfeld, Dr. Sam Yoffe, Dr. Adam Noble and Dr. Enrico Brunetti. Analytic descriptions were developed by the author, based on existing results where stated. Numerical simulations and analysis were performed by the author.

Contents

Chapter 1

Introduction

Since Cockcroft and Walton first demonstrated the acceleration of protons in 1932,[2] particle accelerators have found application in an ever growing range of scientific fields and commercial applications. Initially a niche tool for fundamental nuclear and particle physics, high energy particle accelerators are now used at many facilities worldwide to drive light sources for scientific and industrial imaging, and neutron sources for nuclear physics and materials research. In addition to these large machines, there are a great many smaller accelerators with applications as diverse as medical imaging and cancer treatment, ion implantation for semiconductor fabrication, cargo inspection and polymer crosslinking in plastics.[3,4]

From the initial 600 keV capability of the Cockcroft–Walton accelerator, particle accelerator technology has evolved massively in the following eight decades. First with the Cyclotron, developed later in 1932 by Ernest Lawrence,[5] the prototype of which was capable of accelerating H_2^+ ions to energies of 1 MeV. Unlike the Cockcroft–Walton design it accelerated the ions along a spiral trajectory using a uniform magnetic field and an oscillating electic field to apply an accelerating

---

[2] J. D. Cockcroft and E. T. S. Walton. *Nature* **129**, p. 242, 1932.

[3] S. Hanna. *RF linear accelerators for medical and industrial applications*, Artech House, 2013.

[4] J. V. Crivello. *Nucl. Instrum. Methods Phys. Res., Sect. B* **151**, pp. 8–21, 1999.

[5] E. O. Lawrence and M. S. Livingston. *Phys. Rev.* **40**, pp. 19–35, 1932.

potential twice per revolution. This provided improved performance in a smaller package — the prototype device was only 9 inches in diameter. This design was subsequently employed as the Calutron for uranium isotope separation in the Manhattan Project.[6] The next major development came in the 1950s and '60s with the development of the synchrotron. Rather than accelerating electrons in a spiral the synchrotron ensures a fixed orbit using dipole magnets for bending while the RF phase is varied with the increasing electron velocity. The addition of "strong-focusing" magnets using alternating gradient quadrupoles reduced the required beam aperture size allowing for stronger and more compact bending magnets, which in turn increased the maximum achievable beam energy. This strong focusing was demonstrated in 1960 with the Alternating Gradient Synchrotron (AGS) machine at Brookhaven National Laboratory producing 33 GeV proton beams and in 1966 with the still-functioning Stanford Linear Accelerator, which accelerates electrons and positrons up to 50 GeV. The latter employs no bending magnets, instead accelerating particles in a straight line over its 3.2 km length.

The strong focusing linear accelerator and synchrotron are still the primary accelerator technologies in use today, with all major modern accelerators, including the LHC, and LCLS and European X-FEL light source being built on these principles. While this conventional accelerator technology continues to make vast strides, there is a fundamental limit to the energy that can be achieved from a given size of accelerator. This is due in large part to the mechanical and physical limitations of the accelerating cavities and the focusing and bending magnets. RF accelerating cavities are typically limited to a breakdown field strength of $\sim 100s\,\mathrm{MV/m}$ which limits the maximum energy gain per unit length of linear accelerators. Meanwhile circular accelerators are limited by the peak fields achievable in the superconducting beam-bending magnets of $\sim 8\,\mathrm{T}$, which places an upper limit on the energy of a beam that can be guided around the accelerator.

---

[6] W. E. Parkins. *Phys. Today* **58**, pp. 45–51, 2005.

Overcoming these limits necessitates very large machines — such as the 4 TeV-per-beam LHC — and achieving more than incremental gains on this energy will require a fundamental change in accelerator technology.

1.1 Introducing Plasma-based Accelerators

An exciting new alternative accelerator technology is being developed that makes use of charge separation in a plasma to generate the accelerating and focusing fields. Using plasma to create the accelerating structure means that there is no material breakdown threshold and so electric field strengths of $100s\,\mathrm{GV/m}$ can be realised. This allows electrons to be accelerated to GeV energies over distances of centimetres, rather than the metres or kilometres required by conventional accelerators.

The laser wakefield accelerator (LWFA) concept was first proposed by Tajima and Dawson in the 1979.[7] They showed that charge separation of a neutral plasma, driven by an intense laser pulse, had the potential to accelerate electrons to GeV energies over millimeters. This initial work considered the "linear-regime" of acceleration, where the charge separation is incomplete, the electric field strength is relatively low and the driven plasma wave behaves according to linear theory with an approximately sinusoidal electric field shape in the acceleration direction. This work was followed by several other proposed schemes, including the particle beam driven analogue, usually known as the plasma wakefield accelerator (PWFA),[8] and alternative laser drives schemes intended to increase the acheivable acceleration field strength, such as the plasma beat wave accelerator (PBWA). This uses two lasers that are tuned to interfere at the plasma frequency and drive a high amplitude plasma wave.[7]

More recently, advances in laser technology have allowed the plasma wave

---

[7] T. Tajima and J. M. Dawson. *Phys. Rev. Lett.* **4**, pp. 267–270, 1979.

[8] P. Chen et al. *Phys. Rev. Lett.* **54**, pp. 693–696, 1985.

to be driven more strongly, leading to complete charge separation, and strongly non-linear behaviour of the plasma wave. This produces a stronger electric field and has additional advantages that will be discussed in chapter 3. This strongly non-linear regime was first investigated theoretically for the beam driven PWFA case by Rosenzweig *et al.*,[9] and more recently for the LWFA case by Pukhov and Meyer-ter-Vehn in 2002,[10] as advances in laser power made such a scheme feasible. Pukhov and Meyer-Ter-Vehn, coined the term “bubble” to refer to the spherical shape of the electron-evacuated cavity generated by the driver, which is surrounded by a high density electron “sheath”. They also demonstrated the possibility of spontaneous “self-injection” of electrons from the background plasma into the accelerating fields of the bubble. This was experimentally demonstrated in 2004, in three experiments,[11–13,*] in which a high energy electron beam with small energy spread was produced by the acceleration of self-injected electrons in a non-linear plasma wake.

Since the publication of these inaugural papers, the state-of-the-art in LWFA has continued to advance, pushing to higher final electron energies and exploring methods to improve the electron beam quality.[14,15] However, the process of self-injection still remains a crucial area for study, because control of the injected bunch properties is a key requirement for use of the LWFA as source of high quality electron beams. The key mechanism by which self-injection occurs has been identified as “wave-breaking”. This occurs when electrons in the sheath region gain sufficient forward momentum to enter the bubble cavity. Here they co-propagate in the accelerating phase of the bubble fields and are rapidly accelerated

---

[9] J. B. Rosenzweig et al. *Phys. Rev. A* **44**, 1991.
[10] A. Pukhov and J. Meyer-ter-Vehn. *Appl. Phys. B: Lasers Opt.* **74**, pp. 355–361, 2002.
[11] S. P. D. Mangles et al. *Nature* **431**, pp. 535–8, 2004.
[12] C. G. R. Geddes et al. *Nature* **431**, pp. 538–541, 2004.
[13] J. Faure et al. *Nature* **431**, pp. 541–544, 2004.
[14] S. P. Mangles et al. *Phys. Plasmas* **14**, 2007.
[15] J. Ferri et al. *Sci. Rep.* **6**, pp. 1–10, 2016.

[*] These three papers are often referred to collectively as the “dream-beam” papers.

to high energy. However, a complete theoretical description of this self-injection process is still lacking[*]. This is partly due to the highly complex and non-linear dynamics of the electron motion in the laser-bubble system, which makes detailed theoretical analysis extremely challenging. In particular, no adequate self-consistent model exists for describing the electron dynamics in the bubble, and therefore the details of the electric field structure. Several approximate "piecewise" models of the bubble fields and sheath electron behaviour have been derived,[16–20] which provide good approximations for the general bubble shape and electron behaviour. However, they still do not correctly model the finer details of the sheath structure. This is particularly true at the rear of the bubble[19–21] where the sheath electrons return to the laser axis, creating a "sheath crossing region" where they have complex behaviour, which further complicates the picture. Particle-in-cell (PIC) simulations show that it is this rearmost point of the bubble where self-injection occurs, but analytical study of this behaviour is extremely challenging due to the need to accurately model electron dynamics in the region.

An important additional aspect of plasma-based acceleration is the transverse electric field structure. This exerts strong focusing forces on injected bunches, which can lead to transverse oscillation with large transverse acceleration. As a result, electron bunches within the LWFA bubble emit intense XUV to X-ray radiation.[22] This makes the LWFA a very useful radiation source as well as a particle source, where its compact size and cost advantages promise to enhance accessibility for potential users. Typically, however, this radiation is broadband due to the rapid acceleration of the electrons and so its usefulness is limited for

---

[16] I. Kostyukov et al. *Phys. Plasmas* **11**, p. 5256, 2004.
[17] S. Y. Kalmykov et al. *Phys. Plasmas* **18**, p. 056704, 2011.
[18] F. Y. Li et al. *Phys. Rev. E: Stat., Nonlinear, Soft Matter Phys.* **90**, p. 043104, 2014.
[19] D. Lu et al. *Phys. Plasmas* **20**, p. 063104, 2013.
[20] A. G. R. Thomas. *Phys. Plasmas* **17**, pp. 1–12, 2010.
[21] M. R. Islam et al. *New J. Phys.* **17**, p. 093033, 2015.
[22] A. G. Khachatryan et al. *New J. Phys.* **10**, pp. 1–12, 2008.

[*] At the time of writing.

those applications of XUV and X-ray radiation which require monochromatic or coherent beams.[3] Therefore, to make the LWFA a tuneable light source requires either an external wiggler magnet, essentially a LWFA-driven synchrotron source or free-electron laser (FEL),[23,24] or an alternative scheme for controlling the emission bandwidth.

1.2 Aims of the Thesis

For a particle accelerator to be useful it should not just provide accelerated particles, but do so in a controllable and repeatable manner. This is particularly important for realising the full potential of the LWFA as an inexpensive and compact machine, which would enable its widespread use in academic, industrial and clinical contexts. Therefore, an important next step in LWFA research is to develop methods to control the process of self-injection. To date, control schemes which use laser intensity and plasma density modulation, plasma ionisation,[25] colliding laser pulses,[26] and magnetic field gradients,[27] have been suggested and demonstrated.

The aim of this thesis is to develop a method for controlling self-injection in the LWFA and investigate its impact on subsequently emitted radiation. It is divided broadly into three parts. In chapters 2 and 3 the theoretical background for plasma-based accelerators and radiation production is described. Chapter 4 develops a theoretical model for the control of self-injection using arbitrary density modulations in the plasma. This is investigated and validated using PIC simulations. It is shown that both the injected bunch length and charge can be controlled in this manner, and that the injection of trains of multiple bunches is possible. In chapter 5 the application of these results to controlling and tuning

---

[23] M. Fuchs et al. *Nat. Phys.* **5**, pp. 826–829, 2009.

[24] A. Bernhard et al. *Nucl. Instrum. Methods Phys. Res., Sect. A*,, 2017.

[25] B. Hidding et al. *Proc. AIP* **1507**, pp. 570–575, 2012.

[26] M. Zeng et al. *Phys. Rev. Lett.* **114**, p. 084801, 2015.

[27] J. Vieira et al. *Phys. Rev. Lett.* **106**, p. 225001, 2011.

the emittted radiation is considered. Bunching of the beam is shown to provide frequency dependent coherent enhancement, allowing enhancement of the broadband single-bunch emission spectrum within a narrow frequency window. The robustness of this effect with respect to energy spread of the beam is considered and the scheme is shown to be viable for tuning in the XUV range for current state-of-the-art LWFAs. Finally the results are summarised and the potential for future developments is discussed in chapter 6.

Chapter 2

The Laser-Electron Interaction

The first building block in understanding laser wakefield acceleration is the laser-electron interaction. Although the laser-plasma interaction is characterised by collective effects, these depend upon individual electrons reacting to irradiation by an intense laser pulse. This chapter provides a brief overview of the physical concepts required to build a theoretical description of the LWFA and the radiation emitted by the electrons accelerated within it. Beginning with Maxwell's equations for electromagnetism we consider electromagnetic plane waves as an approximation for intense laser radiation and the single electron response to such fields. We then discuss the issue of self-consistent solutions for the motion of N-body systems of charges in such fields and the numerical techniques used by PIC codes to model these systems. The emission of radiation by accelerated electrons is then discussed, including the calculation of the frequency spectrum of the emitted spectrum, and the interference effects of emission from multiple particles. Finally, common strategies for the numerical calculation of radiation emitted by electron bunches are outlined and their relative accuracy considered.

2.1 Electromagnetism

Laser light, like all other forms of electromagnetic radiation, interacts with charges and currents via the electromagnetic force. The interaction between a charge distribution $\rho(\bar{x}, t)$, and current density distribution $\bar{J}(\bar{x}, t)$, and electric and magnetic fields $\bar{E}(\bar{x}, t)$ and $\bar{B}(\bar{x}, t)$ is described in the classical limit by Maxwell's famous equations:

$$\begin{aligned} \nabla \cdot \bar{E} &= \frac{\rho}{\varepsilon_0} \quad & \nabla \times \bar{E} &= -\frac{\partial \bar{B}}{\partial t} \\ \nabla \cdot \bar{B} &= 0 \quad & \nabla \times \bar{B} &= \mu_0 \bar{J} + \frac{1}{c^2}\frac{\partial \bar{E}}{\partial t}. \end{aligned} \tag{2.1}$$

The electric and magnetic fields may also be expressed in terms of a vector and scalar potential pair $\bar{A}$ and ϕ,

$$\begin{aligned} \bar{E} &= -\nabla\phi - \frac{\partial \bar{A}}{\partial t} \\ \bar{B} &= \nabla \times \bar{A}. \end{aligned} \tag{2.2}$$

Using the relations above we can write the source terms ϕ and $\bar{J}$ in terms of the potentials

$$\begin{aligned} \nabla^2\phi + \nabla \cdot \frac{\partial \bar{A}}{\partial t} &= -\frac{\rho}{\varepsilon_0} \\ \frac{1}{c^2}\frac{\partial^2 \bar{A}}{\partial t^2} - \nabla^2 \bar{A} + \nabla\left(\nabla \cdot \bar{A} + \frac{1}{c^2}\frac{\partial \phi}{\partial t}\right) &= \mu_0 \bar{J}. \end{aligned} \tag{2.3}$$

This gives two coupled inhomogeneous equations that can be solved to find $\bar{A}$ and ϕ from the source terms. However, if one attempts to do this directly, it becomes apparent that the system has redundant degrees of freedom in the potentials which admit many possible solutions. A solution therefore requires some additional constraint that reduces the space of solutions to a single, complete and unambiguous set.

2.1.1 Gauge Fixing

Considering the definitions of the electric and magnetic fields in terms of the vector and scalar potentials, we see that the magnetic field is defined purely as the curl of the vector potential. This means that under a transformation of the vector potential, which adds a purely irrotational component

$$A \mapsto A' = A + \nabla\psi, \tag{2.4}$$

the magnetic field will remain unchanged

$$\bar{B} = \nabla \times \left(\bar{A} + \nabla\psi\right) = \nabla \times \bar{A}. \tag{2.5}$$

The electric field, on the other hand, is affected by such a transformation of the vector potential, and so the scalar potential must undergo a related transformation to cancel the effect,

$$\phi \mapsto \phi' = \phi - \frac{\partial\psi}{\partial t}. \tag{2.6}$$

As we have discussed above, imposing an additional constraint upon the system restricts this redundant degree of freedom. Whilst there are infinitely many valid choices for this additional constraint, it is typically chosen to simplify the calculations we wish to perform.

2.1.2 The Lorenz Gauge

Consider a constraint of the form

$$\nabla \cdot \bar{A} + \frac{\partial\phi}{\partial t} = 0, \tag{2.7}$$

which is commonly known as the *Lorenz* gauge. Applying this constraint to the potentials allows the inhomogeneous equations (2.3) to be decoupled, giving a pair of inhomogeneous wave equations, one for ϕ and one for $\bar{A}$:

$$\nabla^2\phi - \frac{1}{c^2}\frac{\partial^2\phi}{\partial t^2} = -\frac{\rho}{\varepsilon_0}, \tag{2.8}$$

$$\nabla^2\bar{A} - \frac{1}{c^2}\frac{\partial^2\bar{A}}{\partial t^2} = -\mu_0\bar{J}. \tag{2.9}$$

We can also show that for any potentials $\bar{A}$ and ϕ, a function ψ always exists that allows transformation to potentials satisfying the Lorenz gauge condition.

Assuming that such a function ψ exists, then, because the transformed potentials satisfy the Lorenz condition,

$$\nabla \cdot \bar{A}' + \frac{1}{c^2}\frac{\partial \phi}{\partial t} = 0, \tag{2.10}$$

$$\nabla \cdot \left(\bar{A} + \nabla\psi\right) + \frac{1}{c^2}\frac{\partial}{\partial t}\left(\phi + \frac{1}{c^2}\frac{\partial \psi}{\partial t}\right) = 0, \tag{2.11}$$

the function ψ is related to the original potentials by

$$\nabla \cdot \bar{A} + \frac{1}{c^2}\frac{\partial \phi}{\partial t} = \frac{1}{c^2}\frac{\partial^2 \psi}{\partial t^2} - \nabla^2\psi. \tag{2.12}$$

Because the LHS of (2.12) is a known quantity, and as the RHS is in the form of the d'Alembertian acting on ψ, which has the property of always being invertible, there always exists a family of solutions for ψ. This means that even in the case of a potential satisfying the Lorenz gauge condition, there remains a restricted family of transformations that continue to satisfy the Lorenz gauge,

$$\begin{aligned} \bar{A} &\mapsto \bar{A}' + \nabla\psi, \\ \phi &\mapsto \phi' + \frac{1}{c^2}\frac{\partial \psi}{\partial t}, \end{aligned} \tag{2.13}$$

provided

$$\nabla^2\psi - \frac{1}{c^2}\frac{\partial^2 \psi}{\partial t^2} = 0. \tag{2.14}$$

For any choice of *gauge fixing condition*, a set of potentials that satisfy the condition are known as *gauge potentials* and a function that maps arbitrary potentials to gauge potentials a *gauge function*.

2.1.3 The Coulomb Gauge

Another commonly chosen gauge condition is

$$\nabla \cdot \bar{A} = 0. \tag{2.15}$$

This has the useful property that the scalar potential satisfies the Poisson equation

$$\nabla^2\phi = -\frac{\rho}{\varepsilon_0} \tag{2.16}$$

and therefore the scalar potential is the instantaneous electrostatic coulomb potential, hence this gauge is typically known as the *Coulomb gauge*. Note that in the absence of a charge density ρ any potentials that satisfy the Coulomb condition will also satisfy the Lorenz condition, because the Lorenz condition is a generalisation of the Coulomb condition.

2.2 Electromagnetic Radiation

In the absence of any free charges or currents, the inhomogeneous wave equations in the Lorenz gauge become the homogeneous equations

$$\begin{aligned} \nabla^2\phi - \frac{1}{c^2}\frac{\partial^2\phi}{\partial t^2} &= 0 \\ \nabla^2\bar{A} - \frac{1}{c^2}\frac{\partial^2\bar{A}}{\partial t^2} &= 0, \end{aligned} \tag{2.17}$$

and while there are admissible solutions for the case that the vector potential $\bar{A} = 0$, they are electrostatic solutions to Laplace's equation that do not permit radiation. Solutions with non-zero $\bar{A}$ admit travelling waves, and as there are many classes of valid solutions, there is freedom to craft radiation packets with interesting properties.

2.2.1 The Plane Wave Solution

We will initially concern ourselves with the class of solutions of the form

$$\begin{aligned} &\bar{A} = \bar{A}_0\, \mathrm{e}^{i\left(\bar{k}\cdot\bar{x}-\omega t\right)}, \\ &\phi = 0, \end{aligned} \tag{2.18}$$

where $\bar{A}_0$ is a complex constant. These solutions represent plane waves with frequency ω, travelling in the direction of the wavevector $\bar{k}$. The amplitude and polarization of the plane wave are encoded into the vector amplitude $\bar{A}_0$. The electric and magnetic fields associated with this follow from (2.2),

$$\begin{aligned}\bar{E} &= \mathbf{Re}\left[-i\omega\bar{A}_0\,\mathrm{e}^{i\left(\bar{k}\cdot\bar{x}-\omega t\right)}\right] = -\omega\bar{A}_0\sin\left(\bar{k}\cdot\bar{x}-\omega t\right),\\ \bar{B} &= \mathbf{Re}\left[i\left(\bar{k}\times\bar{A}_0\right)\,\mathrm{e}^{i\left(\bar{k}\cdot\bar{x}-\omega t\right)}\right] = \left(\bar{k}\times\bar{A}_0\right)\sin\left(\bar{k}\cdot\bar{x}-\omega t\right),\end{aligned} \tag{2.19}$$

assuming that $\bar{A}_0$ is real. Note that although we only take the real part of the expressions for the physical fields, the complex nature of the vector potential is important, as it allows the encoding of complex phase information. It should also be noted that Maxwell's equations further constrain the valid choices of potential amplitude $\bar{A}_0$. In the absence of a charge density ρ both the $\bar{E}$ and $\bar{B}$ fields must be divergence free, and we therefore find that:

$$\begin{aligned}\nabla\cdot\bar{E} = 0 &= \nabla\cdot\left(-i\omega\bar{A}_0\,\mathrm{e}^{i\left(\bar{k}\cdot\bar{x}-\omega t\right)}\right)\\ &= -i\,\mathrm{e}^{i\left(\bar{k}\cdot\bar{x}-\omega t\right)}\left(\bar{k}\cdot\bar{A}_0\right).\end{aligned} \tag{2.20}$$

The $\bar{B}$ field is the curl of the vector potential, therefore it is, by definition, always divergence free. Therefore, this constraint simplifies to the requirement that the wavevector is orthogonal to the potential

$$\bar{k}\cdot\bar{A}_0 = 0. \tag{2.21}$$

Because $\bar{E}$ is parallel to the vector potential, and $\bar{B}$ perpedicular to it (2.2), we find that for plane wave radiation propagating in vacuum, the electric and magnetic fields are perpedicular both to each other, and to the propagation direction of the wave.

2.2.2 Applicability of the Plane Wave Solution

Since the plane wave solution has no spatial dependence in the plane perpendicular to the wavevector, it is infinite in extent in this plane. This is unphysical and cannot exist in reality. Nevertheless, the plane wave solution is still an extremely powerful and much used tool. It is useful for approximating real-world radiation, for example, in understanding the interaction of electrons with intense laser radiation.

Due to its infinite power and extent the plane wave cannot be used as a model system for the evolution of a laser in plasma, however it is useful as a model for understanding the interactions of a system with intense laser radiation.

Consider, for example, an electron irradiated by a highly intense laser beam that has an approximately flat intensity profile in the plane transverse to the wavevector. In this case, provided the width of this “flat section” is large compared to the laser wavelength, it can be approximated as a plane wave. This can be shown by considering a potential with a transverse component as described and a longitudinal component that is required to remove the divergence of the fields:

$$\bar{A} = A_x(y)\,\mathrm{e}^{i(kx-\omega t)}\hat{x} + A_y(y)\,\mathrm{e}^{i(kx-\omega t)}\hat{y}. \tag{2.22}$$

For simplicity we make the assumption that the components A_i vary only in the y-direction. If we now take the divergence of the $\bar{E}$ field produced by such a potential we find the relationship that must be satisfied by these components in order to describe a divergence free field,

$$\begin{aligned} 0 = \nabla\cdot\bar{E} = -\nabla\cdot\frac{\partial\bar{A}}{\partial t} &= i\omega\nabla\cdot\bar{A}, \\ \implies \frac{\partial A_y}{\partial y}\,\mathrm{e}^{i(kx-\omega t)} &= -ikA_x\,\mathrm{e}^{i(kx-\omega t)}. \end{aligned} \tag{2.23}$$

If we now make the assumption that A_y varies with a characteristic length scale $k_\perp$, we may use a Fourier transform to approximate its derivative,

$$\begin{aligned} A_y &= \int \tilde{A}\,\mathrm{e}^{iky}\,\mathrm{d}k \sim \tilde{A}(k_\perp) \\ \implies \frac{\partial A_y}{\partial y} &= i\int k\tilde{A}\,\mathrm{e}^{iky}\,\mathrm{d}k \sim ik_\perp\tilde{A}(k_\perp). \end{aligned} \tag{2.24}$$

Taking advantage of the fact that the Fourier integral of A_y is dominated by the value of $\tilde{A}(k_\perp)$ and substituting this back into the relation obtained in (2.23), we see that the ratio of the longitudinal to transverse components is proportional to the ratio of the scale lengths of the components,

$$\frac{A_x}{A_y} \sim \frac{k_\perp}{k} \tag{2.25}$$

This implies that in the limit that the scale length of changes in the transverse envelope is much larger than the laser wavelength, we may neglect the longitudinal component of the potential and approximate the laser as a plane wave.

2.2.3 The Normalised Vector Potential

When working with the plane wave approximation of a laser pulse it is often useful to parameterise the intensity in terms of its effect on a particle in the laser field. It is usual to normalise the laser vector potential to units of the electron mass, as

$$a_0 = \frac{eA_0}{m_e c}, \tag{2.26}$$

where e is the fundamental charge, m_e the electron mass and c the speed of light in vacuum. This means that the value $a_0 = 1$ delineates the boundary between the regimes where the electron motion is non-relativistic $a_0 << 1$ and highly relativistic $a_0 > 1$.

The vector potential is related to the laser intensity by

$$I = \frac{4\pi^2 c^3 m_e^2}{e^2 \mu_0} \frac{a_0^2}{\lambda_0^2}, \tag{2.27}$$

which follows from the Poynting vector that gives the energy flux through a surface normal to the laser propagation direction (see section 2.7.2).

2.3 Single Electron Motion in a Laser Field

Consider the motion of an electron in a laser field of constant small amplitude such that the motion is non-relativistic:

$$\bar{A} = A_0 \,\mathrm{e}^{i(kz-\omega t)} \hat{x}. \tag{2.28}$$

This leads to electric and magnetic field components

$$\bar{E} = -iA_0 \omega \,\mathrm{e}^{i(kz-\omega t)} \hat{x}, \tag{2.29}$$

$$\bar{B} = iA_0 k \,\mathrm{e}^{i(kz-\omega t)} \hat{y}. \tag{2.30}$$

Using the Lorentz force $\bar{F} = q\bar{E} + \bar{v} \times \bar{B}$ we write the equations of motion for the electron,

$$\frac{\mathrm{d}P_x}{\mathrm{d}t} = \left(eA_0\omega + \frac{eA_0k}{m}P_z \right) i\,\mathrm{e}^{ikz-\omega t}, \tag{2.31}$$

$$\frac{\mathrm{d}P_y}{\mathrm{d}t} = 0, \tag{2.32}$$

$$\frac{\mathrm{d}P_x}{\mathrm{d}t} = -\frac{eA_0k}{m}P_x i\,\mathrm{e}^{ikz-\omega t}, \tag{2.33}$$

where P_x, P_y, P_z are the components of the momentum in x, y, z. Because the motion is non-relativistic $P_z << mc$, and the P_z term in (2.31) may be neglected as negligible compared to the term due to E_0. Writing $A_0k = A_0\omega/c$, we get an approximate solution for the non-relativistic motion:

$$P_x = -eA_0\,\mathrm{e}^{i(kz-\omega t)} + P_{x,0} \tag{2.34}$$

$$P_y = P_{y,0} \tag{2.35}$$

$$P_z = -\frac{e^2A_0^2}{2mc}\,\mathrm{e}^{2i(kz-\omega t)} + \frac{eA_0P_{x,0}}{mc}\,\mathrm{e}^{i(kz-\omega t)} + P_{z,0}. \tag{2.36}$$

An analytic solution may also be found for the relativistic case, as described for example by Krüger and Bovyn[28] or Sarachik and Schappert[29]. In this case the equations of motion are solved with respect to the proper time τ, however it is not reproduced here as the fine-scale motion of the electrons within the laser pulse is not directly useful to the discussion of laser wakefield acceleration.

2.4 The Ponderomotive Approximation

So far we have considered the fine scale motion of an electron the laser pulse, however, in many cases we are not interested in the fine details of the electron motion within the laser pulse, but desire an expression for the final results of the interaction. For example we may consider the electron-laser interaction as a

---

[28] J. Kruger and M. Bovyn. *J. Phys. A: Math. Gen.* **9**, pp. 1841–1846, 1976.

[29] E. Sarachik and G. Schappert. *Phys. Rev. D: Part. Fields* **1**, pp. 2738–2753, 1970.

scattering event, where given momentum and impact parameter for an incoming electron we may find an outgoing momentum and trajectory. Such an approximation exists, known as the "ponderomotive" approximation,* and is found by taking the average over the fast oscillatory motion to find the motion of the guiding centre.

There are many derivations of the ponderomotive force in the literature.[30,31] However, the simplest qualitative understanding follows from the approach taken by Gibbon,[32] which considers the motion of an electron moving in a laser plane wave, the form of which can be split into fast and slow timescales

$$\bar{A}(\bar{r},t) = \bar{A}_0(\bar{r},t)\,\mathrm{e}^{-i\omega t}. \tag{2.37}$$

Here the exponential component represents the rapid oscillation of the field and $\bar{A}_0(\bar{r},t)$ is an amplitude envelope function, which may either be constant w.r.t. time or vary slowly compared to the laser period. The equation of motion for an electron in this field is given by the Lorentz force,

$$\frac{\mathrm{d}\bar{p}}{\mathrm{d}t} = -q\left[\frac{\partial \bar{A}}{\partial t} - \bar{v}\times\left(\nabla\times\bar{A}\right)\right] = -q\left[\frac{\mathrm{d}\bar{A}}{\mathrm{d}t} - \nabla_A\left(\bar{v}\cdot\bar{A}\right)\right], \tag{2.38}$$

where the vector cross product has been expanded to recover the total derivative of $\bar{A}$ w.r.t time, and the second term uses Feynman subscript notation to denote the gradient operation acts only on $\bar{A}$.† The final term contains the spatial derivative of $\bar{A}$ which provides the laser envelope contributions to the average motion of the particle.

---

[30] J. D. Lindl. *Phys. Fluids* **14**, p. 371, 1971.

[31] D. Bauer et al. *Phys. Rev. Lett.* **75**, pp. 4622–4625, 1995.

[32] P. Gibbon. *Short Pulse Laser Interactions with Matter: An Introduction*, Imperial College Press, 2007.

[*] It appears to be common practice in the literature to refer to the "ponderomotive force", however this is inaccurate. The force causing motion remains the Lorentz force of which a gross timescale approximation is made, with accompanying caveats on the limitations to its accuracy.

[†] This may be expressed as $v_i \partial_j A_i$, which follows from expanding the vector triple product using the Levi-Civita symbol and the identity $\varepsilon_{ijk}\varepsilon_{ilm} = \delta_{jl}\delta_{km} - \delta_{jm}\delta_{lk}$.

The motion is similarly split into a fast component, varying at timescales of the order of the laser period, and a component that evolves slowly compared with this. The momenta are denoted $\bar{p}_f$ and $\bar{p}_s$ respectively, and taking the average over one laser cycle ($\langle \ldots \rangle$), gives

$$\frac{\mathrm{d}\bar{p}_f}{\mathrm{d}t} = -q\frac{\mathrm{d}\bar{A}}{\mathrm{d}t}, \qquad \frac{\mathrm{d}\bar{p}_s}{\mathrm{d}t} = \left\langle q\nabla_A \left(\bar{v}\cdot\bar{A}\right)\right\rangle. \tag{2.39}$$

Upon averaging over a laser cycle we find that the fast timescale component vanishes and we need only consider the envelope contribution to the motion.

Using the relation $\bar{p} = \gamma m v$ we may replace the expression for velocity in the slow timescale motion by taking the cycle average of the Lorentz factor

$$\begin{aligned} \langle\gamma\rangle &\simeq \sqrt{1 + p_s^2/m^2c^4 + \langle p_f^2\rangle/m^2c^4} \\ &= \sqrt{1 + p_s^2/m^2c^4 + \langle a^2\rangle} \\ &= \sqrt{1 + p_s^2/m^2c^4 + \chi a_0^2} \end{aligned} \tag{2.40}$$

where the average of fast component of the momentum is given by the r.m.s of the normalised laser vector potential, which may be written in terms of the peak laser intensity a_0, where $\chi = 1/2$ for a linearly polarised laser and $\chi = 1$ for a circularly polarised laser. This allows the equation for the average motion to be expressed as the usual ponderomotive approximation

$$\frac{\mathrm{d}p_s}{\mathrm{d}t} \simeq mc^2\frac{1}{\langle\gamma\rangle}\left\langle \bar{A}\cdot\left(\nabla\cdot\bar{A}\right)\right\rangle = -mc^2\nabla\langle\gamma\rangle. \tag{2.41}$$

2.5 The Vlasov-Maxwell Description of Plasma

So far we have considered the electron-laser interaction in isolation, however, the electrons we are considering are part of an electron-ion plasma, formed in the LWFA through the ionisation of gas atoms by the laser. For typical LWFA experiments the plasma will have electron and ion number densities on the order of 10^{23}–10^{25} m^{-3}. At these densities the plasma is approximately collisionless, and so long-range coloumb interactions will dominate the plasma behaviour.

The behaviour of the electron-ion plasma is described by the Vlasov-Maxwell equations[33]

$$\begin{aligned}\frac{\partial f_e}{\partial t} + \bar{v}_e \cdot \nabla f_e - e\left(\bar{E} + \bar{v}_e \times \bar{B}\right)\frac{\partial f_e}{\partial \bar{p}} = 0,\\ \frac{\partial f_i}{\partial t} + \bar{v}_i \cdot \nabla f_i - Z_i e\left(\bar{E} + \bar{v}_i \times \bar{B}\right)\frac{\partial f_i}{\partial \bar{p}} = 0,\\ \nabla \cdot \bar{E} = \frac{\rho}{\varepsilon_0}, \quad \nabla \times \bar{E} = -\frac{\partial \bar{B}}{\partial t},\\ \nabla \cdot \bar{B} = 0, \qquad \nabla \times \bar{B} = \mu_0 \bar{J} + \frac{1}{c^2}\frac{\partial \bar{E}}{\partial t}.\end{aligned} \tag{2.42}$$

These extend Maxwell's equations using a distribution function for the electrons and ions in the plasma and a continuity equation for each species. This provides a self-consistent model of the collisionless plasma system, where arbitrary boundary conditions such as an impinging high-intensity laser pulse can be implemented.

For a relativistic electron-ion plasma the quantities ρ, $\bar{J}$ and species velocity $\bar{v}_\alpha$ are given by

$$\begin{aligned}\rho &= e\int \left(Z_i f_i - f_e\right) \mathrm{d}[3]p\\ \bar{J} &= e\int \left(Z_i f_i \bar{v}_i - f_e \bar{v}_e\right) \mathrm{d}[3]p\\ \bar{v}_\alpha &= \frac{1}{m_\alpha}\frac{\bar{p}}{\sqrt{1+\frac{p^2}{m_\alpha^2 c^2}}}\end{aligned} \tag{2.43}$$

where Z_i is the ion charge and m_α the species rest mass. Because of the complexity of the problem numerical simulation is the only method available to solve the Vlasov-Maxwell equations for non-trivial systems.

2.6 Simulating Plasma Physics Problems: The Need for Fully Self-Consistent Modelling

The complexity of plasma systems arise from the fact that they contain many particles, and are therefore a class of n-body problems with no guaranteed analytic solutions. While approximate analytic methods are extremely useful for advancing

---

[33] P. M. Bellan. *Fundamentals of Plasma Physics*, Cambridge University Press, 2006.

the understanding of plasma processes, there is also a need for validation through fully self-consistent numerical modelling. This is particularly important in the cases of high energy density plasma systems such as LWFA, which exhibit many forms of complex non-linear behaviour.[33]

There are multiple potential approaches to the modelling of plasmas, the main approaches typically using magneto-hydrodynamic, Vlasov-Maxwell or explicit relativistic electrodynamic descriptions of the plasma system. For the domain of plasma-based accelerators the primary method of simulation is through PIC codes, which model the plasma through the electrodynamics of the constituent particles.

2.6.1 Particle-In-Cell Codes

PIC codes are implemented by explicitly numerically integrating the Vlasov-Maxwell equations with respect to time, a scheme which is usually termed a finite-difference time-domain (FDTD) method.[34,35] The electron and ion distribution functions are represented in the simulation by a collection of discrete pseudoparticles, each representing a large number of individual electrons or ions. The resulting individual charges and currents due to these particles are "deposited" onto a grid of cells and the electric and magnetic fields computed at each grid node. These fields are then interpolated back to the position of each particle, the Lorenz force on the particle calculated, and the particle motion over the timestep calculated. The size of timestep is important to the stability and accuracy of the algorithm, and must be less than, but similar in magnitude to, the Courant-Friedrichs-Lewy (CFL) condition to guarantee good convergence and eliminate numerical instability.[36] This basic algorithm, shown schematically in section 2.6.1,

---

[34] C. K. Birdsall and A. B. Langdon. *Plasma physics via computer simulation*, McGraw-Hill, 1985.

[35] K. S. Yee. *IEEE Trans. Antennas Propag.* **14**, pp. 302–307, 1966.

[36] B. M. Cowan et al. *Phys. Rev. Spec. Top. Accel Beams* **16**, p. 041303, 2013.

is applied many tens of thousands of times, until the simulation has covered the desired time period.

Typically FDTD schemes are designed to maximise calculation accuracy while minimizing computational cost. The most commonly implemented scheme is the "Yee" scheme,[35] which uses a "leapfrog" scheme, with the electric and magnetic field grids staggered in space and time. This method is used to avoid the instability inherent in simpler schemes with co-located electric and magnetic field components, and reduced (though non-zero) numerical dispersion compared to these simpler methods.[34] FDTD schemes such as the Yee scheme are numerically stable provided the CFL condition is met, and can be constructed to provide arbitrary accuracy - the standard Yee scheme is accurate to second order in both space and time. This approach can also be extremely effectively parallelised over a large number of CPUs due to its mesh structure, allowing scaling of simulations to many thousands of cores on a high performance computer (HPC).[37]

As in the case of the field solver, the particle "pusher" which updates particle position and velocity at each timestep requires careful treatment to ensure correctness. Simple forward integration has large error leading to numerical acceleration of the particles. While in theory this can be solved using implicit integration methods, these are comparatively expensive, and so instead the most popular solution is the Boris algorithm.[34] This uses a time centered leap-frog method to integrate the force due to the electric field, which treating the magnetic field as a phase space rotation which cannot introduce any error in the particle energy. Although this pusher is computationally efficient, it is not Lorentz-invariant and so suffers from inaccuracies for ultra-relativistic beams. To combat this an alternative pusher that is commonly used is the Vay pusher[38], which is Lorent invariant but more computationally expensive. The version of the EPOCH PIC code used in this thesis implements the Boris pusher while FBPIC implements a Vay pusher.

---

[37] T. D. Arber et al. *Plasma Phys. Controlled Fusion* **57**, p. 113001, 2015.

[38] J.-L. Vay et al. *J. Comput. Phys.* **230**, pp. 5908–5929, 2011.

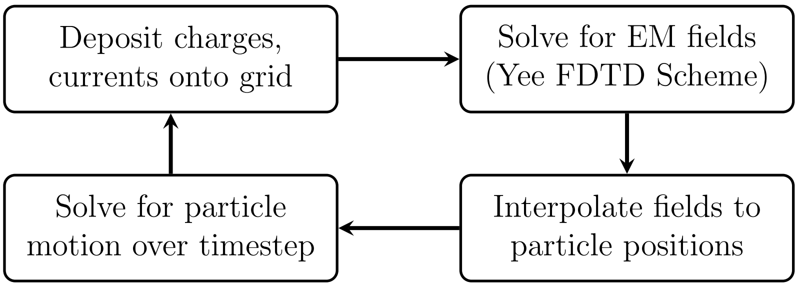

Figure 2.1: General Outline of the Particle-In-Cell algorithm.

2.6.2 Geometric Considerations

In this thesis simulations are performed in both 2-D and 3-D cartesian geometries using the EPOCH[37] code, as well as the 3D cylindrical modal decomposition of the FBPIC[39] code. The difference in geometry between the 2-D and 3-D cases leads to different quantative behaviour between 2-D and 3-D simulations of a LWFA setup with otherwise identical parameters. These effects include the propagation behaviour of the laser in the plasma[40,41] in addition to the reaction of the electrons to the laser and the electron plasma wave properties.[1,42] These geometric differences can be seen by considering the conserved quantity of laser action,

$$\mathcal{A} = \int_V (\varepsilon_0 \bar{E}^2 + \frac{1}{\mu_0}\bar{B}^2) d^3\bar{x}, \tag{2.44}$$

which scales as $a_0^2 w^2$ in 3-D and $a_0^2 w$ in 2-D, where w is the laser pulse waist.

Of particular relevance in this thesis will be the difference in the energy gained by electrons from interaction with the laser, as will be discussed in chapter 4. The expression for the ponderomotive approximation, (2.41) above, is valid for both of these cases, however, the differing geometries must be accounted for when calculating the effects of the laser on the plasma. Integrating the expression for the ponderomotive force over a symmetrical pulse yields an approximation for the

---

[39] R. Lehe et al. *Comput. Phys. Commun.* **203**, pp. 66–82, 2015.
[40] C. D. Decker et al. *IEEE Trans. Plasma Sci.* **24**, pp. 379–392, 1996.
[41] K. C. Tzeng and W. B. Mori. *Phys. Rev. Lett.* **81**, pp. 104–107, 1998.
[1] M. P. Tooley et al. *Phys. Rev. Lett.* **119**, p. 044801, 2017.
[42] M. Zeng et al. *Phys. Plasmas* **21**, 2014.

total energy of an electron scatter by the laser

$$\gamma_e \sim g\sqrt{1 + \chi a_0^2}, \tag{2.45}$$

where $g = 2$ in the 3-D case, and $g = 1$ in the 2-D case, which follows from the form of the gradient in the differing geometries.

2.6.3 Simulation Convergence

A key consideration for any numerical method is that of convergence of the solver to the correct solution. In the case of PIC simulation this requires that the resolution of the field grids, and the pseudoparticle number density are both sufficiently high to fully and correctly resolve the dynamics of interest.

For all simulations in this thesis convergence of the simulations was confirmed empirically for each combination of code, dimensionality, and plasma density. The process was performed as follows: An initial choice for the grid resolution was made to ensure the laser pulse was well resolved longitudinally and the plasma wavelength was well resolved in the transverse direction, as these are the shortest physically relevant wavelengths. The initial choice of number of particles per cell was 8. Having run simulations with these parameters, additional simulations were performed with both reduced and increased cell size and number of particles. The relevant quantitative analysis was performed on the various simulations to ensure that differences were negligible ($\ll 1\%$) thus ensuring that the simulations were being performed in a regime that was insensitive to changes in cell size and particle number.

2.7 Electromagnetic Radiation from Charged Particles

The second major focus of this thesis is on the production of radiation by accelerating electron bunches in the LWFA. The classical theory of radiation production, described below, lays the groundwork for this investigation. We begin by considering the radiation field due to a single charged particle. This follows the approach used by Jackson[43] and leads to an invariant formulation of the famous Liénard-Wiechert potentials for radiation by a charged particle.

The starting point is the inhomogeneous wave equation for the vector field A^α with source current J^β:

$$\Box A^\alpha(x) - \partial^\alpha(\partial_\beta A^\beta) = \mu_0 J^\alpha. \tag{2.46}$$

Choosing the Lorentz gauge $\partial_\alpha A^\alpha = 0$ ensures that the potentials are solutions to the wave equation,

$$\Box A^\alpha = \mu_0 J^\alpha, \tag{2.47}$$

which may be found through the use of Green's functions. In the case of a free particle with no boundary surfaces in the system, there exists a pair of such functions[43,44]:

$$D_r(\mathbf{x}-\mathbf{r}) = \frac{1}{2\pi}\theta(x_0 - r_0)\delta([\bar{x}-\bar{r}]^2), \tag{2.48}$$

$$D_a(\mathbf{x}-\mathbf{r}) = \frac{1}{2\pi}\theta(r_0 - x_0)\delta([\bar{x}-\bar{r}]^2), \tag{2.49}$$

where the four-vector $\mathbf{r}$ is the integration variable and $\mathbf{x}$ the observation point. The physical implications of these functions can be seen by considering the effect of the Heaviside step (θ) and Dirac delta (δ) functions on the points $\mathbf{r}$ that contribute to the field at $\mathbf{x}$. The function D_r, known as the "retarded" or "causal"

---

[43] J. Jackson. *Classical Electrodynamics, 3^{rd} ed.* Wiley, 1999.

[44] M. Kaku. *Quantum Field Theory: A Modern Introduction*, Oxford University Press, 1993.

Green's function, vanishes in the case that $r_0 > x_0$, and therefore in using this function we restrict contributions to the field at $\mathbf{x}$ to events that occur prior to the observation time. In the opposite case, the "advanced" Green's function D_a considers only events that occur after the observation time. The delta function term is an expression of the light-cone condition which restricts consideration of events contributing to the radiation field at $\mathbf{x}$ to those which occur on the light cone of the point $\mathbf{x}$.

Use of these Green's functions gives solutions

$$A^\alpha(\mathbf{x}) = A^\alpha_{in} + \mu_0 \int \mathrm{d}^4\mathbf{r}\, D_r(\mathbf{x}-\mathbf{r}) J^\alpha(\mathbf{x}), \tag{2.50}$$

$$A^\alpha(\mathbf{x}) = A^\alpha_{out} + \mu_0 \int \mathrm{d}^4\mathbf{r}\, D_a(\mathbf{x}-\mathbf{r}) J^\alpha(\mathbf{x}), \tag{2.51}$$

where A^α_{in} and A^α_{out} are solutions of the homogeneous wave equation, which may be interpreted as incident and outgoing radiation respectively, because the integral vanishes at $x_0 \to -\infty$ in the retarded case, and at $x_0 \to +\infty$ in the advanced case.

2.7.1 The Liénard-Wiechert Potentials

We now apply this general solution to the trajectory of a single particle in arbitrary motion. In this case the 4-current $J^\alpha(\mathbf{x}')$ has the form

$$J^\alpha(\mathbf{x}') = q \int \mathrm{d}\tau\, u^\alpha(\tau)\, \delta^4[\mathbf{x} - \mathbf{r}(\tau)], \tag{2.52}$$

where $\mathbf{r}(\tau)$ is the 4-position and $\mathbf{u}(\tau)$ the 4-velocity of the particle with respect to proper time τ.

As we are interested in the radiation emitted by a charged particle, causality dictates we find the solution using the retarded Green's function. If, in addition, we specify that there is no incident radiation then the solution will be purely the radiation emitted by the particle. Inserting the current density (2.52) and integrating over $\mathrm{d}^4\bar{r}$ gives an integral over the proper time

$$A^\alpha = \frac{q\mu_0}{2\pi}\int \mathrm{d}\tau\, u^\alpha(\tau)\theta[x_0 - r_0(\tau)]\,\delta([\bar{x} - \bar{r}(\tau)]^2) \tag{2.53}$$

where the theta function constrains evaluation to retarded times and the delta function constrains to contributions at $\tau = \tau_0$, which is an expression of the light cone constraint

$$[\bar{x} - \bar{r}(\tau_0)]^2 = 0. \tag{2.54}$$

Therefore, the only contribution to A^α comes from the retarded point $r^\alpha(\tau_0)$, and we can evaluate the integral using the delta function property

$$\delta[f(x)] = \sum_i \frac{\delta(x - x_i)}{|f'(x_i)|}, \tag{2.55}$$

where x_i are the roots of $f(x)$. Noting that

$$\frac{\mathrm{d}}{\mathrm{d}\tau}[\mathbf{x} - \mathbf{r}(\tau)]^2 = -2[\mathbf{x} - \mathbf{r}(\tau)]_\beta\, u^\beta(\tau), \tag{2.56}$$

we may use (2.55) to write the potential as

$$A^\alpha(\mathbf{x}) = \frac{q}{4\pi}\int \mathrm{d}\tau\, \frac{u^\alpha(\tau)\theta[\tau - \tau_0]}{|[\mathbf{x} - \mathbf{r}(\tau)]_\beta\, u^\beta(\tau)|}\delta(\tau - \tau_0). \tag{2.57}$$

Upon integration, the sifting property of the delta function, combined with the retardation requirement from the theta function yield the *Liénard-Wiechert* potential

$$A^\alpha(\bar{x}) = \frac{\mu_0}{4\pi}\frac{qu^\alpha(\tau)}{\mathbf{u}\cdot[\mathbf{x} - \mathbf{r}(\tau)]}\bigg|_{\tau=\tau_0}, \tag{2.58}$$

which is evaluated at the retarded time τ_0 as defined by (2.54).

This can be also written in the more familar, non-invariant form, by writing the distance from observer to source as $R \equiv x_0 - r_0(\tau) = |\bar{x} - \bar{r}(\tau)|$ and rewriting the scalar product

$$\begin{aligned}\bar{u}\cdot[\bar{x} - \bar{r}(\tau)] &= u_0[x_0 - r_0(\tau)] - \gamma\bar{u}\cdot[\bar{x} - \bar{r}(\tau)],\\ &= \gamma cR - \gamma\bar{u}\cdot\hat{n}R,\\ &= \gamma cR(1 - \bar{\beta}\cdot\hat{n}),\end{aligned} \tag{2.59}$$

where $\hat{n}$ is the unit vector in the direction of observation $[\bar{x} - \bar{r}(\tau)]$ and $\bar{\beta} = \bar{u}/c$. Recalling the four-vectors $\mathbf{A} = [\phi/c, \bar{A}]$ and $\mathbf{u} = \gamma[c, \bar{u}]$, we can write the scalar and three-vector potentials as

$$\phi(\bar{x}, t) = \frac{q}{4\pi\epsilon_0}\left[\frac{1}{(1 - \hat{n}\cdot\bar{\beta})R}\right]_{\text{ret}}, \quad \bar{A}(\bar{x}, t) = \frac{q\mu_0 c}{4\pi}\left[\frac{\bar{\beta}}{(1 - \hat{n}\cdot\bar{\beta})R}\right]_{\text{ret}}, \tag{2.60}$$

where "ret" requires the subscripted quantity be evaluated at the retarded time τ_0 given by the light cone condition (2.54). In the non-relativistic case $\beta \to 0$ these potentials reduce to the expected results for electro- and magnetostatic fields.

The field F^{α}_{β} can be found by directly differentiating the potential

$$F^{\alpha}{}_{\beta} = \partial_\alpha A^\beta - \partial^\alpha A_\beta, \tag{2.61}$$

however it is mathematically more straightforward to take the form of A^α before integration w.r.t τ (2.53) and exchange the order of operations. We differentiate with respect to $\bar{x}$ this time and therefore only act upon the theta and delta functions. The derivative of the theta function gives $\delta[x_0 - r(\tau_0)]$, which constrains this term to evaluation at $R = 0$. This may be safely disgarded as it represents a singularity due to a point charge located at the observation point. The remaining terms give

$$\partial^\alpha A_\beta = 2\mu_0 q \int \mathrm{d}\tau u_\beta(\tau)\, \delta[x_0 - r_0(\tau)]\partial^\alpha\theta([\mathbf{x} - \mathbf{r}(\tau)]^2), \tag{2.62}$$

and using the chain rule:

$$\partial^\alpha\delta[f] = \partial^\alpha f \cdot \frac{\mathrm{d}}{\mathrm{d}f}\theta[f] = \partial^\alpha f \cdot \frac{\mathrm{d}\tau}{\mathrm{d}f}\cdot\frac{\mathrm{d}}{\mathrm{d}\tau}\cdot\delta[f], \tag{2.63}$$

where $f = [\mathbf{x} - \mathbf{r}(\tau)]^2$, giving

$$\partial^\alpha A_\beta = \frac{q\mu_0}{2\pi}\int \mathrm{d}\tau \left[\frac{-(\mathbf{x} - \mathbf{r})^\alpha u_\beta}{\mathbf{u}\cdot(\mathbf{x} - \mathbf{r})}\right]\theta[x_0 - r_0(\tau)]\delta([\mathbf{x} - \mathbf{r}(\tau)]^2). \tag{2.64}$$

In the integration by parts the theta function does not give a contribution, and using the same substitution for $\theta[x_0 - r_0(\tau)]$ as previously,

$$F^{\alpha}{}_{\beta} = \frac{\mu_0}{4\pi}\frac{q}{\mathbf{u}\cdot[\mathbf{x} - \mathbf{r}(\tau)]}\frac{\mathrm{d}}{\mathrm{d}t}\left[\frac{[\mathbf{x} - \mathbf{r}(\tau)]^\alpha u_\beta - [\mathbf{x} - \mathbf{r}(\tau)]_\beta u^\alpha}{\mathbf{u}\cdot[\mathbf{x} - \mathbf{r}(\tau)]}\right]\Bigg|_{\tau=\tau_0}. \tag{2.65}$$

Expanding this yields the more intuitive non-invariant form

$$\begin{aligned}\bar{E}(\bar{x},t) &= \frac{q}{4\pi\epsilon_0}\left[\frac{\hat{n}-\bar{\beta}}{\gamma^2(1-\hat{n}\cdot\bar{\beta})^3R^2}\right]_{\text{ret}} + \frac{q}{4\pi\epsilon_0 c}\left[\frac{\hat{n}\times[(\hat{n}-\bar{\beta})\times\dot{\bar{\beta}}]}{(1-\hat{n}\cdot\bar{\beta})^3R}\right]_{\text{ret}}, \\ \bar{B}(\bar{x},t) &= \frac{1}{c}[\hat{n}\times\bar{E}]_{\text{ret}},\end{aligned} \tag{2.66}$$

which illustrates the fact that the field is made up of two components. The first term describes fields dependent only on the position and velocity of the particle. These are referred to as the "velocity fields" and have magnitude which scales with R^{-2}. They describe the fields due to a charge moving with constant velocity, and are the Lorentz transformation of the fields due to a static charge. The second term scales as R^{-1} and depends additionally on the acceleration of the particle. This, as we shall see, describes the radiation field due to the acceleration of the particle.

2.7.2 Poynting's Theorem and Propagating Radiation

To investigate the behaviour of propagating electromagnetic radiation we must consider the energy balance in the volume containing an emitting particle. The approach taken here is similar to that used by Poynting[43,45,46] when first deriving his eponymous theorem and associated vector.

Consider a volume of space V that contains both fields and charges. At any time the energy contained within the field may change through interaction with the particles within the volume, or as a result of the flow of radiation through the surface of the volume. We express this as an energy conservation equation

$$-\int_V \frac{\partial u(\bar{x})}{\partial t}\,\mathrm{d}^3\bar{x} = \frac{\mathrm{d}W(\bar{x})}{\mathrm{d}t} + \oint_s \bar{S}(\bar{x})\cdot\hat{n}\,\mathrm{d}a, \tag{2.67}$$

where u is the energy density of the field within the volume, W is the work done by the field on the charges within the volume and $\bar{S}$ is the energy flux of the field. (2.67) explicitly states that the rate of energy loss by the electromagnetic field

---

[45] J. H. Poynting. *Philos. Trans. Roy. Soc. London* **175**, pp. 343–361, 1884.

[46] A. Garg. *Classical Electrodynamics in a Nutshell*, Princeton University Press, 2012.

within any volume is equal to the rate of work done by that field on any charges within the volume, plus the net radiation flux through the surface of that volume.

Now consider the rate of work done on a charge distribution ρ per unit time:

$$\frac{\mathrm{d}W}{\mathrm{d}t} = \int_V \bar{F} \cdot \bar{v} \; \mathrm{d}^3\bar{x} = \int_V \rho(\bar{E} + \bar{v} \times \bar{B}) \cdot \bar{v} \; \mathrm{d}^3\bar{x} = \int_V \bar{J} \cdot \bar{E} \; \mathrm{d}^3\bar{x}, \tag{2.68}$$

where $\bar{F}$ denotes the Lorentz force acting on a charge at a point $\bar{x}$ and $\bar{v}$ the velocity of the charge at that point. To gain the form on the RHS we note that $\bar{J} = \rho\bar{v}$ and that the magnetic field does no work as the force is perpendicular to the motion.

The work done changes the energy contained within the field, which can be seen using the Maxwell-Ampère expression for the field due to the current density $\bar{J}$

$$\int_V \bar{J} \cdot \bar{E} \; \mathrm{d}^3\bar{x} = \int_V \left[(\nabla \times \bar{H}) - \frac{\partial \bar{D}}{\partial t} \right] \cdot \bar{E} \; \mathrm{d}^3\bar{x}. \tag{2.69}$$

Using the identity $\nabla \cdot (\bar{E} \times \bar{H}) = \bar{H} \cdot (\nabla \times \bar{E}) - \bar{E} \cdot (\nabla \times \bar{H})$ and the Maxwell-Faraday Law yields

$$\int_V \bar{J} \cdot \bar{E} \; \mathrm{d}^3\bar{x} = -\int_V \left[\nabla \cdot (\bar{E} \times \bar{H}) + \bar{H} \cdot \frac{\partial \bar{B}}{\partial t} + \bar{E} \cdot \frac{\partial \bar{D}}{\partial t} \right] \mathrm{d}^3\bar{x}, \tag{2.70}$$

which allows us to write

$$\int_V \frac{\partial u(\bar{x})}{\partial t} \, \mathrm{d}^3\bar{x} = -\int_V \bar{J} \cdot \bar{E} \; \mathrm{d}^3\bar{x} + \oint_s (\bar{E} \times \bar{H}) \cdot \hat{n} \, \mathrm{d}a. \tag{2.71}$$

We see that this result maps neatly onto the expected form of (2.67), where we identify the energy density of the field to be

$$u = \frac{1}{2} \left(\bar{D} \cdot \bar{E} + \bar{B} \cdot \bar{H} \right), \tag{2.72}$$

and the energy flux vector $\bar{S} = \bar{E} \times \bar{H}$.

The result (2.71) is Poynting's Theorem, which is more commonly seen in the differential form

$$\frac{\partial u}{\partial t} + \nabla \cdot \bar{S} = -\bar{J} \cdot \bar{E}, \tag{2.73}$$

and the vector $\bar{S}$ is known as Poynting's Vector, which may be interpreted as the energy flux of a propagating electromagnetic field.

The Poynting Vector

Assuming a non-dispersive, linear medium, such as the case for vacuum propagation, the constitutive relations are simply $\bar{D} = \varepsilon\bar{E}$ and $\bar{B} = \mu\bar{H}$, with $\varepsilon = \varepsilon_r\varepsilon_0$ the permittivity of the medium. Therefore the form of Poynting's Vector simplifies to

$$\bar{S} = \frac{1}{\mu}\bar{E} \times \bar{B}, \tag{2.74}$$

and we see that the electric and magnetic field components must be perpendicular for energy to be transferred (i.e propagating radiation), a result we have already seen for the plane wave.

2.7.3 Physical Interpretation of the Liénard-Wiechert Potential

The equation (2.66) obtained for the Liénard-Wiechert fields demonstrated that the total field was composed of two terms that differ in the rate at which they decrease off with distance from the source. As has already been hinted, at, one of these terms describes radiation from the particle and the other is the transformed static field. We shall now demonstrate this in more detail.

By applying Gauss's Law to an arbitrary enclosing volume around our source distribution we may integrate the Poynting vector to find the the total radiation flux passing through the surface:

$$\frac{\mathrm{d}P}{\mathrm{d}t} = \frac{1}{\mu}\oint_s \mathrm{d}\bar{a}\cdot(\bar{E}\times\bar{B}) \quad = \frac{1}{\mu c}\oint_s \mathrm{d}a\,\hat{n}\cdot[\bar{E}\times(\hat{n}\times\bar{E})] = \frac{1}{\mu c}\oint_s \mathrm{d}a\,E^2 - (\hat{n}\cdot\bar{E})^2. \tag{2.75}$$

Considering the electric field as the sum of the velocity and radiation terms $\bar{E} = \bar{E}_v + \bar{E}_r$ from (2.66) , we may write the integrand as

$$E^2 - (\hat{n}\cdot\bar{E})^2 = E_v^2 + 2\bar{E}_v\cdot\bar{E}_r + E_r^2 - (\bar{E}_r\cdot\hat{n})^2 - (\bar{E}_r\cdot\hat{n})\cdot(\bar{E}_v\cdot\hat{n}) - (\bar{E}_r\cdot\hat{n})^2. \tag{2.76}$$

Using the fact that $\bar{E}_r\cdot\hat{n} = 0$ and

$$(\hat{n}-\bar{\beta})^2 - [(\hat{n}-\bar{\beta})\cdot\hat{n}]^2 = 0 \rightarrow E_v^2 - (\bar{E}_v\cdot\hat{n})^2 = 0, \tag{2.77}$$

most of the terms in (2.76) vanish, leaving

$$\frac{\mathrm{d}P}{\mathrm{d}t} = \frac{1}{\mu c}\oint_s \mathrm{d}a \left\{ \frac{2(\hat{n}-\bar{\beta})\cdot\hat{n}\times[(\hat{n}\times\bar{\beta})\times\dot{\bar{\beta}}]}{c\gamma^2(1-\hat{n}\cdot\bar{\beta})^5 R^3} + \frac{\hat{n}\times[(\hat{n}\times\bar{\beta})\times\dot{\bar{\beta}}]}{c^2(1-\hat{n}\cdot\bar{\beta})^6 R^2} \right\}. \tag{2.78}$$

Upon integration we can see that the surface element $\mathrm{d}a = R^2 \sin\theta \, \mathrm{d}\theta \, \mathrm{d}\phi$ renders the second term a constant with respect to the radial distance R from the source, whereas the first will decay as R^{-1}. Therefore in the far field limit $R \to \infty$ the contribution from the velocity term vanishes and we are left with the radiation term. Furthermore, we see that as the second term has no R dependence and the total energy flux through the surface is constant, as is required to describe propagating radiation. The form of the denominator encodes an important dependence on the velocity of the particle, showing that the intensity of the emitted radiation scales strongly with the magnitude of the component of the particle's velocity which is parallel to the observation direction. Finally, we discover the all important result hinted at at the beginning of this section, namely, that for a particle to radiate it must be accelerating, and that the the radiation will be emitted in the direction perpendicular to the direction of the acceleration. Therefore, for a particle to radiate strongly in a particular direction it must have a large velocity component in that direction and be accelerated perpendicular to that direction.

2.7.4 Frequency of Emitted Radiation

The frequency spectrum of the emitted radiation is an essential property, which can be found from the expression that we already have for the radiated power in the time domain, using Parseval's Theorem.[43,46]

Starting with the Poynting Vector, and using just the radiation term, we find the radiation intensity (power per unit area) to be

$$[\bar{S}\cdot\hat{n}]_{\mathrm{ret}} = \frac{1}{\mu}\hat{n}\cdot[\bar{E}_r\times\bar{B}_r]_{\mathrm{ret}} = \frac{1}{\mu c}|E_r|^2_{\mathrm{ret}}. \tag{2.79}$$

This gives the power per unit solid angle

$$\frac{\mathrm{d}P}{\mathrm{d}\Omega} = [R^2(\bar{S} \cdot \hat{n})]_{\,\mathrm{ret}} = |\bar{A}(t)|^2 \qquad \bar{A}(t) = \frac{1}{\sqrt{\mu c}}[R\bar{E}_r]_{\,\mathrm{ret}}, \tag{2.80}$$

where $\bar{E}_r$ is the radiation field for an arbitrarily moving charge, and we work in lab time as we wish to find an expression for the frequencies observed in the lab frame.

We assume that the period of acceleration is finite, and that the observer is a sufficiently large distance from the charge that its transverse motion subtends a small solid angle element at the observation point. The total radiated energy is therefore the time integral

$$\frac{\mathrm{d}W}{\mathrm{d}\Omega} = \int_{-\infty}^{\infty} \mathrm{d}t\, |\bar{A}(t)|^2. \tag{2.81}$$

If we choose to express $\bar{A}(t)$ as an integral over the frequency spectrum

$$\bar{A}(t) = \frac{1}{\sqrt{2\pi}} \int_{-\infty}^{\infty} \mathrm{d}\omega \bar{A}(\omega)\, \mathrm{e}^{i\omega t}, \tag{2.82}$$

then,

$$\frac{\mathrm{d}W}{\mathrm{d}\Omega} = \frac{1}{2\pi} \int_{-\infty}^{\infty} \mathrm{d}t \int_{-\infty}^{\infty} \mathrm{d}\omega \int_{-\infty}^{\infty} \mathrm{d}\omega' \bar{A}^*(\omega') \cdot \bar{A}(\omega)\, \mathrm{e}^{i(\omega'-\omega)t}. \tag{2.83}$$

Integrating first w.r.t. t we find that the time integral is simply the Fourier representation of the Dirac delta function $\delta(\omega' - \omega)$ and therefore

$$\frac{\mathrm{d}W}{\mathrm{d}\Omega} = \int_{-\infty}^{\infty} \mathrm{d}\omega\, |\bar{A}(\omega)|^2, \tag{2.84}$$

which by Parseval's Theorem is equal to the time integral.[47]

Changing the limits to avoid integrating over negative frequencies, as this lacks any physical meaning, we may consider the integrand to be the spectral energy (energy per unit solid angle per unit frequency),

$$\frac{\mathrm{d}W}{\mathrm{d}\Omega} = \int_{0}^{\infty} \mathrm{d}\omega\, I(\omega, \Omega), \tag{2.85}$$

---

[47] K. F. Riley et al. *Mathematical Methods for Physics and Engineering*, Cambridge University Press, 2006.

where

$$I(\omega,\Omega) = \frac{\mathrm{d}^2 W(\omega)}{\mathrm{d}\omega\,\mathrm{d}\Omega} = |\bar{A}(\omega)|^2 + |\bar{A}(-\omega)|^2 = 2|\bar{A}(\omega)|^2, \tag{2.86}$$

because $\bar{A}(t)$ is real and therefore $\bar{A}^*(\omega) = \bar{A}(-\omega)$.

The Fourier transform of $\bar{A}(t)$ may be found from the expression for the radiation field

$$\bar{A}(\omega) = \frac{1}{\sqrt{2\pi\mu c}} \int_{-\infty}^{\infty} \mathrm{d}t\; \mathrm{e}^{i\omega t} \frac{q}{4\pi\epsilon_0 c} \left[\frac{\hat{n}\times[(\hat{n}-\bar{\beta})\times\dot{\bar{\beta}}]}{(1-\hat{n}\cdot\bar{\beta})^3}\right]_{\mathrm{ret}}, \tag{2.87}$$

evaluated at the retarded time $t = t' + R(t')/c$. Changing variable to t' gives

$$\bar{A}(\omega) = \frac{q}{\sqrt{32\pi^3\epsilon_0 c}} \int_{-\infty}^{\infty} \mathrm{d}t'\; \mathrm{e}^{i\omega[t'+R(t')/c]} \left[\frac{\hat{n}\times[(\hat{n}-\bar{\beta})\times\dot{\bar{\beta}}]}{(1-\hat{n}\cdot\bar{\beta})^2}\right], \tag{2.88}$$

this uses the fact that $\mathrm{d}t/\,\mathrm{d}t' = 1 - \mathrm{d}\{R(t')/c\}/\,\mathrm{d}t = 1 - \hat{n}\cdot\bar{\beta}$, which is shown diagrammatically in figure 2.2.

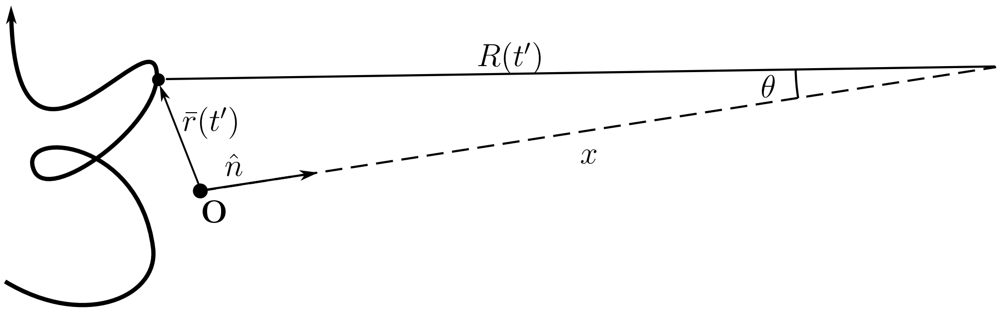

Figure 2.2: The geometric relationship between $R(t')$, $\hat{n}$ and $\bar{r}(t')$ may be simplified under the assumptions of far field and finite emission time we have already made.

Since the observation point is assumed to be a large distance from the source point, we may take $\hat{n}$ to be a constant, and so the distance R may be approximated as

$$R(t') \simeq x - \hat{n}\cdot\bar{r}(t'), \tag{2.89}$$

where we may validly approximate $x\cos(\theta)$ as x since we already assume the distance is large enough to have $\theta \simeq 0$ at all times, given a suitable choice of origin **O**. Finally, because the expression for R only occurs in the exponential, the constant value x is simply a phase factor, which may be neglected. This gives (dropping primes for the sake of brevity),

$$\bar{A}(\omega) = \frac{q}{\sqrt{32\pi^3\epsilon_0 c}} \int_{-\infty}^{\infty} \mathrm{d}t \; \mathrm{e}^{i\omega[t-\hat{n}\cdot\bar{r}(t)/c]} \left[\frac{\hat{n}\times[(\hat{n}-\bar{\beta})\times\dot{\bar{\beta}}]}{(1-\hat{n}\cdot\bar{\beta})^2} \right], \tag{2.90}$$

and therefore the spectral energy is

$$I(\omega,\Omega) = \frac{q^2}{16\pi^3\epsilon_0 c} \left| \int_{-\infty}^{\infty} \mathrm{d}t \; \mathrm{e}^{i\omega[t-\hat{n}\cdot\bar{r}(t)/c]} \left[\frac{\hat{n}\times[(\hat{n}-\bar{\beta})\times\dot{\bar{\beta}}]}{(1-\hat{n}\cdot\bar{\beta})^2} \right] \right|^2. \tag{2.91}$$

This form, with explicit dependence on $\dot{\bar{\beta}}$, demonstrates clearly the fact that we need only integrate over the period when the acceleration is non-zero. However, a more useful form can be found by integrating (2.91).

Observing that the vector part of $A(\omega)$ is a total derivative

$$\frac{\hat{n}\times[(\hat{n}-\bar{\beta})\times\dot{\bar{\beta}}]}{(1-\hat{n}\cdot\bar{\beta})^2} = \frac{\mathrm{d}}{\mathrm{d}t}\left[\frac{\hat{n}\times(\hat{n}\times\bar{\beta})}{1-\hat{n}\cdot\bar{\beta}} \right], \tag{2.92}$$

integrating by parts leads to the expression

$$I(\omega,\Omega) = \frac{q^2\omega^2}{16\pi^3\epsilon_0 c} \left| \int_{-\infty}^{\infty} \mathrm{d}t \, \hat{n}\times(\hat{n}\times\bar{\beta})\, \mathrm{e}^{i\omega[t-\hat{n}\cdot\bar{r}(t)/c]} \right|^2, \tag{2.93}$$

which removes the explicit dependence on $\dot{\bar{\beta}}$, and yields a simpler form, at the expense of obscuring the fact that the integral vanishes when there is no acceleration.

It is important to note that in the above approach polarisation information is lost when the integral is squared. Therefore to correctly calculate the radiation spectrum due to the superposition of fields from multiple charges, we must perform the summation inside the square

$$I(\omega,\Omega) = \frac{q^2\omega^2}{16\pi^3\epsilon_0 c} \left| \sum_j \int_{-\infty}^{\infty} \mathrm{d}t \, \hat{n}\times(\hat{n}\times\bar{\beta}_j)\, \mathrm{e}^{i\omega[t-\hat{n}\cdot\bar{r}_j(t)/c]} \right|^2, \tag{2.94}$$

or in the case of a continuous distribution of current $\bar{J}(\bar{x},t)$

$$I(\omega,\Omega) = \frac{\omega^2}{16\pi^3\epsilon_0 c} \left| \int \mathrm{d}t \int \mathrm{d}^3\bar{x} \hat{n}\times(\hat{n}\times\bar{J}(\bar{x}))\, \mathrm{e}^{i\omega[t-\hat{n}\cdot\bar{x}/c]} \right|^2 \tag{2.95}$$

where

$$\lim_{N\to\infty} \sum_j^N q_j\bar{\beta}_j \, \mathrm{e}^{-i\omega\hat{n}\cdot\bar{r}_j(t)/c} = \frac{1}{c}\int \mathrm{d}^3\bar{x} \; \bar{J}(\bar{x},t)\, \mathrm{e}^{-i\omega\hat{n}\cdot\bar{x}/c}. \tag{2.96}$$

2.7.5 Coherence Effects

The discussion of the multiple particle case above leads naturally to the concept of coherent emission. Consider a bunch of charged particles that all follow the same trajectory with a small time delay between each. For such a bunch the integral over the motion will be the same for all particles, and therefore we would expect the total radiation intensity to depend only on the relative phases of the particles. For the case of a pair of particles, labelled 1 and 2, separated by a time $\delta t = t_2 - t_1$, the trajectories are related as follows:

$$\begin{aligned} \bar{r}_1(\tau_1) &= \bar{r}_2(\tau_2), & \tau_1 + R_1(\tau_1) &= t, \\ \bar{\beta}_1(\tau_1) &= \bar{\beta}_2(\tau_2), & \tau_2 + R_2(\tau_2) &= t. \end{aligned}$$

In the far field limit, $R_1 = x - \hat{n} \cdot \bar{r}_1(\tau_1)$, and $R_2(\tau_2) = R_1(\tau_1)$, therefore $A(\omega)$ is given by

$$\begin{aligned} A(\omega) = \frac{e}{\sqrt{32\pi^3 \varepsilon_0 c}} & \left\{ \int_{-\infty}^{\infty} \mathrm{e}^{i\omega t} \left[\frac{\hat{n} \times [(\hat{n} - \bar{\beta}_1) \times \dot{\bar{\beta}}_1]}{(1 - \hat{n} \cdot \bar{\beta}_1)^3} \right]_{\text{ret}} \mathrm{d}t \right. \\ & + \left. \int_{-\infty}^{\infty} \mathrm{e}^{i\omega t} \left[\frac{\hat{n} \times [(\hat{n} - \bar{\beta}_2) \times \dot{\bar{\beta}}_2]}{(1 - \hat{n} \cdot \bar{\beta}_2)^3} \right]_{\text{ret}} \mathrm{d}t \right\}. \end{aligned} \tag{2.97}$$

Changing integration variables to the retarded times and again using $\mathrm{d}t/\,\mathrm{d}\tau_1 = 1 - \hat{n} \cdot \bar{\beta}_1(\tau_1)$ (figure 2.2), yields

$$\begin{aligned} A(\omega) = \frac{e}{\sqrt{32\pi^3 \varepsilon_0 c}} & \left\{ \int_{-\infty}^{\infty} \mathrm{e}^{i\omega(\tau_1 + R_1(\tau_1)/c)} \frac{\hat{n} \times [(\hat{n} - \bar{\beta}_1) \times \dot{\bar{\beta}}_1]}{(1 - \hat{n} \cdot \bar{\beta}_1)^2} \, \mathrm{d}\tau_1 \right. \\ & + \left. \int_{-\infty}^{\infty} \mathrm{e}^{i\omega(\tau_2 + R_2(\tau_2)/c)} \frac{\hat{n} \times [(\hat{n} - \bar{\beta}_2) \times \dot{\bar{\beta}}_2]}{(1 - \hat{n} \cdot \bar{\beta}_2)^2} \, \mathrm{d}\tau_2 \right\}. \end{aligned} \tag{2.98}$$

This can be simplified to an integral over a single particle trajectory multiplied by a phase factor that depends on the time delay between the two particles

$$A(\omega) = \frac{e}{\sqrt{32\pi^3 \varepsilon_0 c}} \left(1 + \mathrm{e}^{i\omega\Delta\tau}\right) \left\{ \int_{-\infty}^{\infty} \mathrm{e}^{i\omega(\tau - \hat{n} \cdot \bar{r}(\tau)/c)} \frac{\hat{n} \times [(\hat{n} - \bar{\beta}) \times \dot{\bar{\beta}}]}{(1 - \hat{n} \cdot \bar{\beta}_1)^2} \, \mathrm{d}\tau \right\}, \tag{2.99}$$

and it follows, after integrating by parts as previously, that the radiation frequency spectrum is

$$\frac{\mathrm{d}^2W}{\mathrm{d}\omega\,\mathrm{d}\Omega}(\omega) = \frac{e^2\omega^2}{16\pi^3\varepsilon_0 c}\left|1 + \mathrm{e}^{i\omega\Delta\tau}\right|^2 \cdot \left|\int_{-\infty}^{\infty} \mathrm{e}^{i\omega(\tau - \hat{n}\cdot\bar{r}(\tau)/c)}\hat{n}\times(\hat{n}\times\bar{\beta})\,\mathrm{d}\tau\right|^2, \quad (2.100)$$

which generalises to the N-particle case as

$$\frac{\mathrm{d}^2W}{\mathrm{d}\omega\,\mathrm{d}\Omega}(\omega) = \frac{e^2\omega^2}{16\pi^3\varepsilon_0 c}\left|\sum_{n}^{N} \mathrm{e}^{i\omega\Delta\tau_n}\right|^2 \cdot \left|\int_{-\infty}^{\infty} \mathrm{e}^{i\omega(\tau - \hat{n}\cdot\bar{r}(\tau)/c)}\hat{n}\times(\hat{n}\times\bar{\beta})\,\mathrm{d}\tau\right|^2. \quad (2.101)$$

We can now investigate the effect of the particle distribution on the emitted radiation. Writing the phase factor term as the sum times its complex conjugate,

$$\left|\sum_{n}^{N} \mathrm{e}^{i\omega\Delta\tau_n}\right|^2 = \sum_i \sum_j \mathrm{e}^{i\omega(\Delta\tau_i - \Delta\tau_j)}, \quad (2.102)$$

we see that if the particles are distributed with random phases, the cross-correlation terms $j \neq i$ will, on average, give no contribution, and the radiated power will scale simply as the number of particles N. In the case where the particles are distributed such that they have phases $\Delta\tau_n = 2\pi I_n/\omega_0$, then at the frequency ω_0 the radiation fields will interfere constructively, scaling in amplitude as N, resulting in the radiated power scaling as N^2. The radiation emitted by such a group of particles is said to be coherent. This means that, with the exception of the trivial case $\Delta\tau_n = 0 \ \forall\ n$,[*] a bunch will emit coherently only at a single frequency (and its harmonics), while radiating a comparatively small, incoherent signal at other frequencies. In the real world, the behaviour of a radiation source will lie between these two extremes, with the radiated power scaling between N and N^2, although for large N even a small level of radiation coherence can overwhelm the incoherent contribution. A possible diagnostic for the level of coherence of the source is then the relationship between the radiation intensity and the total charge of the radiating bunch.

---

[*] Which behaves as a single particle of charge qN.

2.8 A Numerical Radiation Solver

Finding the spectral energy emitted by an accelerated electron requires evaluation of the integral over the electron trajectory given in (2.93). For many of the cases explored in this thesis the electron trajectory will be calculated by numerical techniques, therefore the integration over the electron trajectory will also be performed numerically. This naïve approach to this integration is to use a Simpson or Gaussian quadrature type integration scheme, using data sampled at fixed timesteps such as that from a PIC simulation. However, to resolve high frequency components of the radiation this requires data with a suitable high sampling frequency to resolve the electron motion correctly. This approach is usually impractical for the calculation of XUV (extreme UV with wavelengths from 10 nm – 124 nm and X-ray radiation from PIC simulation or other explicitly precomputed trajectory data as the computational requirements to produce such finely grained data, as well as the size of the resulting datasets, are unfeasibly large.

Thankfully there are alternative methods available for more efficiently evaluating the integral in (2.93), which are dependent on the method by which the trajectory data is produced. Typically the method for calculating the trajectory data will fall into one of two categories, either a fully explicit solver with a fixed timestep e.g PIC simulation, or an implicit calculator where the electron position and velocity may be calculated for an arbitrary timestep such as for the model described in section 3.2.4.

If the electron trajectory can be efficiently evaluated at arbitrary times then the integral can be efficiently and accurately evaluated using adaptive integration algorithms which recursively subdivide the integration region until the desired accuracy is achieved. Such integrators provide high accuracy and error estimation, and high quality implementations exist in a many scientific software packages. For the work in this thesis the adaptive integration methods of the Scipy[48] and Gnu Scientific Library[49] are used.

For trajectory data with fixed timesteps such as PIC simulation output an adaptive integrator cannot be used. In such cases it is possible to interpolate the trajectory data by making appropriate assumptions about the form of the trajectory. Such an interpolation can be used to provide input to an adaptive integration algorithm or alternatively the form of the interpolation function can be chosen such that the total integral can be replaced by the sum over a series of analytically calculable integrals. This is the approch taken by Thomas,[20] who derived an expression for the radiation by considering the integral as the sum of integrals over quadratic trajctory segments for which an analytic form exists. Both of these techniques allow resolution of radiation at frequencies much larger than the Nyquist frequency of the electron trajectory data. A radiation solver using the algorithm described by Thomas is used extensively in this thesis. It was implemented in the “radt” code by Dr Enrico Brunetti at the University of Strathclyde, and is used by kind permission in this work.

2.9 Conclusions

Solving the equations of motion for relativistic electrons in strong fields is a complex undertaking. This is made more complicated still for the LWFA by the need for self-consistency of the solution for plasma electrons moving collectively in their self-field. PIC codes present a high-accuracy solution to this problem, and will be used extensively throughout chapters 3 and 4 to investigate complex and non-linear plasma behaviours which cannot be modelled analytically.

Similarly, calculation of the radiation emitted by accelerated electrons in the LWFA requires numerical solution. This is achieved by integrating over the motion

---

[48] E. Jones et al. *SciPy: Open source scientific tools for Python*

[49] M. Galassi et al. *GNU Scientific Library*, GNU Software Foundation,

[20] A. G. R. Thomas. *Phys. Plasmas* **17**, pp. 1–12, 2010.

to calculate the Liénard-Wiechert potentials at the observation point, typically in the frequency domain. Direct numerical integration is one possible option although the work of Thomas[20] demonstrates that quadratic interpolation of the trajectory prior to integration yields accurate results for much lower temporal resolution particle trajectories. Such numerical calculation of the emitted radiation will be of central importance to the investigation of coherent enhancement of betatron radiation presented in chapter 5.

Chapter 3

The Laser Wakefield Accelerator

Since plasma is a collection of many charged particles in close proximity, it exhibits collective behaviour that can manifest as plasma waves. Many potential classes of waves exist, differentiated by the properties of the electric and magnetic fields involved. For LWFAs we are interested primarily in electrostatic waves. These are caused by displacement of plasma electrons relative to the ion background, which remains approximately static on the timescale of the LWFA process. The LWFA accelerator structure is a wave of this type with complex 3-dimensional structure and relativistic velocity, driven by an intense laser or charged particle beam. Initially however, it is useful to consider the case of a non-relativistic, one-dimensional standing wave, which serves to highlight key properties of such waves using a simple analytic model. These concepts can then be used to understand the more complex 3D case of the LWFA "bubble" regime.

3.1 1-Dimensional Plasma Waves

The behaviour of a 1D system of electrons performing nonlinear wave motion was first derived by Akhiezer and Polovin.[50] However, the treatment a few years later

---

[50] A. I. Akhiezer and R. V. Polovin. *J. Exp. Theor. Phys.* **3**, pp. 696–705, 1956.

by Dawson and Oberman[51,52] is more conceptually accessible.

Consider a plasma described as a (1-D) fluid made up of an infinite stack of electron and ion sheets. For simplicity in this case we assume a Hydrogen plasma with $Z = 1$. The locations of the ion sheets remain fixed on the timescales that interest us, and we consider them simply as a uniform background charge density n_0. We define the location of the electron sheets in terms of their displacement $\xi(x_0)$ from an equilibrium location x_0,

$$x = x_0 + \xi(x_0). \tag{3.1}$$

In moving a distance ξ from the equilibrium position, an electron passes over a quantity of positive ion charge $en_0\xi$. If we make the assumption that the ordering of the electrons is not changed, then the charge excess on either side of the electron is equal but opposite, and Gauss' Law gives the expression for the electric field at the electron position ξ

$$E = \frac{en_0}{\epsilon_0}\xi(x_0). \tag{3.2}$$

The requirement that the ordering of particles does not change is a typical assumption used in description of wave phenomena, which allows simple models of this type to be formulated. However, there are limits to the validity of such a model, which will become apparent later.

Using (3.2), the equation of motion for the electrons can be written:

$$\begin{aligned} m\frac{\mathrm{d}^2\xi}{\mathrm{d}t^2} &= -eE = -\frac{e^2n_0}{\epsilon_0}\xi(x_0), \\ \frac{\mathrm{d}^2\xi}{\mathrm{d}t^2} &= -\omega_p^2\,\xi(x_0), \end{aligned} \tag{3.3}$$

which shows that they will perform simple harmonic motion at the electron plasma frequency

$$\omega_p(n_0) = \sqrt{\frac{e^2n_0}{\epsilon_0 m_e}}. \tag{3.4}$$

---

[51] J. M. Dawson. *Phys. Rev.* **113**, pp. 383–387, 1959.

[52] J. M. Dawson and C. Oberman. *Phys. Fluids* **2**, pp. 103–111, 1959.

This is the characteristic frequency at which electrons in the plasma will oscillate, provided that relativistic and thermal effects can be neglected. The full general solution for the electron motion is given by

$$\xi(x_0) = \xi_1(x_0)\sin(\omega_p t) + \xi_2(x_0)\cos(\omega_p t), \tag{3.5}$$

with arbitrary functions for ξ_1 and ξ_2. However, this is not the full story as we must still contend with the requirement that the ordering of the electrons does not change, placing limits on the validity of the model.

3.1.1 Wavebreaking

Since the expression (3.2) for the electric field due to the wave is predicated on the assumption electron trajectories do not cross, the model is valid only in this circumstance. Naturally the question then arises 'what happens if the electron trajectories *do* cross?' We can consider this qualitatively by analogy with water waves, which have the advantage of intuitive familiarity. An ocean wave begins far out to sea as a small amplitude oscillation in the water, easily described by a simple oscillatory function as we have used in our plasma wave model so far. As the wave approaches the shore the reducing water depth will cause distortion of the fluid element trajectories, reducing the group velocity and increasing the amplitude of the wave. Eventually, when the distortion becomes large enough, the wave will start to break: the fluid elements at the peak of the wave running ahead of the bulk, producing the characteristic arching shape. This means that the equation of motion for the fluid elements is no longer single-valued as there are two populations to describe: those still in the bulk of the wave, and those that are in the part of the wave that is breaking. Therefore the ordering of the fluid elements in the wave has changed, and so the simple single fluid picture of the unbroken wave no longer applies.

Returning to our plasma wave description we see that the ordering will be maintained provided that for a two electrons a small distance Δx_0 apart, the resultant value of $\xi(x_0)$ and hence position x is more positive for the electron with a more positive equilibrium position x_0. Considering this as a transformation $x_0 \mapsto x = x_0 + \xi$, to ensure trajectories do not cross, the Jacobian of the transformation must satisfy the inequality

$$\frac{\partial \xi}{\partial x_0} > -1. \tag{3.6}$$

This is the wavebreaking condition for a cold plasma in 1-dimension.

An illustrative example of this behaviour can be found by considering a solution (3.5) with the form $\xi_1 = A\sin(k_p x_0)$, $\xi_2 = 0$ where $k_p = 2\pi/\lambda_p$ is the plasma wavenumber. This solution is a standing density wave due to an initially uniform electron population with a sinusoidal velocity distribution, and has a peak electric field strength at $t = \pi/2\omega_p$:

$$\begin{aligned} x &= x_0 + \xi = x_0 + A\sin(k_p x_0), \\ E &= \frac{e n_0}{\epsilon_0} A\sin(k_p x_0), \\ n_e &= n_0 - \frac{\varepsilon_0}{e}\nabla\cdot\bar{E} = n_0\left(1 - \frac{A k_p\cos(k_p x_0)}{1 + A k_p\cos(k_p x_0)}\right). \end{aligned} \tag{3.7}$$

Figure 3.1 shows the behaviour of the peak electric field and density perturbation for increasing initial amplitudes A. We see that as the amplitude increases the electric field due to the wave also increases, until the amplitude reaches the wavebreaking limit $A = k_p^{-1}$, which follows immediately from (3.6) for the choice of ξ. At this point the electron density distribution and electric field become singular, and the wave description of the plasma breaks down. This is very clearly demonstrated for the case where $A > k_p^{-1}$ as the function $E(x)$ ceases to be single valued. The wavebreaking condition can also be considered as the limit of the electron density distribution: figure 3.1(b) demonstrates that in the case that $A \geq k_p^{-1}$ the model requires that the electron density becomes infinite! This amplitude limit leads to to an expression for the maximum electric field attainable

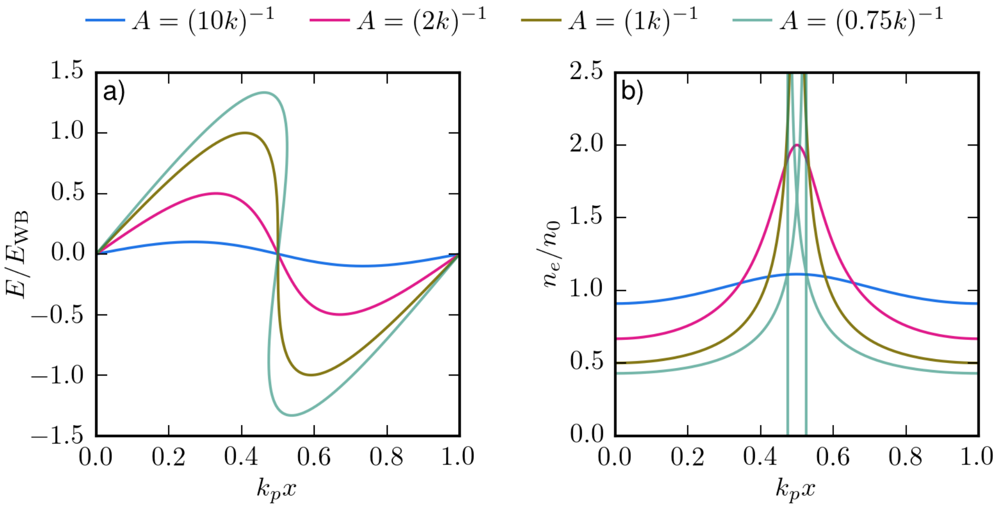

Figure 3.1: Wave behaviour with increasing displacement amplitudes: a) Electric field as a fraction of the wavebreaking field, b) Electron number density as a fraction of the unperturbed density n_0.

for a given plasma density, often referred to as the wavebreaking field

$$E_{\rm WB} = \frac{e n_0}{\epsilon_0 k_p}. \tag{3.8}$$

We therefore see that the utility of fluid models such as this one is limited in the case that we wish to investigate the behaviour of breaking plasma waves. While we may be able to see the behaviour of the wave up to the point at which it breaks we will get no further. As we shall see, the behaviour of the wave during and after wavebreaking is of crucial importance for self-injection in LWFAs and so we must look beyond such approaches and consider individual particle trajectories if we wish to accurately model the self-injection process.

3.2 3-Dimensional Laser Driven Plasma Waves

The 1D model in section 3.1 is useful for qualitatively understanding the behaviour of an electrostatic plasma wave, however it is also somewhat unphysical as it, like the laser plane wave, has infinite transverse extent. Any real plasma wave must have a driver with finite extent, and for the extreme energy densities required

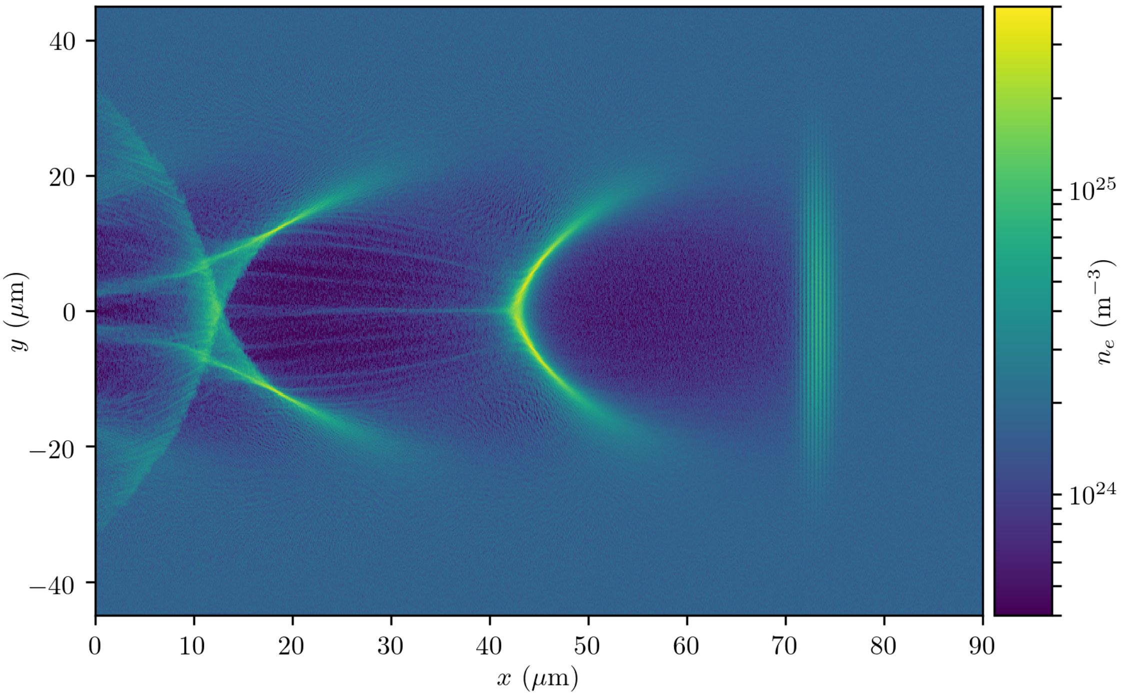

Figure 3.2: Electron number density for an LWFA bubble in a uniform plasma with normalised density $n_e/n_{\mathrm{crit}} = 0.001$, driven by a laser which propagates from left to right. The laser has wavelength 800 nm, with normalised peak intensity $a_0 = 4.0$, and a gaussian amplitude envelope of width $\sigma_\perp = 20\,\mu$m and duration $\sigma_t = 10\,$fs.

to drive accelerating wakefields in LWFA schemes, such drivers are extremely compact, typically having a size comparable to the electron plasma wavelength

$$\lambda_p = \frac{2\pi c}{\omega_p}. \tag{3.9}$$

The plasma waves resulting from the passage of such drivers will have a complex transverse structure, and as such a full 3-dimensional treatment of the problem is necessary to correctly model the physical behaviour.

3.2.1 The Bubble Regime

As in the 1D case, there is both a linear and non-linear regime for the 3D wakefield. A weak driver will drive a linear wake, characterised by a sinusoidal density perturbation and associated sinusoidal electric fields. Alternatively, if the driver is sufficiently intense to completely expel electrons from some part of the region behind the driver, the density profile and associated electric fields will be distorted. The regime in which this effect is most extreme is typically known as the "bubble" or "blowout" regime.[9,10,16] Figure 3.2 shows the result of a 2D PIC simulation of an LWFA, demonstrating the typical electron density behaviour in the bubble regime. The simulation was performed with the EPOCH PIC code with cell size 40 nm × 200 nm length×width, in a 90 μm × 90 μm moving window. The laser is linearly polarised in the simulation plane, with wavelength 800nm, normalised peak intensity $a_0 = 4.0$, a gaussian temporal and spatial envelope with length $\sigma_t = 10\,\mathrm{fs}$ and width $\sigma_\perp = 20\,\mu\mathrm{m}$. The plasma has a flat top density profile with normalised electron number density $n_e/n_{\mathrm{crit}} = 0.001$ and an initial linear upramp region of length 300 μm to couple the laser smoothly into the plasma. The complete input deck used as a basis for all simulations in this thesis is given in appendix E. The bubble regime is characterised by an approximately spherical region behind an extremely intense driver, from which all plasma electrons have been expelled by the driver. This leaves a cavity populated only by the plasma ions, which remain approximately stationary on the timescales of the interaction. This cavity region is surrounded by a high density "sheath" of displaced electrons that travel around the periphery of the bubble before crossing the laser axis at the rear of the bubble. The nature of the electron motion typically means that there will be a train of many bubbles formed in the structure trailing behind the driver, the first two of which can be seen in the figure, however there can be many more. This is because the electrons are, to a good approximation, performing simple harmonic motion in the ion column that is left behind the laser pulse as it displaces the electrons. Therefore, after travelling around the first bubble the electrons continue to trace out additional bubble structures in addition to the

---

[9] J. B. Rosenzweig et al. *Phys. Rev. A* **44**, 1991.

[10] A. Pukhov and J. Meyer-ter-Vehn. *Appl. Phys. B: Lasers Opt.* **74**, pp. 355–361, 2002.

[16] I. Kostyukov et al. *Phys. Plasmas* **11**, p. 5256, 2004.

first. This is a simplified view, as in reality we find that many electrons will be lost due to large transverse momentum at the rear of the bubble, and therefore the field strength in subsequent bubbles will be lower. Typically this means that the first bubble is of the most interest as it is the largest and most completely evacuated and hence has the strongest accelerating fields. However, the behaviour and effects of the additional bubbles must be considered as they may also trap and accelerate electrons.

3.2.2 The Shape of the Bubble

As we can see from the PIC simulation results in Figure 3.2, the LWFA bubble is approximately spherical. Indeed this is found to be broadly true across the parameter range for which the bubble regime exists both for laser and beam drivers.[9,10,16,53]

For the laser case the bubble radius can be approximated by considering the force balance between the laser ponderomotive force and the ion channel restoring force. Assuming that the laser spot size is matched for optimal self guiding with spot radius r_m, the force balance equation is[54]

$$\begin{aligned} F_{\text{pond}} &\sim F_{\text{rest}}, \\ \frac{a_0^2}{\bar{\gamma} k_p r_m} &\sim k_p r_m, \\ k_p r_m &\sim \sqrt{a_0}\,. \end{aligned} \tag{3.10}$$

Which assumes that the average electron energy is comparable to the normalised vector potential of the laser $\bar{\gamma} \sim a_0$. Various refinements to this approximate scaling have been made in the literature, typically finding through PIC simulation that the scaling is better described as $k_p r_m \simeq 2\sqrt{a_0}$.[53,54] A more complete model, which seeks to better model the true shape of the bubble, is given by Yi *et al.*[55]

---

[53] E. Esarey et al. *Rev. Mod. Phys.* **81**, pp. 1229–1285, 2009.

[54] W. Lu et al. *Phys. Plasmas* **13**, p. 056709, 2006.

[55] S. A. Yi et al. *Phys. Plasmas* **20**, p. 013108, 2013.

However, the model given above is sufficiently accurate for approximating the spherical bubble radius and matched beam width for use as initial conditions in PIC simulations.

An analytical expression showing the elliptical nature of the sheath electron trajectories around the bubble periphery can be derived *a-posteriori* from the form of the fields in a spherical bubble. This is given in section 3.2.5 and goes some way towards demonstrating that the picture of a spherical ion cavity surrounded by a dense electron sheath is self-consistent.

3.2.3 Analytic Description of the Bubble Fields

For a perfectly spherical and fully evacuated bubble, the electric fields inside the cavity are purely radial in the frame comoving with the bubble.[16] This gives the sawtooth longitudinal field profile that we previously found in the (1-D) case, along with a linear transverse component which will exert a focusing force on any electrons within the cavity. The motion of the bubble against the static ion background additionally results in an azimuthal magnetic field within the bubble. Alternatively this can be found from the Lorentz transformation of purely electrostatic bubble. Figure 3.3 shows these fields for the case of the bubble in figure 3.2.

There are multiple derivations of these fields in the literature that vary in their level of rigour and complexity. These include 3-dimensional fluid treatments that attempt to more accurately capture the bubble shape,[55,56] and various "piecewise" models that attempt to include additional terms to model the effects of the electron sheath on the fields around the bubble.[55,57] However, in order to describe the fields inside an ideal bubble, the simple model first described by Kostyukov *et al.*[16] provides an adequate description.

---

[56] W. Lu et al. *Phys. Rev. Lett.* **96**, p. 165002, 2006.

[57] I. Kostyukov et al. *New J. Phys.* **12**, p. 045009, 2010.

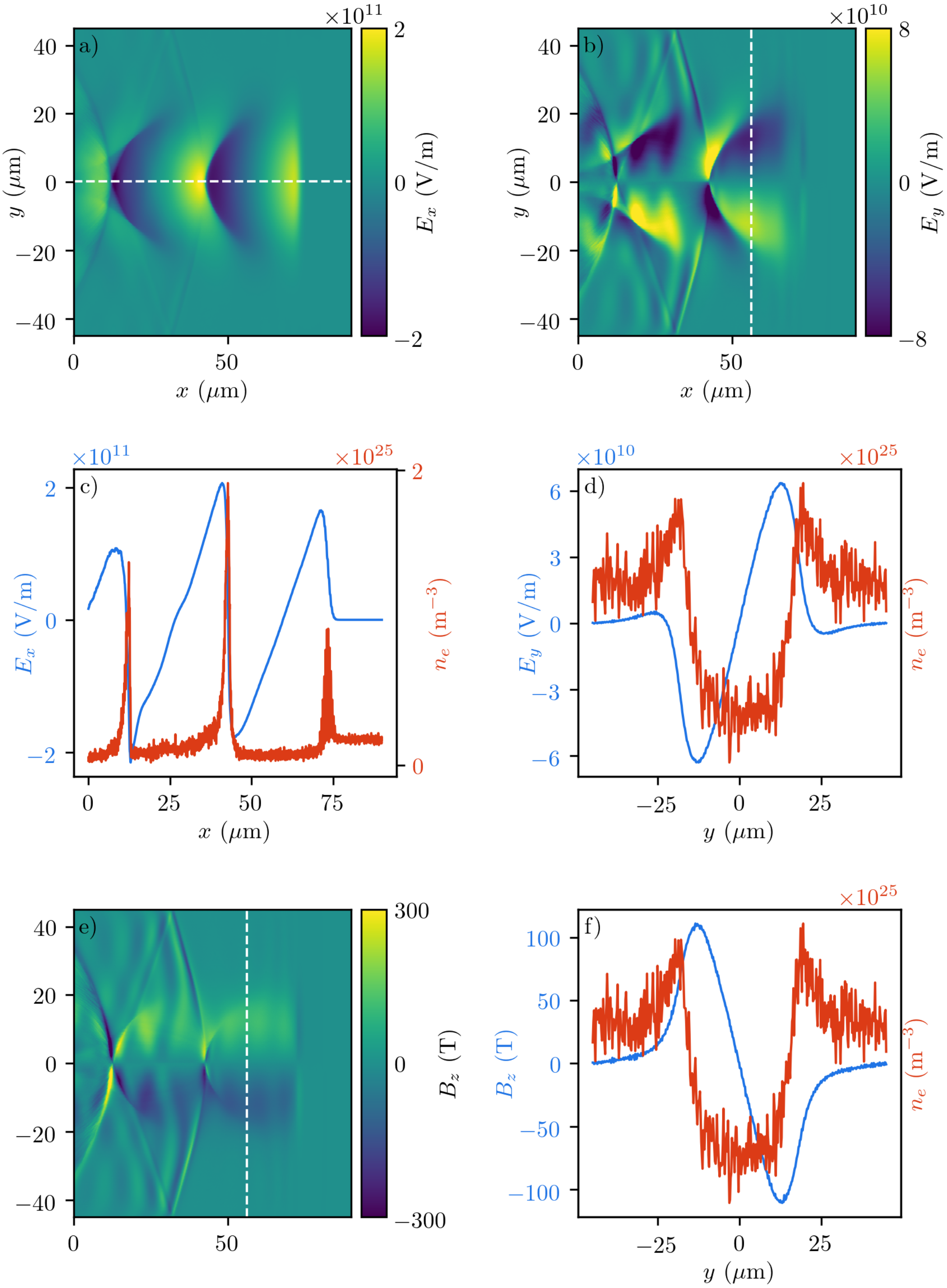

Figure 3.3: Longitudinal, a), and transverse, b), electric fields and azimuthal magnetic fields, e), in and around the bubble structure for the bubble shown in figure 3.2, driven by an 800 nm laser with $a_0 = 4.0$ in a uniform plasma with normalised density $n_e/n_{\text{crit}} = 0.001$ ($n_e \simeq 1.74 \times 10^{24}\,\text{m}^{-3}$). The dashed white lines indicate the position of the lineout data: c), the on-axis accelerating field structure, d), the transverse focusing field in the bubble f) the azimuthal magnetic field (blue), along with the respective electron density at these positions (red).

An analytical form for the ideal bubble fields may be found by making a Galilean transformation to the comoving coordinate $\zeta = z - \beta_\phi ct$. This is termed the "Quasistatic Approximation" referring to the assumption that the bubble can be approximated as a nonevolving structure moving through the plasma at approximately the speed of light.[58] Within the boundary of the bubble cavity the electric field is then given by

$$\nabla \cdot \bar{E} = \frac{en_e}{\epsilon_0} = \frac{1}{r}\frac{\partial(rE_r)}{\partial r} + \frac{\partial E_r}{\partial \zeta}, \tag{3.11}$$

where for a fully evacuated bubble the total charge density is simply the ion density q_i, which is equal to the electron charge density, en_e, of the quiescent plasma. In cylindrical coordinates, this equation has the solutions

$$E_r = \frac{en_e r}{4\epsilon_0}, \qquad E_z = \frac{en_e}{4\epsilon_0}\zeta, \tag{3.12}$$

if spherical symmetry of the bubble is assumed.

As we haved already noted, because the bubble, and hence electric fields, are moving there will also be a magnetic field component as the electric field at any given z will not be constant with respect to time. This field may be found using the Ampère-Maxwell equation

$$\nabla \times \bar{B} = \frac{1}{c^2}\frac{\partial \bar{E}}{\partial t} = \frac{1}{c^2}\frac{\partial \bar{E}}{\partial \zeta}\frac{\mathrm{d}\zeta}{\mathrm{d}t} = -\frac{\beta_\phi}{c}\frac{en_e}{2\epsilon_0}\hat{z}, \tag{3.13}$$

$$\frac{1}{r}\frac{\partial(rB_\theta)}{\partial r} - \frac{\partial B_r}{\partial \theta} = -\frac{\beta_\phi}{c}\frac{en_e}{2\epsilon_0}, \tag{3.14}$$

where

$$\frac{\mathrm{d}\zeta}{\mathrm{d}t} = \frac{\partial \zeta}{\partial t}\frac{\mathrm{d}t}{\mathrm{d}t} + \frac{\partial \zeta}{\partial z}\frac{\mathrm{d}z}{\mathrm{d}t} = -c\beta_\phi. \tag{3.15}$$

This has the solution

$$B_\theta = -\frac{\beta_\phi}{c}\frac{en_e}{4\epsilon_0}r, \tag{3.16}$$

where, once again, azimuthal symmetry is assumed.

---

[58] P. Sprangle et al. *Phys. Rev. Lett.* **64**, pp. 2011–2014, 1990.

3.2.4 Electron Motion in the Bubble Regime

Using the results for the fields from previous section we can express the force on an electron in the bubble as

$$\bar{F} = -e(\bar{E} + c\bar{\beta} \times \bar{B}), \tag{3.17}$$

$$F_z = -\frac{1}{2}m_e\omega_p^2\left(\zeta + \frac{\beta_r\beta_\phi r}{2}\right) \simeq -\frac{1}{2}m_e\omega_p^2\left(\zeta + \frac{\beta_r r}{2}\right), \tag{3.18}$$

$$F_r = -\frac{1}{4}m_e\omega_p^2\left(r + \beta_z\beta_\phi r\right) \simeq -\frac{1}{2}m_e\omega_p^2 r, \tag{3.19}$$

$$F_\theta = 0, \tag{3.20}$$

where $\bar{\beta} = \beta_r\hat{r} + \beta_z\hat{z} + \beta_\theta\hat{\theta}$ is the electron velocity. Typically the bubble velocity and longitudinal electron velocity are approximated to be the speed of light in vacuum, $\beta_\phi = \beta_z = 1$.

The trajectory of a trapped electron in the idealised bubble has been studied analytically by many authors,[16,20,59] all of whom use fundamentally similar approaches. The zeroth order evolution of the total electron energy, γ, is first found and used to derive an adiabatic approximation of the evolution of the transverse motion. The longitudinal motion then follows from the difference between the total and transverse energies.

Under the assumption that the transverse motion is small, then to a first approximation the longitudinal motion is decoupled from the transverse motion, and may be approximated as

$$\frac{\mathrm{d}p_z}{\mathrm{d}t} \simeq -\frac{1}{2}m_e\omega_p^2\zeta. \tag{3.21}$$

Further assuming that the electron is accelerated sufficiently rapidly that there is negligible period when its velocity cannot be approximated by c, it will progress forward in the bubble at a rate

$$\beta_{\text{slip}} \simeq 1 - \beta_\phi \simeq \frac{1}{2\gamma_\phi^2}, \tag{3.22}$$

---

[20] A. G. R. Thomas. *Phys. Plasmas* **17**, pp. 1–12, 2010.

[59] S. Corde et al. *Rev. Mod. Phys.* **85**, pp. 1–48, 2013.

and hence we may write the equation of motion in terms of the time t and the initial electron location at the edge of the bubble $\zeta(t=0) = \zeta_i$,

$$\frac{\mathrm{d}p_z}{\mathrm{d}t} \simeq -\frac{1}{2} m_e \omega_p^2 \left(\zeta_i + \frac{ct}{2\gamma_\phi^2} \right), \tag{3.23}$$

which upon integration gives an expression for the evolution of the longitudinal momentum in the absence of transverse motion

$$p_z(t) \simeq p_{z,0} - \frac{1}{2} m_e \omega_p^2 \left(\zeta_i t + \frac{ct^2}{4\gamma_\phi^2} \right). \tag{3.24}$$

Since we have assumed that the transverse motion is small, this is a good approximation of the total electron energy $\gamma \simeq p_z$. Inspecting the form (3.24) we see that the electron energy evolves as a quadratic, and has a maximum at a time

$$t_d = -2\zeta_i \gamma_\phi^2 / c. \tag{3.25}$$

This is generally referred to as the dephasing time as it can be seen that it is the time at which the electron moves from the accelerating phase of the bubble fields into the decelerating phase. Therefore, this also provides an expression for the maximum achievable energy for the electron at dephasing

$$\gamma_d \simeq \frac{p_{z,\mathrm{max}}}{m_e c} \simeq \gamma_i + \frac{k_p^2}{2} \zeta_i^2 \gamma_\phi^2, \tag{3.26}$$

where the γ_i is the initial energy.

It is also typical for the “dephasing length” of a system to be discussed. This refers to the lab frame distance over which an injected electron, and therefore the bubble, will propagate between injection and dephasing. Typically this is calculated as simply

$$L_\mathrm{d} = ct_\mathrm{d}, \tag{3.27}$$

since the electron velocity can be fairly well approximated as the speed of light during the acceleration process. The dephasing length is a key parameter of the LWFA as for efficient acceleration the electron must be accelerated over a distance close to, but not greater than this. This can be acheived by choosing laser and plasma parameters such that the energy of the laser is depleted and the accelerating fields collapse before reaching this point, or by choosing a plasma vessel with length such that the electrons exit the plasma before dephasing occurs.

The initial energy follows from the initial longitudinal and transverse momentum of the electron,

$$\gamma_i = \sqrt{1 + \frac{p_{z,0}^2}{m^2c^2} + \frac{p_{\perp,0}^2}{m^2c^2}}, \tag{3.28}$$

where typically $1 + p_{z,0}^2/m^2c^2 = \gamma_\phi$ can be assumed as the longitudinal velocity will be approximately equal to the bubble velocity at injection. The contribution to the total electron energy of small amplitude transverse motion can be neglected. However, for larger perturbations the contribution to the total γ may be approximated through the average momentum contribution

$$\gamma_i = \sqrt{1 + p_{z,0} + \langle p_{\perp,\mathrm{max}} \rangle} \tag{3.29}$$

$$= \sqrt{1 + p_{z,0}^2 + \frac{1}{16}\frac{k_p^2 r_\beta^2}{\gamma_i}}. \tag{3.30}$$

γ_i may then be found either by solving the cubic equation above, or approximating the value of γ_i on the r.h.s as γ_ϕ, as it is assumed that while non-negligible, the contribution of the perpendicular motion is still small compared to the longitudinal.

An expression for the transverse motion can be found by differentiating the Hamiltonian for the electron motion

$$\mathcal{H}_\perp = \gamma mc^2 + e\phi(\bar{r}) = c\sqrt{m^2c^2 + p_x^2 + p_y^2 + p_z^2} + e\phi(\bar{r}), \tag{3.31}$$

$$\frac{\mathrm{d}y}{\mathrm{d}t} = \frac{\partial \mathcal{H}}{\partial p_y} = \frac{p_y}{m\gamma}, \tag{3.32}$$

$$\frac{\mathrm{d}p_y}{\mathrm{d}t} = -\frac{\partial \mathcal{H}}{\partial y} = -\frac{1}{2}m\omega_p^2 y. \tag{3.33}$$

This gives a second order differential equation for the motion

$$\frac{\mathrm{d}^2 p_y}{\mathrm{d}t^2} + \omega_\beta^2(t) p_y = 0, \tag{3.34}$$

which is the equation for a harmonic oscillator with a slowly varying frequency $\omega_\beta(t) = \omega_p/\sqrt{2\gamma(t)}$. If the variation of γ is slow compared with ω_p^{-1} then the action $J = 2\pi\mathcal{H}_\perp/\Omega_\beta(\tau)$ will be approximately conserved.[60] Therefore we may use the WKB approximation[61] (see appendix A), which approximates the solution to (3.34) as

$$\begin{aligned} p_y(t) &= p_y(t_0)\sqrt[4]{\frac{\omega_\beta(t_0)}{\omega_\beta(t)}}\exp\left[\pm i\int_{t_0}^{t}\omega_\beta(t')\,\mathrm{d}t'\right], \\ &= p_y(t_0)\sqrt[4]{\frac{\omega_\beta(t_0)}{\omega_\beta(t)}}\cos\left[\int_{t_0}^{t}\omega_\beta(t')\,\mathrm{d}t' + \phi_{y,0}\right]. \end{aligned} \tag{3.35}$$

where the second form makes use of the properties of phasor addition.

Similarly, a solution may be found for the transverse position

$$y(t) = \frac{p_y(t_0)}{m_e\gamma(t_0)\omega_\beta(t_0)}\sqrt[4]{\frac{\omega_\beta(t)}{\omega_\beta(t_0)}}\sin\left[\int_{t_0}^{t}\omega_\beta(t')\,\mathrm{d}t' + \phi_{y,0}\right], \tag{3.36}$$

$$= y(t_0)\sqrt[4]{\frac{\omega_\beta(t)}{\omega_\beta(t_0)}}\sin\left[\int_{t_0}^{t}\omega_\beta(t')\,\mathrm{d}t' + \phi_{y,0}\right]. \tag{3.37}$$

It is helpful at this point to make the substitution[59]

$$\tau = \frac{\omega_p(t-t_d)}{\sqrt{\omega_p^2t_d^2 + 8\gamma_i\gamma_\phi^2}} = \frac{k_p(ct + 2\zeta_i\gamma_\phi^2)}{\sqrt{8\gamma_d\gamma_\phi^2}}. \tag{3.38}$$

which allows the integral in the phase term to be written $\arcsin(\tau)$. This is a normalised time variable such that the interval from -1 to 0 represents the full acceleration period from zero energy to dephasing, and similarly the interval from 0 to 1 the full deceleration period. Recalling that the time was defined such that $t = 0$ at injection, and since at injection the electron velocity is equal to the bubble velocity, $\gamma = \gamma_\phi$, it follows that the value of τ at injection is

$$\tau_{\text{inj}} = \tau(t=0) = \frac{-\omega_p t_d}{\sqrt{\omega_p^2 t_d^2 + 8\gamma_\phi^3}}. \tag{3.39}$$

---

[60] H. Goldstein et al. *Classical Mechanics*, Addison Wesley, 2002.

[61] R. Shankar. *Principles of Quantum Mechanics*, Springer US, 1994.

Substituting τ into the expression for the zero-order evolution of the longitudinal momentum, (3.24), gives

$$p_z(\tau) = (1-\tau^2)p_{z,\mathrm{max}}. \tag{3.40}$$

Assuming that the total energy is well approximated by the longitudinal energy $\gamma(\tau) \simeq p_z(\tau)/mc$, then we can also assume

$$\gamma(\tau) = \gamma_d(1-\tau^2), \tag{3.41}$$

which will be valid if the transverse motion is small $p_z^2 \gg (p_x^2 + p_y^2)$.

Using this substitution (3.35) and (3.36) become

$$p_y(\tau) = P_0\left(1-\tau^2\right)^{-\frac{1}{4}} \cos\left[2\gamma_\phi \arcsin(\tau) + \phi_0\right], \tag{3.42}$$

$$y(\tau) = Y_0 \sqrt[4]{1-\tau^2} \cos\left[2\gamma_\phi \arcsin(\tau) + \phi_0\right], \tag{3.43}$$

where P_0 and Y_0 are constants which can be found using the oscillation amplitude and energy of an electron at any point during the acceleration process $P_0 = p_y(t)[\gamma(t)/\gamma_d]^{1/4}$, $Y_0 = y(t)[\gamma_d/\gamma(t)]^{1/4}$.

From this we see that the acceleration causes the oscillation frequency and amplitude to decrease as the relativistic mass of the electron grows. In addition, we find that the that the total number of oscillations between injection and dephasing is approximated by the Lorentz factor of the bubble $N_\beta \sim \gamma_\phi$. An expression for the normalised transverse velocity may be found by differentiating the expression for the position

$$\beta_y(\tau) = \frac{1}{c}\frac{\mathrm{d}y}{\mathrm{d}\tau}\frac{\mathrm{d}\tau}{\mathrm{d}t} = \frac{Y_0\omega_p}{4\gamma_\phi c\sqrt{2\gamma_d}}\left\{\frac{\tau\cos\left[2\gamma_\phi\arcsin(\tau)+\phi_0\right]}{(1-\tau^2)^{5/4}} - \right. \\ \left. \frac{4\gamma_\phi\sin[2\gamma_\phi\arcsin(\tau)+\phi_0]}{(1-\tau^2)^{3/4}}\right\}. \tag{3.44}$$

The longitudinal velocity can be calculated by completing the square with the total gamma and the longitudinal velocity. The longitudinal position follows by integration. Since, however, we have already made the assumption that the transverse

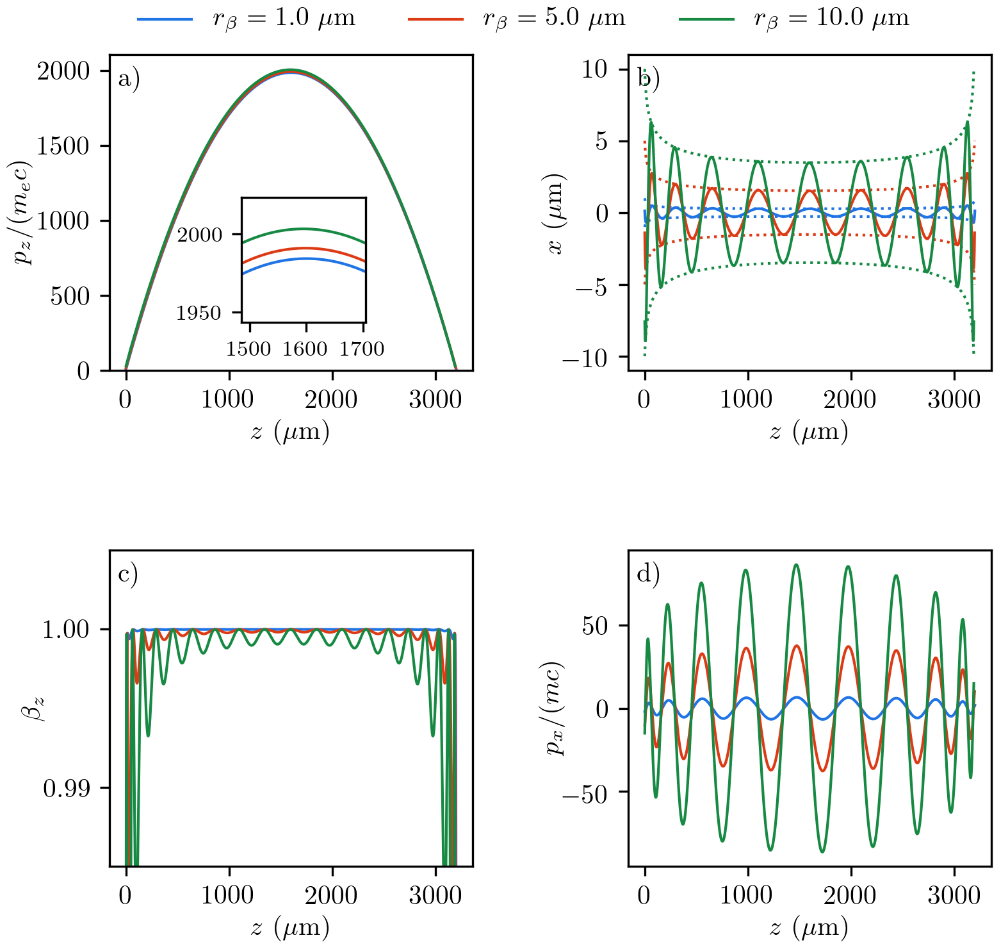

Figure 3.4: Electron acceleration behaviour in an ideal bubble for increasing betatron oscillation amplitude. Subfigure a) shows the longitudinal momentum of the electron, with respect to the electron position z in the lab frame, b) shows the transverse position of the electron (solid line), and the evolution of the oscillation amplitude (dotted line). Subfigure c) shows the longitudinal velocity and d) the transverse momentum of the electron. The plasma density as a fraction of the critical density $\eta^2 = 0.01$ corresponding to an electron number density of $\sim 1.74 \times 10^{25}\,\mathrm{m}^{-3}$ for an 800 nm laser wavelength.

momentum is small compared to the longitudinal momentum, the longitudinal velocity may also be estimated as

$$\beta_z(\tau) \simeq \sqrt{1 - \frac{1}{\gamma^2}} = \sqrt{1 - \frac{1}{\gamma_d^2(1-\tau^2)^2}}. \tag{3.45}$$

This behaviour is illustrated graphically in figure 3.4, which shows the evolution of electrons with increasing initial betatron oscillation amplitudes for an ideal bubble in plasma with fractional density $\eta^2 = 0.01$ relative to a laser with wavelength 800 nm, corresponding to an electron number density of $\sim 1.74 \times 10^{25}\,\mathrm{m}^{-3}$. The dephasing length ct_d for an electron in these conditions is approximately $L_{\text{deph}} = 1600\,\mu\mathrm{m}$ as given by (3.25) with an energy at dephasing of $\gamma \sim 2000$. Figure 3.4(a) shows the parabolic nature of the total energy evolution, symmetric about the peak in energy at the dephasing time. The small differences in the peak energies (inset) are due to the additional contribution to the total energy γ from the transverse motion. Figure 3.4(b) shows this transverse motion, which reduces in amplitude (dotted line) with $\gamma^{-1/4}$. The longitudinal velocity obtained from completing the square with the transverse momentum is shown in figure 3.4(c), this shows the expected oscillation at twice the transverse oscillation frequency. The effect diminishes as the energy contribution from the longitudinal motion increases rapidly relative to the fixed contribution from the transverse motion. Figure 3.4(d) shows the evolution of the transverse momentum with respect to time, which increases with $\gamma^{1/4}$ due to the increasing relativistic mass of the electron. It is important to note, however, that this picture is not quite correct: in order to ease calculation the model assumes the behaviour of the total energy γ is parabolic in time. In reality however, it is the longitudinal momentum that has this behaviour, and γ^2, as the quadrature sum of the longitudinal and transverse momenta, will have the oscillatory behaviour. This incorrectly suggests that the transverse momentum has an oscillatory component, and also means that the effects of the oscillation of γ are not correctly included in the calculation of the longitudinal velocity. Since injection and acceleration are both highly sensitive to the small difference between the electron velocity and the bubble velocity, small errors in the velocity can lead to large errors in the calcultion of dephasing length, and maximum energy. Small errors in velocity can also lead to very different predictions for the behaviour of the electrons at injection as will be seen in chapter 4.

3.2.5 Electron Trajectories in the Sheath Region

Thomas[20] gives an elegant demonstration of the elliptical nature of the sheath electron trajectories around the periphery of the bubble: transforming to the frame comoving with the bubble, the equations of motion in proper-time for an electron in the bubble fields are

$$\frac{\mathrm{d}p'_z}{\mathrm{d}\tau} = -m_e\frac{\omega_p^2}{2\gamma_p}\left(\gamma' z' - \gamma_\phi^2 \frac{p'_y}{m_e c} y'\right), \tag{3.46}$$

$$\frac{\mathrm{d}p'_r}{\mathrm{d}\tau} = -\gamma\omega_\phi\omega_p^2 2c\left(\gamma' m_e c + p'_z\right) r'. \tag{3.47}$$

Assuming that the longitudinal momentum is much larger than the transverse momentum $p'^2_z \gg p'_r$ the Lorentz factor may be approximated as

$$\gamma' m_e c = |p'_z|\sqrt{1 + \frac{p'^2_r + 1}{p'^2_z}} \simeq |p'_z| + \frac{p'^2_r + 1}{2|p'_z|} \tag{3.48}$$

and so we may write the equations of motion as

$$\frac{\mathrm{d}p'_z}{\mathrm{d}\tau} = -\frac{\omega_p^2}{2\gamma_p c}\left(|p'_z| z' + \frac{p'^2_r + 1}{2|p'_z|} z' - \gamma_\phi^2 \frac{p'_y}{m_e c} y'\right) \tag{3.49}$$

$$\frac{\mathrm{d}p'_r}{\mathrm{d}\tau} = -\gamma\omega_\phi\omega_p^2 2c\left(|p'_z| + \frac{p'^2_r + 1}{2|p'_z|} + p'_z\right) r'. \tag{3.50}$$

For electrons streaming backwards around the bubble the two p'_z terms in (3.50) cancel, and the remaining expression may be substituted into (3.49) to give

$$\frac{\mathrm{d}p'_z}{\mathrm{d}\tau} + \frac{\mathrm{d}p'_r}{\mathrm{d}\tau}\frac{z'}{\gamma_\phi^2 r'} = \frac{\omega_p^2}{4\gamma_\phi c}\frac{\mathrm{d}}{\mathrm{d}\tau}\left(z'^2 + \gamma_\phi r'^2\right). \tag{3.51}$$

This equation is satisfied by any trajectory that has the form $x^2/\gamma_\phi^2 + y^2 = R^2$. Therefore we can see that for the spherical bubble form we have assumed, electrons that have experienced an initial transverse kick from the laser and with large backward velocity relative to the bubble will travel in approximately elliptical trajectories around the periphery of the bubble.

This view of the electron sheath behaviour is limited by two factors. The first is the assumption that the longitudinal momentum is much larger than the transverse momentum, which breaks down close to the back of the bubble and distorts the trajectory. This is because the electrons will be approaching a maximum of transverse momentum and a minimum of longitudinal momentum at this point, and therefore the model underestimates the transverse acceleration. This means the sheath will close more rapidly and the bubble will be shorter than that due to truly elliptical electron trajectories.

The second limitation is due to the shielding effects of the sheath electron population, which distorts the fields seen by individual sheath electrons. Therefore, we expect that the behaviour of the sheath electrons, whilst broadly described by an elliptical trajectory, will be highly complex and require a fully self-consistent approach in order to be correctly modelled.

3.2.6 PIC Simulation of the Bubble

Using PIC simulation data it is possible to track the behaviour of the electron pseudoparticles in the laser and bubble fields. Although each pseudoelectron represents many millions of individual electrons the charge to mass ratio is the same, and therefore the trajectories are representative of individual electrons in the physical plasma. In order to extract the trajectory data a C++ code, “SDFTracks”, was written to take the snapshot data from the PIC simulation and identify pseudoparticles matching certain criteria. The code then extracts the data for the full trajectories of these particles and stored it in the more convenient form of per-particle time-series data. A complete discussion of the code is given in appendix B. For comparison with the predictions made by Thomas, we consider all

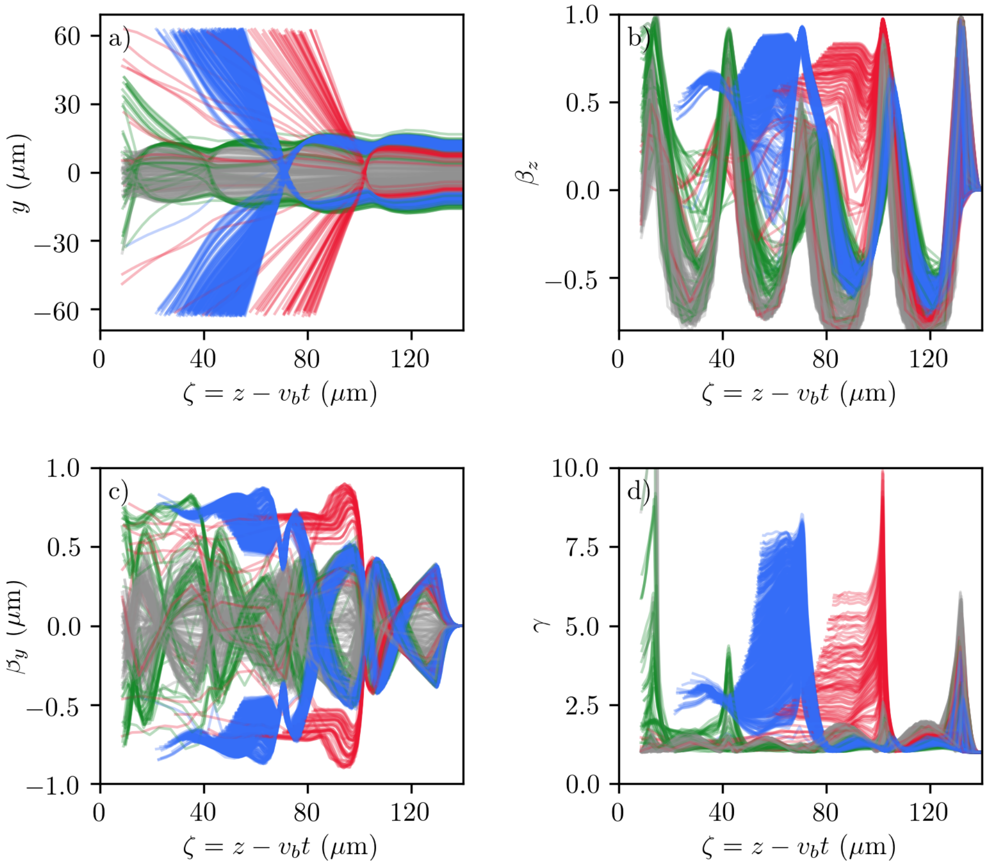

Figure 3.5: Trajectories of the electrons interacting with the bubble structure from the simulation shown in figures 3.2 and 3.3. All parameters are plotted with respect to the coördinate ζ which is comoving with the bubble. a) shows the electron trajectory as it propagates around the bubble, b) the longitudinal velocity, c) the transverse velocity, d) the electron energy as the relativistic parameter γ. Particles are colour coded based on the bubble for which they form the sheath: red - first bubble, blue - second bubble, green - third bubble, grey - no strong transverse component of motion.

pseudoelectrons which interact with the laser and form the bubble, using results from the same 2D EPOCH PIC simulation shown in figures 3.2 and 3.3. As the laser is relativistically intense ($a_0 > 1$) electrons that interact strongly with the laser field may be identified as those which have $\gamma > 2$ at some point during their lifetime. It is not feasible to consider all the electrons meeting this condition as they are simply too numerous to produce a meaningful analysis plot. Therefore, electrons were extracted using the SDFTracks program if they had maximum energy $\gamma > 3$, hence ignoring electrons that only interact minimally with the laser; within a time period of $1.80 - 1.81\,\mathrm{ps}$ of elapsed simulation time, equivalent to a laser propagation distance of $3\,\mu\mathrm{m}$. To further reduce the number of particles, a random subset of 20% of these were taken to produce the trajectory plots in figure 3.5.

The electron behaviour is broadly split into two different populations, some (coloured) performing large movement in the transverse direction, others (grey) having little transverse motion. We see from this that the sheath electrons do indeed follow the elliptical trajectories predicted by Thomas. As is also predicted, we see that the bubble is not a true ellipse, and at the rear of the bubble the trajectories suddenly close very rapidly, as the approximations made in the description break down. In this region the electron velocities are small, so that the electron behaviour is particularly sensitive to small changes in the electric fields in this region. This region also contains the largest electron space charge because the sheath flows converge and cross, with a large local space charge (seen in figure 3.3) leading to large distortion of the bubble fields away from the ideal model.[21]

An interesting depedence can be seen here of the electron's impact parameter (transverse distance from the axis prior to interaction with the laser) in the initial laser scattering, on its future behaviour. It is typically assumed[62] that the sheath electrons oscillate in the ion channel left by the laser over multiple periods, with

---

[21] M. R. Islam et al. *New J. Phys.* **17**, p. 093033, 2015.

[62] S. M. Hooker. *Nat. Photonics* **7**, pp. 775–782, 2013.

the same electrons forming the sheath for all the bubbles in the train. However, the behaviour in figure 3.5 does not support this. Instead we see that after the electrons cross the axis, the majority are in fact ejected transversely from the bubble and simulation domain. These electrons have a gamma in the range $\gamma \sim 2 - 10$, equivalent to an energy of a few MeV. This energy is split approximately equally between the transverse and longitudinal directions, as shown in the figure, and so we would expect a spray of electrons to be ejected from the LWFA at a forward angle of approximately 45°. These beams were initially observed experimentally on the ALPHA-X beamline at the University of Strathclyde.[63] Further theoretical and experimental investigations reveal that total charge of the resulting beam is of the order of 10s of nanocoulombs, and accounts for $5 - 10\%$ of the total laser energy input into the system.

The details of the sheath electron trajectories have been investigated by a number of authors,[19,21,55,56,64] who attempt to include the space charge effect of the sheath electrons on their motion. In particular, Lu *et al.*[56] found that this gave excellent agreement with simulation results until close to the rear of the bubble, but at this crucial point the good agreement is lost. They suggest this is due to the fact that they assume the sheath density profile has a constant width and magnitude, failing to take into account any evolution around the bubble and the sheath crossing region at the rear where there is a sudden increase in the electron density. This is consistent with results found by Thomas and also the work performed by Islam *et al.*[21] who consider the effect that this large local space charge has in perturbing the electron trajectories such that they are injected into the bubble. The sensitivity of the injection process to the behaviour of the rear of the bubble is of great importance, as will be discussed in chapter 4.

---

[63] X. Yang et al. *Sci. Rep.* **7**, pp. 1–10, 2017.

[19] D. Lu et al. *Phys. Plasmas* **20**, p. 063104, 2013.

[64] X. F. Li et al. *Phys. Plasmas* **21**, p. 73109, 2014.

3.2.7 Beam Emittance

The emittance of a particle bunch is a measure of the spread of the momentum and position distributions of the bunch particles about a reference trajectory. This distribution will occupy some volume in the 6-dimensional position-moment phase space, and can be a useful measure of bunch properties. In most cases, rather than consider the distribution in all dimensions simultaneously the emittance is considered separately in three orthogonal directions, typically parallel and perpendicular to the direction of propagation.

In deriving a statistical expression for the emittance it is normally assumed that the phase space area in each dimension is approximately elliptical, with the semi-major and semi-minor axes being the maximum deviation from the mean of the position and momentum. These maxima are typically scaled to represent the core of the bunch rather than including low density fringes, the common choice being to use the RMS width of the distributions as a measure of the area of the high density core of the bunch. In this case, in one dimension, the emittance is given by either[65]

$$\varepsilon_{\mathrm{n,rms}} = \frac{1}{m_0 c}\sqrt{\langle x^2\rangle \langle p_x^2\rangle - \langle x p_x\rangle^2}, \tag{3.52}$$

or

$$\varepsilon_{\mathrm{rms}} = \frac{\varepsilon_{\mathrm{n,rms}}}{\bar{p}_z}, \tag{3.53}$$

where $\varepsilon_{\mathrm{n,rms}}$ is the normalised emittance, so called because it is invariant with changes in the total bunch energy or reference frame, and $\varepsilon_{\mathrm{rms}}$ the true or geometric emittance. This latter is the physically measurable quantity, which is adiabatically damped with increasing (bunch average) longitudinal momentum $\bar{p}_z$.

The usefulness of the beam emittance follows from it being a measure of phase space volume: the emittance is a conserved quantity under any interaction of

---

[65] K. Floettmann. *Phys. Rev. Spec. Top. Accel Beams* **6**, pp. 80–86, 2003.

the bunch with a conservative force,[*] a result known as Liouville's theorem.[60] The static electric and magnetic fields used in the beam optics of a conventional accelerator are a conservative system, thus the beam emittance will be conserved,[†] and indeed a maximum emittance or acceptance is a key property of the machine. For a given set of beam optics and a given size of beam pipe into which the bunch must fit, the acceptance is the largest emittance that guarantees the fringes of the bunch will not collide with the beam pipe wall at the extrema of their oscillations.

The emittance is a useful measure of the bunch distribution in the LWFA. However, there is an important difference between the behaviour of emittance in the LWFA compared to the conventional strong-focusing accelerator. In a conventional accelerator, where the beam transport is achieved by alternating quadrupole magnets in a alternating focusing-defocusing (FODO) configuration, the oscillation wavelength of the electrons in the magnetic field is externally imposed. However in the LWFA the betatron oscillation wavelength and period depend upon γ and are therefore properties of individual electrons rather than of the bunch. As a result, if there is a spread in total energy of the electrons, the beam emittance will grow over time as the phase difference between the electrons in the bunch grows.[66] This can be considered in transverse phase space as a set of initially overlapping ellipses representing bunch electrons, with the electrons in each having the same distribution in x and p_x but having a different total energy γ. As the betatron oscillation period depends upon gamma the rotation rate of each ellipse will vary, therefore over time, the decoherence of the rotations causes the total phase space volume of the bunch to increase. This effect also couples

---

[66] T. Mehrling et al. *Phys. Rev. Spec. Top. Accel Beams* **15**, p. 111303, 2012.

[*] A conservative force is one for which the work done in moving a particle between two points is independent of the path taken

[†] Note that this is only true in the absence of space charge effects or other nonlinear effects, these are non-conservative and so in reality beam emittance will slowly grow during beam transport in such an accelerator

to the longitudinal emittance, where the difference in transverse momentum can lead to variations in the average longitudinal velocity of the electrons, causing the bunch length to increase. These effects are important when considering the effects of finite bunch spread on the radiation emitted by the bunch. This is discussed in chapter 5, where a small bunch emittance at injection is found to grow as the bunch propagates, leading to a potentially large bunch spread and reduced radiation coherence at dephasing, where the electron energy and hence radiation intensity are largest.

3.3 Laser Propagation in the Plasma

As we have seen in the previous section, the electron and bubble behaviour depends upon the details of the driver. The key figure of merit for a LWFA driver is the normalised vector potential a_0 (2.26), which scales with the electric field strength and inversely with frequency, and therefore determines the peak energy of electrons that are scattered by the laser. This behaviour has already been described via the ponderomotive approximation in section 2.4. The energy of the sheath electrons "kicked" by the driver sets the size of the bubble, and hence the maximum acceleration distance and field strength, which controls the maximum attainable electron energy. Because of this, understanding and controlling the laser behaviour is a crucial factor in building a stable and tuneable LWFA system.

The major processes governing the laser propagation in the plasma are the beam divergence, refractive focusing and energy depletion. The interplay between these effects, determines the propagation dynamics of the laser, the evolution of the laser intensity and the total distance the laser propagates before either diverging or being depleted of energy such that it is no longer of useful intensity.

3.3.1 Propagation Velocity and the Critical Density

The propagation velocity of the laser pulse within the plasma follows from the dispersion relation. For a transverse EM wave in a cold unmagnetised plasma the dispersion relation is

$$k^2 = \frac{\omega^2 - \omega_p^2}{c^2}, \tag{3.54}$$

where ω is the frequency and k the wavenumber of the EM radiation. Therefore, in order for the wavenumber to be real and the wave to propagate, the laser frequency must be higher than the electron plasma frequency. It follows from this that for a laser pulse with a given frequency or wavelength in vacuum, there is a maximum plasma density above which the laser will be unable to propagate. This is termed the "critical density"

$$n_{\text{crit}} = \frac{\omega^2 m_e \epsilon_0}{e^2}, \tag{3.55}$$

for a given laser frequency ω.

The group velocity v_{dr} of a laser driver in plasma will therefore depend upon the electron plasma frequency and hence plasma density,

$$v_{\text{dr}} = \frac{\partial \omega}{\partial k} = c\sqrt{1 - \frac{\omega_p^2}{\omega^2}}. \tag{3.56}$$

It is useful to express the plasma density n_e for the LWFA as a fraction of the critical density η such that $\eta^2 = n_e/n_{\text{crit}}$ and therefore $\eta = \omega_p/\omega_0$. In this case, provided $\eta << 1$, the pulse group velocity may be expressed as

$$v_{\text{dr}} = c\sqrt{1 - \eta^2} \simeq c\left(1 - \frac{1}{2}\eta^2\right). \tag{3.57}$$

3.3.2 Beam Divergence

When a laser beam is focused to a small spot size in a linear medium, the beam will rapidly diverge over a short distance. For a beam with approximately Gaussian transverse profile, the characteristic divergence length is given by the Rayleigh length

$$z_r = \frac{\pi w_0^2}{\lambda}, \tag{3.58}$$

where w_0 is the beam waist at the focus, (radius at which intensity drops to e^{-2} of maximum), and λ is the laser wavelength. The Rayleigh length is the distance over which the cross-sectional area of the beam doubles, increasing the radius by a factor $\sqrt{2}$. Typically for LWFA the beam waist will be of order $10\,\mu$m and the laser wavelength of order $1\,\mu$m, giving a Rayleigh length of order $100\,\mu$m. As we have seen, typical dephasing lengths for the LWFA are of the order of mm or more, so for efficient acceleration some method of guiding the laser driver is required to sustain an accelerating bubble over large propagation distances.

3.3.3 Refractive Focusing

The divergence of the laser may be controlled by the introduction of a density channel in the plasma with a minimum of density on axis and increasing density with increasing radial distance. This structure produces a transverse refractive index gradient that serves to re-focus the laser pulse towards the channel centre.[67] Such a gradient may be produced either by some external means, or for sufficiently intense lasers, by the action of the front of the pulse creating a channel that focuses the bulk of the laser pulse.[68,69]

3.3.4 Channel Guiding

Typically externally produced guiding channels for LWFA are formed either by using a laser prepulse[70,71] or plasma arc discharge in a capillary.[72–74] A plasma

---

[67] E. Esarey et al. *IEEE J. Quantum Electron.* **33**, pp. 1879–1914, 1997.
[68] H. Hora. *J. Opt. Soc. Am.* **65**, p. 882, 1975.
[69] B. Ritchie. *Phys. Rev. E: Stat., Nonlinear, Soft Matter Phys.* **50**, R687–R689, 1994.
[70] A. Zigler et al. *J. Opt. Soc. Am. B* **13**, p. 68, 1996.
[71] C. G. Geddes et al. *Phys. Rev. Lett.* **95**, pp. 1–4, 2005.
[72] C. Durfee and H. M. Milchberg. *Phys. Rev. Lett.* **71**, pp. 2409–2412, 1993.
[73] D. J. Spence and S. M. Hooker. *Phys. Rev. E* **63**, p. 015401, 2000.
[74] T. P. Rowlands-Rees et al. *Phys. Rev. Lett.* **100**, p. 105005, 2008.

guiding channel may be produced in a gas jet by a heating laser pulse, with duration on the order of hundreds of picoseconds, cylindrically focused on the intended propagation axis of the LWFA driver. This heats the plasma on the laser axis by inverse brehmsstrahlung and the subsequent thermal expansion drives a hydrodynamic shock[75] producing a density minimum along the focus of the pulse with an approximately parabolic transverse density profile. The capillary waveguide comprises an open-ended sapphire capillary tube with additional ports along its length for introduction of gas.[73,76] A high voltage discharge along the tube ionizes the gas to create plasma, and in this case cooling of the plasma against the capillary walls produces a parabolic transverse density profile. Capillary waveguides in particular are useful because they can sustain stable guiding channels over lengths of several centimeters,[77] with density controllable over that length by varying the gas pressure and capillary diameter.[78]

In either of these cases, for laser powers not exceeding the critical power for relativistic self-focusing, the effects of the channel profile will dominate the guiding of a laser pulse in the channel.[79] If the laser is centered in the channel, the refractive index gradients will be positive with increasing radial position. The effect of this is that the group and phase velocities of the laser pulse differ across the width of the pulse and so the laser wavefront becomes curved with the centre of the pulse retarded relative to the edges, producing an overall focusing effect. For correctly "matched" parameters of transverse plasma channel and laser profile, it is possible to get stable propagation over many hundreds of Rayleigh lengths, which for typical LWFA wavelengths can be many tens of mm.[79,80]

---

[75] C. G. Durfee et al. *Phys. Rev. E* **51**, pp. 2368–2389, 1995.

[76] A. Butler et al. *Phys. Rev. Lett.* **89**, p. 185003, 2002.

[77] F. Wojda et al. *Phys. Rev. E* **80**, p. 066403, 2009.

[78] S. Abuazoum et al. *Appl. Phys. Lett.* **100**, p. 014106, 2012.

[79] C. Benedetti et al. *Phys. Plasmas* **19**, p. 053101, 2012.

[80] S. Cipiccia et al. *Nat. Phys.* **7**, pp. 867–871, 2011.

3.3.5 Relativistic Self-Guiding

In the case that the laser pulse is relativistically intense, ($a_0 \gg 1$), the pulse can "self-guide" by creating its own plasma density channel[67–69]. This was initially described for very long pulses on the order of hundreds of plasma wavelengths, due to the expulsion of ions from the laser axis,[68] however, short pulses may also be guided by refractive index changes from the electron plasma response. This requires a relativistically intense laser pulse so that electrons are rapidly expelled by the front of the laser pulse. As a result of this, the bulk of the pulse experiences a refractive index gradient that has a peak on axis and so self-focuses. The minimum length of laser pulse that can be guided in this way depends upon the average transverse energy $\gamma_\perp$ of the displaced electrons,[58,81]

$$L_{\mathrm{min}} \lesssim \frac{\lambda_p}{\gamma_\perp}. \tag{3.59}$$

This is the minimum length of pulse required to drive a density gradient, and hence refractive index gradient large enough to cause self-guiding. The critical laser power required for self-guiding to dominate is derived by considering the laser power that balances the pulse diffraction with focusing due to the induced refractive index gradient.[68,69,82,83] This gives an approximate result of[83]

$$P_{\mathrm{cr}} \sim 16.2\frac{\omega_0^2}{\omega_p^2} \times 10^9\,\mathrm{W}. \tag{3.60}$$

In the case that the critical power is exceeded the laser will initially be focused to a more intense spot, however diffraction prevents indefinite focusing and can lead to oscilliatory behaviour about a "matched" size. This oscillatory behaviour was investigated by Sprangle *et al.*[82] using an effective potential to model laser focusing and diffraction. The potential minimum equates to the case that the laser has exactly the critical power, and for laser powers $P > P_{\mathrm{cr}}$ the amplitude of the

---

[81] A. Ting et al. *Phys. Fluids B* **2**, pp. 1390–1394, 1990.

[82] P. Sprangle et al. *IEEE Trans. Plasma Sci.* **15**, pp. 145–153, 1987.

[83] P. Chessa et al. *Phys. Plasmas* **5**, pp. 3451–3458, 1998.

spot size oscillation within the effective potential increases. These equations may be solved numerically to find the potential minimum and hence "matched" laser spot size. As the laser spot size changes through self-focusing, the laser amplitude will also change. These changes affect the shape and behaviour of the bubble, which can subsequently influence injection behaviour, as will be seen in chapter 4.

For the case of the LWFA bubble regime, laser pulses with $a_0 > 1$ and spot size $\sigma < \lambda_p$ are required to produce a stable bubble with linear accelerating fields. This almost always exceeds the critical power for self-focusing, often by a large amount, leading to strong oscillation of the laser spot size and intensity. If good control of self-injection is required, care must be taken to minimize the oscillation of the laser intensity. Therefore, the laser and plasma parameters must be chosen ensure that the laser pulse is closely matched to the plasma. These effects are investigated in detail in section 4.8.

3.3.6 Pulse Erosion

The length L_{min} given in (3.59) is also the approximate length of the region at the front of the pulse which interacts with and does work on the electron plasma. The front section of the pulse is unguided and so will diffract, but it will also lose amplitude as it transfers energy to the plasma. This causes "etching" or "erosion" of the front of the laser pulse,[84] which progresses back through the pulse with velocity

$$v_{\mathrm{etch}} \simeq \frac{\omega_p^2}{\omega_0^2}. \tag{3.61}$$

This modifies the laser group velocity in the plasma, giving an approximate velocity in terms of the laser and plasma frequencies,

$$v_g \simeq = 1 - \frac{3}{2}\frac{\omega_p^2}{\omega_0^2}. \tag{3.62}$$

---

[84] C. D. Decker et al. *Phys. Plasmas* **3**, pp. 2047–2056, 1996.

In the relativistically intense regime of interest, the etching process dominates over the diffraction of the leading edge[81] meaning that significant diffraction of the front of the laser will not be seen until the pump is mostly depleted, at which point the power will be below the critical power for self-guiding and the small remaining pulse will diffract over a Rayleigh length.

3.3.7 Pump Depletion and Photon Deceleration

As an intense laser pulse propagates through plasma it will evolve due to both linear and non-linear effects.[81,85–88] The primary drivers of this laser pulse evolution are depletion of the laser energy as it is coupled into the plasma and the effects of varying plasma density over the length of the pulse, which cause local variations in the pulse group and phase velocities, and hence change the overall pulse shape.

When propagating in the plasma the laser pulse loses energy to the plasma by imparting large quantities of energy to the electrons that form the bubble structure and create the wakefield. Eventually, this process will consume the energy of the pulse, the length scale over which this occurs is known as the pump depletion length. This length depends upon the total energy of the pulse and the density of the plasma, and multiple approaches have been taken in the literature to make analytic approximations of this length scale.[81,85,89] For the commonly used case of a Gaussian temporal pulse profile, the depletion length may be approximated by linearising the energy and action conservation equations for the laser pulse,[86,87] yielding

$$L_{\text{pd}} = \frac{\lambda_p^3}{\lambda^2} \times \begin{cases} \frac{2}{a_0^2} & \text{if } a_0^2 \ll 1, \\ \frac{\sqrt{2}}{\pi} a_0 & \text{if } a_0^2 \gg 1, \end{cases} \tag{3.63}$$

---

[85] D. Teychenné et al. *Phys. Plasmas* **1**, p. 1771, 1994.

[86] E. Esarey. *Proc. AIP* **737**, pp. 578–584, 2004.

[87] B. A. Shadwick et al. *Phys. Plasmas* **16**, p. 056704, 2009.

[88] C. Benedetti et al. *Phys. Rev. E* **92**, p. 023109, 2015.

[89] S. V. Bulanov et al. *Phys. Fluids* **4**, p. 1935, 1992.

where λ is the initial wavelength of the laser and $\lambda_p = 2\pi c/\omega_p$ is the plasma wavelength.

In addition to the loss of energy from the pulse, the laser intensity is affected by two further non-linear processes: frequency redshifting and pulse self-steepening[86,87]. This can, somewhat paradoxically, increase the intensity of the laser pulse as it loses energy into the plasma.[90–92]

The process of self-steepening occurs due to local differences in the laser group velocity within the pulse. As the laser drives the plasma wave and displaces electrons, it creates a density gradient in the electron plasma along its own length, with a lower plasma density at the rear of the pulse than at the front.[91] This results in a lower local group velocity at the front of the pulse relative to the rear and so compresses the pulse longitudinally, consequently increasing the peak intensity.

Frequency redshifting, also commonly referred to as “photon deceleration”,[90] is a consequence of the laser pulse losing energy by doing work on the plasma, whilst conserving the total number of photons in the laser pulse. The requirement for approximate conservation of the photon number follows from the relatively low plasma density, meaning there are minimal opportunities for direct photon-matter scattering processes to modify the photon number. As the laser loses energy to plasma, it therefore follows from the expression for the total pulse energy $U = N\hbar\langle\omega\rangle$, that in order to conserve the total photon number N, the average photon energy $\hbar\langle\omega\rangle$ and hence frequency must decrease. This can be expressed quantitatively for the one-dimensional case,[86] by the conservation of the action

---

[90] S. C. Wilks et al. *Phys. Rev. Lett.* **62**, pp. 2600–2603, 1989.
[91] F. S. Tsung et al. *Proc. Natl. Acad. Sci.* **99**, pp. 29–32, 2002.
[92] J. Vieira et al. *New J. Phys.* **12**, 2010.

$\mathcal{A}$ and total energy U of the pulse

$$\frac{\partial \mathcal{A}}{\partial \xi} = 0 \qquad \mathcal{A} = \int \mathrm{d}\xi k \left\langle a^2 \right\rangle \tag{3.64}$$

$$\frac{\partial U}{\partial z} = -\left(\frac{k_p}{k_0}\right)^2 \left(\frac{E_{\mathrm{max}}}{E_{\mathrm{WB}}}\right)^2 \qquad U = \int \mathrm{d}\xi \left| \left(i + k_0^{-1}\partial_\xi\right) a\, \mathrm{e}^{i\theta} \right|^2 . \tag{3.65}$$

The pulse action is divided into the envelope action, which varies slowly with respect to the laser frequency, and a high frequency component that is assumed to average to zero over a complete cycle (this is the same argument as used in the derivation of the ponderomotive force in section 2.4). $\xi = z - ct$ is the comoving coördinate, a is the evolving normalised vector potential of the laser pulse, E_{max} is the peak amplitude of the plasma wakefield driven by the laser, E_{WB} is the cold plasma wavebreaking field. Linearising these equations yields an approximate analytic solution including the expressions for the pump depletion length (3.63).

These equations have also been solved numerically by Esarey *et al.*[53] and Shadwick *et al.*[87] For the case of a relativistically intense laser ($a_0 \gg 1$), they found that the rates of pump depletion, laser redshift, pulse self-steepening are approximately linear with respect to the propagation distance, giving an associated linear increase in the vector potential a. After some distance the behaviour becomes nonlinear and a_0 increases to a maximum value, followed by a rapid decrease as the laser develops large frequency sidebands and spreads longitudinally. At this point, the pulse intensity has dropped below the relativistic self-focusing threshold, therefore the laser ceases to self-guide and rapidly defracts away. This non-linear behaviour was found to onset more rapidly for larger initial vector potential a_0 at the same density. This shows the importance of considering such non-linear effects as this behaviour contradicts the prediction made by the linearised expression for the pump-depletion length (3.63).

3.3.8 PIC Simulation of Laser Evolution in Plasma

To illustrate these effects for typical LWFA parameters, a series of simulations with the FBPIC code were performed. For all simulations the window size was $60\,\mu\text{m} \times 60\,\mu\text{m}$ with a grid resolution of 2000×400 (longitudinal × radial), using Bessel modes up to $n = 2$. The plasma was a flat top distribution with normalised electron number density $n_e/n_{\text{crit}} = 0.001$ for a laser with wavelength 800 nm. All laser pulses had a gaussian temporal and spatial profile, with temporal pulse length 25 fs. The beam waist and peak normalised vector potential were varied as described.

Although the one-dimensional model described above does not include transverse relativistic focusing or diffraction, the behaviour reported by Esarey *et al.*[53] and Shadwick *et al.*[87] shows good agreement with the behaviour observed in PIC simulations for LWFAs with matched beams in three-dimensions.

Figure 3.6 shows the evolution of the normalised vector potential a_0 for laser pulses with varying initial intensities and spot sizes, while figure 3.7 shows the corresponding evolution of the laser spot size. The smallest chosen spot size of $w = 10\,\mu\text{m}$ is too small to be well matched in the plasma. Therefore at all chosen intensities the laser spot size initially increases, and results in a reduction of a_0. These pulses show only linear behaviour, until, after several mm, the pulse intensity falls below the critical intensity for self-guiding. This causes rapid diffraction and breakup of the laser pulse. For $w = 15\,\mu\text{m}$ initial spot size pulses, the spot size is better matched to the plasma, as can be seen from the much smaller variation of the spot size as the pulse propagates. The rate of decrease of a_0 is also seen to be smaller. The small initial increase in a_0 and decrease in spot size is due to the fact that this size is still not perfectly matched to the plasma and so some amount of oscillatory behaviour occurs. After approximately 3 mm propagation distance, the non-linear behaviour described by Esarey *et al.*[53] and Shadwick *et al.*[87] can be

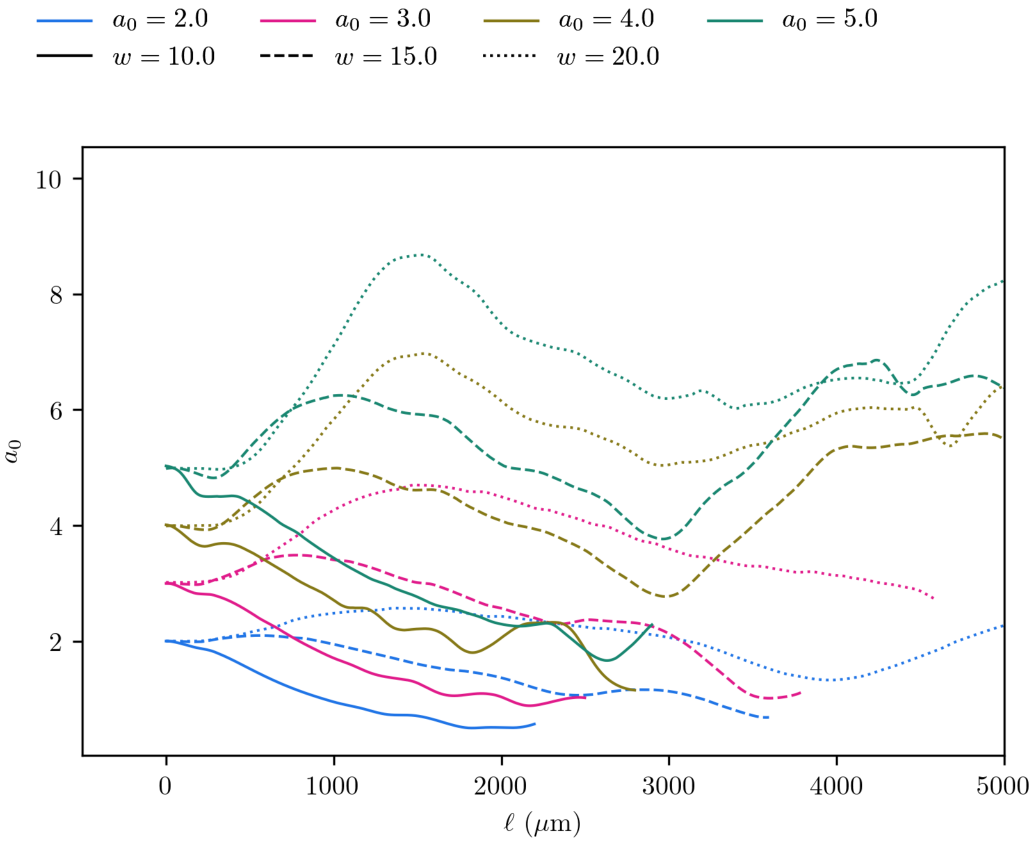

Figure 3.6: Evolution of the normalised vector potential a_0 for laser pulses with varying intensities and spot sizes in a plasma with normalised density $\eta^2 = 0.001$ and a pulse length $\tau_{\mathrm{FWHM}} = 25\,\mathrm{fs}$. The simulations were performed using the FBPIC code which is a cylindrically symmetric code with a frequency domain solver.

seen to take effect, with a rapid increase in a_0 followed by a rapid decline. For the initial $w = 20\,\mu$m spot size pulses, there is initially strong relativistic self focusing, as the spot is oversized compared to the matched beam size. The behaviour is otherwise similar to the $15\,\mu$m case, with a slow depletion of laser pulse energy and accompanying increase in spot size. It is interesting to note that for the large initial spot size, the initial onset of the nonlinear behaviour occurs after a longer propagation distance.

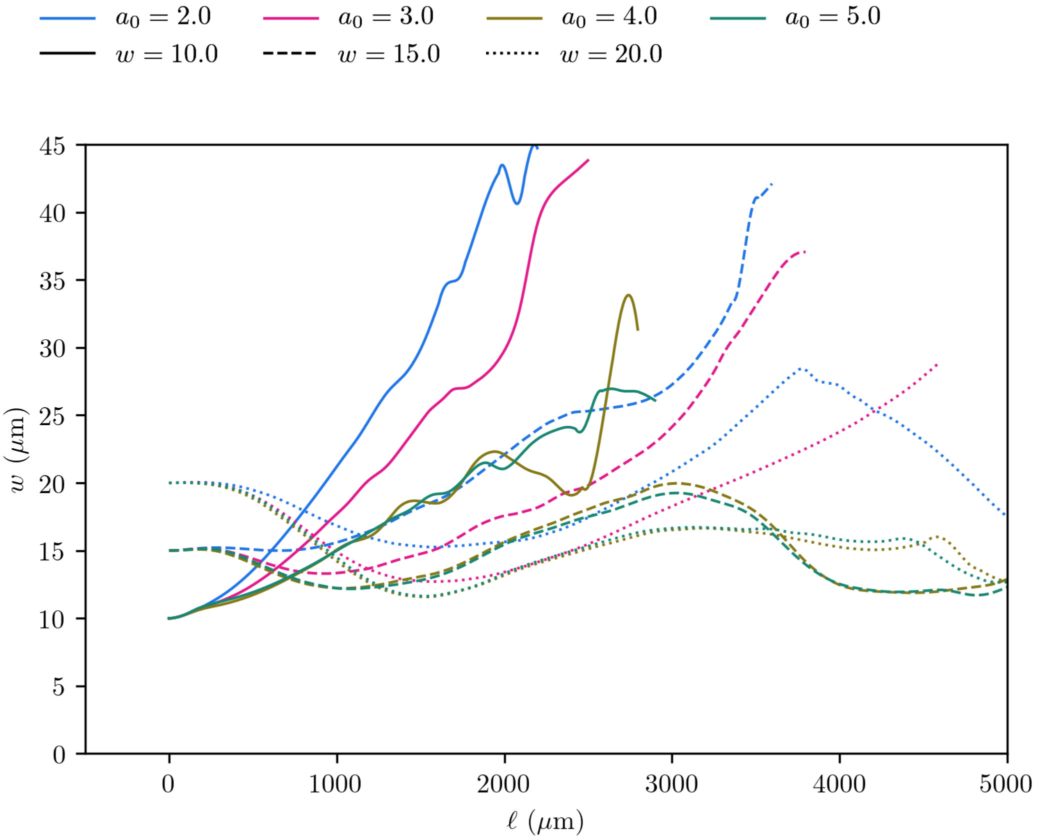

Figure 3.7: Evolution of the spot size w for the pulses shown in figure 3.6.

3.4 Conclusions

The non-linear "bubble" regime in the LWFA provides linear accelerating and focusing fields to the electron bunch within the cavity, and is therefore a desirable choice for producing bunches with low emittance and energy spread. The properties of the laser pulse are an important factor in the overall bubble behaviour, with bubble geometry determined by spot size and laser intensity. Choice of suitable laser parameters is complicated by the non-linear interaction between the laser pulse and the plasma. At high intensities, relativistic self-focusing and photon deceleration can cause large oscillations in the pulse intensity and spot size, whilst at low intensities, below the critical power for self-guiding, the laser pulse will rapidly diffract away. If the laser intensity and spot size are chosen such that the effect of self-focusing is balanced against diffraction the beam is said to be matched to the plasma and will self-guide with minimal evolution of the intensity or spot size. Therefore, in order to provide a stable bubble over large propagation distances, suitable matched beam parameters must be identified for each chosen plasma density. These effects, and the consquences for self-injection are discussed in detail in chapter 4.

Chapter 4

Controlling Self-Injection

As discussed in chapter 1, self-injection is a desirable method to inject a bunch of electrons into the bubble fields. It has the advantage of requiring no additional hardware such as a photocathode injector, and the attendant complexities of synchronisation. However, reliable control of the properties of the injected bunch remains an outstanding problem. In this chapter, a method to control injection is introduced. A model is developed to predict injection due to plasma density or laser intensity variations, and it will be shown how this can be used to control the injection process and produces bunches of a desired length or charge. Finally, this will be demonstrated using PIC simulations.

As already noted in chapter 1, injection is important in determining the properties of the bunch throughout its lifetime.[66] A property of primary importance for an electron bunch is its emittance, which relates the position and momentum distributions of the bunch particles in six-dimensional phase space. This quantity is conserved during interation with any conservative force that the bunch encounters. Therefore, although it is possible to change statistical properties of the bunch e.g transverse energy spread, there will be a corresponding change in the related variable (in this example the transverse size) in order that the emittance is conserved. The conservation of the emittance follows from a fundamental prop-

---

[66] T. Mehrling et al. *Phys. Rev. Spec. Top. Accel Beams* **15**, p. 111303, 2012.

erty of conservative systems, (Liouville's Theorem), which states that for a given n-body system with some initial phase space distribution, the phase-space volume occupied by the distributions will remain unchanged by any conservative force acting on the system. The purely electrostatic fields of the ideal bubble (in the co-moving frame) are such a conservative system, therefore, for an electron bunch subject only to the Lorentz force from constant fields, there is no way to change the emittance once it has been created. In reality, the emittance will evolve as there are other forces that do work on the particle, the most relevant in this case being the effects of non-linear bubble fields and acceleration. Acceleration causes the betatron frequency to change, leading to decoherence of the bunch oscillations as described in section 3.2.7; while driver or bunch evolution can cause the bubble fields to vary with time and position, and the radiation reaction force, which leads to radiative damping of the transverse momentum of the particle.[93] The control of such time varying fields or forces can be used to reduce emittance by addressing individual bunch electrons with corrections in turn, a process known as stochastic cooling,[94] the invention of which won Simon van der Meer and Carlo Rubbia the 1984 Nobel Prize for Physics. However, in the case of the LWFA, we have no such fine control to affect individual electrons, instead relying on the small size of the bunch relative to the length scale of the accelerating and focusing fields, to ensure emittance growth is small.

This chapter focuses on the use of density gradients in the plasma to control the self-injection process. It has been experimentally demonstrated that plasma density gradients may be used to induce self-injection, and this existing body of work forms the starting point for developing a predictive model for the process.

A predictive model for injection is developed using an approach that considers the behaviour of single electrons and compares them to the expected behaviour of the bubble fields. Using this information we can establish the required plasma

---

[93] P. Michel et al. *Phys. Rev. E* **74**, p. 026501, 2006.

[94] J. Marriner. *Nucl. Instrum. Methods Phys. Res., Sect. A* **532**, pp. 11–18, 2004.

parameters for self-injection and predict the properties of the injected electron bunches. The model is validated using PIC simulation, and extension to injection of multiple bunches is investigated. Finally, the limitations of the technique are discussed, in particular with respect to the effects of laser pulse evolution.

4.1 The Self-Injection Process

Self-injection due to wavebreaking was initially observed for the self-modulated LWFA (SM-LWFA)[95] for long ($\sim$ ps) laser pulses with intensities $a_0 < 1$. This causes injection of electrons into the accelerating plasma wave and production of $\sim$ keV electron beams. It was found experimentally[96] that the wavebreaking occurred for field strengths below the wavebreaking limit ($E_{\text{max}}/E_{\text{WB}} \sim 0.3$), which can be explained by thermal effects on the electron energy distribution and plasma instabilities.[97]

For the nonlinear "bubble" regime, initial theoretical investigation by Pukhov and Meyer-Ter-Vehn[10] found that trapping by wavebreaking occurs, once again, for peak field stengths approximately 30% of the cold wavebreaking limit. This is suggested to be due to the complex shape of the electron sheath structure, which leads to trajectory crossing at lower electric field strengths than for the 1-D case assumed in the deriviation of the wavebreaking limit field.

Further theoretical investigation was performed by Kostyukov, *et al.*[16] who developed a Hamiltonian description for the electron motion around the periphery of a non-evolving bubble. This suggested a mechanism by which electrons could be injected into the bubble, provided the normalised bubble radius $k_p r_b$ exceeded the driver gamma factor $k_p r_b > \gamma_{dr}$. It should be noted however that for typical experimental LWFA plasma densities and laser intensities, this requires a spot

---

[95] A. Modena et al. *Nature* **377**, p. 606, 1995.

[96] A. Ting et al. *Phys. Rev. Lett.* **77**, pp. 5377–5380, 1996.

[97] E. Esarey et al. *IEEE Trans. Plasma Sci.* **24**, p. 252, 1996.

[10] A. Pukhov and J. Meyer-ter-Vehn. *Appl. Phys. B: Lasers Opt.* **74**, pp. 355–361, 2002.

[16] I. Kostyukov et al. *Phys. Plasmas* **11**, p. 5256, 2004.

size that is far greater than the matched spot size to produce a sufficiently large bubble for injection. This, as described in section 3.3, leads to strong evolution of the laser pulse, and hence the wakefield bubble. It is also important to note that self-injection is seen for the bubble regime for the case that the bubble radius and laser waist are matched to the plasma,[56,98] suggesting further effects must be involved in self-injection in these regimes.

Subsequent investigations[98,99] into the bubble regime using PIC simulation revealed that the bubble shape and radius evolves as it propagates through the plasma. Because of this, the velocity of the rear of the bubble may increase or decrease relative to the velocity of the driver.[57] These changes in velocity change the requirements for injection of electrons. This was shown by adaptation of the Hamiltonian description of electron motion to the case for an expanding bubble,[57,100] where sufficiently rapid bubble expansion significantly enhanced the self-injection process. The electron sheath and electromagnetic field structure of the bubble are also seen to evolve as the bubble propagates through the plasma.[98] These parameters also have a strong effect on self-injection, as found by Islam *et al.*,[21] who demonstrate that changes in the wake potential at the rear of the bubble strongly influence the injection behaviour. Similarly, the overall shape of the bubble has been shown to be important,[18] as deviations away from a spherical bubble shape alter the electric field structure and electron trajectories, inhibiting the self-injection process.

---

[56] W. Lu et al. *Phys. Rev. Lett.* **96**, p. 165002, 2006.

[98] W. Lu et al. *Phys. Rev. Spec. Top. Accel Beams* **10**, p. 061301, 2007.

[99] A. Zhidkov et al. *Phys. Rev. E: Stat., Nonlinear, Soft Matter Phys.* **69**, p. 035401, 2004.

[57] I. Kostyukov et al. *New J. Phys.* **12**, p. 045009, 2010.

[100] S. a. Yi et al. *Plasma Phys. Controlled Fusion* **53**, p. 014012, 2011.

[21] M. R. Islam et al. *New J. Phys.* **17**, p. 093033, 2015.

[18] F. Y. Li et al. *Phys. Rev. E: Stat., Nonlinear, Soft Matter Phys.* **90**, p. 043104, 2014.

4.1.1 Controlling Injection

These results show that there are many potential ways to control self-injection through the many electron and bubble parameters that have been shown to affect it. In this thesis the focus is on the effects of density perturbations, as well as investigation of the potential effects of laser intensity variation.

Injection due to variations in the plasma density was suggested by Bulanov *et al.*[101] for the linear LWFA regime. They showed that a plasma density down-ramp leads to wave-breaking by downshifting of electron plasma frequency and an associated decrease in the wave-breaking threshold. This results in eventual breaking of waves that initially have too small an amplitude to break. This method of injection was subsequently investigated for both the nonlinear, beam-driven PWFA[102] and for the LWFA bubble regime,[103] and demonstrated experimentally for both cases,[104–106] which produce stable, low momentum spread beams. A more complete theoretical description was offered by Brantov *et al.*[107] where the wave-breaking condition in a density down-ramp is determined for the LWFA bubble regime, provided the sheath electron velocity is known. This provides a necessary and sufficient condition for injection, but makes no prediction of the electron bunch properties after injection. In this chapter we build upon this theory to create a predictive model for injection due density perturbations in a plasma. For known bubble and electron parameters propagating in uniform plasma, the threshold for injection and duration of injected bunches can be predicted for any arbitrary perturbation.

---

[101] S. Bulanov et al. *Phys. Rev. E* **58**, p. 5257, 1998.

[102] H. Suk et al. *Phys. Rev. Lett.* **86**, pp. 1011–1014, 2001.

[103] T. Ohkubo et al. *Phys. Plasmas* **13**, p. 033110, 2006.

[104] C. G. R. Geddes et al. *Phys. Rev. Lett.* **100**, p. 215004, 2008.

[105] W. P. Leemans et al. *C. R. Phys.* **10**, pp. 130–139, 2009.

[106] M. Hansson et al. *Phys. Rev. Spec. Top. Accel Beams* **18**, p. 071303, 2015.

[107] A. V. Brantov et al. *Phys. Plasmas* **15**, p. 073111, 2008.

4.2 An Injection Condition

The starting point for any self-injection theory is a clear definition of an injected electron. The simplest definition of an injected electron is one that is inside the bubble and co-propagating with the accelerating field. This is not, however, the most useful form for establishing a criterion for discriminating between electrons that will and will not be injected. We may use the simple picture of injection we have already discussed in section 4.1 to find a more useful injection criterion. As we have seen in section 3.2.5, electrons in the LWFA are initially displaced by the laser and then propagate around the evacuated bubble forming an electron sheath. Figure 3.5 shows that the sheath electrons return to the axis at the back of the bubble forming a "sheath-crossing" region where some electrons are then injected into the bubble structure from the rear. Therefore, to become injected, an electron in the sheath crossing region must have a forward velocity greater than the phase velocity of the bubble structure. If this criterion is met then it can move forward into the accelerating phase of the bubble field. This condition may be compactly expressed as

$$\beta_e > \beta_{ph}, \tag{4.1}$$

where β_e is the velocity of the electron in the sheath crossing region and β_{ph} is the phase velocity of the electric field structure at the bubble rear. The following sections detail how these two velocities are determined.

4.3 Bubble Phase Velocity Behaviour

As we have seen, a complete, self-consistent analytical model of the bubble does not exist, and we therefore require a reduced model to establish an analytic approximation consistent with the relevant bubble properties. To create a reduced model we begin with the simplest possible description and add additional features until we arrive at a model that reproduces the features of the full model to sufficient accuracy for our purposes, whilst remaining straightforward to evaluate, either analytically or numerically.

To find an expression for the phase velocity at the back of the bubble we consider the bubble as a dynamic structure, defined by the electron sheath around the outside of the ion cavity, and trailing behind the driver. If the driver passes a point z in the plasma at a time t_{dr}, then the back of the bubble will pass the point z at a later time $t_b = t_{dr} + \tau$, where τ is the time taken for the sheath electrons that are expelled by the driver to perform half an oscillation in the ion cavity potential and arrive at the point z. Differentiating this time relation yields an expression for the velocity of the back of the bubble in terms of the driver velocity and the change in the sheath electron propagation time τ with respect to the position z in the plasma:

$$\frac{1}{\beta_b} = \frac{1}{\beta_{dr}} + c\frac{\mathrm{d}\tau}{\mathrm{d}z}. \tag{4.2}$$

To evaluate τ we use a simple model of a single electron in the lab frame that receives an initial transverse kick from the driver before oscillating in the purely radial electrostatic field of a spherical bubble. This results in the electron performing a half period of simple harmonic motion at the betatron* frequency ω_β, before arriving back at the axis after a time

$$\tau \simeq \frac{\pi}{\omega_\beta} = \frac{\lambda\sqrt{\gamma_e}}{2\eta c}, \tag{4.3}$$

where γ_e is the rest-mass-normalised electron energy (Lorentz factor) and η^2 is the plasma density normalised to the critical plasma density (3.55) for a laser of wavelength λ^*.

A complication arises here because this approach considers the motion of a single electron. As we have seen in chapter 3 and section 4.2, the electron sheath around the bubble is made up of a large number of electrons, with a finite distribution of energies and positions due to the effect of the electron's impact parameter on its interaction with the laser. Therefore, we should consider the average behaviour of the entire sheath population rather than just a single electron. Based on our assumptions so far, electrons arriving at the back of the bubble at a time t_b, would all have received identical, purely transverse, kicks at a time $t_b - \tau$, implying that the sheath electron population at the back of the bubble at any instant is made up of electrons sourced from a single longitudinal position. In reality the spread of the energy and momentum distributions imparted to the sheath electrons by the laser will both increase the sheath width and smear out the range of locations at which the electrons cross the axis at the back of the bubble.

Considering first the effects of varying total energy γ_e, we can see from (4.3) that the relativistic modification to the mass of the electron changes the period of its transverse oscillation, meaning that a population of electrons that are initially kicked by the laser at a time t_k, will have a spread $\delta\tau$ in their flight times to the rear of the bubble. Conversely, at any given instant electrons that are returning to the laser axis will have started from a longitudinal position that depends upon their flight time. We may estimate the sheath width due to the energy spread, assuming normally distributed electron energies about a mean energy $\bar{\gamma}_e$ with a

---

[*] "Betatron" motion is the transverse motion of the electron in the radial potential of the bubble, and is of interest due the associated radiation production. It is discussed in detail in sections 3.2.4 and 5.1.

[†] It is a common choice to normalise the plasma density to some reference density in this way. For a laser driver the choice of the critical density is a natural one, however in general the choice of reference density and its associated plasma wavelength is entirely arbitrary.

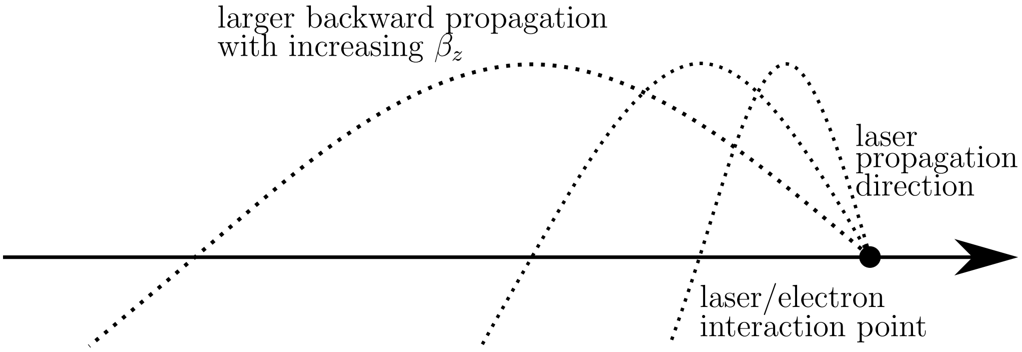

Figure 4.1: Idealised trajectories for electrons which interact with the laser at the same point but acquire varying quantities of longitudinal momentum.

variance σ^2, as

$$\Delta s \sim c\beta_{dr}\Delta\tau = \frac{\lambda\beta_{dr}}{2\eta}\left[\frac{1}{\sqrt{2\sigma^2\pi}}\int_0^\infty \gamma\,\mathrm{e}^{-(\gamma-\bar{\gamma}_e)^2/(2\sigma^2)}\,\mathrm{d}\gamma\right]^{1/2}. \tag{4.4}$$

Sheath electrons will also acquire negative longitudinal momentum from their interaction with the laser. Therefore, in the time $\tau = \pi/\omega_\beta$ taken for an electron to perform one half oscillation in the transverse direction, it will also have moved some distance backwards from its initial location. This can be up to $\lambda_p/2$ for an electron that has a longitudinal velocity approaching c. Therefore, electrons arriving at the back of the bubble at a position z_b can have come from an initial position z up to one-half plasma wavelength ahead, $z_b \leq z \leq z_b + \lambda_p/2$, this is shown diagrammatically in figure 4.1.

The fact that the sheath has a finite width makes the concept of the "back" of the bubble somewhat nebulous. However, a pragmatic definition is to consider the point at which the sheath electron density peaks on the bubble axis. Since the electron sheath shields the electric field inside the bubble, this is also close to the point at which the longitudinal electric field on axis is reduced to zero. This zero point of the electric field also delineates the beginning of the accelerating field region inside the bubble. Therefore, the back of the bubble is assumed to be both the zero point of the accelerating field, and also the axis crossing location of an "average" sheath electron, where "average" implies that its position and momentum are the means of the respective distributions, and its trajectory lies approximately at the centre of the sheath. Due to the noise inherent in the particle density of PIC simulations, when locating the back of the bubble from simulation data, we use the definition of the zero point of the electric field, which produces results consistent with following the peak of the electron density, and gives a smoother, less noisy, result.

The effect of the density gradient on the velocity of the bubble rear can be qualitatively understood in terms of the effect of the plasma density on the bubble size. The radius of the bubble depends upon the plasma wavelength (3.10), therefore changes in the plasma density will also change the bubble size. Consequently, when measured relative to the position of the front of the bubble, which is "fixed" to the driver, the back of the bubble will move as the density changes and have a non-zero velocity relative to the front of the bubble.

In the case of a uniform plasma driven by a matched laser, such that the electron momentum distribution does not evolve as the laser propagates, the bubble length will remain constant and the back of the bubble will move at the driver velocity $\beta_{ph} = \beta_{dr}$. To correctly calculate β_b for the general case, where the electron energy and plasma density are evolving, we must ensure that we correctly calculate the motion of the "average" electron and hence the position of the sheath density peak at the back of the bubble for all times of interest. Considering some arbitary point z_b in the plasma we know that the electrons returning to axis at this point can have come from any point $z_b \leq z \leq z_b + \lambda_p/2$. Therefore, we estimate the travel time $\langle\tau\rangle$ of the average electron, using the average over this range of the plasma density and average electron energy,

$$\langle\tau(z)\rangle = \frac{\lambda\sqrt{\langle\bar{\gamma}_e\rangle}}{2c\,\langle\eta\rangle}, \tag{4.5}$$

where $\langle\ldots\rangle$ indicates an average over the range z to $z + \lambda_p/2$.

Inserting this form for τ into (4.2), we find an expression for the phase velocity at the back of the bubble in terms of the change in both the electron energy and plasma density gradient:

$$\beta_b = \beta_{dr}\left[1 - \frac{\lambda\,\beta_{dr}}{2}\left\langle \frac{\gamma_e'}{2\eta\sqrt{\gamma_e}} - \frac{\eta'\sqrt{\gamma_e}}{\eta^2}\right\rangle\right]^{-1}, \tag{4.6}$$

where a prime denotes differentiation with respect to the longitudinal position z.

It remains now to insert expressions for η, γ_e and their derivatives to complete the model. We initially concern ourselves with the effects of changing density, under the assumption that γ_e is constant. Since the source of the electron energy is the driver, we can see that if the intensity of the driver is constant, then we can expect the energy distribution of the sheath electrons to remain similarly constant. As discussed in section 2.6.2, we can use the ponderomotive approximation to estimate the energy of the displaced electrons in terms of the peak normalised vector potential a_0,

$$\gamma_e \sim g\sqrt{1 + \chi a_0^2}. \tag{2.45}$$

This depends on the laser polarisation, with $\chi = 1/2$ or 1 for linear or circular polarisation respectively, and simulation geometry, where $g = 1$ for 2-D slab geometry and $g = 2$ for 3-D geometry.

4.3.1 Bubble Phase Velocity with a Non-Evolving Laser

If the laser spot size is matched to the plasma then there will be no significant evolution of the laser intensity, and the derivative of the electron energy γ_e' will vanish, leaving only the plasma density to affect the propagation of the bubble.

The details of the bubble velocity response will depend non-trivially on the exact form of the plasma density profile, because, in addition to a dependence on the magnitude and gradient of the plasma density it also has a “memory” of the effects of the plasma density over the preceeding bubble length. However, since the model derived here is valid only for density profile perturbations with length scales larger than the bubble length the effect is mostly one of averaging, as described in the model derivation. Figure 4.2 shows the response of the bubble phase velocity

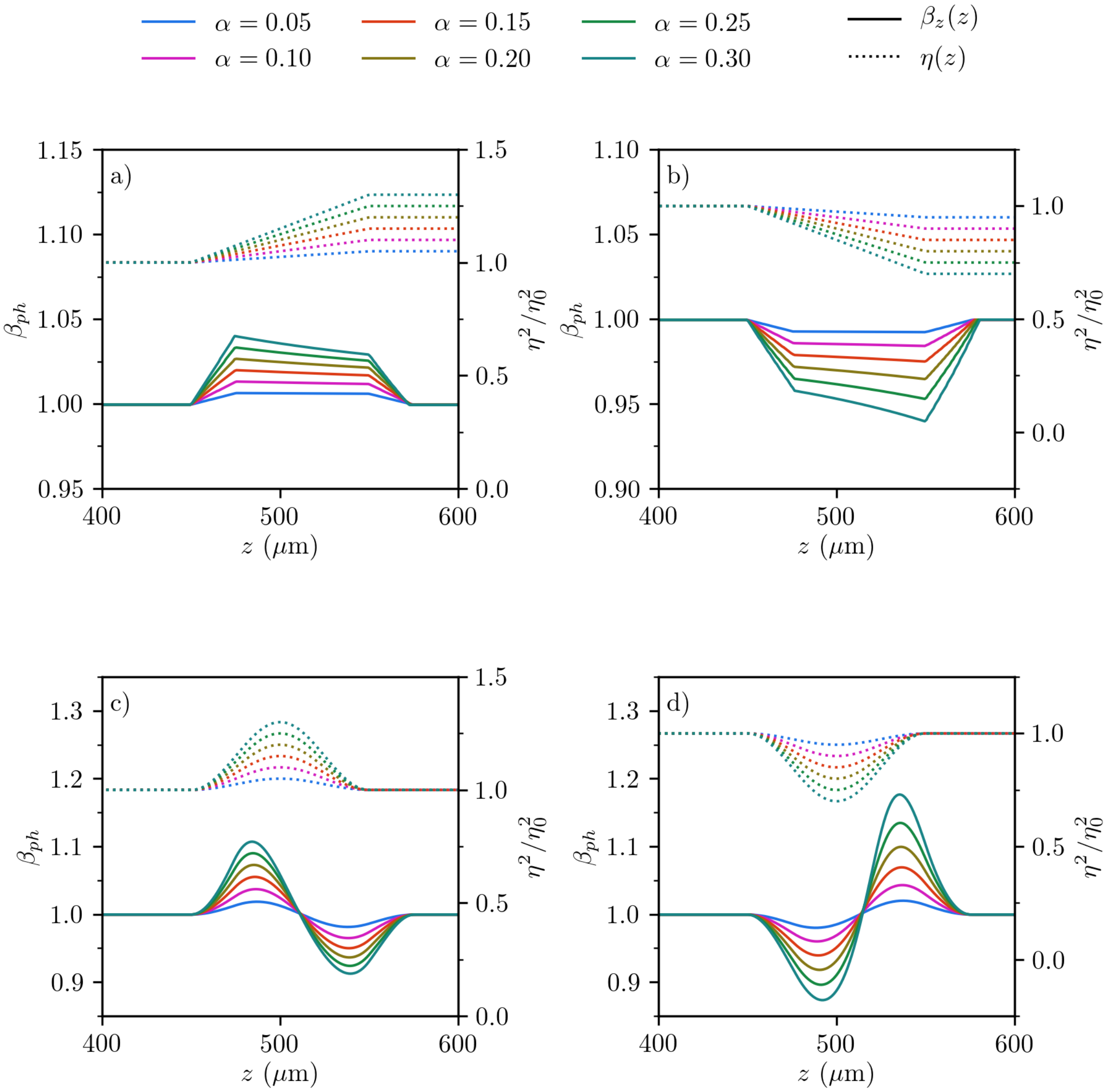

Figure 4.2: Model predictions for the behaviour of the bubble phase velocity β_z (solid line) for four simple plasma density structures consistent with potential gas cell and gas jet experimental setups. The plasma density (dotted line) is perturbed by linear up-ramps (a), and down-ramps (b) which can be created with a gas cell, while smooth $\sin^2$-like perturbations (c, d) can be produced with a gas jet and supersonic shocks. The normalised background density of the plasma is $\eta^2 = 0.001$ in all cases, and the fractional amplitude change $\alpha = [0.05 - 0.30]$.

to four simple plasma density perturbations: up-ramp and down-ramp profiles, as could be created in a gas-cell experiment, and positive and negative $\sin^2$ profiles, which are closer to the expected behaviour in a gas jet experiment. The profiles in figure 4.2 are defined by

$$\text{Linear Profile :}\frac{\eta^2}{\eta_0^2} = \begin{cases} 1 & \text{if } z \leq z_c - \ell/2, \\ 1 \pm \alpha\left(\frac{1}{2} + \frac{z-z_c}{\ell}\right) & \text{if} |z - z_c| < \ell/2, \\ 1 \pm \alpha & \text{if} z \geq z_c + \ell/2 \end{cases}, \tag{4.7}$$

$$\text{Sin}^2\text{ Profile :}\frac{\eta^2}{\eta_0^2} = \begin{cases} 1 \pm \alpha \cos^2\left(\pi\frac{z-z_c}{2\ell}\right) & \text{if } |z - z_c| < \ell/2, \\ 1 & \text{otherwise} \end{cases}, \tag{4.8}$$

where ℓ is the width of the perturbation, α is the fractional amplitude of the perturbation, z_c is the position of the centre of the perturbation, and η_0^2 is the fractional density of the bulk plasma.

Considering first the up- and down-ramp cases the bubble velocity displays the behaviour predicted by the model: a density up-ramp in the plasma causes contraction of the bubble, and hence an increase in the velocity of the back of the bubble relative to the front over the contraction length. For the linear ramp the effect is approximately a step-change in velocity, however the effect of the bubble length smooths out the initial and final sections, and the central section is not a flat plateau since the contraction rate is dependent also on the magnitude of the plasma density. In the down-ramp case the decreasing plasma density causes the bubble to grow in size, and the bubble phase velocity is reduced. The effect of the magnitude of the density is evident here since for the same initial density and perturbation amplitude the velocity excursion is larger for the down-ramp case than the up-ramp case. These predictions lead us to expect injection to occur in the case of a density down-ramp, as it is easier for electrons to penetrate into the bubble, and injection to be supressed on a plasma up-ramp as the superluminal phase velocity of the bubble rear prevents electrons entering.

For the case of the $\sin^2$ profiles, the presence of both positive and negative density gradient sections leads to the potential for injection in each case, however there are key differences which lead the positive (up-ramp first) profile to be preferable for stimulation self-injection. As for the linear ramp cases we see that the density depression has a larger velocity excursion, due to the effect of lower plasma density, which may or may not be a beneficial effect, depending on experimental requirements. The major issue with the density depression, however, is the fact that the bubble first grows and then shrinks back to its unperturbed size, rather than first shrinking and then growing as in the positive profile case. This means that electrons may be injected when the bubble is larger, then end up outside the bubble as it returns to its unperturbed size. In order to avoid this, the rate at which the bubble shrinks must be smaller than the rate at which the electron progress forward in the bubble. Approximating the electron velocity as c provides a best-case approximation of the electron velocity relative to the bubble as $\beta_{e,\mathrm{rel}} = \gamma_{dr}^{-2} = 1 - \beta_{dr}^2$. Therefore for typical LWFA parameters, where $\gamma_{dr} \gtrsim 10$, the up-ramp gradient to prevent de-injection is negligibly different from a flat plasma. The correct choice to stimulate injection in the gas jet regime is therefore a positive density perturbation.

The predicted phase velocity behaviour can be directly compared to PIC simulation results. Figure 4.3 shows the behaviour of the bubble phase velocity for the case that the laser pulse is matched for minimum evolution but there is a small perturbation to the plasma density (red line). The prediction made by the model is compared with results derived from 2D EPOCH PIC simulation by analysis of the bubble electric field as described above. The simulation cell size was $40\,\mathrm{nm} \times 200\,\mathrm{nm}$ length×width, in a $90\,\mu\mathrm{m} \times 90\,\mu\mathrm{m}$ moving window. The laser is linearly polarised in the simulation plane, with wavelength 800nm, normalised peak intensity $a_0 = 4.0$, a gaussian temporal and spatial envelope with length $\sigma_t = 10\,\mathrm{fs}$ and width $\sigma_\perp = 20\,\mu\mathrm{m}$. The plasma has a flat top density profile with normalised electron number density $n_e/n_{\mathrm{crit}} = 0.001$ and an initial linear upramp

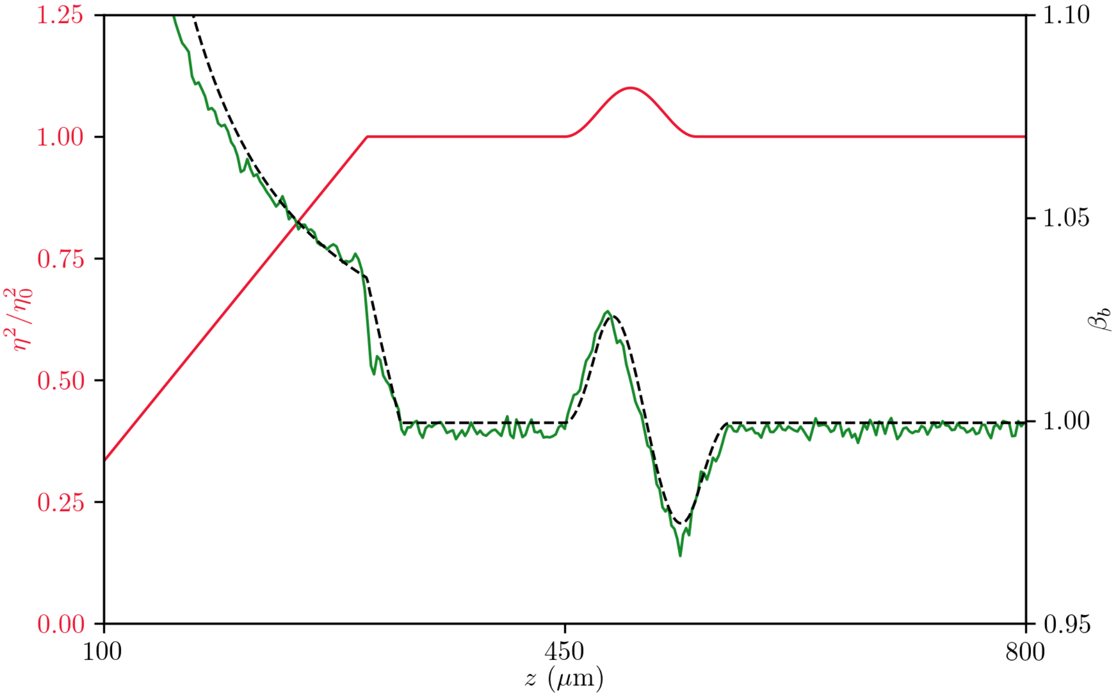

Figure 4.3: Comparison of predicted and PIC simulated bubble phase velocity for a matched laser pulse $a_0 = 4.0$ driving a bubble in a plasma $\eta^2 = 0.001$. The predicted phase velocity (black line) is in excellent agreement with that of the simulated bubble (green line), for both the initial upramp and the small perturbation (width $\ell = 100\,\mu$m) used to stimulate injection.

region of length $300\,\mu$m to couple the laser smoothly into the plasma. On top of the flat region a the perturbation, shown in figure 4.3, has a $\sin^2$ profile with fractional amplitude $\alpha = 0.1$ of the base plasma density and width $\ell = 100\,\mu$m, with the peak of the perturbation located $500\,\mu$m into the plasma. This was chosen as it is a good approximation to the profiles reported by Schmid and Veisz.[108]

4.4 Electron Velocity

The other key parameter required to determine if an electron will be injected is the velocity of the electron at the rear of the bubble. Both the longitudinal and transverse velocities are important in determining injection, because as well

---

[108] K. Schmid and L. Veisz. *Rev. Sci. Instrum.* **83**, pp. 1–10, 2012.

as having sufficient forward momentum to co-propagate with the bubble, the electron must have sufficiently small transverse momentum not to escape the bubble potential in the transverse direction.

As discussed in section 3.2.4, no self-consistent analytic solution exists to describe the motion of electrons both in the sheath and at the rear of the bubble. Therefore, although an approximation of the trajectories may be made, to find accurate electron velocity results for a particular set of plasma parameters we must rely on PIC simulation of the problem. In spite of this restriction, however, we may retain reasonable predictive power, as a single PIC simulation can be used to create predictions for many varying plasma profiles. This greatly reduces the computational cost of searching the space of plasma parameters for viable experimental setups.

The approach developed in this thesis is to use PIC simulation to determine the behaviour of sheath electrons for the case of a constant plasma density. This provides a reference against which potential plasma density profiles may be compared to determine if injection will occur. Figure 4.4 shows the trajectory data for a subset of sheath electrons from a pair of simulations, one with an unperturbed plasma and the other with a small perturbation to the plasma profile with fractional $\alpha = 0.15$. All other parameters are identical to those described in section 4.3 above. Figure 4.4(a) shows the trajectories followed by sheath electrons in the frame comoving with the bubble, the region bracketed by black lines is the sheath crossing region at the rear of the bubble. The same region is bracketed in figure 4.4(b) which shows the longitudinal electron velocity in the same comoving frame. This shows that the peak forward velocity of the sheath electrons does indeed occur at the sheath crossing point. This validates the assumptions we have made so far that we should indeed be interested in the rear of the bubble as the most likely point of injection. Figure 4.4(c) shows the velocity of the same electrons, at the rear of the bubble. However, this time, the velocities are shown

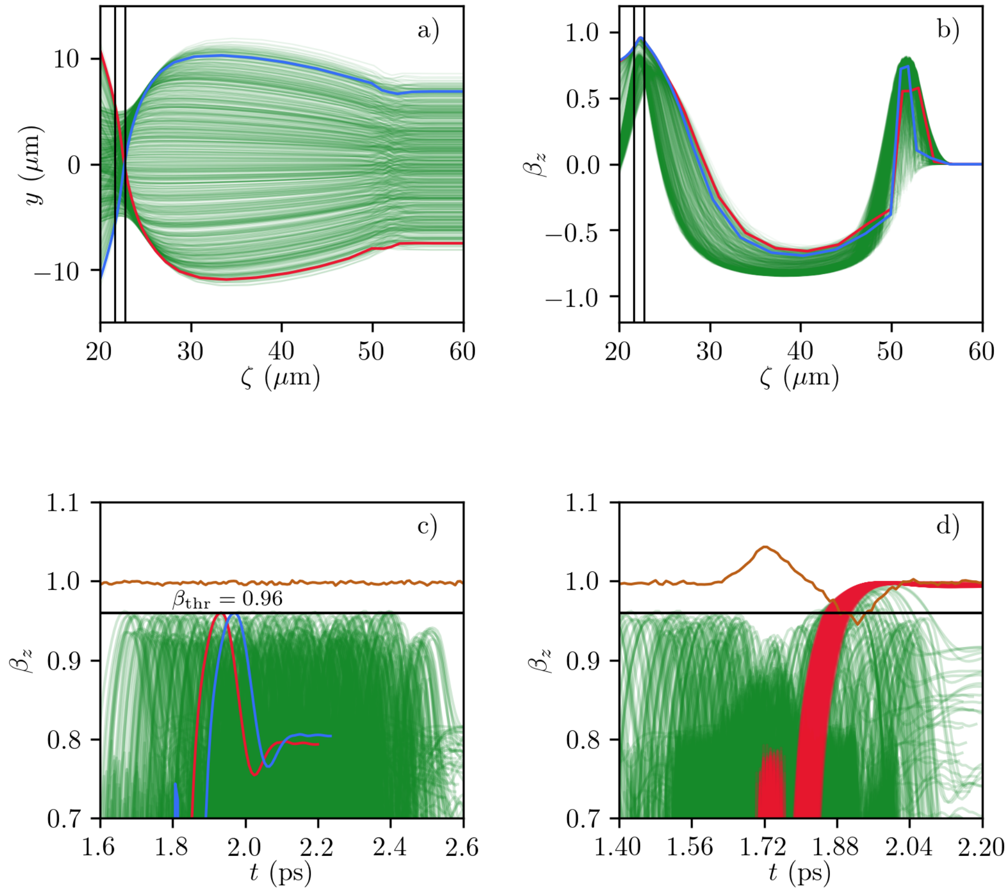

Figure 4.4: Sheath electron trajectories for the first bubble from PIC simulation of an unperturbed plasma and a case with injection caused by density perturbation $\alpha = 0.15$. The spatial (a) and longitudinal velocity (b), trajectories of electrons in the non-injecting case are shown for reference, with two candidates for potential injection highlighted in red and blue. Below this, the velocity behaviour with respect to time of the electron population passing through the bubble rear is shown for the non-injecting (c) and injecting (d) case. The phase velocity of the bubble rear is plotted for each case (orange line) and the injected electron trajectories are highlighted in red.

with respect to time. This demonstrates that although there will be a distribution of electrons with different velocities in the sheath, over periods of picoseconds, i.e laser propagation distances of hundreds of microns, the peak velocity of the distribution remains constant. Comparing this with the phase velocity of the bubble (orange line), we see that for these plasma parameters, the peak sheath electron velocity does not exceed that of the bubble and so injection does not occur. In contrast, figure 4.4(d) shows the situation where a small density perturbation is introduced into the plasma. This causes the bubble phase velocity to be temporarily reduced to below the peak of the sheath electron velocity distribution, leading to injection of an electron bunch (red).

We use the peak of this sheath electron velocity distribution as the threshold velocity below which the bubble phase velocity must drop in order for injection to occur.

4.5 Injection Threshold

Comparing the value of the threshold velocity and the expression for the bubble phase velocity (4.6) as in (4.1) yields an injection condition in terms of the plasma density profile, electron energy and threshold velocity:

$$\left\langle \frac{\eta' \sqrt{\gamma_e}}{\eta^2} \right\rangle - \left\langle \frac{\gamma_e'}{2\eta\sqrt{\gamma_e}} \right\rangle < \frac{\lambda}{2}\left(\frac{1}{\beta_{dr}} - \frac{1}{\beta_{thr}}\right). \tag{4.9}$$

In the case that the average electron energy γ_e does not evolve on the timescale of the injection event, such as for the case of a matched laser pulse, this may be simplified and rearranged to give the threshold as a density change per plasma wavelength,

$$\left\langle \lambda \frac{\eta'}{\eta} \right\rangle < \frac{2}{\sqrt{\gamma_e}}\left(\frac{1}{\beta_{dr}} - \frac{1}{\beta_{thr}}\right). \tag{4.10}$$

This condition may be expressed graphically, as shown in figure 4.5, where β_{thr} is extracted from the simulation described in section 4.4 for a matched laser pulse with $\lambda = 800\,\mathrm{nm}$, $a_0 = 4.0$, in uniform plasma with normalised density

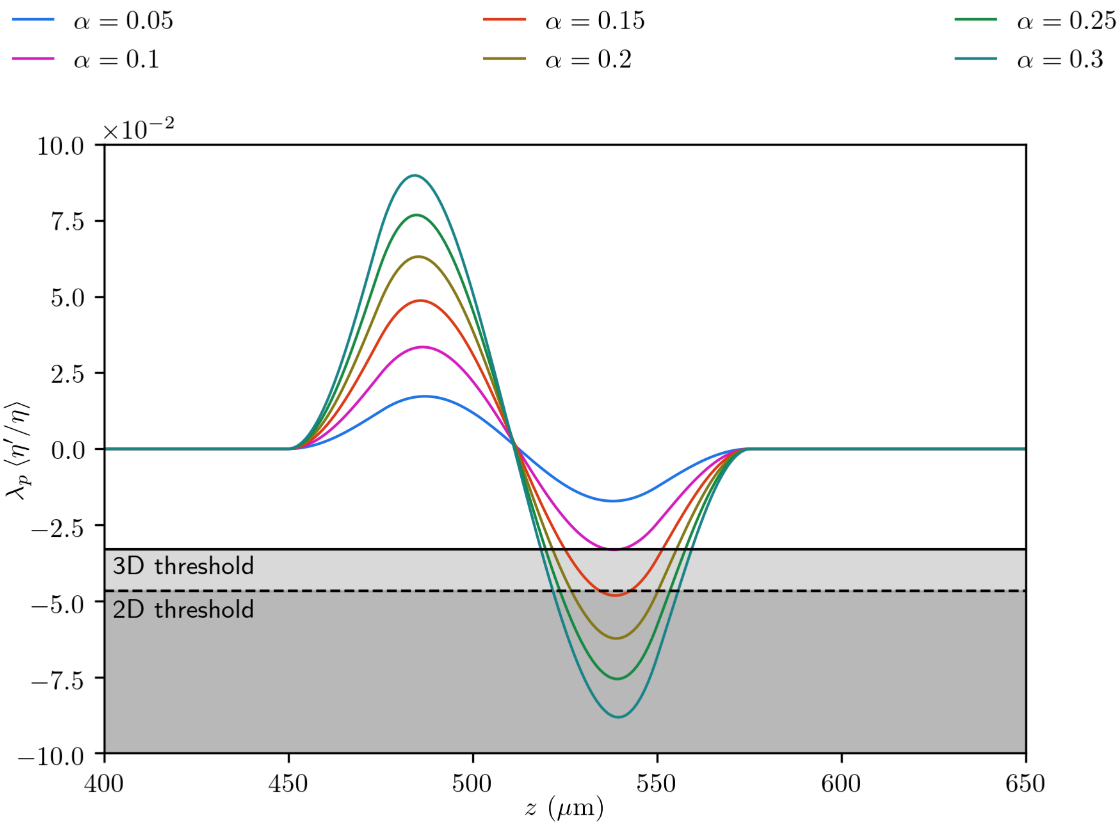

Figure 4.5: The plasma density gradient, normalised to the plasma wavelength (y-axis), *vs.* laser propagation distance z (x-axis), for the $\sin^2$ density perturbations in figure 4.2(c). The injection threshold for these conditions is calculated using (4.10) (black lines) for the 3D (solid) and 2D (dashed) cases. The grey area beneath the line is region in which injection will occur.

$\eta^2 = 0.001$. This is shown by the black lines in the figure for both 3-dimensional geometry (solid line) and for the 2-dimensional slab geometry (dotted line) often used in PIC simulations. The coloured lines in the figure show the evolution of the plasma density gradient with respect to the propagation distance of the laser. For these parameters, the threshold gradient is found to be $\lambda\eta'/\eta \simeq -0.03$ for the 3-dimensional case. This means that for the $100\,\mu$m $\sin^2$ density perturbation shown in the figure, which is comparable to the length scale of the density perturbations described by Schmid and Veisz,[108] the injection threshold is at a fractional amplitude $\alpha \simeq 0.1$. The length of the injected bunch will be strongly related to the length of time the bubble phase velocity spends below the injection threshold velocity, with larger values of α yielding longer bunches for the same total width of density perturbation. Using the scaling between 2-D and 3-D geometries that was discussed in section 2.6.2 we see that for simulations in the 2-D slab geometry we expect the injection threshold at a fractional amplitude $\alpha \simeq 0.15$. This also sets the threshold for acceptable density non-uniformity in the plasma region where no injection is desired.

4.5.1 Injected Bunch Length

The threshold condition (4.9) can now be used to predict the length of the injected bunch. Making the assumption that the bunch has a finite length, there will be a point z_1 along the propagation axis at which the inequality in (4.10) is first satisfied and injection commences, followed by a point z_2, beyond which the inequality ceases to be satisfied and injection stops. Solving for the location of the points z_1 and z_2 for a given density profile and electron energy evolution allows the period of injection to be found from the integral over the injection distance:

$$\Delta t_{inj} = \int_{z_1}^{z_2} \mathrm{d}t = \int_{z_1}^{z_2} \frac{\mathrm{d}t}{\mathrm{d}z'}\,\mathrm{d}z' = \frac{1}{c}\int_{z_1}^{z_2} \frac{1}{\beta_b(z')}\,\mathrm{d}z' = \frac{\Delta L}{c\bar{\beta}_b}, \tag{4.11}$$

where $\bar{\beta}_b$ is the harmonic mean[109,*] of β_b over the injection period, and $\Delta L = z_2 - z_1$.

Assuming that the injected electrons are accelerated sufficiently rapidly that their velocity may be immediately approximated by c, the bunch length is given by the distance that the head of the bunch has travelled beyond the back of the bubble, at the point that the tail of the bunch is injected. This gives the bunch temporal length τ in the lab frame

$$\tau = \Delta t_{inj}(1-\bar{\beta}_b) = \Delta L \cdot \frac{1-\bar{\beta}_b}{c\bar{\beta}_b} \simeq \frac{\Delta L}{2c\bar{\gamma}_b^2} = \frac{\Delta L}{2c}\left(1-\bar{\beta}_b^2\right), \tag{4.12}$$

---

[109] *NIST Digital Library of Mathematical Functions.* http://dlmf.nist.gov/

[*] The harmonic mean H of the real function $f(x)$ is defined to be $H = \left(\frac{1}{b-a}\int_a^b f(x)^{-1}\,\mathrm{d}x\right)^{-1}$ and is the reciprocal of the arithemetic mean for positive arguments.[109]

with $\bar{\gamma}_b = (1 - \bar{\beta}_b^2)^{-1/2}$ the Lorentz factor associated with the average bubble velocity. Typically, experimental measurements report temporal lengths for electron bunches, however in PIC simulations the spatial length is more readily and accurately determined from snapshots at any given timestep. For a bunch travelling with velocity v, the spatial length ℓ is related to the temporal length by $\ell = v\tau$.

4.6 Simulation of Density Controlled Injection

The primary means of validating the model is by 2-D and 3-D PIC simulation using the EPOCH[37] PIC code. This provides both a complete and self-consistent simulation of the injection process, and a method to diagnose the macro- and microscopic behaviour of the plasma in a way that is impossible with currently available experimental diagnostics.

The primary information relevant to this analysis is the behaviour of the individual pseudoparticle electrons in the simulated bunch, which may then be used to determine the bunch properties. In addition, the properties of the laser and bubble as they propagate must be extracted. Analysis is performed on the output of the EPOCH PIC code using a custom analysis script written in Python. Figure 4.6 shows typical results from this analysis script for the simulation of injection shown in figure 4.4(d). The complete bubble with injected bunch is shown in figure 4.6(a), and a zoom to the injected bunch in figure 4.6(b). Injected electrons can be programatically identified by having a position within the boundary of the bubble and a longitudinal momentum greater than or equal to that associated with the injection threshold velocity, the electrons meeting these criteria are shown in figure 4.6(c). After the occurrence of injection, the primary prediction made by the model is the bunch length, the measurement of which is shown in figure 4.6(d), and the width in figure 4.6(e). This is determined using the standard deviation, RMS, FWHM, and FW100M (full width at 1/100th maximum), since

---

[37] T. D. Arber et al. *Plasma Phys. Controlled Fusion* **57**, p. 113001, 2015.

different methods will be appropriate dependent upon the shape of the bunch. The measure of FW100M is an unusual one, however it is relevant in this case as the model predicts the total length of the bunch, rather than the more typically used statistical measure, and so for comparison with the model this is an appropriate measure as it will include any low charge tails in the bunch.

4.6.1 Density Perturbation with Matched Laser

A parameter scan was performed using both 2-D and 3-D EPOCH PIC simulation for varying amplitudes of $\sin^2$ density perturbation on an otherwise uniform plasma. In all cases, cell sizewas $40\,\mathrm{nm} \times 200\,\mathrm{nm}(\times 200\,\mu\mathrm{m})$ length×width(× *height*), in a $90\,\mu\mathrm{m} \times 90\,\mu\mathrm{m}$ moving window. The laser is linearly polarised in the simulation plane, with wavelength 800nm. A base plasma electron density $\eta^2 = 0.001$ was selected to allow direct comparison with previous figures. This corresponds to $n_e \simeq 1.75 \times 10^{18}\,\mathrm{cm}^{-3}$ for the 800 nm laser wavelength. The fractional perturbation amplitude was varied within the range $\alpha \in [0.0 - 0.4]$. The laser pulse was chosen to be linearly polarised with $a_0 = 4.0$ such that the laser pulse self-guides in the plasma, a beam waist $w_0 = 15\,\mu$ m, and pulse length $\tau_{\mathrm{FWHM}} = 10\,\mathrm{fs}$. The transverse and temporal laser envelope profiles were both

$$f(x) = \begin{cases} \sin^2(\pi(x - x_0)/(x_1 - x_0)) & \text{if } x_0 < x < x_1 \\ 0, & \text{otherwise} \end{cases}, \tag{4.13}$$

which reasonably approximates a Gaussian profile whilst having compact support.[*] This avoids unphysical behaviour at the boundaries of the simulation window, where the fields are assumed to be zero.

Figure 4.7 shows the resulting bunch lengths and charges for all simulations where injection occurred, (note that the 2D line charges are scaled by a factor $1.2 \times 10^{-5}\,\mathrm{m}$ to allow direct comparison). As discussed in section 2.6.2, the differences

---

[*] A function has compact support if it is non-zero only over some closed and bounded range, in this case $[x_0, x_1]$.

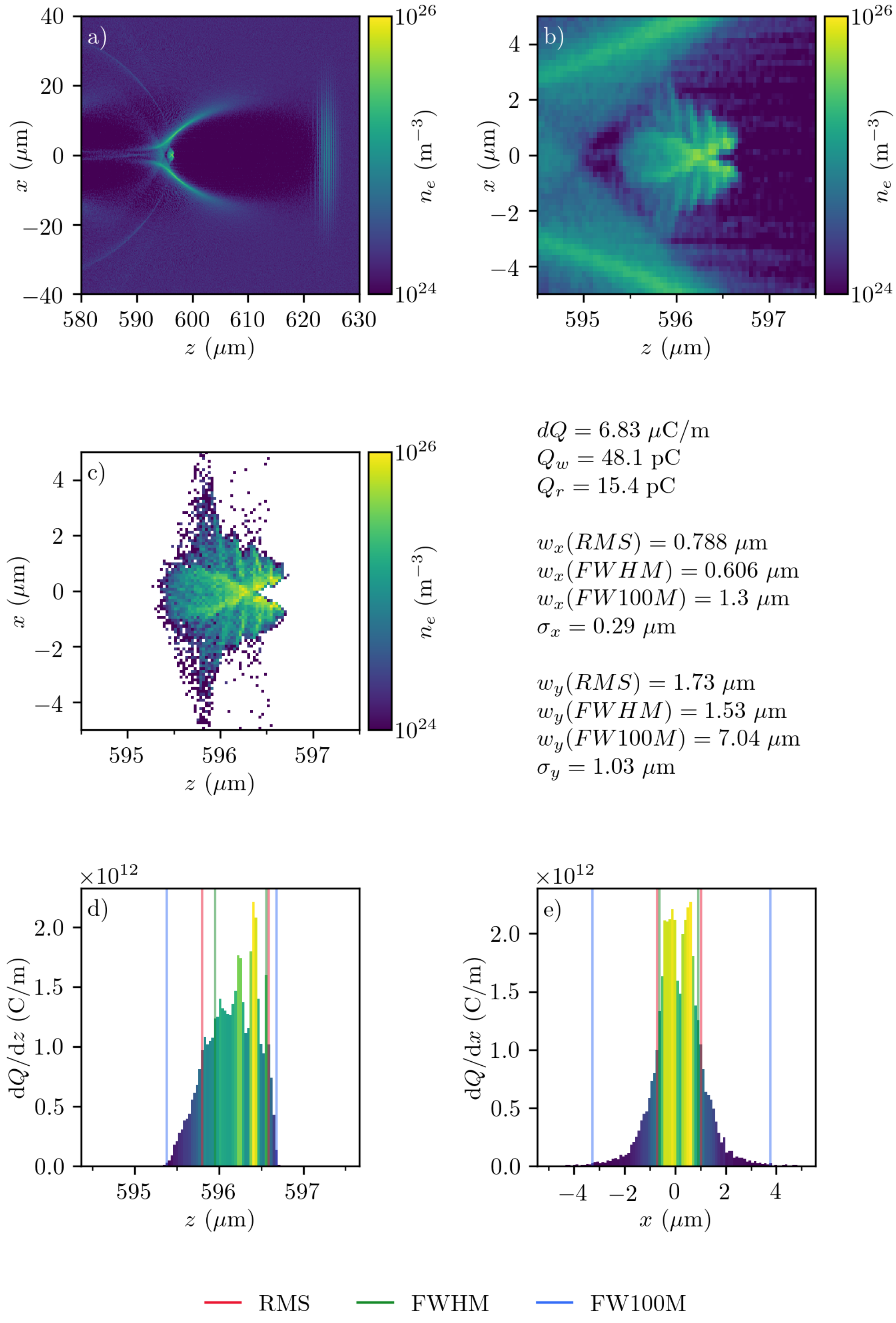

$dQ = 6.83\ \mu$C/m
$Q_w = 48.1$ pC
$Q_r = 15.4$ pC

$w_x(RMS) = 0.788\ \mu$m
$w_x(FWHM) = 0.606\ \mu$m
$w_x(FW100M) = 1.3\ \mu$m
$\sigma_x = 0.29\ \mu$m

$w_y(RMS) = 1.73\ \mu$m
$w_y(FWHM) = 1.53\ \mu$m
$w_y(FW100M) = 7.04\ \mu$m
$\sigma_y = 1.03\ \mu$m

Figure 4.6: Plasma electron density in the full simulation domain (a), detail of the injection region (b), bunch electron density (c), longitudinal charge distribution (d) and transverse charge distribution (e), for the bunch injected by a density perturbation $\alpha = 0.15$ as described in the text.

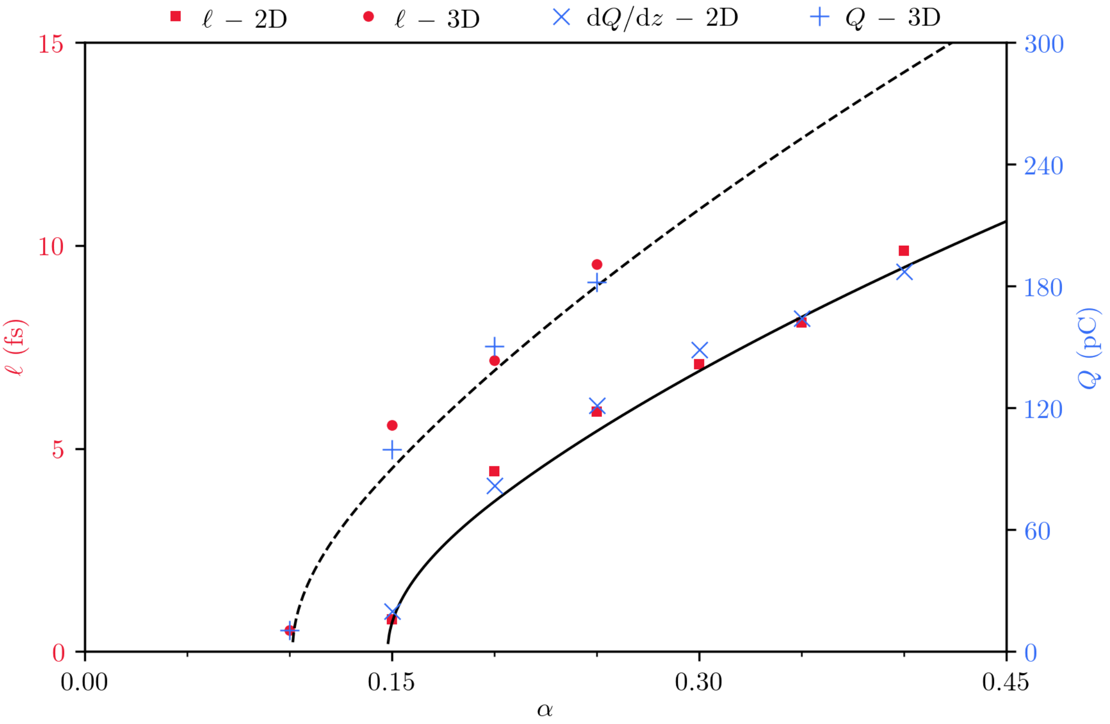

Figure 4.7: Injected FW100M bunch length (■, ●) and charge (×, +) for a parameter scan of perturbation amplitude α. Injected bunch length predicted by the analytic model is shown for comparison with solid (2-D) and dashed (3-D) lines. The 2-D charge density is scaled by a factor 1.2×10^{-5} m to allow plotting on the same axes.

in the behaviour of the ponderomotive force in the 2D and 3D cases leads to differences in the electron energies and bubble behaviours. In particular, the reduced electron energy in the 2D case causes an increase in the magnitude of density gradient required to cause injection. As predicted in section 4.5, injection first occurs in the 3-D case for a fractional amplitude $\alpha = 0.1$ ($\alpha = 0.15$ in the 2D case), and continues to increase in excellent agreement with the model.

The particular shape of the curve relating the bunch length to the perturbation amplitude in part follows from the shape of the perturbation itself. Revisiting figure 4.5 we see that as the amplitude of the velocity excursion increases below the injection threshold, the propagation distance ΔL over which injection occurs initially rapidly increases, but then slows to asymptotically approach the total perturbation length ℓ. The other factor in the injected bunch length is the average bubble velocity over injection $\bar{\beta}_b$ as described in (4.12). The average velocity decreases approximately linearly with increasing perturbation amplitude, causing the injected bunch length to increase approximately linearly. After the initial rapid increase in the injection length ΔL, this second effect causes the bunch length to continue increasing approximately linearly with the perturbation amplitude. For the case of a ramp such as those in figure 4.2, both the injection length ΔL and the average velocity $\bar{\beta}_b$ change linearly with α, in which case a linear relationship between α and the bunch length can be expected.

Figure 4.7 also shows that the injected bunch charge scales linearly with the bunch length. This is an interesting result because although the model does not make any direct predictions regarding the magnitude of charge injected, it is predicated on the assumption that electrons are injected provided they have longitudinal velocity greater than that of the back of the bubble. From figure 4.2 we see that as the perturbation amplitude increases there is both an increase in the time and distance over which the injection event occurs, and an increase in the number of electrons that have sufficient velocity to be injected. Putting both of these effects together it would be reasonable to expect that the total injected bunch charge should increase superlinearly with α.

A possible explanation for why this superlinear relationship is not seen is the effect of "beam loading".[110,111] This refers to the effect whereby the already injection electrons modify the electric field structure at the rear of the bubble. Specifically, the electric field due to the charge of the already injected portion of the bunch creates a potential barrier for more electrons to enter the bubble. This increases the required energy or longitudinal velocity for further electrons to be injected reducing the injected beam current as fewer electrons have sufficient energy to overcome this additional barrier and enter the accelerating field region of the bubble. In the extreme case, if the space charge of the injected bunch

---

[110] S. Wilks et al. *IEEE Trans. Plasma Sci.* **15**, pp. 210–217, 1987.

[111] M. Tzoufras et al. *Proc. Part. Accel. Conf. (PAC'07)*, pp. 3061–3063, 2007.

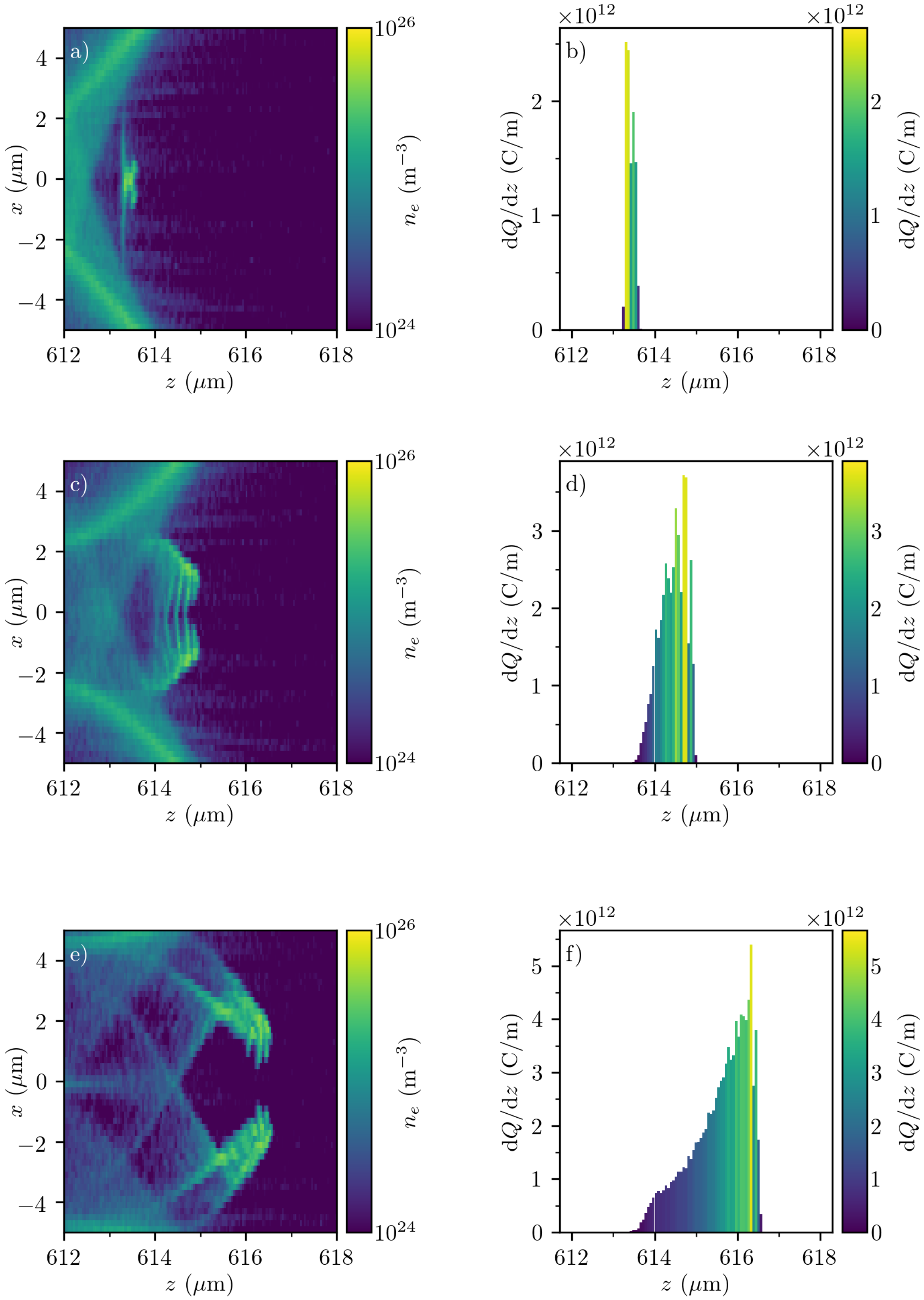

Figure 4.8: Electron plasma density (a, c, e) and longitudinal bunch charge density (b, d, f) for the 2D PIC simulations with $\alpha = 0.15$, $\alpha = 0.20$, and $\alpha = 0.40$ respectively.

becomes comparable to the wakefield strength, the injection process can be shut down entirely.[112] The theory that beam loading effects limit the total injected charge is supported by the profiles of the injected bunches. Figure 4.8 shows the longitudinal charge distribution for three of the 2-D cases simulated. The shortest bunch, injected with $\alpha = 0.15$, is shown in figures 4.8(a) and 4.8(b) and has a narrow, but approximately symmetric charge distribution. This is what would be expected from the symmetrical nature of the bubble velocity's excursion below the threshold, with the injected beam current increasing with the magnitude of the excursion. Were beam loading not present we would expect that the longitudinal charge distribution of longer injected bunches to have similar distributions with increasing width. However, for the increasing bunch lengths in figures 4.8(c) and 4.8(d), injected with $\alpha = 0.20$; and figures 4.8(e) and 4.8(f), injected with $\alpha = 0.40$; the longitudinal charge distribution becomes increasingly asymmetric. In all three cases the beam current initially increases rapidly, with larger peak current for larger α as expected. However, for these longer bunches, the beam current peaks in advance of the bunch centroid and then rapidly tails off towards the rear of the pulse. The effect of this large initial injected current acts to inhibit further injection due to the large space charge distorting the fields at the bubble rear, leading to the reduction of injected charge we observe.[113]

The beam loading induced shape of the longer bunches is a potentially useful side effect of this method because they have current distributions which leads to low longitudinal emittance growth during the acceleration process. The ideal current distribution, described by Tzoufras *et al.*[114,115] is a “wedge” shape with an initial maximum current that tapers linearly to zero and a sufficiently large total bunch charge that the wake field behind the bunch vanishes. Such a bunch has a self-field that cancels the change in magnitude of the accelerating field along

---

[112] S. P. Mangles et al. *Phys. Plasmas* **14**, 2007.

[113] G. Fubiani et al. *Phys. Rev. E: Stat., Nonlinear, Soft Matter Phys.* **73**, p. 026402, 2006.

[114] T. Katsouleas. *Phys. Rev. A* **33**, pp. 2056–2064, 1986.

[115] M. Tzoufras et al. *Phys. Plasmas* **16**, 2009.

the bunch, and therefore the entire bunch experiences the same acceleration field and there is no longitudinal emittance growth.

4.7 Injection of Multiple bunches

The description of injection of a single bunch in section 4.5.1 can be extended to include multiple, discrete, density perturbations, which should lead to multiple injection events, with a bunch spacing determined by the spacing of the perturbations and the bubble velocity.

Consider a pair of density perturbations separated by a distance S. Assuming a matched, non-evolving laser beam, in the absence of beam loading effects, the normalised velocity β_b of the back of the bubble will perform multiple excursions as in figure 4.3. If the injection threshold is met, a pair of bunches will be injected with lengths given by (4.12). It therefore follows, by the same argument, that the separation between injected bunches, s, is given by

$$s = \Delta S \cdot \frac{1 - \bar{\beta}_b}{\bar{\beta}_b}, \tag{4.14}$$

where $\bar{\beta}_b$ is the average velocity of the back of the bubble. This may be calculated using (4.11) between the midpoints of the injection locations. In the specific case that the two density perturbations are identical, the average velocity must be equal to the driver velocity, $\bar{\beta}_b = \beta_{dr}$, to preserve the bubble length in the uniform plasma regions. In such cases, the inter-bunch spacing depends only upon the plasma density and the distance between plasma density perturbations, and so in principle, by varying these two parameters, the bunch spacing may be tuned over a wide range as shown in figure 4.9.

For the scheme investigated here a problem presents itself. As discussed in section 4.3 if an injection-causing density downramp section is followed by a density upramp, the shrinking of the bubble that this causes can lead to the electron being de-injected as it is no longer within the accelerating field region.

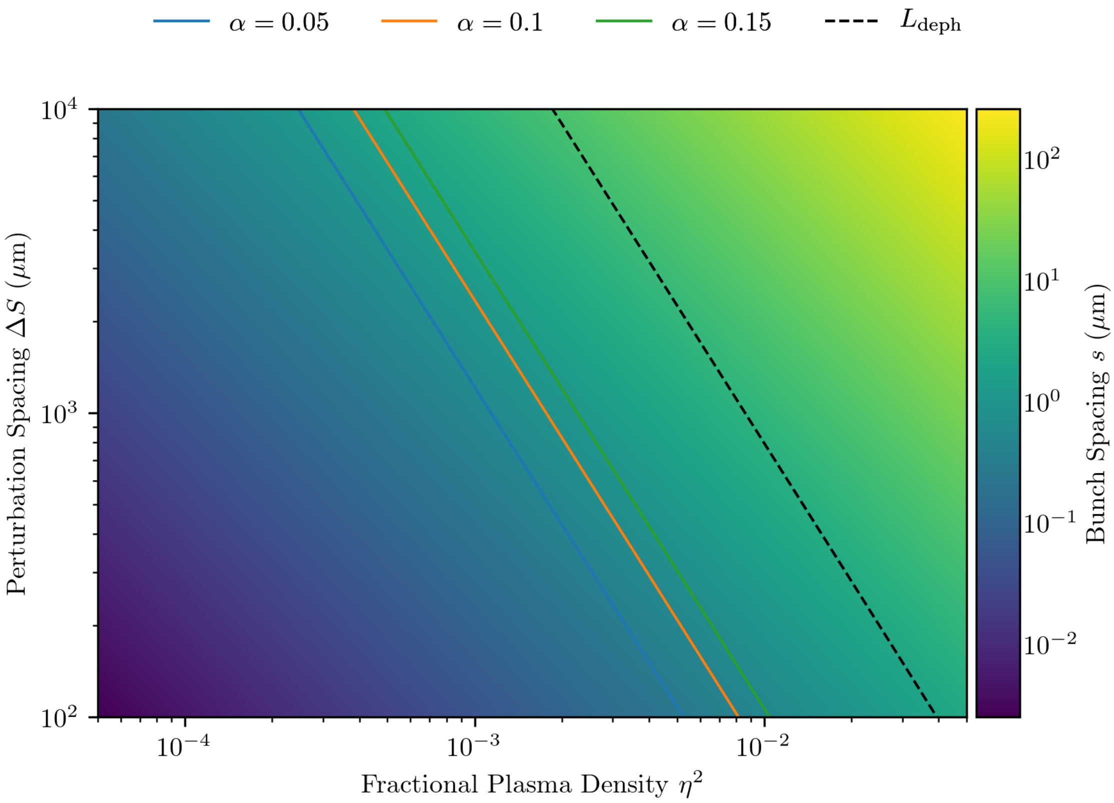

Figure 4.9: The parameter space of possible inter-bunch spacing for multiple injected bunches possible for the typical range of LWFA plasma densities and realistically achievable distances between density perturbations. Minimum achievable inter-bunch spacings for different values of α are shown as coloured lines, along with the dephasing length (black dashed line). Calculations are made assuming a laser with $a_0 = 3.0$ and $\lambda = 800\,\text{nm}$, representative of modern LWFA experiments.

While the bunch may also be re-injected as the bubble size increases once more, the effects of the sheath fields passing over, the emittance will likely be increased by the exposure to the non-uniform defocusing and decelerating fields in and behind the electron sheath. Therefore, in order to preserve the existing injected bunch, it must be allowed to propagate forward to beyond the point to which the bubble will contract in order to avoid interaction with the sheath and extra-bubble fields.

The minimum safe propagation distance can be estimated using the model of the bubble behaviour we have already described. From (4.3) we can get an expression for the bubble length as the distance travelled by the driver over the sheath electron travel

$$L_b = \beta_{dr} \frac{\lambda\sqrt{\gamma_e}}{2\eta}, \tag{4.15}$$

Therefore, for a change in the density with fractional amplitude α, the change in the bubble length is

$$\begin{aligned} \Delta L_b &= \beta_{dr} \frac{\lambda\sqrt{\gamma_e}}{2\eta} - \beta_{dr} \frac{\lambda\sqrt{\gamma_e}}{2\eta\sqrt{1+\alpha}}, \\ &= \beta_{dr} \frac{\lambda\sqrt{\gamma_e}}{2\eta} \left(1 - \frac{1}{\sqrt{1+\alpha}}\right), \\ &\simeq \beta_{dr} \frac{\lambda\sqrt{\gamma_e}}{2\eta} \frac{\alpha}{2} = L_b \frac{\alpha}{2}. \end{aligned} \tag{4.16}$$

This sets the minimum attainable value for the bunch spacing for a "perturbations on flat plasma" scheme to be of the order of 1 μm for typical LWFA intensities. This is illustrated in figure 4.9 which shows the parameter space of possible inter-bunch spacings for a range of plasma densities and perturbation separation distances for $a_0 = 3.0$. This demonstrates the tunability range of the final bunch spacing using the perturbation spacing and plasma density. Minimum bunch lengths assuming different values of α are shown by coloured lines, and the dephasing length by the black dashed line. The minimum bunch length scales with the bunch length, so that $s \propto \eta^{-1} \propto n_e^{-1/2}$, meaning that bunch trains with smaller inter-bunch spacing can be injected at higher densities. This translates to less than an order of magnitude in the bunch spacing over the three orders of magnitude typical range of LWFA densities.

An upper limit on the maximum bunch spacing is set by the dephasing length of the LWFA, since, in order to make efficient use of the laser energy, bunches must be extracted before this point. However, in order to ensure minimum difference in the energies of the bunches the minimum possible bunch spacing is desirable, this ensures the bunches experience acceleration fields that are similar. The dephasing length for the chosen parameters is illustrated on figure 4.9 as a dashed line.

This multiple injection scenario was simulated using FBPIC with a base plasma density $\eta^2 = 0.001$ and $\sin^2$ perturbations with fractional amplitude $\alpha = 0.1$ and

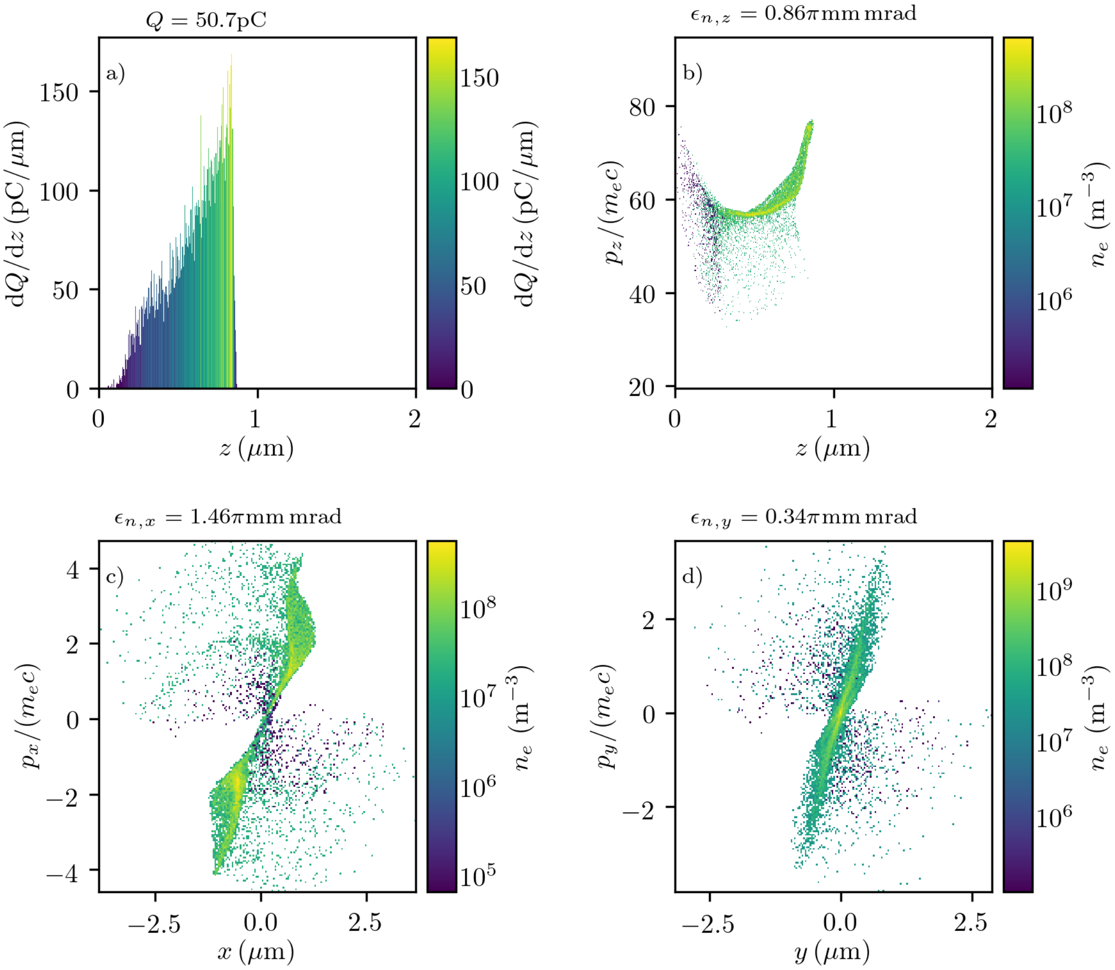

Figure 4.10: Measured bunch properties for the bunch train injected with a 200 μm inter-perturbation spacing. Longitudinal charge distribution (a) and z (b), x (c) and y (d) position-momentum phase space are shown before injection of the second bunch.

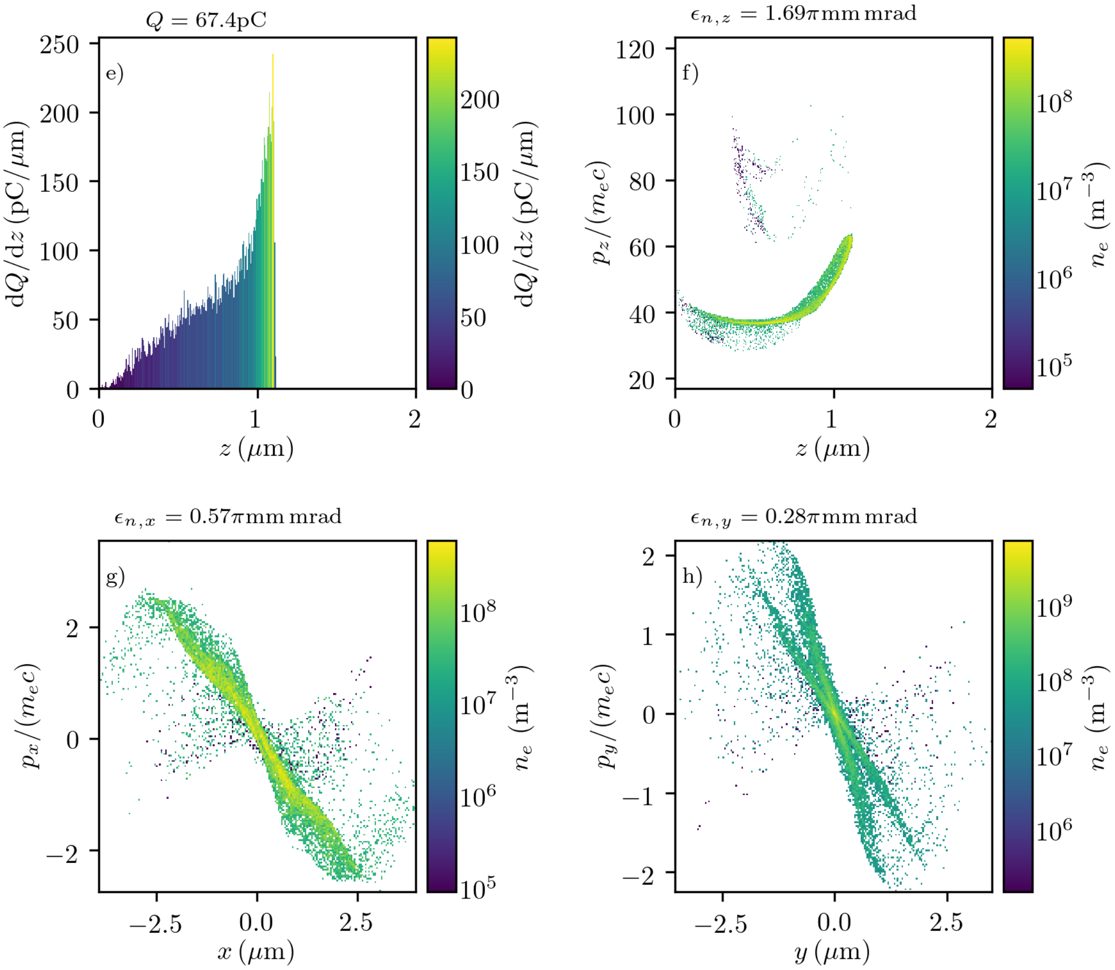

Figure 4.11: Measured bunch properties for a two bunch train injected with a 200 μm inter-perturbation spacing. Longitudinal charge distribution (a) and z (b), x (c) and y (d) position-momentum phase space are shown after injection of the second bunch. The two separate bunches can be discerned in phase space by their different phase space rotations which superpose to an “X” shape.

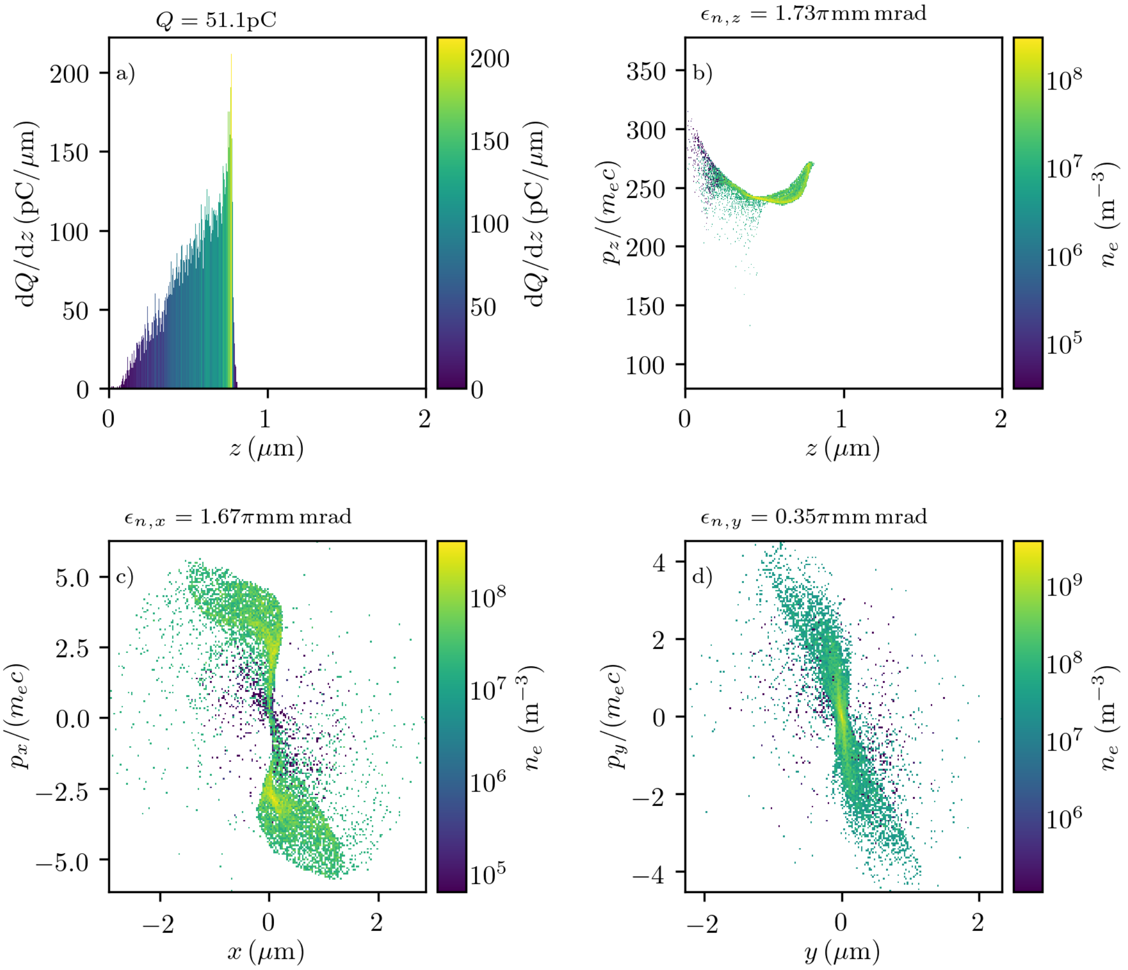

Figure 4.12: Measured bunch properties for the first bunch of a train injected with a 600 μm inter-perturbation spacing. Longitudinal charge distribution (a) and z (b), x (c) and y (d) position-momentum phase space are shown before injection of the second bunch.

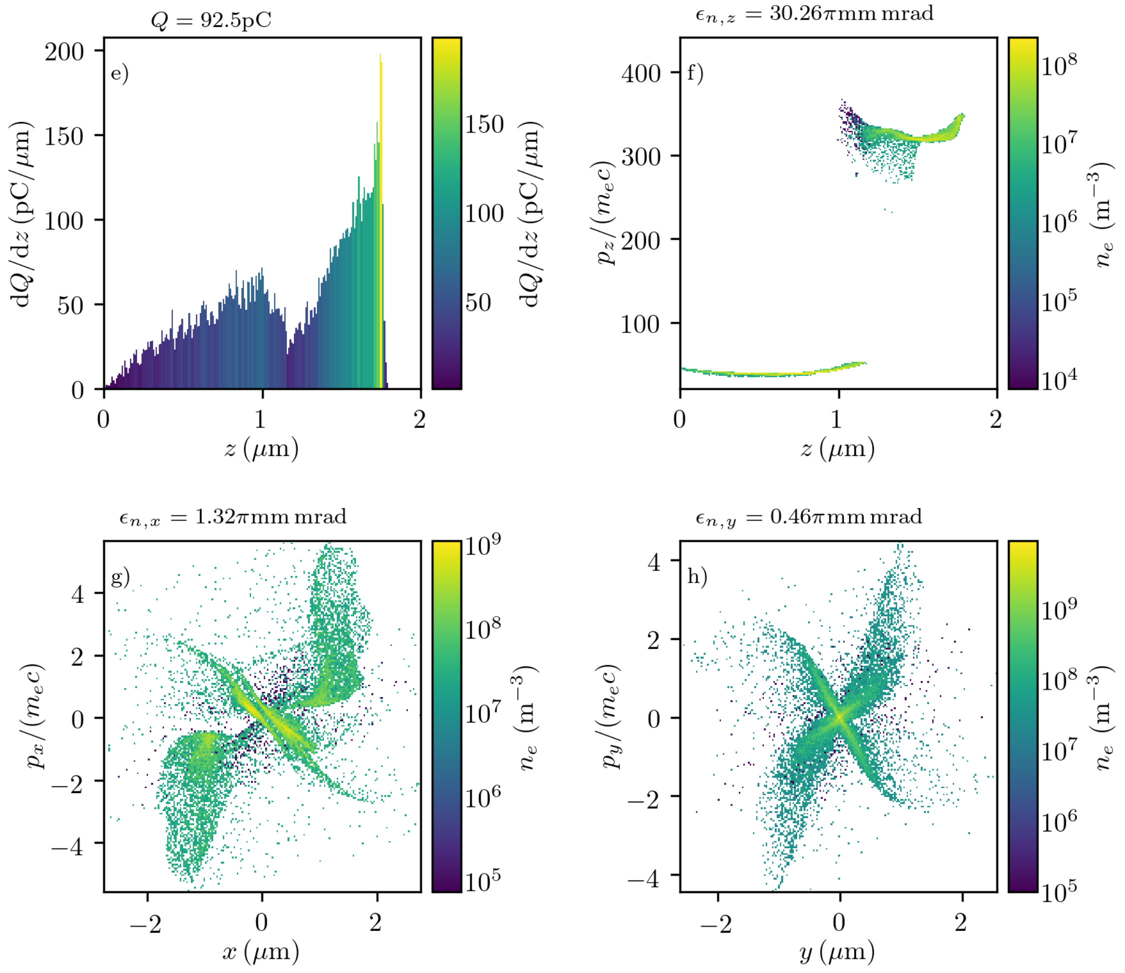

Figure 4.13: Measured bunch properties for a two bunch train injected with a 600 μm inter-perturbation spacing. Longitudinal charge distribution (a) and z (b), x (c) and y (d) position-momentum phase space are shown after injection of the second bunch. The two separate bunches can be discerned in phase space by their different rotations which superpose to create an "X" shape. The angle between bunches is larger in this case due to the longer propagation distance between the two injections compared to figure 4.11

$\ell = 100\,\mu$m. For all simulations the window size was $60\,\mu$m $\times$ $60\,\mu$m with a grid resolution of 2000×400 (longitudinal $\times$ radial), using Bessel modes up to $n = 2$. The driver was a quasi-matched laser pulse with $a_0 = 3.0$, beam waist $w = 15\,\mu$m, pulse length 25 fs, and gaussian spatial and temporal envelopes. As described in section 2.6.2, there are numerical differences in the behaviour of FBPIC and EPOCH which follow from the choice of geometry and solver. In this case these differences lead to a slightly higher peak electron velocity β_{thr} for FBPIC, and thus longer injected bunches for $\alpha = 0.1$ than found with EPOCH. However, the predictive nature of the model is unaffected once this is accounted for. Considering the charge distribution before and after the second injection event, both the bunch spacing and transverse emittance may be determined. Figures 4.10 and 4.11 show the longitudinal charge distribution and transverse phase-space immediately before and after the second injection event for $200\,\mu$m spacing between density peaks. Figures 4.12 and 4.13 show the same analysis for a $600\,\mu$m spacing. Before injection, in both cases we find that the emittance is much larger in the x direction, which is the laser polarisation plane, than the y direction, perpendicular to the laser polarisation. This is to be expected for a linearly polarised laser, due to direct acceleration by the electric field in the polarisation direction.[116] Following the bubble interaction with the second density perturbation we find that for the $200\,\mu$m spacing case, although there is an increase in the overall bunch charge, the longitudinal bunch profile remains broadly unchanged. There is a small increase to the peak at the front of the bunch and an elongation of the low density tail. The injection of additional electrons can also be seen in the phase-space distribution, where the distribution of the originally injected electrons is rotated relative to the newly injected electrons, forming the visible “X” shape in the phase space plots. There is small growth in the emittance in the y plane, as is expected from the already injected electrons interacting with the sheath fields, but more suprisingly,

---

[116] S. P. Mangles et al. *Phys. Rev. Lett.* **96**, pp. 1–4, 2006.

there is a large reduction in the emittance in the x plane.

For the case of injection after 600 μm shown in Figures 4.12 and 4.13, there is clear evidence of a second bunch injected behind the first. This time a much larger charge is injected, although the peak charge of the second bunch is reduced compared to the first. This is due to the beam loading effects of the first bunch. Although the distance the first bunch propagates before the second injection is larger than in the 200 μm case, reducing the effect, there is still some overlap between bunches, reducing the total charge and injection current of the second bunch. Once again the phase space plots show the characteristic cross shape from separated injection events, this time with a larger phase space rotation between the bunches due to the longer propagation distance between the two injection points.

The inter-bunch spacing and injected charge for all the simulated separation distances are summarised in figure 4.14 along with the bunche emittances before and after injection of a second bunch. The predicted linear relationship between ΔS and s can be clearly seen. What is not predicted, however, is the fact that there is an offset in the relationship such that there is no double bunch structure found at short perturbation separations. The black line shows the linear relationship as predicted by (4.14) with the offset found by least squares fitting. This lack of any double bunching structure for the 100 μm and 200 μm cases can be explained by the beam loading effects of the first bunch. As in the case for the injection of a single bunch, the already injected charge increases the potential barrier for further injection, therefore, little additional charge is injected by the second injection event, and the bunch structure is not markedly changed. This is reflected by the behaviour of the total injected charge, which is constant across bunches prior to the second injection event, but increases only minimally for the 100 μm and 200 μm cases whilst almost doubling once the first bunch has propagated far enough to allow further injection.

The other notable feature of the double bunch injection is the large variability in the transverse emittance following the injection of the second bunch. This would appear to be due to the differences in interaction between the first injected bunch and the bubble sheath region during the second injection event. When the electrons are first injected they do not enter at the very back of the bubble, but with a non-zero radial position and momentum such that they perform betatron motion as described in section 3.2.4. This oscillation period is of the order of the plasma period, and scales with respect to the electron energy as ${\gamma_e}^{-1/2}$. This motion leads to the bunch interacting with different regions of the sheath field dependent upon the propagation distance ΔS between injection events. Revisiting the bubble field structure as described in section 3.2.2 and shown in figure 3.3, shows that at either side of the axis at the bubble rear there is a region of strongly defocusing radial field. Depending upon the oscillation phase in which the electrons of the first bunch encounter these fields during the second injection event, they can either be focused or defocused. In the case that the electrons are returning to the bubble axis as they encounter this defocusing field, the field will do work on them to reduce their momentum and hence total transverse energy, thus reducing the beam emittance. In the case that they are moving away from the axis as they encounter the field, they will be accelerated by the defocusing field, increasing the bunch emittance. This effect is most marked for the x plane as the emittance is largest, however a much smaller effect can be seen in the y plane, where the betatron oscillation has the same phase.

4.7.1 Further Potential Customisation

The density configurations investigated here were chosen as simple cases which have been demonstrated to be producible experimentally. However, there is potential for many other configurations to be used to produce different effects in the injected bunch or bunch train, the effects of which may be predicted using the

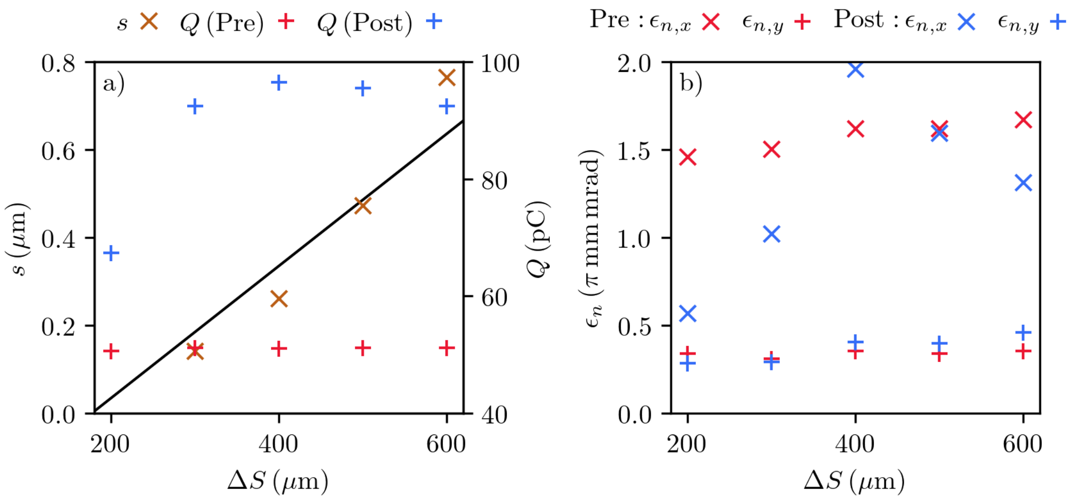

Figure 4.14: Inter-peak spacing (a) and transverse emittance (b) for bunches injected with $\sin^2$ density perturbations spaced by $\Delta S \in [200, 600]\,\mu$m. Bunch spacing (red +) is in good agreement with the predicted scaling of the inter-bunch spacing (black line). Beam emittance in the x (×), and y (+) planes both before (red) and after (blue) injection of the second bunch.

framework described here.

In particular a configuration that is of potential interest for the production of more closely spaced bunches is a “stepped down-ramp”. This would allow injection of multiple short bunches on the down-ramp steps of the injection, while mitigating the effects of the bubble sheath interfering with already injected bunches. While more complicated to realise experimentally than the simple structures investigated here, the ability to inject a customised bunch train has potential for increasing the flexibility of LWFA technology. Such flexibility is highly desirable for the transition of the technology from the laboratory to deployment as a scientific and industrial tool.

4.8 Effects of Laser Pulse Evolution

As we have seen in sections 4.3 and 4.4, the behaviour of the back of the bubble and of the sheath electrons themselves is sensitive to the laser behaviour, in particular

		a_0			
		2.0	3.0	4.0	5.0
w	$10\,\mu$m	No	No	No	No
	$15\,\mu$m	No	No	Yes	Yes
	$20\,\mu$m	No	Yes	Yes	Yes

Table 4.1: Occurence of injection for the various laser strengths and and spot sizes shown in figure 4.15.

the intensity of the laser pulse. However, as we have also seen in section 3.3, the pulse will unavoidably evolve to some extent as it propagates through the plasma. It is therefore important to understand the behaviour caused by an evolving laser and its potentially deleterious effects on the controlled injection process previously described. The primary goal was to investigate the behaviour of the laser with respect to the choice of normalized vector potential a_0, laser spot size w and plasma density fraction η^2. This allowed the selection of "quasi-matched" i.e. minimally evolving laser pulses for the investigation of density controlled injection.

The model we derived for the behaviour of the bubble velocity includes a term dependent upon the change in the average electron energy, which is directly connected to the laser intensity. Combined with information on the electron velocity at the bubble rear it would then be possible to predict injection. However, unlike with the constant intensity case, if the laser intensity is varying, the electron energy, and hence velocity at the bubble rear also varies. This makes the strategy of extracting a suitable value from a single PIC simulation to make predictions across a range of parameters impossible, as the velocity will change with each change in laser parameters.

However, it is still possible to investigate the effects of strongly varying laser intensity numerically, and make qualitative predictions and explanations of behaviour using the theory developed so far.

Figure 4.15 shows again the results of the laser evolution study first discussed at the end of chapter 3. Table 4.1 lists whether or not injection occurs for each combination of the chosen parameters. This follows from the fact that the occur-

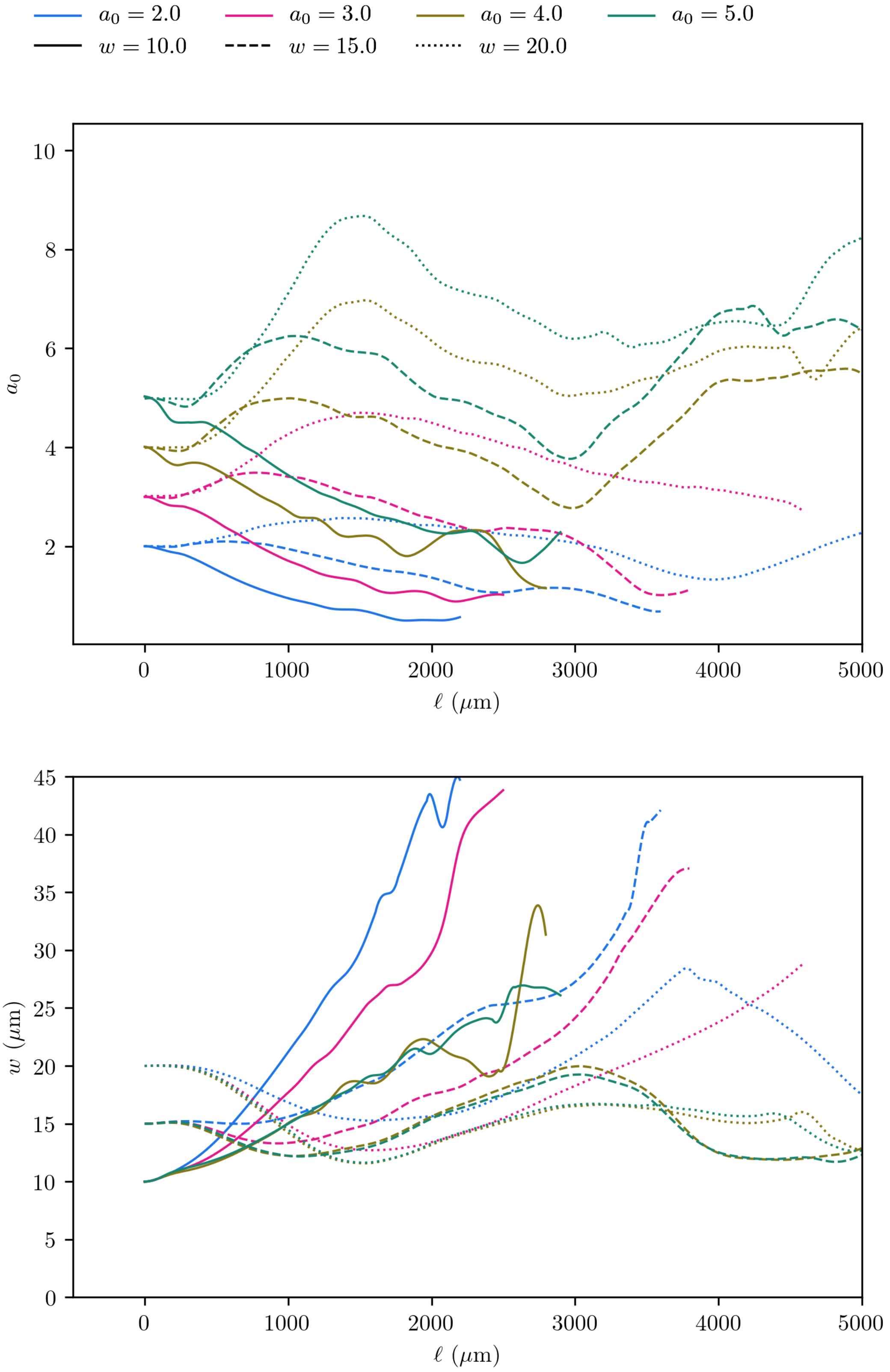

Figure 4.15: Evolution of the a) normalised vector potential a_0, and b) spot size w for laser pulses with varying intensities and spot sizes in a plasma with normalised density $\eta^2 = 0.001$ and a pulse length $\tau_{\text{FWHM}} = 25\,\text{fs}$. These results are also shown in figure 3.6.

rence of injection is dependent not merely on the normalized vector potential as suggested by static bubble models,[16] but on the laser pulse self-focusing sufficiently strongly to cause the bubble to evolve.[55,57] Increasing laser intensity leads to an increase in the bubble size and slowing of the bubble phase velocity, as the model describes. However, the changing laser intensity also strongly affects the behaviour of the sheath electrons. This turns out to be a major effect, thus this model alone is insufficient for correctly predicting injection due to strongly evolving laser pulse intensity. This more complex case of injection for an evolving bubble is considered using a Hamiltonian formalism by Yi *et al.*,[55] which demonstrates that accurate modelling of these fields at the bubble rear is crucial for correct prediction of self-injection.

Focusing on the cases for $a_0 = 3.0$ provides a clear demonstration of the possible laser evolution situations. As can be seen in figure 4.15, the chosen “quasi-matched” spot size of 15 μm still undergoes a small amount of self-focusing, but is very closed to matched. In comparison the larger, 20 μm, which strongly self focuses, over-focusing to a smaller spot size before rapidly diverging. The smaller 10 μm spot begins over-focused and immediately diverges, rapidly losing intensity such that the normalised vector potential is reduced to half after only 1 mm propagation. It is possible that a $\sim 14\,\mu$m spot or slightly reduced a_0 could have produced a better matched beam still. However, the chosen 15 μm spot size was adequately stable to allow density controlled injection without laser evolution causing additional spurious injection due to laser evolution.

Figure 4.16 shows the measured velocity of the back of the bubble for the three simulations with $a_0 = 3$ discussed above. While it can be seen that the change in laser intensity does correlate with subtle increases and decreases in the bubble phase velocity, they alone are not sufficient to explain the occurence, or lack of injection. As we have already discussed, the details of the electron dynamics at

---

[55] S. A. Yi et al. *Phys. Plasmas* **20**, p. 013108, 2013.

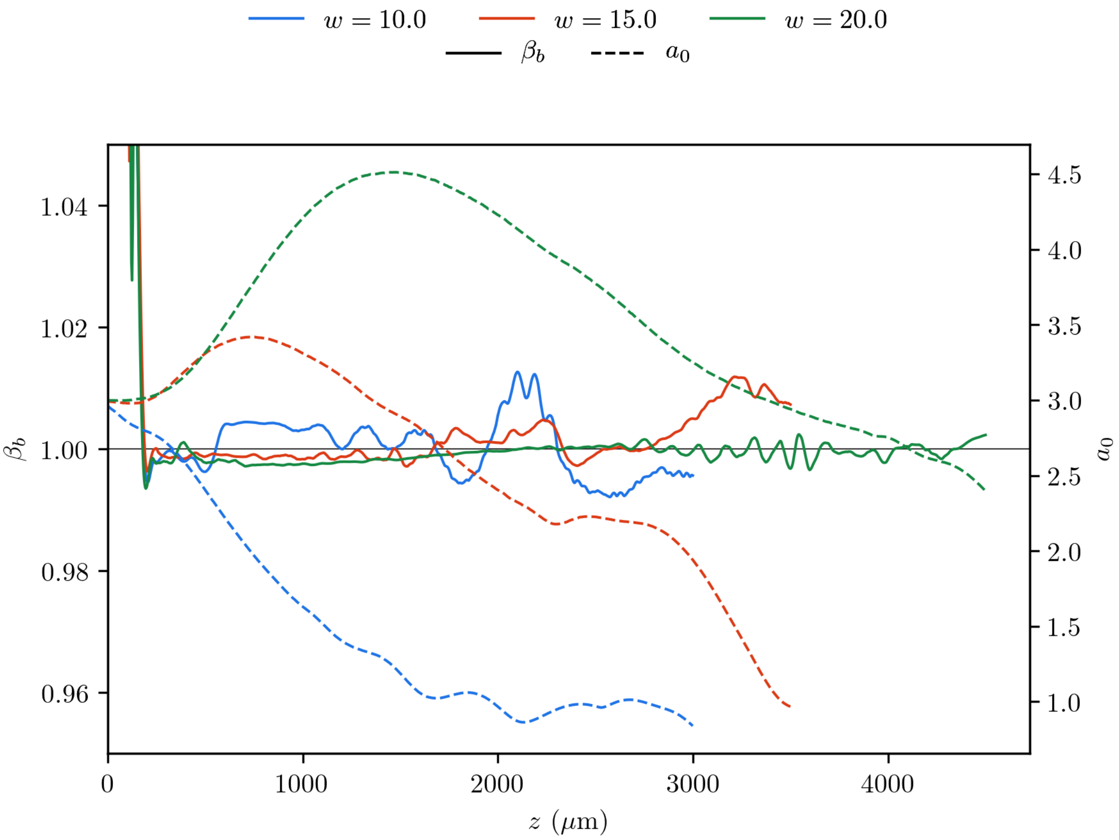

Figure 4.16: Phase velocity β_b of the back of the bubble for the pulses with $a_0 = 3.0$ and varying spot size as shown in figure 4.15. The bubble phase velocities (solid lines) are shown alongside their respective driver pulse normalized vector potentials (dashed lines). The vacuum speed of light $\beta = 1$ (black line) is shown for reference.

the back of the bubble are crucial to whether or not injection will occur. However, as the laser pulse is evolving, the shape, energy distribution and resulting fields of the electron sheath will be constantly changing. The differing evolution of the sheath geometries for these three cases is shown in figure 4.17. The results for $w = 10\,\mu$m show the wakefield amplitude rapidly decreasing consistent with the rapid decrease in laser intensity. The results for the larger spot sizes show more complex sheath structure and temporal evolution. In the case of the initial $15\,\mu$m and $20\,\mu$m spots, the sheath has a clearly bifurcated structure where some of the electron current “peels off” as it travels around the periphery of the bubble.[21] In the $15\,\mu$m case, over the 1 mm propagation distance of figures 4.17(b), 4.17(e) and 4.17(h) this structure clearly evolves, with the location of the bifurcation

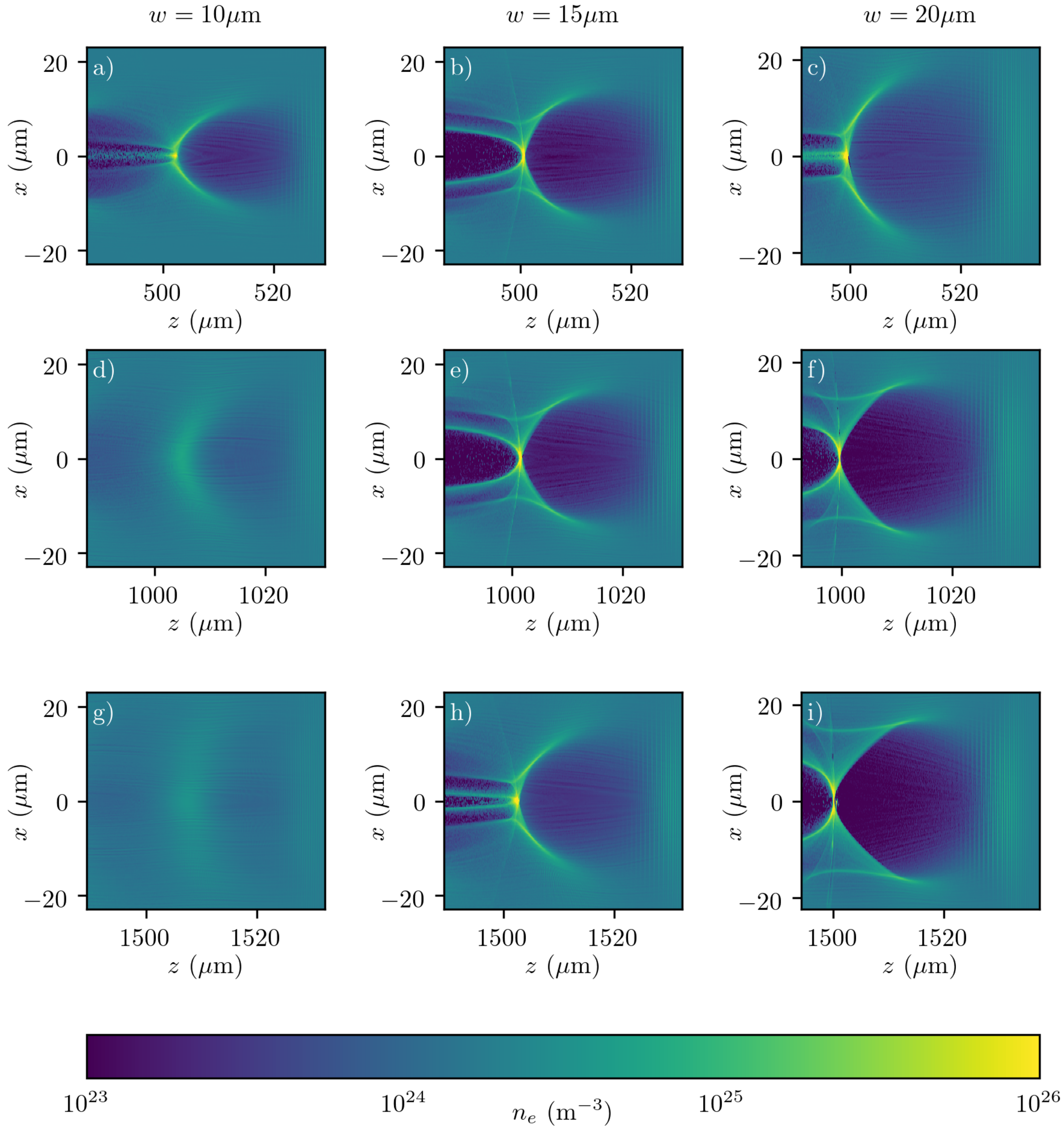

Figure 4.17: Evolution of the bubble for the pulses with $a_0 = 3.0$ and varying spot size as shown in figure 4.15. The bubbles are shown after propagation over 500 μm (a, b, c), 1000 μm (d, e, f), 1500 μm (g, h, i) for initial spot sizes 10, 15, and 20 μm respectively.

changing. The behaviour in figures 4.17(c), 4.17(f) and 4.17(i) for the 20 μm case is similar but more pronounced. The location of the bifurcation point appears to be correlated with the intensity of the laser pulse, moving outward between 500 μm and 1000 μm in the 15 μm spot case as the laser self-focuses, and then inward again at 1500 μm as the laser intensity decreases. The intensity of the 20 μm spot size pulse only increases over the snapshot range shown here, with the bifurcation radius increasing accordingly. These results are consistent with those reported from simulation by Shen *et al.*[117] and experimentally by Yang *et al.*[63] where high current "beams" are identified as being produced from the bubble sheath. Variation in this sheath behaviour leads to variations in the strength and geometry of the fields at the back of the bubble. Local bubble field changes of this nature have been demonstrated as another means to cause self-injection,[21,64] in constrast to the evolution of bubble size a demonstrated in this chapter. In light of the complex dependence between laser intensity, bubble structure and self-injection it is unsurprising that the small bubble phase velocity perturbations induced by the laser evolution are not the primary factor in self-injection caused by laser evolution.

4.9 Conclusions

The main result from this chapter is the development of an analytic model describing the self-injection of electron bunches due to a density perturbation in the plasma. The model describes the phase velocity changes of the back of the LWFA bubble due to plasma density perturbations, and a threshold velocity below which the bubble velocity must drop for injection to occur. The model also allows prediction of the length of the injected electron bunch, which is related to the length of the density perturbation region and average velocity of the bubble. The

---

[117] Z.-C. Shen et al. *Phys. Plasmas* **23**, p. 103112, 2016.

[63] X. Yang et al. *Sci. Rep.* **7**, pp. 1–10, 2017.

[64] X. F. Li et al. *Phys. Plasmas* **21**, p. 73109, 2014.

scheme was then validated using PIC simulation with the EPOCH code, with excellent agreement between the model and simulation for both the minimum required amplitude for injection to occur and length of the injected bunches. By using density perturbations which are close to threshold, injection of ultra-short bunches with durations of $\sim$ fs is demonstrated. Injected bunch charge is found to scale linearly with the injected bunch length. This ability to control the bunch length and total charge is a crucial factor in making the LWFA suitable for a range of applications, making it possible to produce both the short, low emittance, low charge bunches desirable for producing monochromatic, FEL-like radiation as well as the long, high charge bunches suited to producing intense, broadband synchrotron radiation.

For large density perturbations beam loading is found to have a strong effect on the bunch shape. Close to the injection threshold, the longitudinal current distributions of the bunches are approximately symmetric in shape around the bunch centroid, while for longer, higher charge bunches, the beam current is largest at the head of the bunch and decreases approximately linearly to the tail. This is in agreement with result found by Tzoufras *et al.*[115] and Mangles *et al.*[112] who show that this is due to beam loading, where the injected bunch charge approaches the maximum injected charge that the bubble can support, preventing further injection of electrons.

Injection of a train of multiple bunches using a series of plasma density perturbations is shown to be feasible. The spacing between injected bunches, analogous to the bunch length, depends upon the inter-perturbation spacing and the average bubble velocity between these points. This demonstrates that it is possible to inject a train of bunches with femtosecond spacing, corresponding to XUV wavelengths. The exploitation of such bunch trains for coherent enhancement of betatron radiation is investigated in chapter 5.

The final sections of this chapter concern the effects of laser evolution on self-injection. Due to the dependence of the bubble size on laser intensity, evolution of the laser pulse causes evolution of the bubble and changes in the phase velocity of the back of the bubble. As for the density perturbed case, sufficiently large reductions in this phase velocity can cause injection, and sufficiently large increases can inhibit injection where it may be desired. This result means it is possible to control injection using a mismatched laser which will cause bubble evolution. However, the non-linear nature of the laser evolution (discussed in section 3.3) presents difficulties for accurate tuning compared to the density controlled approach. Therefore, accurate control of injection, achieved using density perturbations, requires that the laser be well matched to the plasma to minimize evolution and hence unwanted, laser induced, bubble evolution.

Chapter 5

Radiation from Injected Bunches

In addition to being accelerated longitudinally, electrons injected into the LWFA bubble are also accelerated in the transverse direction. This acceleration causes them to emit radiation according to the Liénard-Wiechert potentials, as described in section 2.7. The acceleration in the transverse direction is particularly useful for radiation production as we found from (2.78), which shows that the radiation is most intense when the particle motion is highly relativistic and parallel to the observation direction, but the particle acceleration is transverse to the observation direction. Multiple regimes and schemes have been suggested to harness the LWFA as a useful radiation source,[22,23,118,119] making use of the plasma bubble focusing fields as a wiggler to produce either coherent or incoherent radiation. This is conceptually extremely similar to the free electron laser (FEL), which uses an external magnetic wiggler to produce the radiation.[120] However, unlike an external wiggler, the plasma wiggler does not impose a periodicity on the oscillation, leading to more stringent requirements on the beam quality to maintain coherence.[118]

In this chapter we first present the existing analytic description of the electron motion in a focusing ion-channel and the form of subsequently emitted radiation.

---

[22] A. G. Khachatryan et al. *New J. Phys.* **10**, pp. 1–12, 2008.

[23] M. Fuchs et al. *Nat. Phys.* **5**, pp. 826–829, 2009.

[118] B. Ersfeld et al. *New J. Phys.* **16**, p. 093025, 2014.

[119] E. Wallin et al. *Phys. Plasmas* **24**, 2017.

[120] P. Luchini and H. Motz. *Undulators and free-electron lasers*, Clarendon Press, 1990.

We then characterize the radiation due to an accelerating electron in the LWFA, and consider the coherent emission from electron bunches. The coherent enhancement due to single and multiple electron bunches is investigated to determine the feasibility of frequency tuning and coherent enhancement using the bunch control techniques developed in chapter 4. Finally, the robustness of the scheme is considered with respect to the effects of electron energy spread and spread in oscillation amplitude, which can wash out the density modulations.

5.1 The Acceleration Free Case

To find an analytic approximation for the radiation from an electron bunch moving in the LWFA bubble fields, it is necessary to first calculate the radiation due to a single electron moving in the same fields. The total radiation due to a monoenergetic bunch of electrons can then be calculated by including the effects of relative phase between the oscillating electrons.

As we saw in section 3.2.4, the analytic solutions for the betatron motion[*] of the electron in the bubble are extremely complex. Attempting to use these solutions to find the energy spectrum as derived in section 2.7.4 does not yield analytic solutions for the radiation.

It is possible, however, to find an analytic solution for the radiation emitted by an electron moving in a purely transverse focusing field, such as in an ion-channel laser.[118,121] This solution can then be used to build a piece wise approximation of the radiation due to an accelerating electron. We know that the majority of the radiation is emitted in the small turning-point region of the trajectory where the

---

[121] E. Esarey et al. *Phys. Rev. E: Stat., Nonlinear, Soft Matter Phys.* **65**, p. 056505, 2002.

[*] In the literature “betatron motion” is variously used to label the motion of electrons in both accelerating and non-accelerating cases. For clarity here, the non-accelerating case will be referred to as the “ion-channel” motion, and the accelerating case as “bubble” motion.

acceleration is largest (2.92), and we have also assumed that the change in the transverse betatron amplitude is adiabatic. Therefore, we may approximate the total radiation field in the accelerating case as the sum of the contributions for half-cycle segments of the ion-channel radiation at the relevant electron energy and oscillation amplitude.

In this section we will consider the radiation from an electron performing betatron motion in an ion-channel with no longitudinal acceleration, and investigate the dependence of the emitted radiation frequency spectrum on the electron orbit properties.

5.2 Betatron Motion in an Ion-Channel

An approximate analytic solution for the motion of electrons in a plasma focusing channel, is given by Esarey *et al.*[121,122] The equations of motion are found by starting with the Lorentz force equation for coordinate time,

$$\frac{\mathrm{d}}{\mathrm{d}t}(\gamma\beta) = \left[\bar{E} + \bar{\beta} \times \bar{B}\right], \tag{5.1}$$

where $\bar{p} = \gamma\bar{\beta}$ is the normalised electron momentum, and the fields $\bar{E}$ and $\bar{B}$ are normalised to $e/mc\omega_p$.

We assume that the focusing field is purely electrostatic it can be described by the scalar potential ϕ normalised to e/mc^2, hence the force equation becomes

$$\frac{\mathrm{d}}{\mathrm{d}t}(\gamma\beta) = \nabla\phi. \tag{5.2}$$

In the case of an infinitely long ion channel, or at the dephasing point of a plasma bubble where there are no longitudinal force components, the potential is related to the plasma density by Poisson's equation

$$\nabla^2\phi = k_p^2(n_e(r)/n_0 - 1), \tag{5.3}$$

---

[122] S. Chen. "FEL Theory in an Ion Channel Wiggler". PhD. Thesis. 2016.

where n_0 is the uniform background ion density, and n_e is the electron density. For the case that $n_e = 0$ for a completely evacuated ion channel, analogous to the LWFA bubble regime, this becomes

$$\nabla^2 \phi = \frac{1}{r}\frac{\partial}{\partial r}\left(r\frac{\partial \phi}{\partial r}\right) = -k_p^2, \tag{5.4}$$

which has the solution

$$\phi = -\frac{r^2 k_p^2}{4} + B\ln r + C = \phi_0\left(1 - \frac{r^2}{r_0^2}\right), \tag{5.5}$$

with

$$\phi_0 = \frac{r_0^2 k_p^2}{4}, \tag{5.6}$$

for a channel radius r_0, where the potential is chosen to be zero at the edge of the ion channel. The purely transverse potential implies two constants of the motion: $\mathrm{d}p_z/\,\mathrm{d}t = 0$, meaning no longitudinal acceleration of the electron; and $\mathrm{d}(\gamma - \phi)/\,\mathrm{d}t = 0$, conservation of the total energy of the electron. The equations of motion are therefore

$$p_z = p_{z0}, \tag{5.7}$$

$$\gamma(r) = \gamma_0 + \Delta\phi, \tag{5.8}$$

$$p_r^2 = 2\gamma_0\Delta\phi + \Delta\phi^2, \tag{5.9}$$

where $\Delta\phi = \phi(r) - \phi(r_\beta)$ is the instantaneous value of the potential, r_β is the amplitude of the transverse oscillation, assumed to be constant, and γ_0 is the initial kinetic energy, ($\gamma_0^2 = 1 + p_{z0}^2$) assuming the electron has an initial offset r_β and no initial transverse momentum.

Assuming, for simplicity, that the electron motion is in the x-z plane, a solution for the motion is found by assuming that the transverse motion is simple harmonic with a frequency $\omega_\beta = k_\beta c$. The solutions, to first order, are then

$$x \simeq r_\beta \sin(k_\beta ct), \tag{5.10}$$

$$\beta_x \simeq k_\beta r_\beta \cos(k_\beta ct), \tag{5.11}$$

$$z \simeq z_0 + \beta_{z0}(1 - k_\beta^2 r_\beta^2/4)ct - \frac{\beta_{z0}}{8} k_\beta r_\beta^2 \sin(2k_\beta ct), \tag{5.12}$$

$$\beta_z \simeq \beta_{z0}(1 - k_\beta^2 r_\beta^2/4) - \frac{\beta_{z0}}{4} k_\beta^2 r_\beta^2 \cos(2k_\beta ct), \tag{5.13}$$

where $\beta_{z0} = p_{z0}/\gamma_0$, $k_\beta = \sqrt{2\phi_0/\gamma_0 r_0^2}$ and $k_\beta^2 r_\beta^2 \ll 1$ is assumed. For the bubble regime analogue, as we have already noted, $\phi_0 = k_p^2 r_0^2/4$, which means $k_\beta = k_p/\sqrt{2\gamma_0}$, and therefore $k_\beta^2 r_\beta^2 = 2r_\beta^2 \pi^2/(\lambda_p^2 \gamma_0^2) \ll 1$, which is true for the bubble regime provided r_β is small compared with the plasma wavelength and the electrons are highly relativistic.

5.3 Radiation from Betatron Motion in an Ion-Channel

As described by Esarey *et al.*[121], the radiation from an electron performing the motion given by (5.10) to (5.13) can be calculated using the equations from section 2.7.4, to give the spectral intensity along the observation vector $\hat{n}$:

$$I(\omega, \Omega) = \frac{q^2 \omega^2}{16\pi^3 \epsilon_0 c} \left| \int_{-\infty}^{\infty} \mathrm{d}t \, \hat{n} \times (\hat{n} \times \bar{\beta}) \, \mathrm{e}^{i\omega[t - \hat{n}\cdot\bar{r}(t)/c]} \right|^2 . \tag{2.93 revisited}$$

Moving to spherical coordinates centred on the point at which the electron emits radiation, we can identify that the observation vector $\hat{n} = \hat{r}$. This is view is valid for observation in the far field limit with a short emission time such that the observation vector does not change over the emission time, an assumption we have already made in deriving (2.93), (see section 2.7.4).

It is useful at this point to write down the quantities

$$\begin{aligned}\hat{n}\times(\hat{n}\times\bar{\beta}) = &-(\beta_x\cos\theta\cos\phi + \beta_y\cos\theta\cos\phi - \beta_z\sin\theta)\hat{\theta} \\ &+ (\beta_x\sin\theta - \beta_y\cos\phi)\hat{\phi},\end{aligned} \tag{5.14}$$

$$\hat{n}\cdot\bar{r} = r\hat{r} = r_x\sin\theta\cos\phi + r_y\sin\theta\sin\phi + r_z\cos\theta, \tag{5.15}$$

with the standard definition of the spherical unit vectors

$$\hat{r} = \sin\theta\cos\phi\,\hat{x} + \sin\theta\sin\phi\,\hat{y} + \cos\theta\,\hat{z}, \tag{5.16}$$

$$\hat{\theta} = \cos\theta\cos\phi\,\hat{x} + \cos\theta\sin\phi\,\hat{y} - \sin\theta\,\hat{z}, \tag{5.17}$$

$$\hat{\phi} = -\sin\phi\,\hat{x} + \cos\phi\,\hat{y}. \tag{5.18}$$

Because the radiation will be polarised in the direction $\hat{n}\times(\hat{n}\times\bar{\beta})$ it may be split into orthogonal θ and ϕ components $I = I_\theta + I_\phi$. Also, as we have already assumed that the motion is purely in the x-z plane, the radiation due to the two components may be written as

$$I_\theta = \frac{q^2\omega^2}{16\pi^3\varepsilon_0 c}\left|\int_{-T/2}^{T/2}\mathrm{d}t\,(\beta_x\cos\theta\cos\phi - \beta_z\sin\theta)\;\mathrm{e}^{i\psi}\right|^2, \tag{5.19}$$

$$I_\phi = \frac{q^2\omega^2}{16\pi^3\varepsilon_0 c}\left|\int_{-T/2}^{T/2}\mathrm{d}t\,(\beta_x\sin\theta)\;\mathrm{e}^{i\psi}\right|^2, \tag{5.20}$$

where T is the period of a single cycle, and with the phase factor ψ given by

$$\psi = \psi_0 + \alpha_0 kct - \alpha_x\sin(k_\beta ct) + \alpha_z\sin(2k_\beta ct), \tag{5.21}$$

$$\alpha_0 = 1 - \beta_{z0}(1 - k_\beta^2 r_\beta^2/4)\cos\theta, \tag{5.22}$$

$$\alpha_x = kr_\beta\sin\theta\cos\phi, \tag{5.23}$$

$$\alpha_z = \beta_{z0}(kk_\beta r_\beta^2/8)\cos\theta, \tag{5.24}$$

where $\psi_0 = -kz_0\cos\theta$ and $k = \omega/c$.

To make the expression for the phase factor integrable, the Jacobi-Anger expansion,[109]

$$\mathrm{e}^{i\alpha\sin\theta} = \sum_{n=-\infty}^{\infty} J_n(\alpha)\,\mathrm{e}^{in\theta}, \tag{5.25}$$

is used to write it in terms of the Bessel functions of the first kind $J_n(\alpha)$:

$$\mathrm{e}^{i(\psi+\ell k_\beta ct)} = \sum_{m,n=-\infty}^{\infty} J_m(\alpha_z) J_{n+2m+\ell}(\alpha_x)\,\mathrm{e}^{i(\psi_0+\bar{k}ct)} \tag{5.26}$$

where $\bar{k} = \alpha_0 k - nk_\beta$ and a change of variable $-n = 2m + \ell - p$ is made after applying the Jacobi-Anger expansion, summing the α_x term initially over p and the α_z term over n.

Finding the radiation spectrum requires evaluation of the integrals over the interaction length cT

$$\tilde{I}_{\{x,z\}} = \int_{T_0}^{T_1} \mathrm{d}t \frac{\mathrm{d}\{x,z\}}{\mathrm{d}t}\,\mathrm{e}^{i\psi}. \tag{5.27}$$

The two polarisation components of the intensity may then be expressed in terms of these solutions as

$$\frac{\mathrm{d}^2 I_\theta}{\mathrm{d}\omega\,\mathrm{d}\Omega} = \frac{q^2\omega^2}{16\pi^3\varepsilon_0 c}\left|\tilde{I}_x\cos\theta\cos\phi - \tilde{I}_z\sin\theta\right|^2, \tag{5.28}$$

$$\frac{\mathrm{d}^2 I_\phi}{\mathrm{d}\omega\,\mathrm{d}\Omega} = \frac{q^2\omega^2}{16\pi^3\varepsilon_0 c}\left|\tilde{I}_x\sin\phi\right|^2. \tag{5.29}$$

The integrals are performed using the identity $2\,\mathrm{e}^{i\psi}\cos(\ell k_\beta ct) = \mathrm{e}^{i\psi}\,\mathrm{e}^{i\ell k_\beta ct} +$

---

[109] *NIST Digital Library of Mathematical Functions.* http://dlmf.nist.gov/

$\mathrm{e}^{i\psi}\,\mathrm{e}^{-i\ell k_\beta ct}$, to rewrite the equations of motion (5.11) and (5.13), yielding

$$\begin{aligned}\tilde{I}_x = \frac{k_\beta r_\beta}{2c}\,\mathrm{e}^{i\psi_0} \sum_{n,m=\infty}^{\infty} &\left(\frac{\mathrm{e}^{i\bar{k}cT_1} - \mathrm{e}^{i\bar{k}cT_0}}{ic\bar{k}}\right) \\ &\times J_m(\alpha_z)\left[J_{n+2m-1}(\alpha_x) + J_{n+2m+1}(\alpha_x)\right],\end{aligned} \tag{5.30}$$

$$\begin{aligned}\tilde{I}_z = \frac{\beta_{z0}}{2c}\,\mathrm{e}^{i\psi_0} \sum_{n,m=\infty}^{\infty} &\left(\frac{\mathrm{e}^{i\bar{k}cT_1} - \mathrm{e}^{i\bar{k}cT_0}}{ic\bar{k}}\right) J_m(\alpha_z) \\ &\times \left\{2\left(1 - \frac{k_\beta^2 r_\beta^2}{4}\right) J_{n+2m}(\alpha_x) - \right. \\ &\left. \frac{k_\beta^2 r_\beta^2}{4}\left[J_{n+2m-2}(\alpha_x) + J_{n+2m+2}(\alpha_x)\right]\right\}.\end{aligned} \tag{5.31}$$

The exponentials may be simplified to a sine function by assuming that the integral is symmetric about zero, i.e $T_1 = -T_0 = T/2$. This is reasonable because the point $t = 0$ is a point of maximum acceleration, and so we will always be integrating over a region of interest, with larger T incorporating further cycles. Therefore, the results of integration over a complete number of betatron cycles N_β may be expressed as

$$\begin{aligned}\tilde{I}_x = k_\beta r_\beta\,\mathrm{e}^{i\psi_0} \sum_{n,m=\infty}^{\infty} &\left(\frac{\sin(\pi N_\beta \bar{k}/k_\beta)}{c\bar{k}}\right) \\ &\times J_m(\alpha_z)\left[J_{n+2m-1}(\alpha_x) + J_{n+2m+1}(\alpha_x)\right],\end{aligned} \tag{5.32}$$

$$\begin{aligned}\tilde{I}_z = \beta_{z0}\,\mathrm{e}^{i\psi_0} \sum_{n,m=\infty}^{\infty} &\left(\frac{\sin(\pi N_\beta \bar{k}/k_\beta)}{c\bar{k}}\right) J_m(\alpha_z) \\ &\times \left\{2\left(1 - \frac{k_\beta^2 r_\beta^2}{4}\right) J_{n+2m}(\alpha_x) - \right. \\ &\left. \frac{k_\beta^2 r_\beta^2}{4}\left[J_{n+2m-2}(\alpha_x) + J_{n+2m+2}(\alpha_x)\right]\right\}.\end{aligned} \tag{5.33}$$

The integration time is related to the number of betatron cycles by $cT = \lambda_\beta N_\beta = 2\pi N_\beta/k_\beta$, therefore a single emission event, which is one half of a betatron cycle, is represented by the value $N_\beta = 1/2$.

We can see that there are two main terms involved in the expressions for the radiation: a sinc-like $(\sin(a\bar{k})/(b\bar{k}))$ term, and a Bessel function term. The presence of a term involving an infinite sum over Bessel functions is not a surprise, indeed it is expected since the trajectory of an electron during the high acceleration phase of the emission cycle is a smooth arc section. This is similar to the trajectory of an electron performing synchrotron motion, and so we would expect the form of the radiation spectrum to be similar. The sinc-like term encodes the effects of the interference between multiple radiation cycles. This inteference is due to the fact that the electron and the radiation are approximately co-propagating during the integration time. Therefore, when the electron emits radiation at subsequent extrema of its trajectory it will interfere with the radiation that has previously been emitted. This interference sums constructively at multiples of the resonant frequency, k_n, given by

$$k_n = \frac{nk_\beta}{\alpha_0} = \frac{nk_\beta}{1 - \beta_{z0}(1 - k_\beta^2 r_\beta^2/4)\cos\theta}. \tag{5.34}$$

The effect is to confine the radiation to a series of harmonics of the betatron frequency $k_n = nk_\beta/\alpha_0$, which become increasingly sharply peaked for increasing numbers of betatron oscillations N_β. Additionally, this shows that there is a detuning effect on the resonant frequency as the viewing angle, θ, in the plane of the electron motion increases. This is because the propagation distance of the radiation is increased when propagation is at an angle to the z axis, and so the wavelength at which constructive interference occurs is increased.

Labelling this sinc-like prefactor as the resonance function $Q_n(k)$, we can illustrate more clearly the interference behaviour by rewriting it as

$$Q_n(k) = \frac{\pi N_\beta}{k_\beta}\,\mathrm{sinc}(\pi N_\beta[\alpha_0 k/k_\beta - n]). \tag{5.35}$$

This form also shows that as well as the absolute amplitude scaling with the number of betatron cycles, the width of the frequency window over which $Q_n(k)$ is non-negligible also scales with $1/N_\beta$. Therefore, for any given k, $Q_n(k)$ is only nonneglible for $n \sim \alpha_0 k/k_\beta$. In the case that N_β is small, in addition to the central peak, the first few cycles of the sinc function also provide a non-negligible contribution to the frequency spectrum. This means that for a wavenumber k, there will be multiple values of n for which there is a nonnegligible contribution. The width of the sinc function must therefore be considered in order to determine the contributing range of n. Having identified the resonant frequency nk_β closest to the k of interest, we must also evaluate the surrounding range Δn such that

$$\Delta n > \frac{1}{\pi N_\beta}. \tag{5.36}$$

From this we can see that for more than a few cycles N_β, the width of the resonance peaks becomes sufficiently small that there is no overlap between neighbouring harmonics.

5.3.1 Many Cycle Radiation

In the case of ion-channel radiation it is typically assumed[118,121] that the number of oscillations N_β is large. This separates the harmonics, allowing the cross terms $n \neq n'$ to be neglected upon multiplication in (5.28) and (5.29), thus the energy distribution is approximated by

$$\begin{aligned}\frac{\mathrm{d}^2 I}{\mathrm{d}\omega\,\mathrm{d}\Omega} =& \frac{q^2\omega^2 N_\beta^2}{16\pi\varepsilon_0 c k_\beta^2}\sum_{n=1}^{\infty}\mathrm{sinc}(\pi N_\beta[\alpha_0 k/k_\beta - n])^2 \\ &\times \left(C_x^2[1-\sin^2\theta\cos^2\phi] + C_z^2\sin^2\theta - C_z C_x \sin 2\theta\cos\phi\right),\end{aligned} \tag{5.37}$$

where

$$C_x = k_\beta r_\beta \sum_{m=-\infty}^{\infty} J_m(\alpha_z)[J_{n+2m-1}(\alpha_x + J_{n+2m_1}(\alpha_x)], \tag{5.38}$$

$$\begin{aligned}C_z =& \beta_{z0}\sum_{m=-\infty}^{\infty} J_m(\alpha_z)\left[2\left(1-\frac{k_\beta^2 r_\beta^2}{4}\right)J_{n+2m}\right. \\ &\left. -\frac{k_\beta^2 r_\beta^2}{4}J_{n+2m-1}(\alpha_x + J_{n+2m_1}(\alpha_x)\right].\end{aligned} \tag{5.39}$$

Making the assumption that $\gamma_0 \gg 1$

$$\alpha_0 \simeq \frac{(1+\alpha_\beta^2/2)\cos\theta + 2\gamma_0^2(1-\cos\theta)}{2\gamma_0^2}, \tag{5.40}$$

and using the betatron strength parameter $a_\beta = \gamma_0 r_\beta k_\beta$,

$$\alpha_x \simeq \frac{n(\omega/\omega_n) 2\gamma_0 a_\beta \sin\theta\cos\phi}{(1 + a_\beta^2/2)\cos\theta + 2\gamma_0^2(1 + \cos\theta)}, \tag{5.41}$$

$$\alpha_z \simeq \frac{n(\omega/\omega_n)(a_\beta^2/4)\cos\theta}{(1 + a_\beta^2/2)\cos\theta + 2\gamma_0^2(1 - \cos\theta)}. \tag{5.42}$$

$$\tag{5.43}$$

Additionally, since the majority of the radiation will be emitted in the small forward cone $\theta^2 \ll 1$, and $a_\beta^2/\gamma_0^2 = r_\beta^2 k_\beta^2 \ll 1$ as we have already assumed, this now further simplifies to

$$\frac{\mathrm{d}^2 I}{\mathrm{d}\omega\,\mathrm{d}\Omega} = \frac{q^2\omega^2 N_\beta^2}{16\pi\varepsilon_0 c k_\beta^2} \sum_{n=1}^{\infty} Q_n \left[C_x^2 + C_z^2\theta^2 - 2C_x C_z \theta\cos\phi\right], \tag{5.44}$$

with

$$C_x = \sum_{m=-\infty}^{\infty} \frac{\alpha_\beta}{\gamma_0} J_m(\alpha_z)[J_{n+2m-1}(\alpha_x) + J_{n+2m+1}(\alpha_x)], \tag{5.45}$$

$$C_z = \sum_{m=-\infty}^{\infty} 2J_m(\alpha_z) J_{n+2m}(\alpha_x), \tag{5.46}$$

$$\alpha_x = \frac{n(\omega/\omega_n)(2a_\beta)\gamma_0\theta\cos\phi}{1 + a_\beta^2/2 + \gamma_0^2\theta^2}, \tag{5.47}$$

$$\alpha_z = \frac{n(\omega/\omega_n)(a_\beta^2/4)}{1 + a_\beta^2/2 + \gamma_0^2\theta^2}. \tag{5.48}$$

The resonance function Q_n has the same form as before, and the radiation will be sharply peaked about the harmonic frequencies

$$\omega_n = ck_n = \frac{nck_\beta}{\alpha_0} \simeq \frac{2\gamma_0^2 nck_\beta}{(1 + a_\beta^2/2)\cos\theta + 2\gamma_0^2(1 - \cos\theta)}. \tag{5.49}$$

This resonance function, as we have already seen, describes the harmonic behaviour of the radiation, and we may approximate the associated resonant frequencies, again with the assumption of radiation emitted in a small forward cone angle $\theta^2 \ll 1$, as

$$\omega_n = \frac{nM_0 ck_\beta}{1 + M_0\theta^2/2}, \qquad M_0 = \frac{2\gamma_0^2}{1 + a_\beta^2/2}. \tag{5.50}$$

The intrinsic width of a harmonic about ω_n will be $\Delta\omega_n/\omega_n = 1/(nN_\beta)$, which follows from the definition of Q_n as a sinc function.

5.3.2 The On-Axis Case

For the case of on-axis radiation, $\theta = 0$, there is no contribution from terms containing C_z. In addition, $\alpha_x = 0$ which means all $J_{n+2m\pm1}(\alpha_x)$ terms are zero except $J_0 = 1$, and therefore the infinite sum over m is reduced to only the two terms for which $n + 2m \pm 1 = 0$. This has integer solutions only for odd n and so all even harmonics of the radation vanish. The radiation for the n^{th} odd harmonic is

$$\frac{\mathrm{d}^2 I_n}{\mathrm{d}\omega\,\mathrm{d}\Omega} = \frac{4q^2}{c}\frac{\omega}{\omega_n}\frac{\gamma_0^2 N_\beta^2}{1 + a_\beta^2/2} Q_n X_n \tag{5.51}$$

where X_n is the harmonic amplitude function and contains the Bessel function terms

$$X_n = n\alpha\omega\left[J_{(n-1)/2}(\alpha\omega) + J_{(n+1)/2}(\alpha\omega)\right]^2, \tag{5.52}$$

$$\alpha = \frac{a_\beta^2}{8\gamma_0^2 c k_\beta}. \tag{5.53}$$

Note that these formulae are valid only for odd n.

5.3.3 Few Cycle Radiation

As we already touched upon previously, calculation of the radiation spectrum for an electron that performs only a small number of cycles, $N_\beta \sim 1$, is complicated by the large width of the windowing function. However, we are particularly interested in the results for the single cycle case as they may be used as building blocks for the piecewise description of the radiation from an electron undergoing betatron acceleration.

This work moves beyond the many-cycle description of Esarey *et al.* to consider the few cycle case with non-negligible contribution from the terms where $n \neq'$. Examining again the role of the resonance function (5.35) in the calculation of the intensity (5.28) and (5.29), the magnitude of the interference between any two terms n, n' is given by the product of the resonance functions $Q_n(k) \cdot Q_{n'}(k)$.

Figure 5.1 shows magnitude of the interference between cross terms with adjacent n, n' relative to the maximum amplitude N_β^2 of the diagonal terms $(n = n')$. This shows that the effect of the cross terms can indeed be significant, as much as 20% of the diagonal term contribution in the case of a single betatron cycle. A potential strategy to achieve this along with analytic estimation of the radiation spectrum in the case with acceleration, is outlined in appendix D. Investigation of this possibility is intended to form the basis of future work.

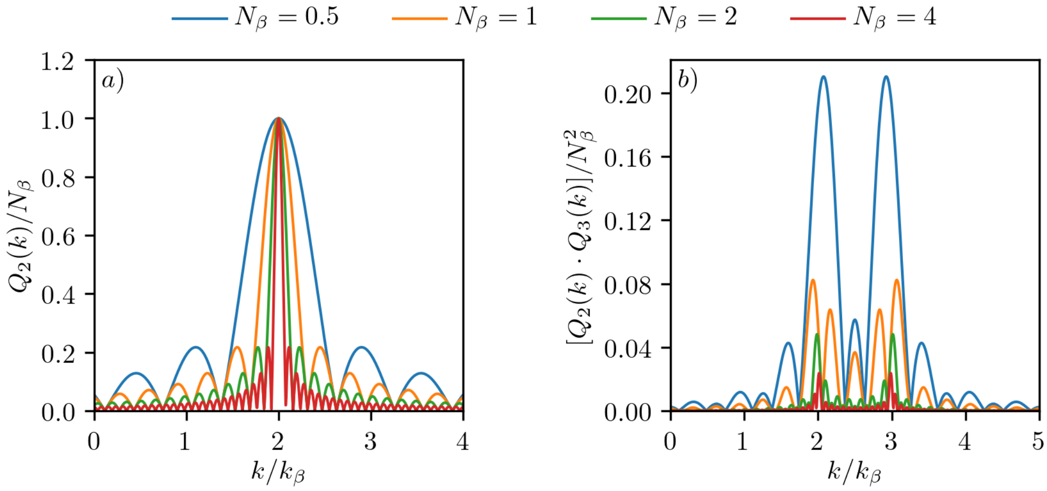

Figure 5.1: Resonance function Q_n behaviour with increasing number of cycles. The resonance function for $n = 2$ is shown in (a), and interference between terms with adjacent $n, n' = 2, 3$ in (b), with increasing number of betatron cycles N_β. The magnitude of the interference is expressed relative to the maximum amplitude of the diagonal $(n = n')$ terms in the calculation of the spectral intensity.

5.4 Radiation Properties

The frequency spectrum of the emitted radiation has a complicated dependence on the parameters a_β, k_β, N_β, ω_n and γ_0. However, noting that these parameters are themselves interrelated, we may simplify matters somewhat. Since

$$k_\beta = \frac{k_p}{\sqrt{2\gamma_0}}, \tag{5.54}$$

$$a_\beta = \gamma_0 k_\beta r_\beta = \sqrt{2\gamma_0 r_\beta^2 k_p^2}, \tag{5.55}$$

$$\omega_n = n M_0 c k_\beta = \frac{n c k_p \sqrt{2\gamma_0}}{1 + a_\beta^2/2}, \tag{5.56}$$

we see that for a fixed plasma wavenumber, k_p, and electron energy, γ_0, the frequency spectrum of the emitted radiation depends only upon the oscillation number N_β and amplitude r_β. Typically, the oscillation amplitude is expressed through the betatron parameter a_β. This rescales the amplitude with respect to the parameters k_p, γ_0 such that a value of $a_\beta = 1$ delineates the boundary between two distinct radiation regimes as we shall see below.

5.4.1 Effects of Varying a_β

Looking at the dependence of the radiation on a_β, we see that the betatron strength parameter affects both the resonant frequency of the radiation and the relative amplitude of the harmonics. As we have seen, the radiation spectrum is given by the interference of multiple cycles of synchrotron-like radiation, which sums constructively about the fundamental resonant frequency and its harmonics. This is described in the model by the sinc^2 windowing function, which samples the radiation only at these frequencies. For $a_\beta < 1$, the radiation is concentrated at the fundamental frequency, whereas for $a_\beta \gtrsim 1$ the fundamental frequency is reduced compared to the case of small a_β, and on-axis radiation is emitted in a series of harmonics with a synchrotron-like amplitude envelope.

Figure 5.2 demonstrates how the fundamental resonant frequency $\omega_1 = 2\gamma_0^2 c k_\beta/(1+a_\beta^2/2)$ varies with a_β: for small $a_\beta << 1$, the denominator term is approximately 1, and so small changes in a_β do not change the resonant frequency of the radiation, affecting only the radiation intensity through the factor α in the harmonic amplitude function. For $a_\beta \gtrsim 1$ this ceases to be the case as the a_β^2 term in the

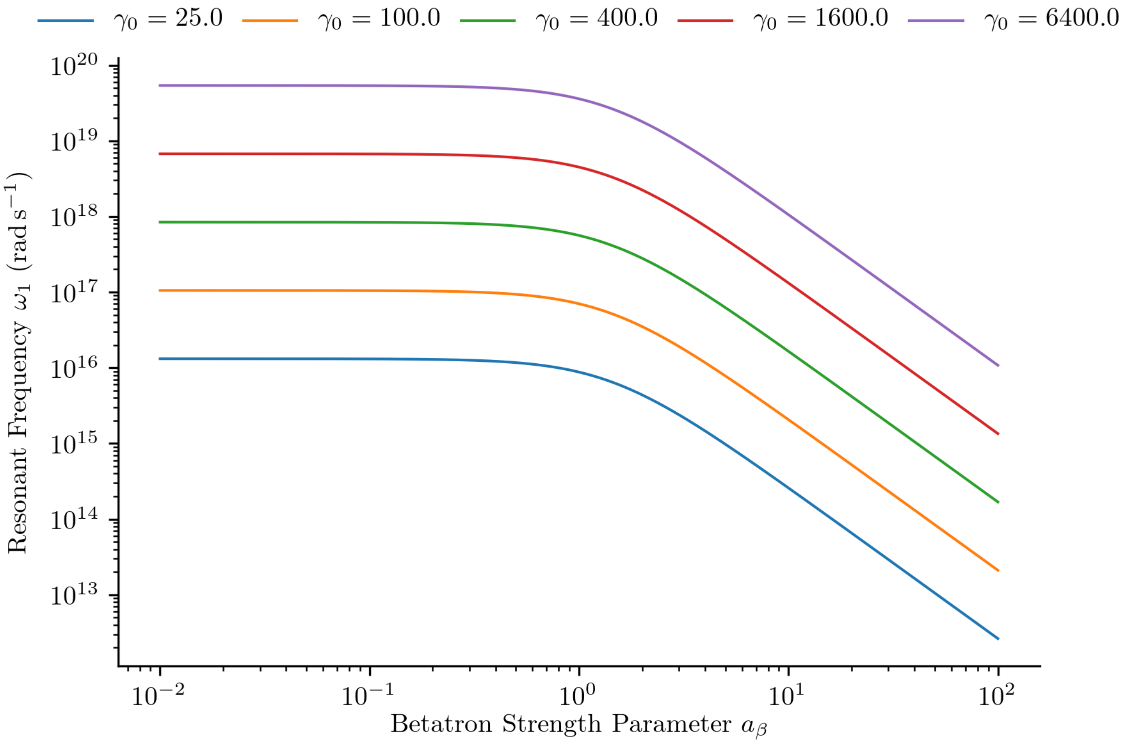

Figure 5.2: Fundamental on-axis resonant frequency ω_1 of ion-channel radiation for an electron with $\gamma_0 \in [25, 6400]$ and strength parameter range $a_\beta \in [0.01, 100]$, for plasma wavenumber $k_p = 2.48 \times 10^5\,\mathrm{m}^{-1}$ which corresponds to a plasma with 0.1% of the critical density for a laser with wavelength 800 nm.

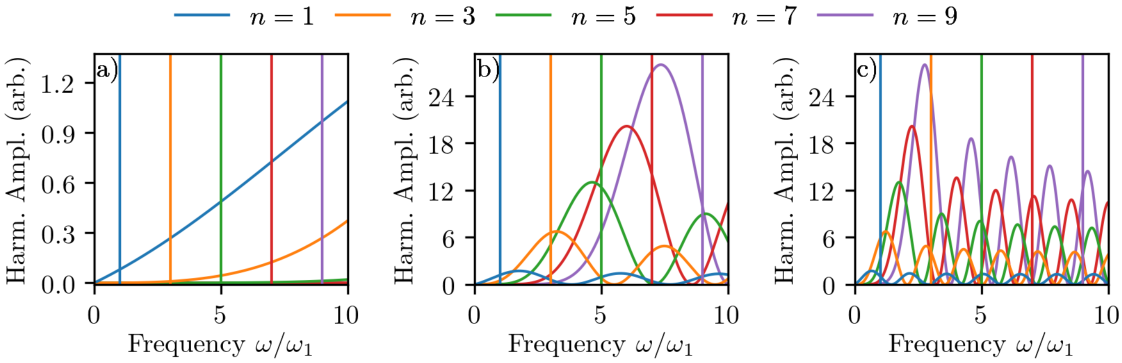

Figure 5.3: Harmonic amplitude function for the first 5 non-zero harmonics of the electron radiation shown in figure 5.4 with a) $a_\beta = 0.25$, b) $a_\beta = 1.0$, c) $a_\beta = 4.0$.

denominator causes the resonant frequency to be reduced. Physically this is a relativistic effect whereby the effective oscillation frequency of the electron is reduced by the additional transverse momentum compared to the $a_\beta \ll 1$ case. In addition to this, the factor α also changes with a_β, which has the effect of moving the peak

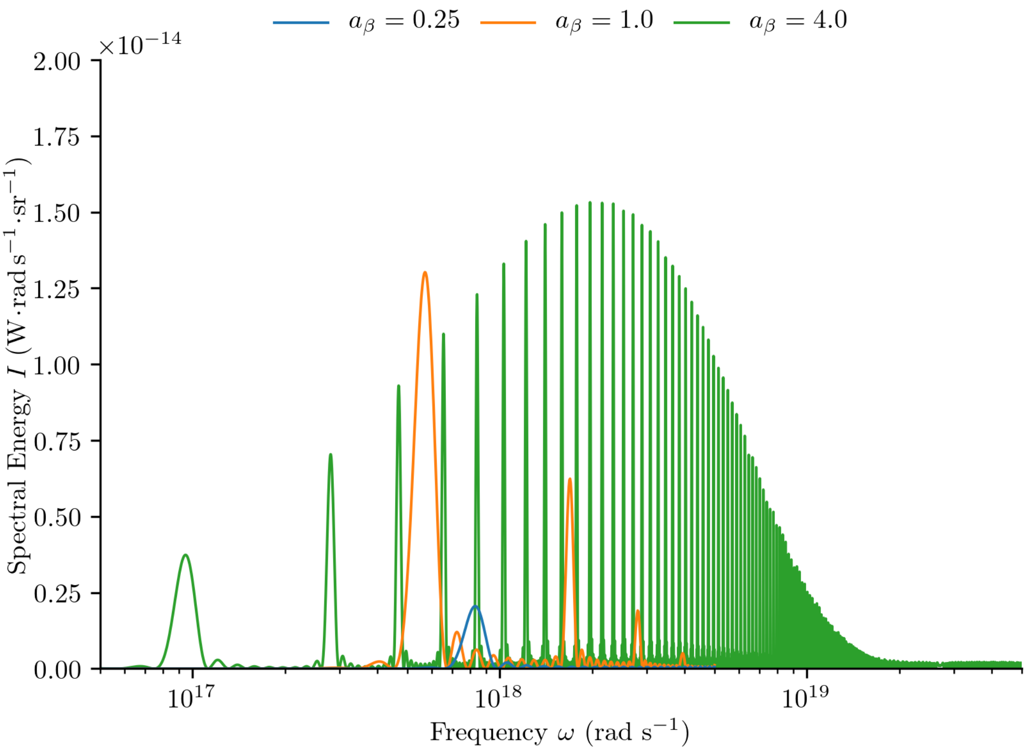

Figure 5.4: Spectral energy emission on axis by an electron with $\gamma_0 = 400$, performing ion-channel motion with $N_\beta = 5$ and $k_p = 2.48 \times 10^5\,\mathrm{m}^{-1}$, with $a_\beta \in [0.25, 4.0]$.

locations of the amplitude functions to smaller values of the frequency. For $a_\beta \ll 1$ the value of the harmonic amplitude function for $n > 1$ is negligible compared to the fundamental. For $a_\beta \gtrsim 1$, the peaks of some higher harmonic amplitude functions occur at frequencies close to their respective resonance frequencies, and so contribute accordingly. This behaviour is demonstrated in figure 5.3: the harmonic amplitude function for the on-axis case (5.52) is plotted for the first 5 harmonics, with vertical lines indicating the resonant frequency associated with that harmonic. We see that for $a_\beta < 1$, only the fundamental, $n = 1$, contributes non-negligbly to the total radiation spectrum. For $a_\beta \gtrsim 1$, the resonance frequencies are reduced by a factor $1/(1+a_\beta^2/2)$ due to the effects of relativistic transverse motion, however the amplitude functions for the higher harmonic numbers begin to contribute strongly, producing a series of harmonics. The resultant spectral energy distribution is shown in figure 5.4, demonstrating the growth in number of harmonics and detuning effect of increasing a_β. The critical harmonic number n_c, corresponding to the harmonic with greatest intensity, is given by,[121]

$$n_c = \frac{3}{8} a_\beta^3. \tag{5.57}$$

5.4.2 Effects of Varying N_β

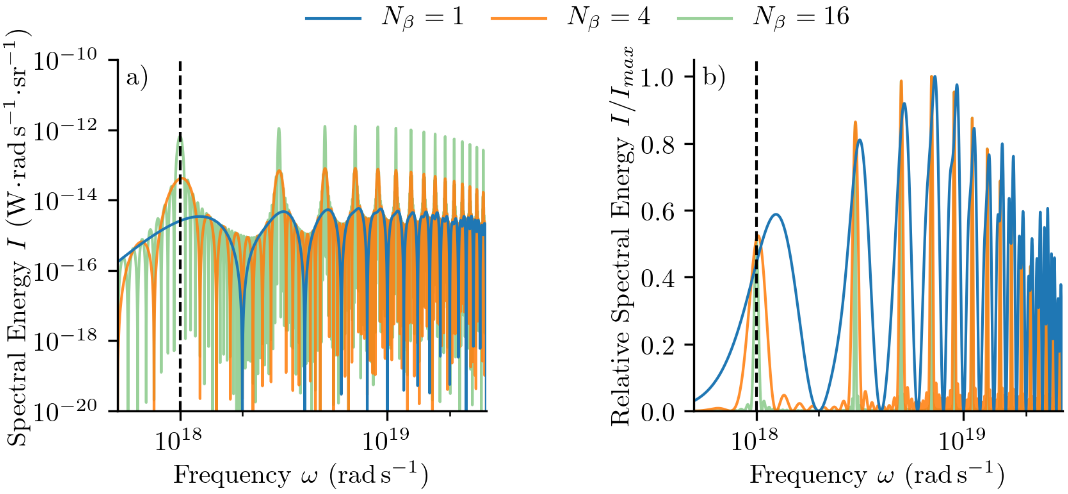

Figure 5.5: Spectral energy emitted by an electron oscillating in an ion channel over a varying number of cycles N_β. The electron properties are $a_\beta = 2.5$ and $\gamma_0 \simeq 1153$ such that the fundamental resonant frequency $\omega_1 = 1 \times 10^{18}\,\mathrm{rad\,s^{-1}}$. In a) the spectral energy is unnormalised to demonstrate the scaling of the spectral energy with the number of oscillations, while b) shows each spectrum normalised relative to its own maximum, allowing the structure of the harmonics to be more clearly seen.

As we have seen in section 5.3.3 the number of oscillations over which the electron radiates will affect both the intensity and the spectrum of the radiation. We may build a qualitative physical picture of the process occurring here by considering the interference of the emitted radiation:

We already know, from the discussion of the Liénard-Wiechert potential in section 2.7.3, that the radiation intensity is proportional to the square of the acceleration. Therefore we expect that the majority of the energy will be emitted due to the short trajectory segment when the electron is furthest from the axis and accelerating most rapidly. This may be approximated as an arc segment and so we expect that the radiation will have a broad synchrotron-like spectrum. After propagation over a further cycle, the electron will emit another burst of synchrotron-like radiation, which will interfere with the previously emitted radiation. This will give constructive interference for multiples of the resonant frequency ω_n, meaning the field strength at these frequencies scales linearly with the number of cycles. The resonant frequency reduces off axis due to the increased propagation distance of the radiation relative to the electron, which increases the wavelength at which contributions will be in phase. Away from the resonance frequencies the field strength will drop rapidly as the contributions from subsequent cycles arrive out of phase. These interference effects give rise to the sinc-like behaviour of the radiation about the resonant frequencies. This behaviour is illustrated in Figure 5.5, which shows the spectral energy emission by an electron performing 1, 4 or 16 oscillation cycles. In figure 5.5(a) the spectral energy is plotted unnormalized, and shows clearly how the spectral energy at the resonant frequencies grows with N_β^2. In figure 5.5(b) each spectrum is plotted normalized to its own maximum spectral energy. This more clearly shows the effects of destructive interference away from the resonant frequencies as N_β becomes large. This rapidly reduces the width of the harmonics, which become delta function like, and the radiation spectrum takes on a “comb-like” structure of sharply defined harmonics.

For emission of radiation over a single cycle it is interesting to note that peaks of the radiation do not coincide exactly with the resonant frequencies. This is because the peak harmonic intensity occurs where the product of the windowing function and the Bessel function term is largest. This can have the effect of shifting the peak intensity away from the resonant frequency for small N_β. This increase in windowing function width is due to the fact that there is no interference between successive cycles, and so destructive interference does not occur to reduce the contributions at these frequencies. In addition to this, the effect of the cross terms

$n \neq n'$ in the radiation calculation (5.30) and (5.31), becomes important here, as discussed in section 5.3.3. In order to correctly calculate the radiation in this case it is therefore necessary to either calculate numerically, or to calculate these cross term effects such as by the method suggested in appendix D.

5.4.3 Angular Extents of Radiation

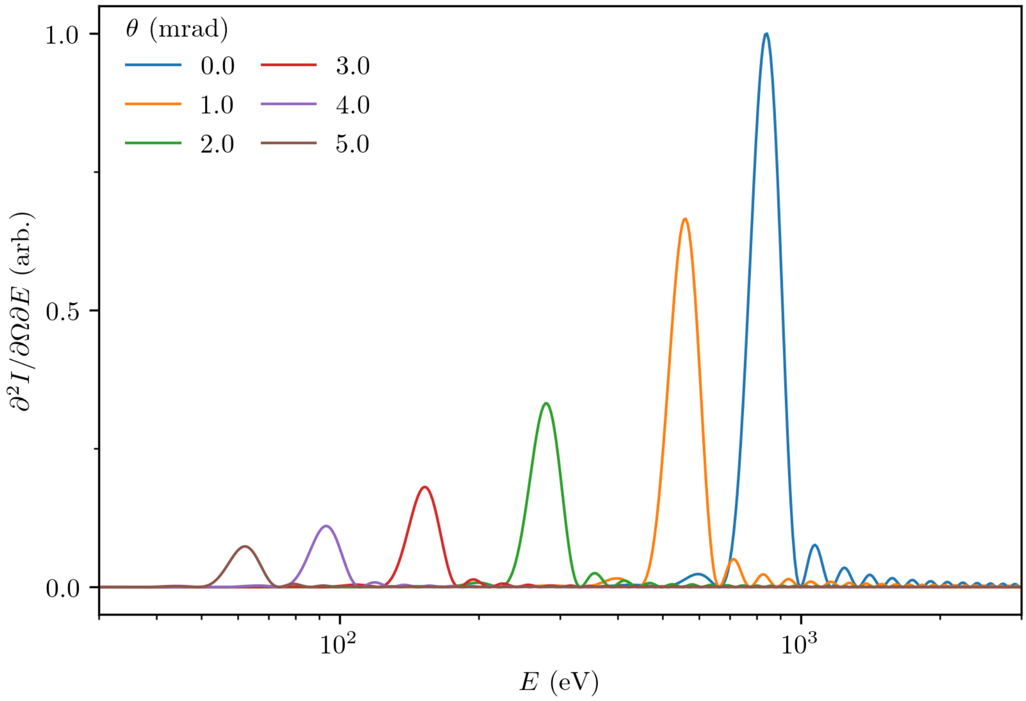

Figure 5.6: Variation of spectral intensity with angle of emission for a single electron performing ion-channel motion. The motion parameters were $\gamma_0 = 1000$, $a_\beta = 0.01$ and $N_\beta = 5$ with the viewing angle θ in the plane of oscillation.

Returning to the expression for the resonant frequency of the radiation, (5.50), we see that the dependence upon the frequency varies as $1/(1 + M_0\theta^2/2)$, with $M_0 \propto \gamma^2$. To achieve emission of XUV and X-ray frequencies on axis requires electron energies $\gamma > 100$, and therefore the emission at these frequencies is confined to a cone with opening half-angle $\theta^2 \lesssim 1/\gamma^2$, corresponding to just a few mrad for $\gamma \sim 1000$. This rapid decrease in resonant frequency is accompanied by a reduction in the radiation intensity as the resonant frequency moves away from the emission range described by the Bessel terms. This behaviour is illustrated in figure 5.6, which shows the spectral intensity of the emission by an electron performing ion-channel motion with $\gamma_0 = 1000$ and $a_\beta = 0.01$ and $N_\beta = 5$ over a small range of viewing angles θ. The detuning effect is rapid, with the resonant frequency and intensity of the radiation decreasing by an order of magnitude. As the majority of the radiation is emitted in this small on-axis cone, the investigations in this chapter focus on the effects of bunch properties on the on-axis radiation.

5.5 The Betatron Radiation Spectrum

As discussed in chapter 3, the typical case for an electron in an ion-cavity includes strong longitudinal acceleration. While such an electron will radiate strongly, the constantly changing electron energy causes the radiation spectrum to be very different to that of an electron in ion-channel motion. This is due to the self-interference of the emitted radiation, which in the betatron case occurs at a different wavelength each half period as the electron accelerates.

Figure 5.7 shows the spatial (z vs. x) and energy (z vs. γ_e) trajectories, and the on-axis spectral emission calculated numerically for a single electron performing betatron motion in an idealised bubble for increasing betatron strength parameter at dephasing $a_\beta = 0.1$ (figures 5.7(a) and 5.7(b)), $a_\beta = 1.0$ (figures 5.7(c) and 5.7(d)), $a_\beta = 10.0$ (figures 5.7(e) and 5.7(f)). The radiation here is expressed as a function of photon energy $E = \hbar\omega$ as this is the more commonly used unit for discussing XUV and X–ray radiation. The electron begins at the bubble radius with $\gamma_e = \gamma_{ph}$, and performs $n \sim \gamma_{ph}$ oscillations up to dephasing. As has already been described, the emission occurs around the extrema of the spatial trajectory where the transverse acceleration is largest. The peak emission frequency for each extremum is indicated by the vertical dashed lines, which increases with the overall electron energy and decreases with betatron strength parameter. In

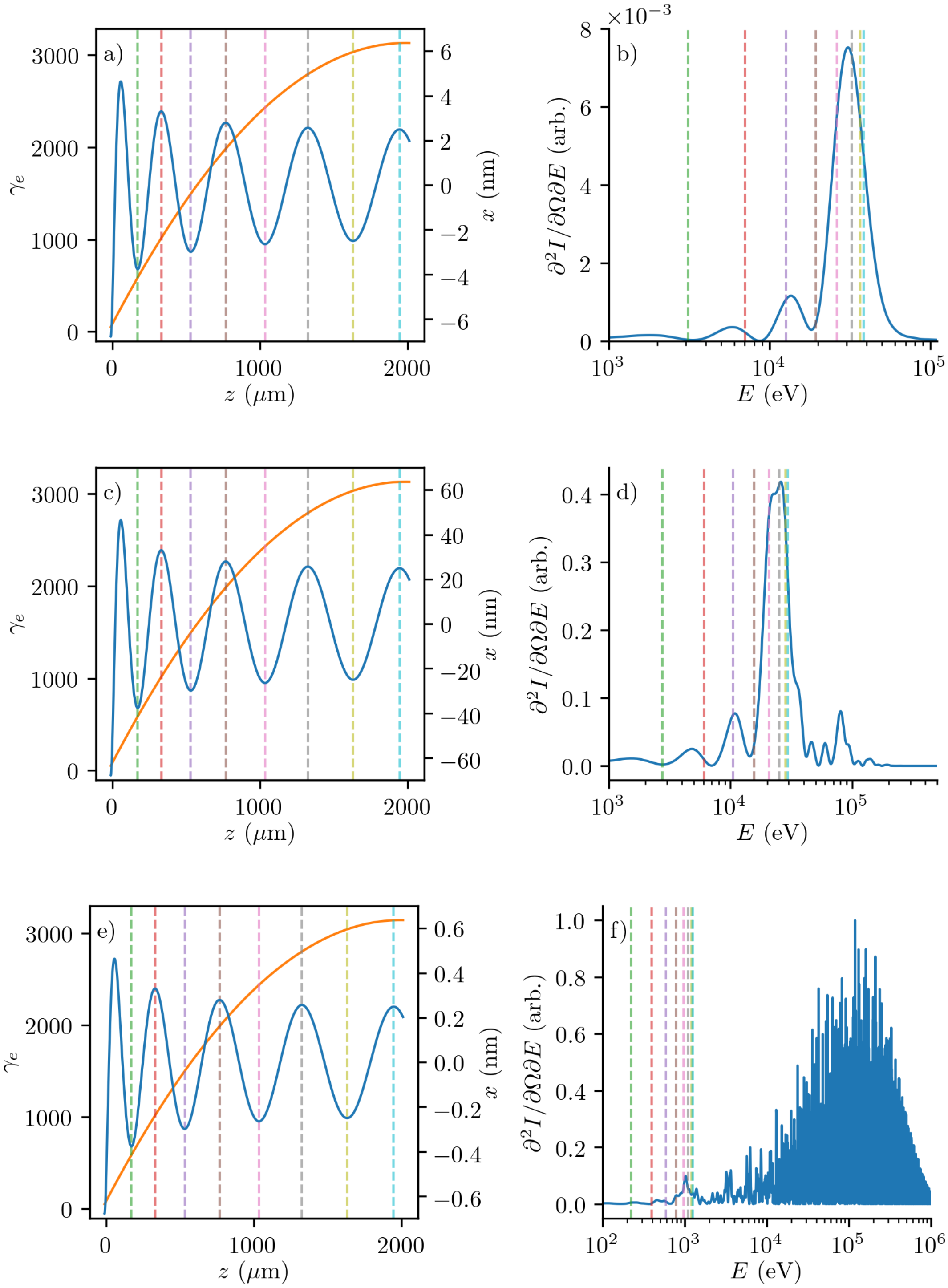

Figure 5.7: Trajectory and energy (a, c, e) and on-axis spectral emission (b, d, f) for a single electron performing betatron motion in an idealised bubble with varying oscillation amplitude. In all cases plasma density fraction $\eta^2 = 0.01$ relative to the critical density for an 800 nm laser driver. The oscillation amplitudes were chosen such that the value of betatron strength parameter a_β at dephasing was $a_\beta = 0.1$ (a, b), $a_\beta = 1.0$ (c, d) and $a_\beta = 10$ (e, f), illustrating the behaviour for both the fundamental and high harmonic emission regimes, as well as the transition region between the two.

addition, unlike the ion-channel laser, where the electron propagation distance between subsequent extrema is constant, the acceleration in the betatron case means the propagation distance between extrema varies along with the emission frequency. The combination of these effects leads to a broader band radiation spectrum with multiple peaks than for the acceleration-free case. In all cases the spectrum is dominated by the contribution from later cycles where the electron γ_0 is large, because the emission intensity scales with γ^2 (as can be seen in (5.51)). Thus to achieve peak radiation intensity the electron bunch must be allowed to propagate all the way to, or even past the dephasing point. For the $a_\beta = 0.1$ case in (figures 5.7(a) and 5.7(b)), as for the ion-channel case, the radiation from each extremum is broadband about the fundamental frequency. The interference between these produces an overall broadband radiation spectrum centered near the emission frequency at dephasing. The $a_\beta = 1.0$ (figures 5.7(c) and 5.7(d)) case is in the transition region between the fundamental and high-harmonic emission regimes. The overall emission is much stronger than the low a_β case, and radiation is emitted at frequencies above the fundamental, but there is still considerable emission at the fundamental frequencies, which are only minimally detuned. Finally, for the case where $a_\beta = 10.0$ (figures 5.7(e) and 5.7(f)), the fundamental emission frequencies are strongly detuned and there is strong emission over a broad range of higher harmonics. The effects of acceleration are less obvious here as the radiation covers a similarly broad bandwidth range of many hundreds of harmonics as for the acceleration-free case with large a_β.

5.6 Numerical Calculation of the Betatron Radiation

Calculating the radiation spectrum requires using the numerical algorithm for radiation calculation described in section 2.8, along with a numerical solver for the electron motion in the ideal bubble. This approach can capture the higher order effects neglected in the analytic approximations and gives an idea of their importance for the applications of interest in this thesis. Ideally, this trajectory calculation would be performed using full PIC simulation to provide better comparison with experimental results. However, for the large number of particles and the high temporal resolution required to correctly resolve the radiation spectrum this is extremely computationally expensive, especially as the simulation needs to be run for a large propagation distance because the majority of the radiation is emitted around the dephasing point where γ is largest. It was therefore necessary to write a numerical integrator for the full equations of motion in the idealised bubble (3.18) to (3.20). The resulting code, described in appendix C, is called Bubblecalc and makes use of the high quality numerical integrators available in the GNU Scientific Library.[49] This code produces high accuracy results in seconds, compared with the thousands of hours of CPU time required to perform high resolution PIC simulations.

Using this solver it is possible to run a lower resolution PIC simulation up to the point of injection, to determine the phase space distribution of the injected bunch. The evolution of a bunch with these phase space parameters may then be calculated using the ideal bubble model.

Alternatively, as is done in this thesis, it is possible to generate bunches with specific characteristics that allow the systematic investigation of the radiation behaviour with respect to changes in bunch and bubble parameters.

5.7 Multiple Particle Effects

The effect of multiple electrons on the total radiation spectrum was touched upon briefly in section 2.7.5 where the contribution to the radiation from multiple electrons with trajectories differing only by a phase factor was considered. This was

---

[49] M. Galassi et al. *GNU Scientific Library*, GNU Software Foundation,

found to modify the single electron radiation by a frequency dependent prefactor

$$F = \left| \sum_{n}^{N} \mathrm{e}^{i\phi_n} \right|^2 , \tag{5.58}$$

where $\phi_n = \omega \Delta t_n + \bar{k} \cdot \bar{x}_n$ is the phase of the n^{th} electron with positional offset x_n and time delay Δt_n relative to a reference trajectory for which the radiation spectrum is calculated.

If we consider the behaviour of just a pair of electrons, separated by a distance δt and with otherwise identical trajectories, then the frequency dependent enhancement of the radiation will be

$$F = \left| 1 + \mathrm{e}^{i\omega\Delta t} \right|^2 = 4\cos^2\left(\frac{\omega\Delta t}{2}\right) = 4\cos^2\left(\pi\frac{\omega}{\nu}\right) , \tag{5.59}$$

where $\nu = 2\pi/\Delta t$ is the resonant frequency associated with the particle spacing. We see therefore that for harmonics of the resonant frequency $n\nu$, the radiation will be enhanced by a factor of 4 (N^2) because the emissions from the two electrons are in phase. In contrast, for frequencies $(n + 1/2)\nu$ between these harmonics, the radiation emission is in antiphase and so interferes destructively. Adding a third electron δt behind the second will produce an enhancement by $N^2 = 9$ at harmonics of ν. A small contribution appears at the antiphase frequencies due to the uncancelled effect of the third electron at these points, and adding further particles will continue this trend.

So far this only allows us to evaluate the effects for single electrons, or bunches that may be approximated as delta-function like. However, as described in section 2.7.5, we may extend (5.58) to consider a continuous current distribution $J(t)$. This gives

$$F(J) = \left| \int_0^T \mathrm{e}^{i\omega t} J(t)\,\mathrm{d}t \right|^2 , \tag{5.60}$$

which may be used to approximate the radiation spectrum from bunches with finite extent expressed as a time dependent bunch current $J(t)$.

It is important to note that this considers only a phase difference between the electrons, which are assumed to have identical longitudinal and transverse energies γ_0 and a_β. For the case where the bunch has a small spread in a_β and γ_0, the radiation from the bunch may be approximated perturbatively as will be discussed later in this chapter.

5.8 Numerical Calculation of Multiple Particle Effects

In chapter 4 the injected bunch charge for the LWFA was found to be $\sim 100s\,\mathrm{pC}$ equivalent to $\sim 10^8 - 10^9$ electrons. As calculation of a single trajectory takes several seconds on the available hardware, this would require millions of cpu hours for a single run. Therefore, in order to make numerical evaluation of the radiation tractable, a smaller number of pseudoparticles representing the electrons must be used.

The coherent emission behaviour of multiple electrons dependens upon the phase difference between electrons, which is in turn depends upon the details of the motion of each electron and also on the total number electrons in the bunch. This has particular implications for the case of numerical simulation and radiation calculation as it means that the use of pseudoparticles representing multiple electrons will, unlike the case of PIC simulation of a plasma, fundamentally alter the result. This is because a pseudoparticle represents N electrons moving perfectly in phase, with resulting radiation multiplied by a factor N^2 relative to that of a single electron, thus overestimating the coherence as compared with N electrons individually calculated with nonzero relative phase differences. In the case that there are M pseudoparticles representing a total N electrons, then assuming random distribution of those pseudoparticles the coherent ehancement will be reduced to a factor N^2/M relative to a single electron.

This effect can be mitigated to some extent by ensuring that there is a sufficient pseudoparticle density relative to the wavelength of interest so that the interference behaviour is correctly calculated. That is to say, the results of a multiparticle simulation with pseudoparticles is valid at a given radiation wavelength λ provided that

$$\sigma_p \lambda \gg 1, \tag{5.61}$$

where σ_p is the pseudoparticle line density in the direction of propagation. This approach is still limited, however, and care must be taken, especially when considering electron distributions with large spread in energy or position that sufficient pseudoparticles are used and the complete N-dimensional phase space contains a sufficient pseudoparticle density.

This effect is illustrated in figure 5.8, which shows the numerically computed radiation due to a monoenergetic electron bunch of length 10 nm performing betatron motion. The simulation was performed with a constant bunch charge 10 pC evenly distributed between $n_p \in [1, 100000]$ pseudoparticles in a uniform random distribution of length 10 nm. The overestimation of coherent effects can clearly be seen, with the radiation intensity at short wavelengths decreasing by a factor $1/n_p$ as expected. The dashed lines indicate the wavelength for which $\sigma_p \lambda = 1000$, which is approximately the point at which the behaviour of a simulation begins to grossly diverge from higher resolution simulations. The key result here is that extreme care must be taken when using numerical simulation of individual particles to ensure that the spectral features of interest are correctly resolved. Indeed, in the case that the electron bunch has a large volume in 6-dimensional phase space, and high energy such that it emits large amounts of radiation at nanometer wavelengths, this can require simulation of all 10^{10} electrons in order to correctly resolve high frequency effects. As has already been discussed, this is unfeasible with the current implementation, and therefore to investigate the effects of finite spreads in spatial and momentum distributions we return to analytic approximations.

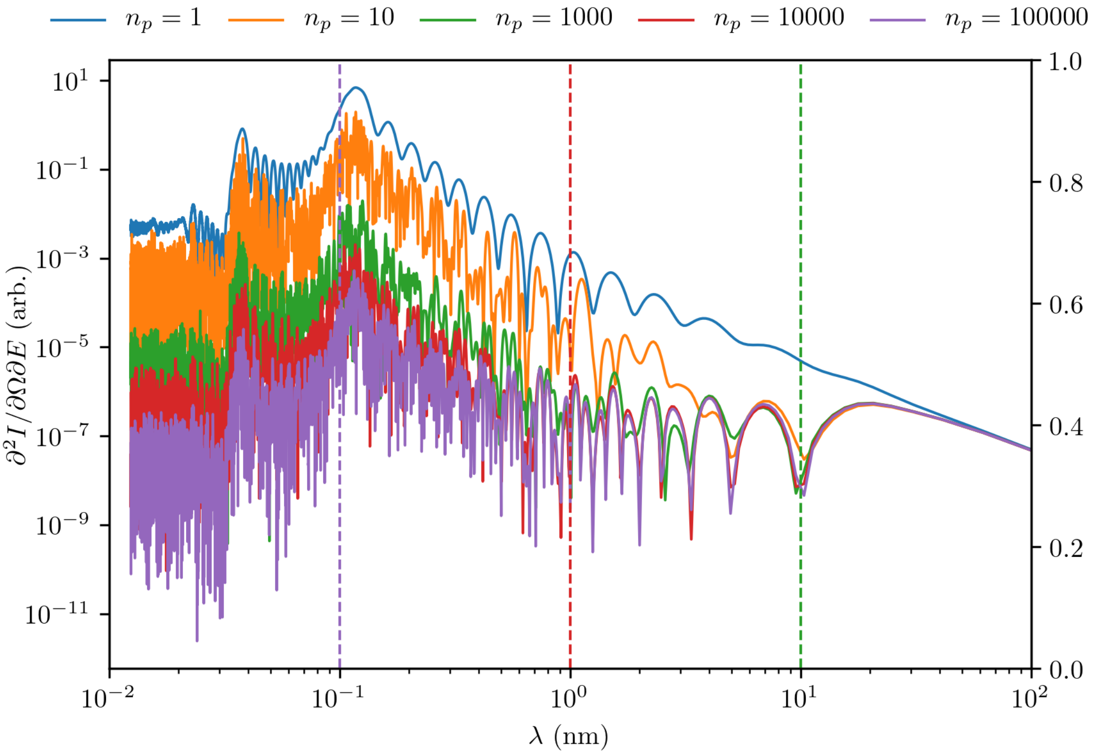

Figure 5.8: Spectral energy emitted by monoenergetic electron bunches performing betatron motion with charge 10 pC represented by a varying number of pseudoparticles $n_p \in [1, 100000]$. The electron trajectories are calculated numerically assuming motion in an ideal bubble with fractional plasma density $\eta^2 = 0.001$ and $\lambda = 800\,\mathrm{nm}$. Transverse oscillation amplitude at injection is $0.1\,\mu\mathrm{m}$, equivalent to betatron strength parameter at dephasing $a_\beta(\tau = 0) = 0.5$.

5.9 Radiation from Constant Current Bunches

A logical starting point for such an analysis is the case for a bunch with a constant current density and varying total length. We have already discussed the results for the two extremes of this case, which recover the single particle case for a charge qN in the limit of a zero-length bunch, and zero resulting radiation in the case of a bunch with length λ_β. We may find the result for a bunch of arbitrary length as follows:

For a bunch with a length $\ell = cT$, and constant current density $J(T) = J_0 =$

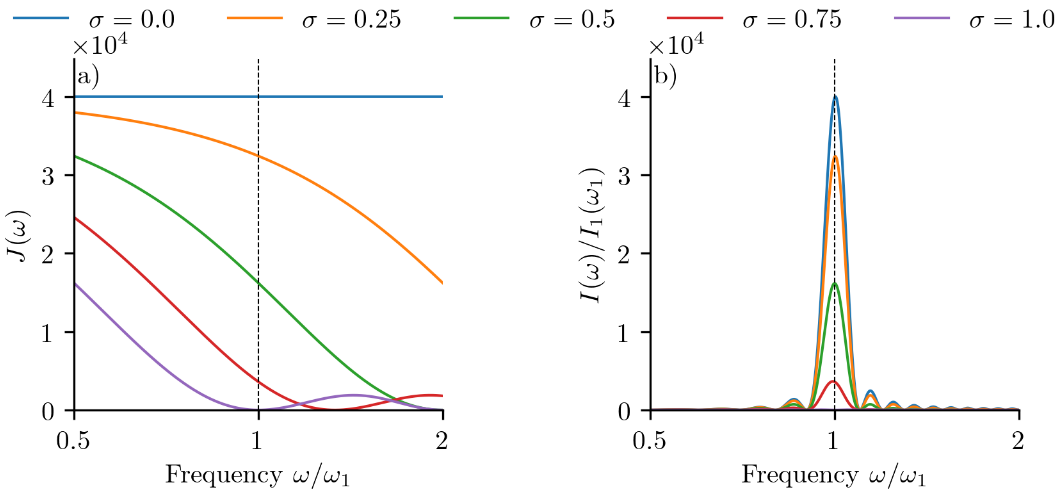

Figure 5.9: Coherent enhancement factor (a) and relative spectral energy (b) emitted by bunches with constant population $N = 200$, and varying length expressed as a fraction $\sigma = 2\pi T/\omega_1$ of the resonant wavelength. For all bunches $N_\beta = 10$, $a_\beta = 0.001$ and γ_0 is chosen such that the resonant frequency of radiation $\omega_1 = 1 \times 10^{18}$ rad s^{-1}. Spectral energies are normalised to the peak spectral energy of single electron emission.

N/T. Using (5.60), we find that

$$F(J) = \left| J_0 \int_0^T \mathrm{e}^{i\omega T} \, \mathrm{d}T \right|^2 = 4 \frac{J_0^2}{\omega^2} \sin^2\left(\frac{\omega T}{2}\right) = N^2 \operatorname{sinc}^2\left(\frac{\omega T}{2}\right), \qquad (5.62)$$

and taking the limit $T \to 0$ for N electrons in perfect phase we recover the expected result that the total radiation will the single electron result multiplied by a factor N^2. Figure 5.9(a) shows the frequency dependent coherent enhancement for bunches with constant population N and varying length expressed as a fraction $\sigma = 2\pi T/\omega_1$ of the resonant wavelength. This applies equally to both the ion-channel and betatron radiation cases, however, for the betatron case the acceleration of the bunch will cause the bunch length to evolve. The on-axis radiation emission for electron bunches performing ion-channel motion with $a_\beta \ll 1$ is shown in figure 5.9(b). This shows that as the bunch length increases the coherent enhancement of the radiation is rapidly reduced and in the extreme case of a bunch with length equal to the resonant wavelength ($\sigma = 1$), each radiating electron has a partner radiating in antiphase, and the sum of the radiation is zero.

This same effect is shown for the case with acceleration in figure 5.10. The coherence effects are separable from the single-particle radiation calculation, the latter being calculated numerically and combined with the analytic result for multi-particle interference. This is necessary as the total number of particles required for a well resolved fully numerical simulation is prohibitively large. In this case bunch lengths and hence enhancement peaks occur at 1, 10 and 100 nm, with the delta-function bunch ($cT = 0$) behaviour provided for reference. Since in this case the cutoff frequencies occur at much longer wavelengths than the peak of the betatron emission, the radiation spectrum is not drastically altered, but instead the total radiated energy is vastly reduced.

This is an important result, which demonstrates that when seeking coherent emission from an electron bunch there is no advantage in having a bunch with a length greater than the desired radiation wavelength. Only the fraction of the bunch that is left after all complete periods have cancelled will contribute strongly to the coherent radiation. It is therefore challenging to increase the total energy emitted as increasing bunch charge will increase the spatial spread of the bunch due to space charge effects. In particular, as seen in the results in chapter 4, the bunch charge in the LWFA is typically a function of the total bunch length. Therefore, to maximise the radiation intensity whilst retaining tuneability a more complex bunch structure must be found which allows efficient coherent radiation at the desired wavelength.

5.10 Improving Monochromaticity and Coherence with Multiple Bunches

To improve the quality of the LWFA as a radiation source it is desirable to reduce the bandwidth and increase the coherence of the radiation emitted due to betatron

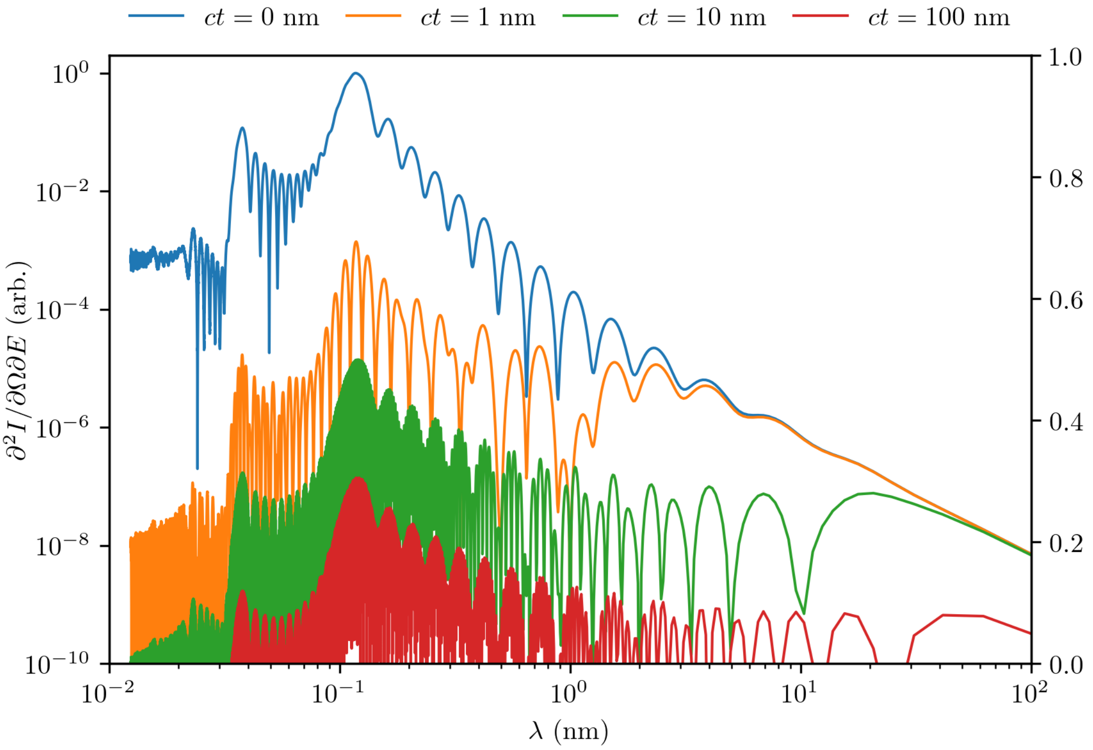

Figure 5.10: Spectral energy emitted by monoenergetic electron bunches with length $cT \in [0, 100]$ nm performing betatron motion with charge 10 pC with constant current $J = N/t$. The electron trajectory is calculated numerically assuming motion in an ideal bubble with fractional plasma density $\eta^2 = 0.001$ and $\lambda = 800$ nm. Transverse oscillation amplitude at injection is 0.1 μm, equivalent to betatron strength parameter at dephasing $a_\beta(\tau = 0) = 0.5$. The coherence effects are calculated analytically as described in the main text.

motion, particularly for the case that includes acceleration,[*] where the incoherent radiation emission is broadband. Since coherent radiation requires the coherent interference of radiation from multiple emission events a potential analogue to a single electron bunch performing multiple oscillations is a train of multiple electrons bunches each performing a single oscillation and separated by a regular spacing. We can model this as a single long electron bunch for which the current is modulated by a regularly oscillating function. We therefore expect coherent enhancement of the radiation at the wavelength consistent with the bunch spacing.

---

[*] For electrons undergoing acceleration N_β has an effective value of 1 for the purposes of the radiation model we have derived so far, as for each oscillation the electron energy differs.

As described in section 2.7.5 the interference from multiple electrons can be found by summing the integrals for the motion of each electron calculated individually prior to taking the norm, preserving the phase information. The total spectral energy is then found by taking the norm of the sum over all electron contributions.

5.10.1 Sinusoidally Modulated Current Density

While the simplest initial case to consider is that of a series of δ-function-like bunches with constant spacing, such a picture is unphysical. Therefore we instead consider the case of a sinusoidally modulated current $J = J_0 \sin^2(\nu t/2)$ with peak current J_0, modulation wavelength $\lambda = 2\pi c/\nu$ and length L. This simulates a more realistic bunch current while also being compactly expressible for clarity of calculation. The coherent enhancement factor due to such a bunch train is

$$\begin{aligned} F(J) =& \left| J_0 \int_0^T \mathrm{e}^{i\omega t} \sin^2(\nu t/2)\,\mathrm{d}t \right|^2 = \left| J_0 \int_0^T \mathrm{e}^{i\omega t} \left(\frac{1}{2} - \frac{1}{2}\cos(\nu t) \right) \mathrm{d}t \right|^2 , \\ =& \frac{J_0^2}{4\omega^2 (\nu^2 - \omega^2)^2} \left| \, \mathrm{e}^{i\omega T} \left[\nu^2 - \omega^2 + \omega^2 \cos(\nu T) - i\omega\nu \sin(\nu T) \right] - i\nu^2 \right|^2 , \\ =& \frac{J_0^2}{4\omega^2 (\nu^2 - \omega^2)^2} \left(\nu^4 - 2\nu^3\omega \sin(\omega T) \sin(\nu T) + \nu^2\omega^2 \sin^2(\nu T) \right. \\ & \left. - 2\nu^2 \cos(\omega T)[\nu^2 - \omega^2 + \omega^2 \cos(\omega T)] + [\nu^2 - \omega^2 + \omega^2 \cos(\omega T)]^2 \right) , \end{aligned} \tag{5.63}$$

where $T = L/c$ is the duration of the electron bunch. This shows the expected presence of a peak at $\omega = \nu$. In general, we expect that a sinusoidally modulated bunch will begin and end smoothly, and so the bunch current profile will be comprised of a complete number of cycles $\nu T = 2n\pi$. In this case, the expression for the prefactor can be simplified to yield

$$F = \frac{J_0^2 \nu^4 \sin^2(n\pi\omega/\nu)}{\omega^2 (\nu^2 - \omega^2)^2} = \frac{N^2 \operatorname{sinc}^2(n\pi\omega/\nu)}{(1 - \omega^2/\nu^2)^2}. \tag{5.64}$$

In the second form of the relationship above the peak bunch current is replaced by the total bunch charge. In general these are related by

$$N = J_0 \int_0^T \sin^2(\nu t/2)\,\mathrm{d}t = \frac{J_0}{2}\left(T - \frac{\sin(\nu T)}{\nu}\right), \tag{5.65}$$

which, for the case of a complete number of bunch current cycles, simplifies to

$$J_0 = \frac{2N}{T} = \frac{N\nu}{n\pi}, \tag{5.66}$$

where the peak bunch current is twice the cycle-average bunch current for a $\sin^2$ distribution.

The expression (5.64) has an indeterminate form at the point $\omega = \nu$. Applying L'Hôpital's rule to determine the behaviour at this point yields

$$\lim_{\omega\to\nu} F(J) = \left[\frac{\frac{\mathrm{d}}{\mathrm{d}\omega} N\sin(n\pi\omega/\nu)}{\frac{\mathrm{d}}{\mathrm{d}\omega} n\pi\omega/\nu(1-\omega^2/\nu^2)}\right]^2 = \frac{N^2}{4}, \tag{5.67}$$

which demonstrates the expected coherent enhancement scaling with N^2 at the bunching wavelength. The reduction by a factor of 4 is due to the fact that the each bunch in the train has finite length and therefore not all radiation is emitted in perfect phase.

Figure 5.11 shows the enhancement factor and spectral energy emission for a sinusoidal bunch train where the spacing and hence frequency ν of the current modulation has been chosen to coincide with the peak of the emission spectrum for the ion-channel motion of the electrons. The effect of increasing the number of bunches in the bunch train is to reduce the bandwidth of the emitted radiation to a small region about the bunching frequency ν. This may be seen in figure 5.11(a) where the coherent enhancement factor $F(J)$ is shown. The peak radiation intensity is independent of N as the coherence at the frequency ν is unaffected by the number of bunches over which the total charge is spread, however, at frequencies away from ν radiation is suppressed by destructive interference.

The effect of a sinusoidal bunch train is also shown for the case of an accelerated electron bunch in figure 5.12. This has the same effect of narrowing the emission bandwidth to a small window around the bunching wavelength, reducing to a nearly monochromatic spike for many bunches. This is very similar to the mechanism by which the free-electron laser produces monochromatic light.[123] A key difference, however, is that in the FEL, the bunching is produced by self-interaction of the electrons with the produced radiation, where in this case a regular structure must be imprinted upon the bunch current by some other means.

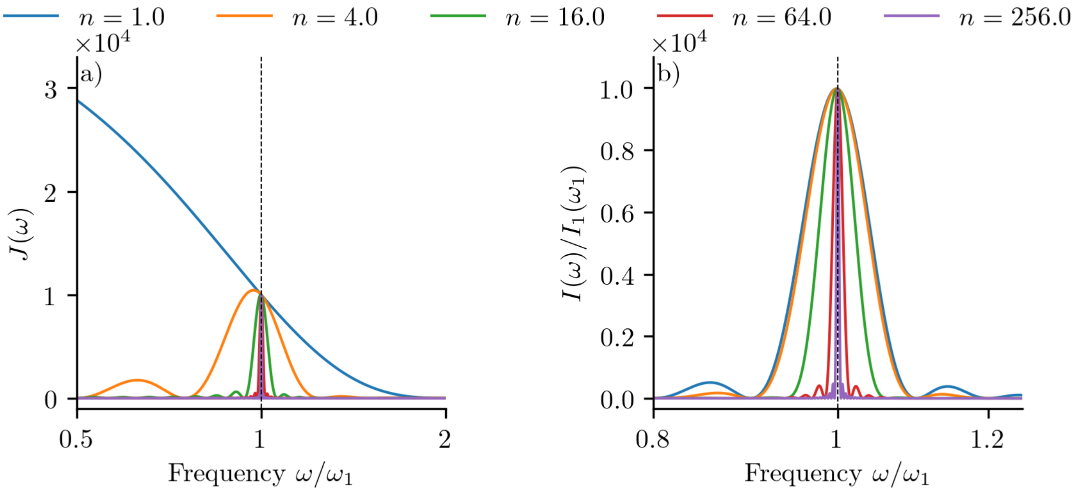

Figure 5.11: Coherent enhancement factor (a) and relative spectral energy (b) emitted by bunch trains performing acceleration-free ion-channel motion with constant total population $N = 200$, smooth, $\sin^2$ current distribution with frequency $\nu = 1 \times 10^{18}\,\mathrm{rad\,s^{-1}}$, and increasing number of bunches N in the train. For all bunches $N_\beta = 10$, $a_\beta = 0.001$ and γ_0 is chosen such that the resonant frequency of radiation $\omega_1 = 1 \times 10^{18}\,\mathrm{rads}^-1$. Spectral energies are normalised to the peak spectral energy of single electron emission.

We find then that a regular bunch structure such as this essentially acts as a "windowing-filter" on the coherent enhancement, localising it to a narrow region around the bunching wavelength. Close to the bunching wavelength the emission intensity is of the order of a perfectly coherent bunch, whilst away from the bunching wavelength emission is strongly suppressed. In all the above cases frequency dependent enhancement of the spectrum is clearly visible, with increasing numbers of bunches causing increased narrowing of the spectrum about the bunching

---

[123] H. P. Freund et al. *Phys. Rev. Spec. Top. Accel Beams* **15**, pp. 4–7, 2012.

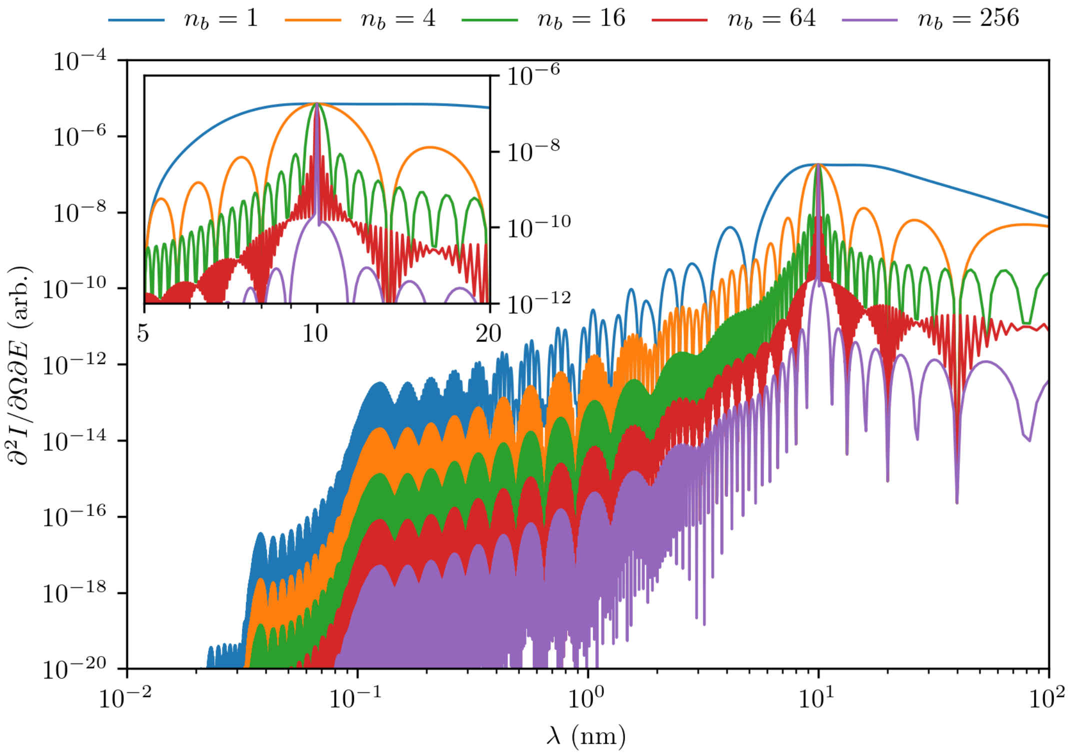

Figure 5.12: Spectral energy emitted by monoenergetic electron bunch performing betatron motion in an ideal wakefield bubble. The bunches have $\sin^2$ modulated current density, with period $\lambda = 10\,\mathrm{nm}$ and total charge 10 pC evenly distributed over an increasing total number of periods N. The electron trajectory is calculated numerically assuming motion in an ideal bubble with fractional plasma density $\eta^2 = 0.001$ and laser wavelength $\lambda_0 = 800\,\mathrm{nm}$. Transverse oscillation amplitude at injection is $0.1\,\mu\mathrm{m}$, equivalent to betatron strength parameter at dephasing $a_\beta(\tau = 0) = 0.5$. The bunch coherences effects are calculated analytically as described in (5.64). Inset shows detail of the intensity around the bunching wavelength.

wavelength. This interest is driven by results from the ALPHA-X beamline at Strathclyde,[124] where observations were made of coherent radiation emission in the XUV range at wavelength of $\sim 10\,\mathrm{nm}$. It is theorised that plasma instabilities within the bubble can imprint some regular longitudinal structure onto an injected electron beam, which will then enhance coherent emission at that wavelength. However, this beam is not a train of clearly spaced bunches, but a single bunch with some additional regular structure. It is likely that the magnitude of such an effect would vary from shot-to-shot, thus it is useful to investigate what

---

[124] L. Reid. "TBC".. PhD. Thesis. 2018.

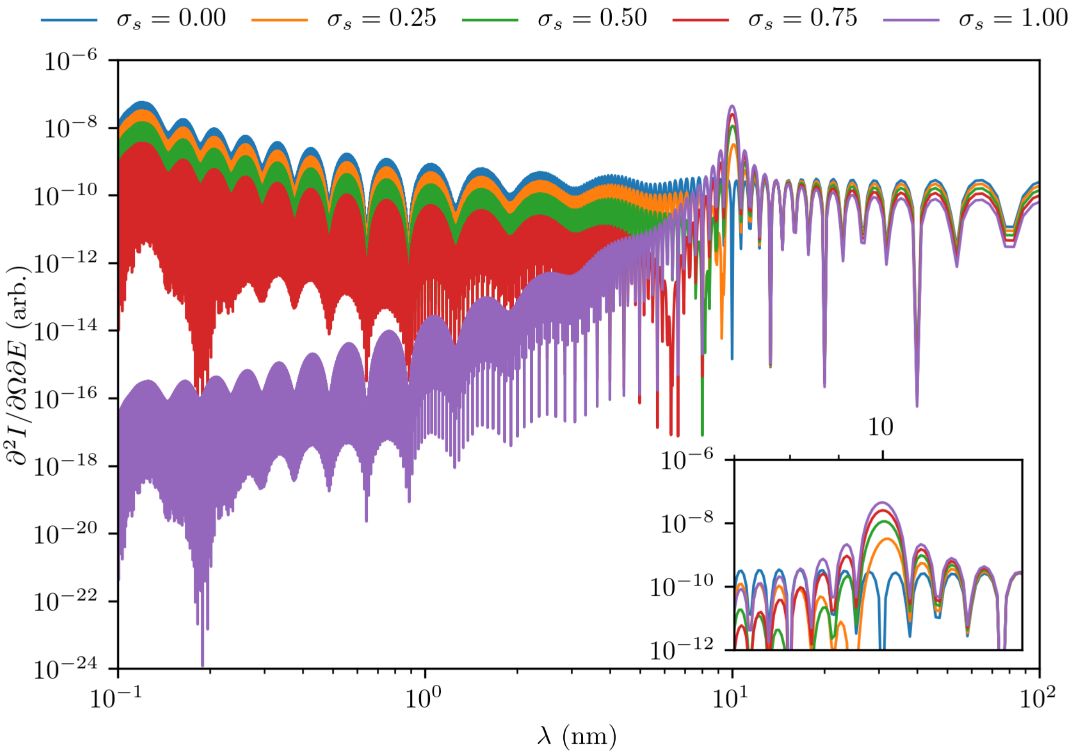

Figure 5.13: Spectral energy emitted by monoenergetic electron bunch with partially modulated current density $\sigma_c J + \sigma_s J \sin^2(\nu t/2)$ $(\sigma_c + \sigma_s = 1)$, charge 10 pC, bunch length 160 nm and bunching wavelength 10 nm. The electron trajectory is calculated numerically assuming motion in an ideal bubble with fractional plasma density $\eta^2 = 0.001$ and $\lambda = 800$ nm. Transverse oscillation amplitude at injection is 0.1 μm, equivalent to betatron strength parameter at dephasing $a_\beta(\tau = 0) = 0.5$. The bunch coherence effects are calculated analytically as described in (5.68). Inset shows the detail of the intensity around the bunching wavelength.

level of bunching is required to produce a clear signal.

5.10.2 Partially Modulated Bunches

The results for a bunched beam show above are useful, but represent an idealised case, and a somewhat artificial comparison with a perfectly coherent bunch. Therefore, it is instructive to also show the behaviour of long bunches with an increasing amount of bunching applied to their structure as shown in figure 5.13. From this we see that although the strongest coherent enhancement comes from complete bunching of the beam, even a partial bunching of the beam structure can provide useful coherent enhancement over a narrow region of the frequency spectrum.

The most likely case for a real LWFA or ICL is that the bunching of the beam will not be perfect, and rather than being a train of small bunches, the beam will be more similar to a long bunch with some periodically varying component to the current. It is therefore important to understand how large the periodically varying component of the current must be in order to produce a significant coherent enhancement at the target radiation wavelength.

To investigate this we consider a bunch current of the form $J_c + J_s \sin^2(\nu t)$, where J_c is a constant background current and J_s is the periodically varying component. The coherent enhancement factor due to such a partially modulated electron bunch is calculated as for the previous cases, yielding

$$\begin{aligned} F(\sigma_s, \sigma_c) &= \left| N \int_0^{n\pi/\nu} \mathrm{e}^{i\omega t} \left(\sigma_c + \sigma_s \sin^2\left(\nu t/2\right)\right) \right|^2 \\ &= N^2 \operatorname{sinc}^2\left(\frac{n\pi\omega}{\nu}\right) \left(\sigma_c^2 + \frac{\sigma_s^2}{(1-\omega^2/\nu^2)^2} + \frac{2\sigma_c\sigma_s}{1-\omega^2/\nu^2} \right), \end{aligned} \tag{5.68}$$

where $\sigma_c + \sigma_s = 1$ are the fractions of constant and sinusoidal current in the bunch.

Taking the limit that $\sigma_s = 0$, the bunch current is constant and we recover (5.62). Similarly, in the case that $\sigma_c = 0$, the beam current is entirely sinusoidally modulated and we recover (5.64).

In between these two extremes the behaviour will have aspects of both of these limits, along with addition interference effects between the two, which are encoded in the mixing term proportional to $\sigma_c\sigma_s$. In this intermediate region, we therefore expect a peak at the bunching frequency ν, as well as reduced emission intensity at wavelengths shorter than the total bunch length, relative to the constant current result. However, since the enhancement at the bunching wavelength scales with σ_s^2, small $\sigma_s \lesssim 0.1$ will not produce a strong effect and significant bunch is required to produce a strong signal. Considering the effects of the mixing term we see that there will be a change of sign in the denominator at the resonant frequency, with the mixing serving to further enhance the radiation intensity at frequencies below the resonance and reduce the radiation intensity above. Therefore it is to be expected that the mixing term will make no contribution at the resonant frequency. These results are demonstrated graphically in figure 5.13, highlighting the fact that in order to obtain noticeable narrowing of the frequency spectrum and enhancement at the bunching wavelength the beam must be relatively strongly bunched $\sigma_s \gtrsim 0.5$.

The vanishing of the mixing term is verifed by taking the limit $\omega \to \nu$ gives

$$\begin{aligned} F(J) &= N^2 \left(\sigma_c^2 \operatorname{sinc}^2(n\pi\omega/\nu) + \frac{\sigma_s^2 \operatorname{sinc}^2(n\pi\omega/\nu)}{(1-\omega^2/\nu^2)^2} \right. \\ &\qquad \left. + \frac{\sigma_c\sigma_s \operatorname{sinc}^2(n\pi\omega/\nu)}{1-\omega^2/\nu^2} \right) \\ &= \lim_{\omega\to\nu} \frac{N^2\sigma_s^2}{4}, \end{aligned} \tag{5.69}$$

where the constant current makes no contribution as the resonant frequency is higher than that associated with the total bunch length. The limit behaviour of the second term is the same as found previously for the case of complete sinusoidal bunching (5.67), and the mixing term is indeed found to vanish upon application of L'Hôpital's rule. Therefore, if the beam has non-neglible bunching $\sigma_s > 0$, then close to the resonant frequency the dominant contribution to the emitted radiation is due only to the bunched portion of the beam current, and any constant current contribution may be disregarded.

5.11 Electron Bunch Evolution in the Ion-Channel

As we have discussed in the previous section, realistic electron bunches will have a finite spread in both energy and position. As a result of this, for both the ion-channel motion (5.10) to (5.13) and the betatron motion (3.41) and (3.42), the trajectories of the electrons within each bunch will be different. As a result the phase space distribution of the bunch will evolve. The evolution of the longitudinal spread, in particular, will affect the properties of the radiation emission.

5.11.1 The Effects of Transverse Spread

We can simplify the investigation of the effects of spread in the transverse motion by noting that, since the total energy of the electron is conserved, the transverse spatial oscillation amplitude and transverse momentum amplitude are directly related. Therefore, we need only analyse the effect of a spread in the transverse spatial oscillation amplitude, as a spread in the transverse momentum can be represented as a spread in the transverse spatial amplitude.

The transverse momentum spread can be introduced by substitution directly into the solutions we have already obtained, and so we consider a small perturbation δr_β to the transverse amplitude:

$$r_\beta = \bar{r}_\beta + \delta r_\beta, \qquad r_\beta^2 \simeq \bar{r}_\beta^2 + 2\bar{r}_\beta \delta r_\beta. \tag{5.70}$$

Throughout this section we will use the overbar notation to denote the parameters of some reference trajectory, about which we make small perturbations.

This can be directly inserted into the expression (5.12) for the longitudinal propagation distance

$$z \simeq z_0 + \beta_{z0} ct - \left(1 + \frac{2\delta\bar{r}_\beta}{\bar{r}_\beta}\right)\left(\beta_{z0}\frac{k_\beta^2 \bar{r}_\beta^2}{4} ct + \beta_{z0}\frac{k_\beta \bar{r}_\beta^2}{8}\sin(2k_\beta ct)\right). \tag{5.71}$$

The difference between this result and the unperturbed trajectory yields the longitudinal spread

$$S = \bar{z} - z = -\frac{\delta\bar{r}_\beta \beta_{z0} \bar{r}_\beta k_\beta}{4}\left(2k_\beta ct + \sin(2k_\beta ct)\right). \tag{5.72}$$

This shows that the bunch spread has both an oscillatory and secular component to its behaviour. Considering first the oscillatory component we see that the bunch will exhibit a “breathing” motion at twice the betatron frequency. This comes as no surprise as it is simply an amplitude perturation of the "figure of 8" guiding centre motion we have already seen. The phase relation between this motion and the transverse motion shows that the bunch spread is at a minimum during the periods of maximum transverse acceleration (at the turning points). As it is during this time that the majority of the radiation will be emitted the effects of this breathing mode on the radiation spectrum should be negligible.

The secular term describes a constant increase in the bunch spread over many betatron cycles. This is because the spread in the transverse momentum of the electrons leads to a spread in the cycle average of γ for the electron bunch. Electrons with a larger average γ will therefore have a smaller cycle average longitudinal velocity β_z for the same longitudinal momentum, and hence the bunch will spread over multiple cycles.

Because there is no net contribution from the oscillatory term over a complete betatron oscillation, the evolution of the spread over many cycles is given by

$$\frac{\mathrm{d}S}{\mathrm{d}t} \simeq \frac{\delta r_\beta \bar{r}_\beta k_\beta^2 c \beta_{z0}}{2}. \tag{5.73}$$

This can be used to place a constraint on the transverse spread such that a given longitudinal spread S_{max} is not exceeded over $N_\beta = k_\beta c t$ betatron cycles:

$$\frac{\delta r_{\beta\mathrm{max}}}{\bar{r}_\beta} = \frac{\delta a_{\beta,\mathrm{max}}}{\bar{a}_\beta} < \frac{2 S_{\mathrm{max}}}{\beta_{z0} \bar{r}_\beta^2 N_\beta k_\beta}. \tag{5.74}$$

Here $\delta r_{\beta,\mathrm{max}}$ is the maximum allowable deviation from the reference betatron amplitude r_β, if the longitudinal spread is not to exceed S_{max}. This may equivalently be expressed as a fractional difference in the betatron strength parameter a_β for a beam with minimal energy spread. We find that the maximum allowable relative spread scales inversely with the transverse oscillation amplitude. This is once again a relativistic effect whereby the longitudinal velocity depends upon the transverse energy through γ, and since the transverse energy is proportional to r^2, this is more pronounced for large $\bar{r}_\beta$.

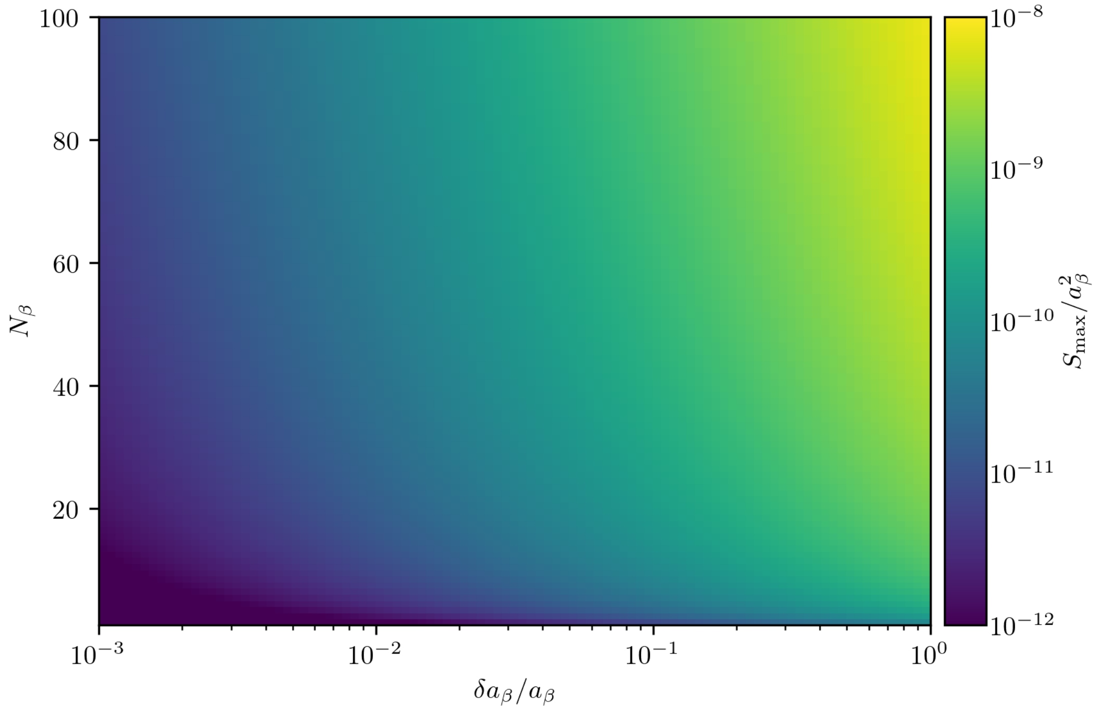

Figure 5.14: Variation of the maximum longitudinal spread S_{max} with relative spread in transverse amplitude $\delta a_\beta/\bar{a}_\beta$ and number of oscillations N_β, for an electron bunch with $\gamma = 500$ in a plasma channel with background density $\eta^2 = 0.001$. The value of S_{max} is plotted normalised by a factor $1/\bar{a}_\beta^2$, such that the result is easily applicable to all values of the betatron strength parameter (and hence transverse amplitude).

For the case of producing coherent radiation by density modulation of the beam, the maximum allowable spread will typically be of order of the modulation wavelength, for the XUV wavelengths discussed previously this requires bunch spacings of order $\sim 10\,\mathrm{nm}$ for the case investigated.

Figure 5.14 illustrates the magnitude of S_{max} with respect to both the maximum relative transverse spread and the number of betatron oscillations N_β for an electron bunch with $\gamma = 500$ and background plasma density $\eta^2 = 0.001$. While the absolute value of S_{max} depends upon the value of a_β, the quantity $S_{\mathrm{max}}/\bar{a}_\beta^2$ depends only upon the relative spread, therefore this graph is valid for all $\bar{a}_\beta$, (and hence average oscillation amplitudes) up to a constant scaling factor of S_{max}.

This demonstrates that if the transverse momentum of the electron is non-negligible compared to the total momentum, relativistic effects lead to coupling between the longitudinal and transverse motion of the injected electrons. Therefore, any spread in the transverse momentum distribution will lead to a spreading of the longitudinal position distribution. As a result, if it is desired to prevent spreading of the bunch longitudinally, the transverse momentum spread of the bunch must be minimized. The effect may also be mitigated by limiting the transverse electron momentum to non-relativistic magnitudes, however, large transverse electron momentum may be needed to increase radiation intensity and frequency. In practice, then, these two competing factors must be balanced against each other to maximise radiation efficiency for the given experimental parameters.

5.11.2 Effects of Longitudinal Momentum Spread

In the longitudinal direction the momentum spread and position spread are not related. Because there are no longitudinal fields a spread in initial longitudinal position will not evolve, however a longitudinal momentum spread will cause evolution of the longitudinal position spread.

Using the same notation as in the previous section, we perturb the initial momentum distribution

$$u_z = \bar{u}_z + \delta u_z, \tag{5.75}$$

then the perturbed gamma is

$$\begin{aligned} \gamma_0 = (1 + u_z^2)^{\frac{1}{2}} \simeq (1 + \bar{u}_z^2 + 2\bar{u}_z \delta u_z)^{\frac{1}{2}} = (1 + \bar{u}_z^2)^{\frac{1}{2}} \left(1 + \frac{2\bar{u}_z \delta u_z}{1 + \bar{u}_z^2}\right)^{\frac{1}{2}} \\ \simeq \bar{\gamma}_0 \left(1 + \frac{\bar{u}_z \delta u_z}{1 + \bar{u}_z^2}\right) = \bar{\gamma}_0 + \bar{\beta}_z \delta u_z. \end{aligned} \tag{5.76}$$

Following the derivation through

$$\frac{\Delta \phi}{\gamma_0} = \frac{1}{2} k_\beta^2 r_\beta^2 \cos(k_\beta c t), \tag{5.77}$$

as previously, but now

$$k_\beta^2 = \frac{1}{\bar{\gamma}_0 + \bar{\beta}_z \delta u_z} \cdot \frac{2\phi_0}{r_0^2} = \left(1 + \frac{\beta_z \delta u_z}{\bar{\gamma}_0}\right)^{-1} \bar{k}_\beta^2, \tag{5.78}$$

with $\bar{k}_\beta$ representing the unperturbed trajectory.

This may be further simplified by expanding the denominator again:

$$\begin{aligned} k_\beta^2 &\simeq \frac{1}{1+\sigma_\epsilon} \bar{k}_\beta^2 \simeq (1-\sigma_\epsilon)\bar{k}_\beta^2, \\ k_\beta &\simeq \left(\frac{1}{1+\sigma_\epsilon}\right)^{\frac{1}{2}} \simeq (1 - \tfrac{1}{2}\sigma_\epsilon)\bar{k}_\beta, \end{aligned} \tag{5.79}$$

where

$$\sigma_\epsilon = \frac{\delta u_z}{\bar{u}_z} = \frac{\bar{\beta}_z \delta u_z}{\bar{\gamma}_0}. \tag{5.80}$$

provided $u_z \gg 1$ which will always be satisfied for the LWFA. Expanding β_z in terms of δu_z yields

$$\begin{aligned} \beta_z &= \frac{u_z}{\gamma_0} = \frac{\bar{u}_z + \delta u_z}{\bar{\gamma}_0 + \bar{\beta}_z \delta u_z} = \frac{1}{\bar{\gamma}_0}(\bar{u}_z + \delta u_z)(1 - \bar{\beta}_z \delta u_z / \gamma_z) \\ &= \bar{\beta}_z + \frac{1}{\bar{\gamma}_0}(1 - \bar{\beta}_z^2)\delta u_z = \bar{\beta}_z + \frac{\delta u_z}{\bar{\gamma}_0^3} = \bar{\beta}_z \left(1 + \frac{\sigma_\epsilon}{\bar{\gamma}_0^2}\right). \end{aligned} \tag{5.81}$$

This gives us all the components required to write the expanded solution for z due to a small longitudinal momentum perturbation:

$$\begin{aligned} z = z_0 &+ \bar{\beta}_z \left(1 + \frac{\sigma_\epsilon}{\bar{\gamma}_0^2}\right)\left(1 - \frac{1}{4}(1-\sigma_\epsilon)\bar{k}_\beta^2 r_\beta^2\right) ct \\ &- \frac{\bar{\beta}_z}{8}\left(1 + \frac{\sigma_\epsilon}{\bar{\gamma}_0^2} - \frac{\sigma_\epsilon}{2}\right)\bar{k}_\beta r_\beta^2 \sin\left(\left[1 - \frac{\sigma_\epsilon}{2}\right]\bar{k}_\beta ct\right). \end{aligned} \tag{5.82}$$

Similar to the case for a transverse spread, there are two components to the longitudinal spread. The oscillatory term, once again, has minimal effect on the bunch when it is radiating strongly, while the secular term causes growth of the spread over many cycles. This spread in the bunch length is due to the differences in longitudinal velocity which follow from differences in the longitudinal momentum.

As before, we may express this as a rate of change of the spread

$$\begin{aligned} \frac{\mathrm{d}S}{\mathrm{d}t} &\simeq \frac{\sigma_\epsilon c \bar{\beta}_z}{\bar{\gamma}_z^2} + \left(1 - \frac{1}{4\bar{\gamma}_0^2}\right)\sigma_\epsilon \bar{\beta}_z k_\beta^2 r_\beta^2 c \\ &\simeq \frac{\sigma_\epsilon c \bar{\beta}_z}{\bar{\gamma}_0}\left(1 + \bar{a}_\beta^2\right), \end{aligned} \tag{5.83}$$

where we find that the growth rate of the longitudinal spread is strongly dependent on the betatron strength parameter $\bar{a}_\beta = \bar{\gamma}_0 \bar{k}_\beta r_\beta$, with larger betatron amplitudes causing greater longitudinal spread in the electron bunch. This once again is a relativistic effect, where non-negligible differences in the transverse momentum are reflected in the longitudinal velocity through changes to γ

Once again this can be alternatively expressed as an upper limit on the energy spread σ_ϵ such that the longitudinal spread does not exceed a limit S_{max} over N_β cycles,

$$\sigma_\epsilon < \frac{S_{\text{max}} k_\beta \bar{\gamma}_0^2}{N_\beta \bar{\beta}_z (1 + a_\beta^2)}. \tag{5.84}$$

The behaviour of the maximum spread with energy spread σ_ε, betatron strength parameter a_β and propagation distance (in terms of oscillations N_β) is shown in figure 5.15. Figure 5.15(a), illustrates the $\sim 1/a_\beta^2$ scaling of the maximum spread with the betatron strength parameter, which follows from the relativistic nature of the electron motion. In figure 5.15(b), this alternatively demonstrates that for even a 25% energy spread, the $a_\beta << 1$ case is capable of many periods of oscillation without decoherence, but that once the betatron strength parameter increases much above unity, and enters the high harmonic generation regime, the onset of decoherence occurs rapidly, even for relatively modest values of a_β. This suggests that for currently achievable energy spreads in the LWFA, which are on the order of one percent,[104,125–127] the betatron strength parameter should not exceed $a_\beta \sim 1$. This does not, however, include the effects of acceleration, which can be expected to improve the situation somewhat through adiabatic damping of the transverse emittance with increasing longitudinal momentum. These effects are discussed in section 5.12.

---

[104] C. G. R. Geddes et al. *Phys. Rev. Lett.* **100**, p. 215004, 2008.
[125] E. Brunetti et al. *Phys. Rev. Lett.* **105**, p. 215007, 2010.
[126] S. M. Wiggins et al. *Plasma Phys. Controlled Fusion* **52**, p. 124032, 2010.
[127] G. H. Welsh et al. *J. Plasma Phys.* **78**, pp. 393–399, 2012.

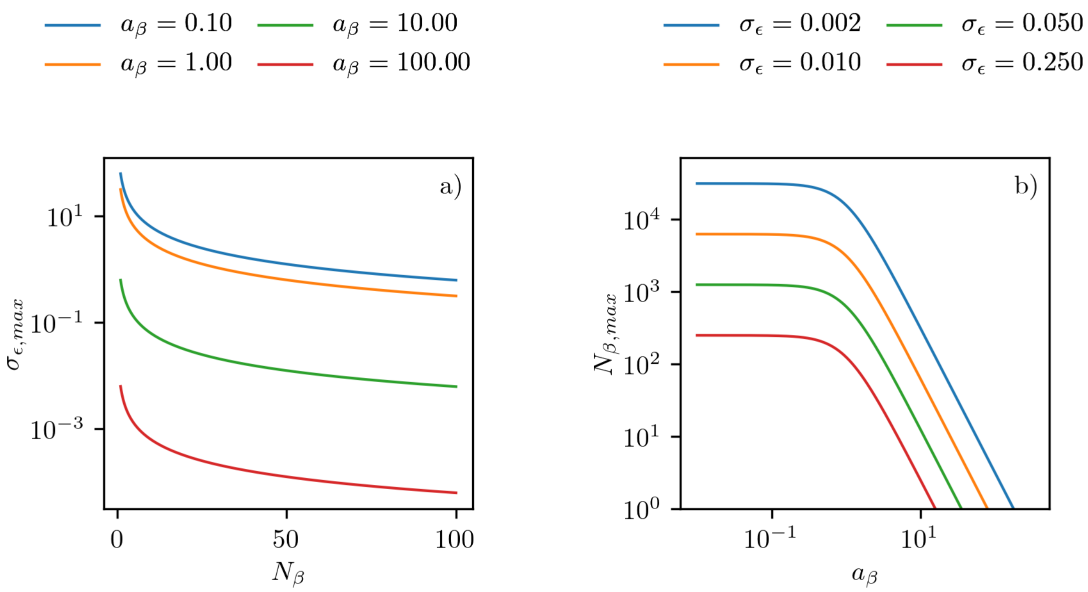

Figure 5.15: Limits for coherent radiation in the ICL with varying bunch parameters: (a) variation of the maximum allowable energy spread σ_ϵ to maintain coherence over a given number of betatron periods for various values of the betatron strength parameter a_β, (b) variation of the maximum number of betatron periods over which coherence is maintained versus betatron strength parameter for varying values of the energy spread.

5.11.3 Relationship with Beam Emittance

Since the maximum longitudinal spread depends linearly on both the propagation distance (measured here in oscillations N_β), and the transverse spread, it is straightforward to calculate the maximum allowable transverse spread. However, the position and momentum distributions of the beam may alternatively be measured in terms of the beam emittance, and therefore it is possible to express the required limits on the bunch spreads as limits on the beam emittance. As described in section 3.2.7, the emittance is a statistical property, and so rather than considering a single particle displacement as above, the emittance must be calculated for a charge distribution. For the case of a spread in the transverse displacement, the normalised emittance may be expressed as

$$\begin{aligned}\varepsilon_{\mathrm{n,rms}} &= \frac{1}{m_e c}\sqrt{\langle x^2\rangle \langle p_x^2\rangle - \langle x p_x\rangle^2} \\ &= \frac{1}{Q^2 m_e c}\Bigg[\int_0^{t_b}\int_0^{\sigma_r} J(r',t')x^2(r+r',t+t')\,\mathrm{d}t'\,\mathrm{d}r' \times \\ &\qquad \int_0^{t_b}\int_0^{\sigma_r} J(r',t')p_x^2(r+r',t+t')\,\mathrm{d}t'\,\mathrm{d}r' - \\ &\qquad \left(\int_0^{t_b}\int_0^{\delta r} J(r',t')p_x(r+r',t+t')x(r+r',t+t')\,\mathrm{d}t'\,\mathrm{d}r'\right)^2\Bigg]^{\frac{1}{2}}.\end{aligned} \tag{5.85}$$

Where the bunch charge distribution $J(r,t)$ is considered over the temporal bunch length $t_b = L_b/c$, and the total bunch width σ_r. Using this, the expression for maximum allowable transverse spread (5.74) may be expressed as a limit on the transverse emittance.

5.12 Betatron Motion with Acceleration

We can apply a similar perturbative approach to the results for the electron motion with acceleration from section 3.2.4. Whilst we expect qualitatively similar results as for the ion-channel case, with phase space rotation causing the bunch to spread in the longitudinal direction, the acceleration effects will change the details of this behaviour. In general, as the acceleration increases the total energy, we can expect the effects of any energy spread to be reduced as the fractional energy spread reduces relative to the increasing total energy. In reality, this is complicated by the fact that the evolution of the particle trajectory depends strongly on the behaviour at early times. This is particularly true for the transverse spread, where the longitudinal velocity is strongly affected by the transverse motion when the total electron energy is small. This can lead to the development of a large longitudinal spread and final energy spread. Conversely, in the case where the transverse spread is small and the longitudinal effects dominate, we expect a reduction in the effects of longitudinal energy spread compared with the ion-channel case, because the acceleration process reduces the absolute longitudinal energy spread.

5.12.1 Effects of Transverse Spread

Using the same notation as in section 5.11.2, we express the perturbed betatron amplitude as

$$r_\beta = (1 + \sigma_r)\bar{r}_\beta, \tag{5.86}$$

with $\sigma_r = \delta r_\beta / \bar{r}_\beta$.

From (3.36) and (3.44) we see that the dependence on the betatron amplitude enters only as a constant multiplicative factor, and therefore we immediately gain the form of the perturbed velocity

$$x = (1 + \sigma_r)\bar{r} \quad \rightarrow \quad \beta_r = (1 + \sigma_r)\bar{\beta}_r. \tag{5.87}$$

An analytic form for the perturbation to the longitudinal motion follows from this, assuming no angular motion,

$$\beta_z^2 = 1 - \beta_r^2 - \frac{1}{\gamma^2}, \tag{5.88}$$

$$\simeq 1 - (1 + 2\sigma_r)\bar{\beta}_r^2 - \frac{1}{\gamma^2}, \tag{5.89}$$

$$\simeq \bar{\beta}_z^2 - 2\sigma_r\bar{\beta}_r^2, \tag{5.90}$$

and taking the square root yields

$$\beta_z \simeq \bar{\beta}_z \sqrt{1 - \frac{2\sigma_r\bar{\beta}_r^2}{\bar{\beta}_z^2}}, \tag{5.91}$$

which may be approximated by

$$\beta_z \simeq \bar{\beta}_z \left(1 - \sigma_r \frac{\bar{\beta}_r^2}{\bar{\beta}_z^2}\right), \tag{5.92}$$

provided that $\sigma_r \bar{\beta}_r^2 / \bar{\beta}_z^2 \ll 1$, i.e., provided the transverse spread is small, and the longitudinal contribution to the total energy is dominant.

In such cases, the rate of longitudinal spread is approximately

$$\frac{\mathrm{d}S}{\mathrm{d}t} = c(\beta_z - \bar{\beta}_z) \simeq c\sigma_r \frac{\bar{\beta}_r^2}{\bar{\beta}_z}. \tag{5.93}$$

This is representative of the evolution behaviour of the LWFA bunch for the majority of its propagation. Initially, just after injection, the longitudinal velocity may be of similar order to the maximum transverse velocity, however, this rapidly ceases to be true. Due to the extremely rapid acceleration in the bubble fields, the magnitude of $\bar{\beta}_r^2/\bar{\beta}_z^2$ rapidly diminishes, and so for the majority of the bunch evolution there will be a relatively small bunch elongation.

Substituting $\bar{\beta}_r^2 = 1 - \bar{\beta}_z^2 - \gamma^{-2}$ in (5.93) and integrating with respect to time yields an expression for the evolution of $S(t)$ over this period

$$S(t) = z(t) - \bar{z}(t) \simeq -2\sigma_r \left(ct - \bar{z}\right). \tag{5.94}$$

We find that, to a first approximation, the bunch spread scales linearly with the propagation distance, and an increase in the transverse amplitude (positive σ_r) causes the electron to slip back relative to the reference electron. This is the same relativistic effect as found for the ion-channel case where increased transverse energy and hence γ reduces the longitudinal velocity although the longitudinal momentum is unchanged. This constant spread rate behaviour is however valid only in the limit of very large longitudinal momentum. Early in the acceleration process, much larger spread rates will occur.

The evolution of the maximum spread over the acceleration period is shown in figures 5.16 and 5.17, calculated both numerically from the model described in chapter 3 (a) and using the reduced model developed in this chapter (b). The plasma parameters are chosen to be similar to those attainable in the ALPHA-X experiment with $\eta^2 = 0.001$, and the electron modeled from injection with $\gamma_i \simeq 31.6$ and unperturbed initial transverse amplitudes $r_\beta = 1\,\mu$m, corresponding to an initial $a_\beta \simeq 1$; and $r_\beta = 0.1\,\mu$m corresponding to $a_\beta \simeq 0.1$. These illustrate the described behaviour with a rapid initial increase in the spread when γ is

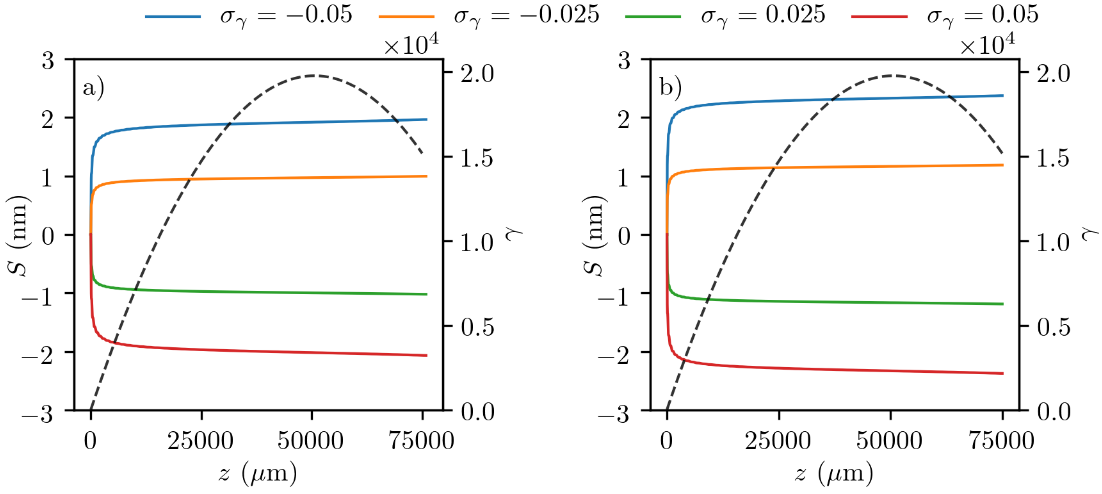

Figure 5.16: Longitudinal spread growth due to transverse momentum spread calculated both numerically using the Bubblecalc code (a), and using the perturbative reduced model (b). The chosen plasma parameters were $\eta^2 = 0.001$, with the electron modeled from injection with $\gamma_i \simeq 31.6$ and an unperturbed initial transverse amplitude $r_\beta = 1\,\mu$m equivalent to an initial $a_\beta = 1$. Dashed black line shows the trajectory of the average energy $\bar{\gamma}$.

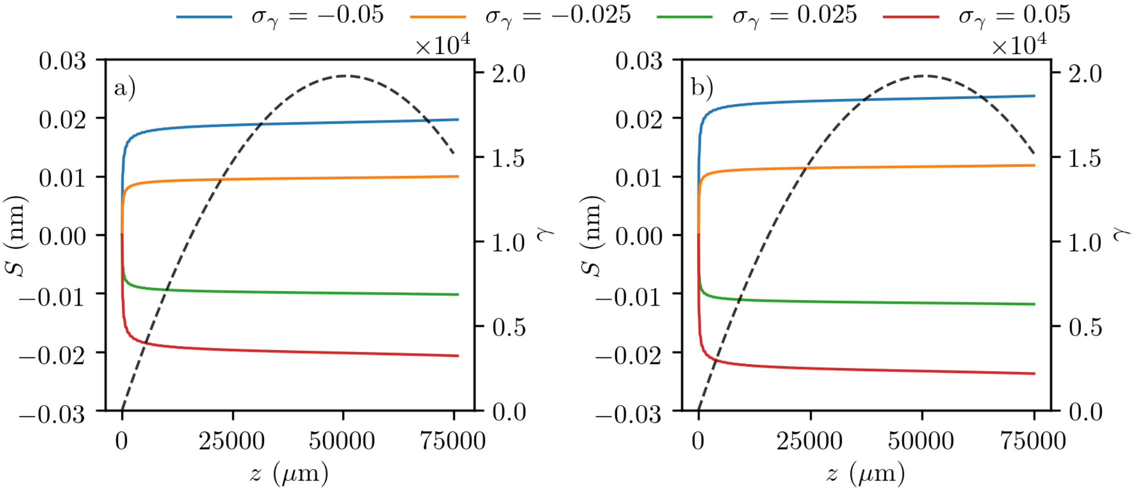

Figure 5.17: Longitudinal spread growth due to transverse momentum spread calculated both numerically using the Bubblecalc code (a), and using the perturbative reduced model (b). The chosen plasma parameters were $\eta^2 = 0.001$, with the electron modeled from injection with $\gamma_i \simeq 31.6$ and an unperturbed initial transverse amplitude $r_\beta = 0.1\,\mu$m equivalent to an initial $a_\beta \simeq 0.1$. Dashed black line shows the trajectory of the average energy $\bar{\gamma}$.

small, followed by very slow, approximately linear, growth for the majority of the propagation distance. The growth rate is also found to be sensitive to the value of a_β with large a_β leading to large spread growth. This follows from the coupling of the transverse and longitudinal motion when the transverse motion is relativistic: the transverse momentum in the $a_\beta = 1$ case is sufficiently large to make a non-negligible contribution to γ and thus the longitudinal velocity of the particle is reduced compared to the $a_\beta \simeq 0.1$ case and more sensitive to changes in the transverse momentum. For the chosen parameters in the $r_\beta = 0.1\,\mu$m case we find that a 5% transverse spread leads to a longitudinal spread which is negligible compared to the 10 nm target wavelength. This suggests that for small transverse amplitudes the coherence should be insensitive to a transverse spread of 10s of percent. In contrast, for the $r_\beta = 1\,\mu$m case, the longitudinal spread due to a 5% transverse spread leads to a spread of several nm, suggesting that for larger transverse amplitudes the transverse spread must be tightly controlled.

We find that there is excellent agreement between the numerical model and the analytic approximation of the evolution behaviour to more extreme values of a_β and σ_r than shown here. This result is perhaps slightly surprising given the approximations made, but this good agreement remains even for cases where $a_\beta \gg 1$ and for perturbations up to $\sigma_r \leq 0.25$.

From these results we also see that the effects of transverse spread on the bunch length will be most pronounced early in the acceleration process when the electron velocity is low. Therefore, in order to reduce the longitudinal bunch spread and emittance growth, lower density plasmas with larger bubble velocities are to be preferred as the longitudinal velocity of the electron must be larger for injection to occur (as discussed in chapter 4).

5.12.2 Phase Evolution due to Transverse Spread

The previous section described the longitudinal spread of the bunch due to relativistic effects, which couple the transverse and longitudinal motion. This is not the complete picture, however, as we must also consider the evolution of the relative phase of the transverse oscillation between electrons caused by the differences in the betatron oscillation frequency due to the transverse momentum spread. This is important because, even if the electrons do not spread appreciably, if their oscillations are dephased, the emitted radiation will not be coherent and the desired enhancement will be lost.

We can attempt to include the effects of the transverse motion by improving upon the approximation used to derive the betatron motion in section 3.2.4. The original derivation by Kostyukov *et al.*[16] assumes that the longitudinal momentum contribution alone is a sufficient approximation for the total electron energy, however, the additional contribution from transverse motion may cause a sufficient change in the betatron frequency to become non-neglible over multiple oscillation cycles, especially for radiation emission at short wavelengths.

Recalling that the model for the electron motion assumes adiabatic variation of the energy, we need only consider the cycle average contribution of the transverse momenta to the total energy. In addition we assume that the transverse energy is small compared to the longitudinal energy even at the point of injection $p_{z,0}^2 \gg p_{\perp,0}^2$ and thus make an improved approximation of γ by the expansion

$$\begin{aligned}\gamma &\simeq \sqrt{u_z^2 + \langle u_r^2 \rangle + 1} \\ &\simeq u_z \sqrt{1 + \frac{\langle u_r^2 \rangle + 1}{u_z}} \\ &\simeq u_z \left(1 + \frac{\epsilon^2}{2u_z^2}\right),\end{aligned} \tag{5.95}$$

where u_i denotes momentum normalised to $m_e c$ and $\epsilon^2 = 1 + \langle u_r \rangle^2$.

---

[16] I. Kostyukov et al. *Phys. Plasmas* **11**, p. 5256, 2004.

Recalling from section 3.2.4 that the betatron frequency $\omega_\beta = \omega_p/\sqrt{2\gamma}$, we may write the phase of the electron as

$$\phi_\beta(\tau\,\epsilon) = \int_{\tau_0}^{\tau} \frac{1}{\sqrt{(1-\tau^2)}}\left(1 - \frac{\epsilon^2}{4\gamma_d^2(1-\tau^2)^2}\right)\mathrm{d}\tau, \tag{5.96}$$

recalling that γ_d is the dephasing energy. Choosing $\phi_\beta(\tau_0) = 0$ for simplicity, performing the integration gives the result

$$\phi_\beta(\tau,\epsilon) = \arcsin(\tau) + \frac{\epsilon^2\tau(3-2\tau^2)}{6\gamma_d^2(1-\tau^2)^{\frac{3}{2}}} \tag{5.97}$$

and so the phase difference at time τ between two particles injected at τ_0 with transverse energy difference $\Delta\epsilon^2 = \epsilon_2^2 - \epsilon_1^2$ is given by

$$\Delta\phi_\beta(\tau,\Delta\epsilon) = \phi_\beta(\tau,\epsilon_2) - \phi_\beta(\tau,\epsilon_1) = \frac{\gamma_\phi\Delta\epsilon^2}{3\gamma_d^2}\left(\frac{\tau(3-2\tau^2)}{(1-\tau^2)^{\frac{3}{2}}} - \frac{\tau_0(3-2\tau_0^2)}{(1-\tau_0^2)^{\frac{3}{2}}}\right). \tag{5.98}$$

Finally this phase difference can be related to the radiation phase difference by considering the time difference between the particles

$$\Delta t = \frac{\Delta\phi_\beta}{\omega_p}, \tag{5.99}$$

thus the phase difference for the radiation is

$$\Delta\phi_r = \omega_r\Delta t = \frac{\omega_r}{\omega_p}\Delta\phi_\beta(\tau,\Delta\epsilon), \tag{5.100}$$

where ω_r is the radiation frequency.

For a given evolution time τ, which would typically be the dephasing time for an electron bunch in the accelerator, the maximum coherent emission frequency can be estimated by requiring that the phase difference must remain small compared to π, and therefore

$$\pi > \frac{\omega_r}{\omega_p}\Delta\phi_\beta(\tau,\Delta\epsilon) = \frac{\omega_r}{\omega_p}\frac{\gamma_\phi\Delta\epsilon^2}{3\gamma_d^2}\left[\theta(\tau) - \theta(\tau_0)\right], \tag{5.101}$$

or

$$\omega_r < \frac{3\pi\omega_p\gamma_d^2}{\gamma_\phi\Delta\epsilon^2}\left[\theta(\tau) - \theta(\tau_0)\right]^{-1}, \tag{5.102}$$

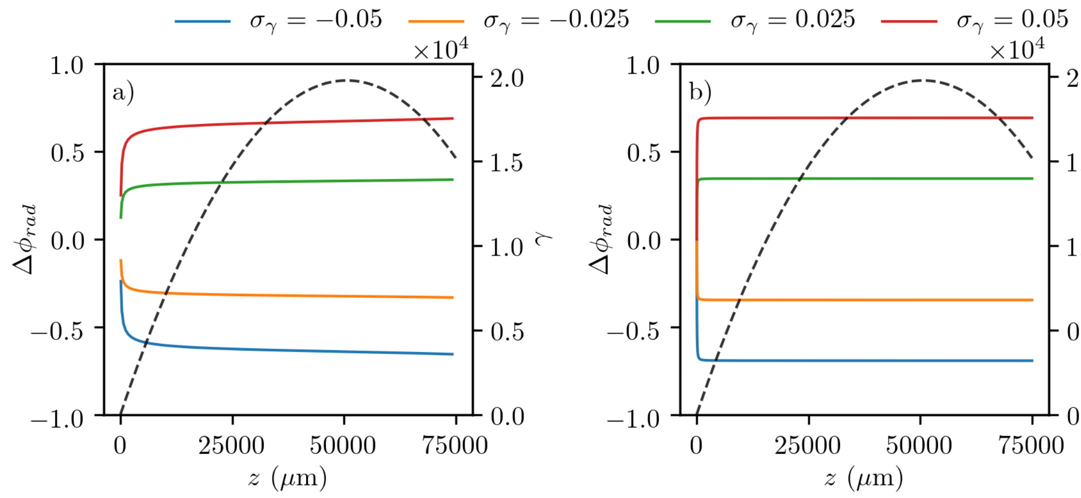

Figure 5.18: Growth in oscillation phase difference at a radiation frequency $\omega_r = 10^{17}\,\mathrm{rad\,s^{-1}}$ due to transverse momentum spread calculated both numerically using the Bubblecalc code (a), and using the perturbative reduced model (b). The chosen plasma parameters were $\eta^2 = 0.001$, with the electron modeled from injection with $\gamma_i \simeq 31.6$ and an unperturbed initial transverse amplitude $r_\beta = 1\,\mu$m equivalent to an initial $a_\beta = 1$. Dashed black line shows the trajectory of the average energy $\bar{\gamma}$.

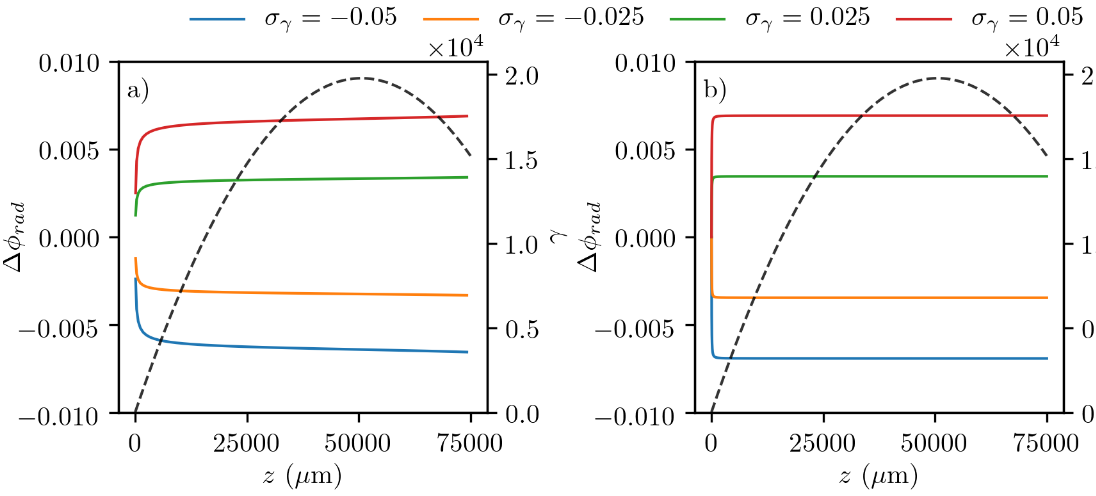

Figure 5.19: Growth in oscillation phase difference at a radiation frequency $\omega_r = 10^{17}\,\mathrm{rad\,s^{-1}}$ due to transverse momentum spread calculated both numerically using the Bubblecalc code (a), and using the perturbative reduced model (b). The chosen plasma parameters were $\eta^2 = 0.001$, with the electron modeled from injection with $\gamma_i \simeq 31.6$ and an unperturbed initial transverse amplitude $r_\beta = 0.1\,\mu$m equivalent to an initial $a_\beta \simeq 0.1$. Dashed black line shows the trajectory of the average energy $\bar{\gamma}$.

where

$$\theta(\tau) = \frac{\tau(3 - 2\tau^2)}{(1 - \tau^2)^{\frac{3}{2}}}. \tag{5.103}$$

Figures 5.18 and 5.19 compare the results of this model (b) with numerical integration over the electron trajectory (a), for the same parameters as the investigation of bunch spread growth. These show resonable agreement of the reduced model with the numerical calculation, however, the reduced model does not provide as accurate a description of the behaviour at early times. This is to be expected because at early times the ratio of the transverse to longitudinal momentum is relatively large and the accuracy of the perturbative approximation is therefore reduced. As in the case of the longitudinal spread we see that the phase difference is sensitive to the transverse oscillation amplitude. This is because, as the transverse momentum becomes large ($a_\beta \gtrsim 1$), it will contribute non-negligibly to the electron γ. This means that for $a_\beta \gtrsim 1$ the betatron frequency $\omega_\beta = \omega_p/\sqrt{2\gamma}$ becomes dependent on the average transverse momentum. Therefore, a difference in average transverse momentum of a pair of electrons, leads to a phase slip between the oscillation of the two electrons over several betatron cycles. For the cases considered here we see that for small $a_\beta \simeq 0.1$ a transverse spread of $\sim 10\%$ yields a minimal phase difference over the acceleration period. In contrast however for $a_\beta \simeq 1$ we see that for a radiation frequency of $10^{17}\,\mathrm{rad\,s^{-1}}$ ($\sim 10\,\mathrm{nm}$), a typical target frequency for XUV radiation production, a transverse spread of $\sim 10\%$ leads to a spread in phase at the radiation frequency comparable to π. Therefore, for XUV and potentially X-ray production, the required transverse spread in the bunch must be restricted to just a few percent in order to guarantee coherent emission and high peak brilliance.

5.12.3 Phase Growth due to Longitudinal Energy Spread

To explore the effects of longitudinal energy spread on an accelerating bunch we again adopt a perturbative approach. Initially, we consider the phase evolution in the case of a small energy spread

$$\gamma(\tau) = \bar{\gamma}(\tau) + \delta\gamma \simeq \gamma_d(1 - \tau^2 + \frac{\delta\gamma}{\gamma_d}). \tag{5.104}$$

This time we must use a different form for the perturbation as the evolution of γ prevents us writing it in the form $\gamma(1 + \sigma_\gamma)$, therefore we perturb with a constant $\delta\gamma$. This expression is not completely physically accurate, as it assumes the perturbation in gamma is constant rather than reducing during the acceleration process as actually occurs. However, correctly modifying the behaviour of $\gamma(\tau)$ does not admit the desired analytic solutions, forcing this approximation to be made.

Inserting the perturbed γ into the integral in (5.96), as previously done for the transverse case, gives an expression for the phase

$$\begin{aligned}\phi_\beta(\tau) &= 2\sqrt{2}\gamma_\phi \int_{\tau_i}^{\tau} \frac{1}{\sqrt{1 - \tau^2 + {}^{\delta\gamma}\!/_{\gamma_d}}}\, \mathrm{d}\tau \\ &= \left[2\sqrt{2}\gamma_\phi \arctan\left(\frac{\tau}{\sqrt{1 + {}^{\delta\gamma}\!/_{\gamma_d} - \tau^2}} \right) \right]_{\tau_i}^{\tau} .\end{aligned} \tag{5.105}$$

In the case that $\delta\gamma = 0$ the arctan term simplifies to $\arcsin(\tau)$ and so the phase difference between a perturbed and unperturbed electron is given by

$$\Delta\phi_\beta = 2\sqrt{2}\gamma_\phi \left[\arctan\left(\frac{\tau}{\sqrt{1 + {}^{\delta\gamma}\!/_{\gamma_d} - \tau^2}} \right) - \arcsin(\tau) \right]_{\tau_i}^{\tau} . \tag{5.106}$$

The predicted phase difference evolution is shown in figure 5.20 along with the numerically calculated result. As in previous cases the phase depends strongly on the value of γ over the acceleration process, and, as in the case of a transverse spread, the majority of the phase spread occurs early in the acceleration process where the ratio $\delta\gamma/\bar{\gamma}(\tau)$ is largest. This agrees well with the magnitude of the phase difference, but does not capture the details of the behaviour. The numerically simulated electron motion shows that after an initial rapid increase the phase difference decreases as the electrons propagate. The reason for this is that, as discussed in chapter 3, the longitudinal momentum calculation is based

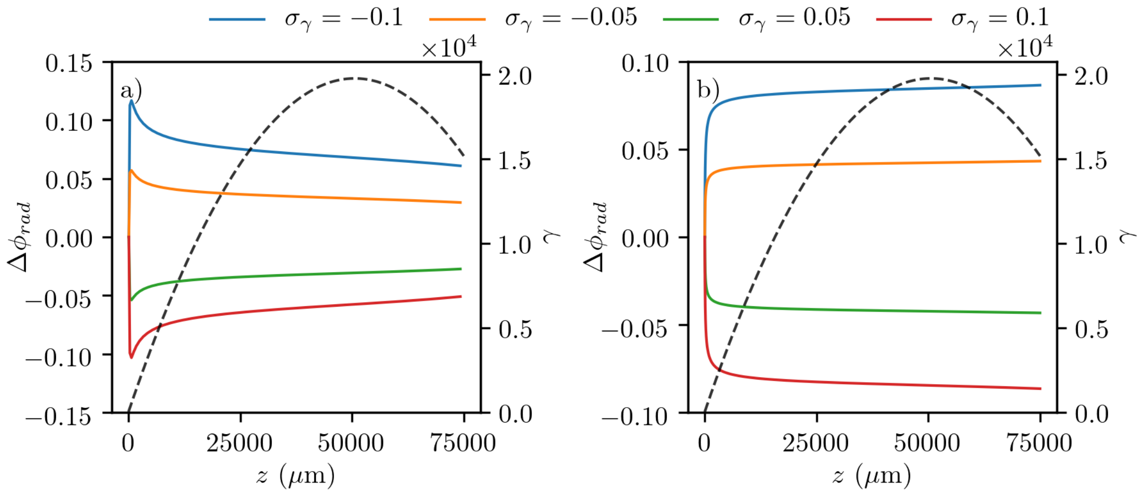

Figure 5.20: Growth in oscillation phase difference at a radiation frequency $\omega_r = 10^{17}\,\mathrm{rad\,s^{-1}}$ due to longitudinal momentum spread calculated both numerically using the Bubblecalc code (a), and using the newly derived approximate model (b). The chosen plasma parameters were $\eta^2 = 0.001$, with the electron modeled from injection with $\gamma_i \simeq 31.6$ and an unperturbed initial transverse amplitude $r_\beta = 1\,\mu$m equivalent to an initial $a_\beta = 1$. Dashed black line shows the trajectory of the average energy $\bar{\gamma}$.

upon the assumption that the longitudinal electron velocity is c, thus failing to account for the effect of small differences in longitudinal momenta or transverse momenta on the longitudinal velocity. This means that during the acceleration the slower moving electrons will experience a stronger accelerating field than their faster moving counterparts, which reduces the energy spread and phase difference between the electrons. In the decelerating phase of the wave this effect is reversed and the energy spread is amplified. These effects are not included in the analytic model derived here, and so it does not predict the reduction in phase difference observed in the numerical simulation.

For the example 10 nm XUV radiation frequency considered here, a small ($\sim 5\%$) energy spread in the bunch does not lead to an appreciable growth in the phase spread at the frequency of interest. The majority of the growth in phase difference occurs rapidly at the beginning of the acceleration period when the energy difference has the greatest effect on the longitudinal velocity, and decreases thereafter, which is consistent with qualitative expectations. This is encouraging for the potential development of tuneable accelerators since bunches with low ($\lesssim 1\%$) energy spread can now be routinely generated in LWFA.[104,125–127] These results suggest that a train of such bunches could therefore be used as a tuneable source of XUV light.

5.12.4 Bunch Spread due to Longitudinal Energy Spread

Finally we must consider the effects of the longitudinal bunch spread due to the longitudinal energy spread. This is the least well defined by the analytic model since an initial assumption in deriving the acceleration behaviour of the electron is that it travels at c and so we cannot correctly describe the effects of small longitudinal momentum differences on the acceleration. However, as discussed in the previous we have seen that longitudinal spreads are reduced by the accelerating fields. Therefore, we may estimate an upper bound on the expected longitudinal position spread in the bunch using the longitudinal energy behaviour.

Beginning in the same way as for the previous derivations the perturbed longitudinal energy is approximated by

$$\gamma(\tau) = \bar{\gamma}(\tau) + \delta\gamma = (1 - \tau^2)\gamma_d + \delta\gamma, \tag{5.107}$$

which gives an approximation for the longitudinal momentum

$$\begin{aligned} \beta_z &= \sqrt{1 - \beta_r^2 - \frac{1}{\gamma^2}} \\ &= \sqrt{1 - \frac{u_r^2 + 1}{\gamma^2(\tau)}} \\ &\simeq 1 - \frac{\langle \epsilon^2 \rangle}{2[(1 - \tau^2)\gamma_d + \delta\gamma]^2}. \end{aligned} \tag{5.108}$$

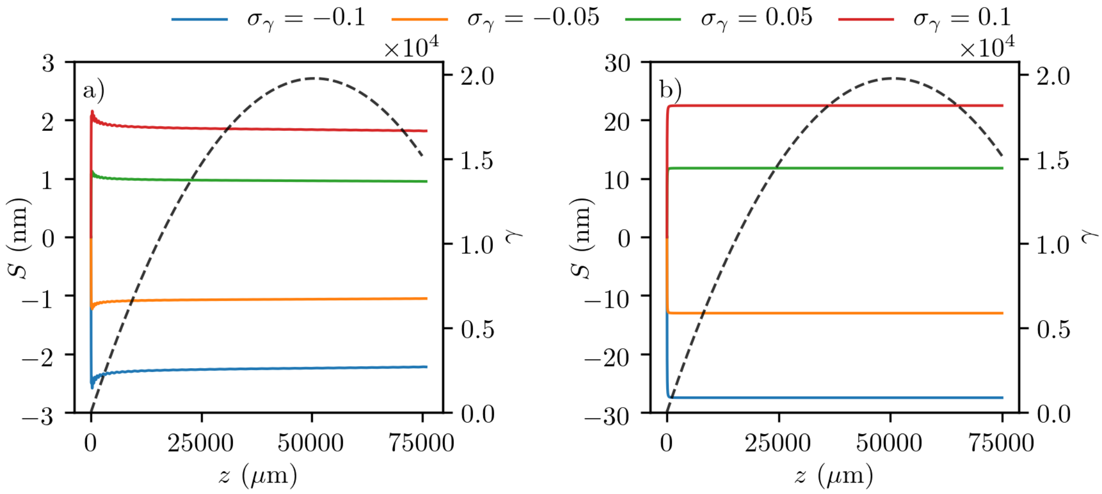

Figure 5.21: Growth in bunch length due to longitudinal momentum spread calculated both numerically using the Bubblecalc code (a), and using the approximate analytic model (b). The chosen plasma parameters were $\eta^2 = 0.001$, with the electron modeled from injection with $\gamma_i \simeq 31.6$ and an unperturbed initial transverse amplitude $r_\beta = 1\,\mu$m equivalent to an initial $a_\beta = 1$. Dashed black line shows the trajectory of the average energy $\bar{\gamma}$.

Integrating this with respect to time gives

$$z \simeq \frac{\gamma_\phi\sqrt{8\gamma_d}}{k_p}\left[\tau - \frac{\langle\epsilon^2\rangle}{4(\gamma_d+\delta\gamma)}\left(\frac{\operatorname{arctanh}\left(\tau\sqrt{\frac{\gamma_d}{\gamma_d+\delta\gamma}}\right)}{\sqrt{\gamma_d(\gamma_d+\delta\gamma)}} + \frac{\tau}{\delta\gamma+\gamma_d(1+\tau^2)}\right)\right]_{\tau_i}^{\tau} \tag{5.109}$$

$$= \lim_{\delta\gamma\to 0}\frac{\gamma_\phi\sqrt{8\gamma_d}}{k_p}\left[\tau - \frac{\langle\epsilon^2\rangle\left(\frac{t}{1-\tau^2} + \arctan(\tau)\right)}{4\gamma_d^2}\right]_{\tau_i}^{\tau}, \tag{5.110}$$

for the cases with and without an energy perturbation respectively.

Subtracting the two gives the longitudinal spread growth ΔS due to a longitudinal energy difference $\delta\gamma$

$$\Delta S = \frac{\gamma_\phi\sqrt{8\gamma_d}}{k_p}\frac{\epsilon^2}{4}\left[\frac{\operatorname{arctanh}(\tau) + \frac{\tau}{1-\tau^2}}{\gamma_d^2} - \right.$$
$$\left.\frac{1}{\gamma_d+\delta\gamma}\left(\frac{\operatorname{arctanh}\left(\tau\sqrt{\frac{\gamma_d}{\gamma_d+\delta\gamma}}\right)}{\sqrt{\gamma_d(\gamma_d+\delta\gamma)}} + \frac{\tau}{\delta\gamma+\gamma_d(1+\tau^2)}\right)\right]_{\tau_i}^{\tau}. \tag{5.111}$$

The behaviour of this approximation relative to the numerically calculated result is shown in figure 5.21. There is an order of magnitude difference between the numerical calculation and the perturbative approximation. This is likely due to the fact that the longitudinal velocity is more sensitive to γ than the phase. It has a $1/\gamma^2$ dependency versus $1/\sqrt{\gamma}$, thus making it more sensitive to errors in the value of γ. Additionally, the Taylor expansion of β is least accurate for small values of γ. Together these factors can account for the discrepancy, with small errors in β_z at the start of the acceleration process causing a large error in ΔS after integration. Unfortunately, no analytic solution exists for the integral without Taylor expanding the square root. Because of this, accurate prediction of the effect of longitudinal energy spread on longitudinal bunch spread requires numerical analysis. Whilst the suggestion of using this analytic approximation as an upper bound is still possible, it places unreasonably strong restrictions on the required monochromaticity to provide good coherent enhancement of the radiation. We do find, however, that the results from the numerical calculation support what was previously found for the phase behaviour: for energy spreads of the order of $\sim 5\%$ the bunch spread is sufficiently small for good coherence of the emitted radiation.

5.12.5 Implications for the LWFA as a Radiation Source

These investigations confirm that transverse and longitudinal energy spreads will cause the bunch to increase in length, and the transverse electron oscillations to dephase. This places strict requirements on beam quality if coherent enhancement is to be observed. For coherent enhancement at XUV wavelengths, with plasma densities and beam energies typical of current LWFA experiments, the results obtained here demonstrate that transverse and longitudinal momentum spread must be limited to the order or a few percent. This has been demonstrated to be achievable with the current state of the art,[127] and therefore coherent enhancement

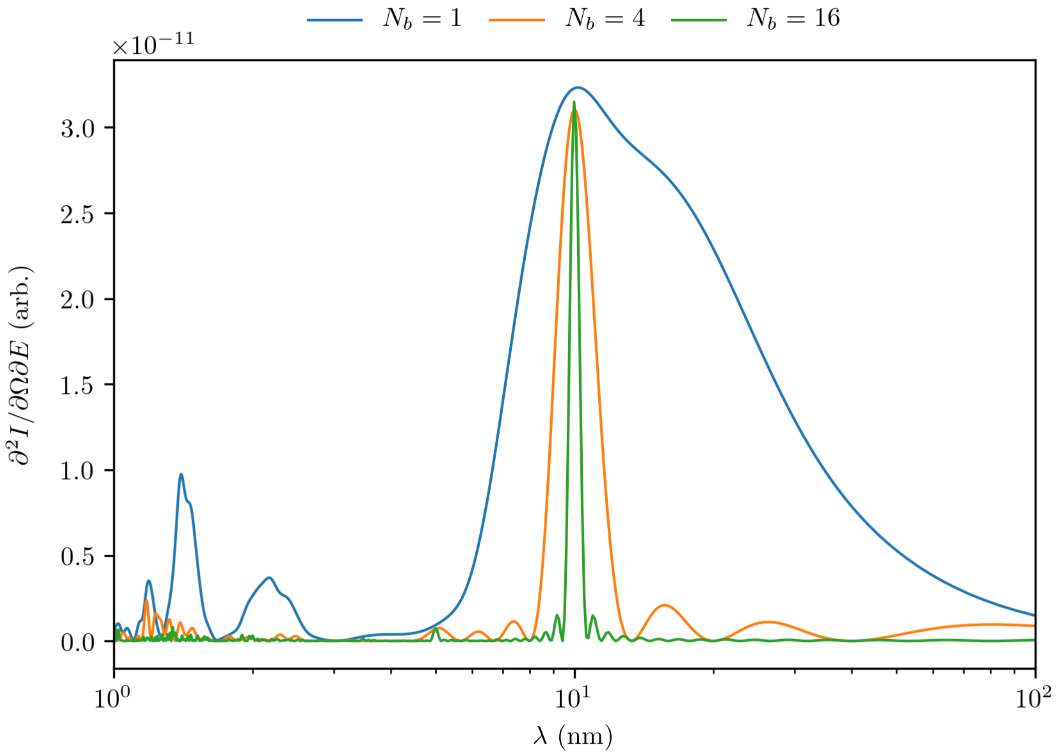

Figure 5.22: Emitted radiation spectrum from a train of n bunches with rms length 2 nm spaced at 10 nm intervals performing betatron motion in an ideal bubble field with relativistic transverse momentum. Electron motion is numerically computed using the Bubblecalc code and radiation computed using the radt code. All bubble and electron parameters are described in the text.

by prebunching of the beam is expected to be experimentally achievable with current LWFA systems.

5.13 Simulated Radiation Emission from Inhomogenous Bunches

As discussed in section 5.8, it is feasible to simulate the radiation emission numerically provided there are sufficient pseudoparticles to correctly resolve the interference effects. It was empirically determinged that the bunch density must be in excess of 1000 pseudoparticles per unit wavelength at the frequency of interest in order to ensure convergence of the simulation results. Convergence in this case being defined as negligible ($\ll 1\%$) change in value in the frequency range of interest for continued increase in pseudoparticle population size. Simulation is therefore feasible for coherent enhancement at 10 nm wavelength with bunches of nominal rms length 2 nm spaced at 10 nm intervals as this requires of order 1000 particles per bunch. These are performed using the same electron and bubble properties as in the previous section to allow comparison with the analytic model as well as providing estimates for the feasibility of such a scheme with the ALPHA-X and SCAPA lasers. The particle motion was simulated using the Bubblecalc code with bunches of rms length 2 nm at injection and initial longitudinal momentum such that their velocity was equal to the bubble velocity, the initial longitudinal position of the bunch was chosen such that it began approximately one bubble radius from the centre of the potential, and is constant for all simulations. Simulations were performed using two different initial transverse positions for the bunch $r_b = 0.1\,\mu\text{m}$ and $r_b = 1\,\mu\text{m}$, allowing investigation of the behaviour for non-relativistic and relativistic transverse motion respectively. Multiple bunches were launched with identical properties separated by a period $t_s = \lambda_s/(c\beta_b)$ where the bunch spacing $\lambda_s = 10\,\text{nm}$, the total charge of the bunch train was fixed at 10 pC regardless of the number of bunches in the train. Results were calculated for trains of 1, 4 and 16 bunches. The results for the control simulation of bunches with relativistic transverse motion and no longitudinal or transverse spread are shown in figure 5.22. This clearly shows the coherent enhancement effect with increasing number of bunches, with very similar behaviour to that seen in figure 5.5 for increasing N_β in the acceleration free case. The broader band emission spectrum of a single bunch is strongly reduced by the interference effects, narrowing the bandwidth to a narrow spike about the 10 nm bunching wavelength. Below 1 nm the spectrum begins to become noisy as the number of pseudoparticles is insufficient to fully resolve interference effects at this wavelength.

The radiation was calculated using the radt code provided by Dr. Enrico

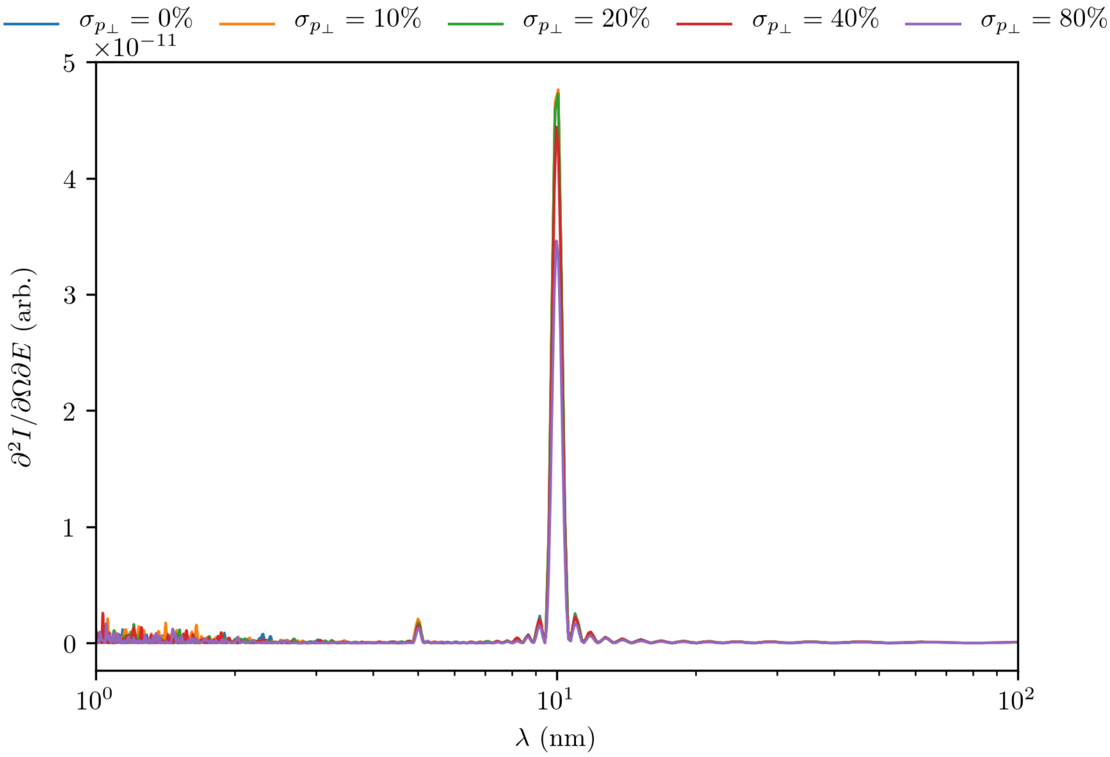

Figure 5.23: Emitted radiation spectrum from a train of 16 bunches with rms length 2 nm spaced at 10 nm intervals and varying transverse momentum spread $\sigma_{p_\perp}$ performing betatron motion in an ideal bubble field with non-relativistic transverse momentum. Electron motion is numerically computed using the Bubblecalc code and radiation computed using the radt code. All bubble and electron parameters are described in the text.

Brunetti. For these parameters it was found that approximately 3000 particles per bunch were needed to correctly resolve interference effects for low energy spread. This requirement increases to 6000 particles per bunch for energy spreads above $\sim 20\%$ which cause the bunch length to spread further and so reduce the density per unit length close to dephasing where the majority of emission occurs.

Figure 5.23 shows the results for a spread in the transverse amplitude and hence momentum of the bunch, for a 16 bunch train in the case that the transverse motion is non-relativistic. We find that the radiation coherence is insensitive to even very large $\sim 50\%$ spreads in the transverse momentum. This is expected due to the non-relativistic nature of the motion which makes a negligible contribution to the γ of an oscillating electron. Since it is through changes in γ that the

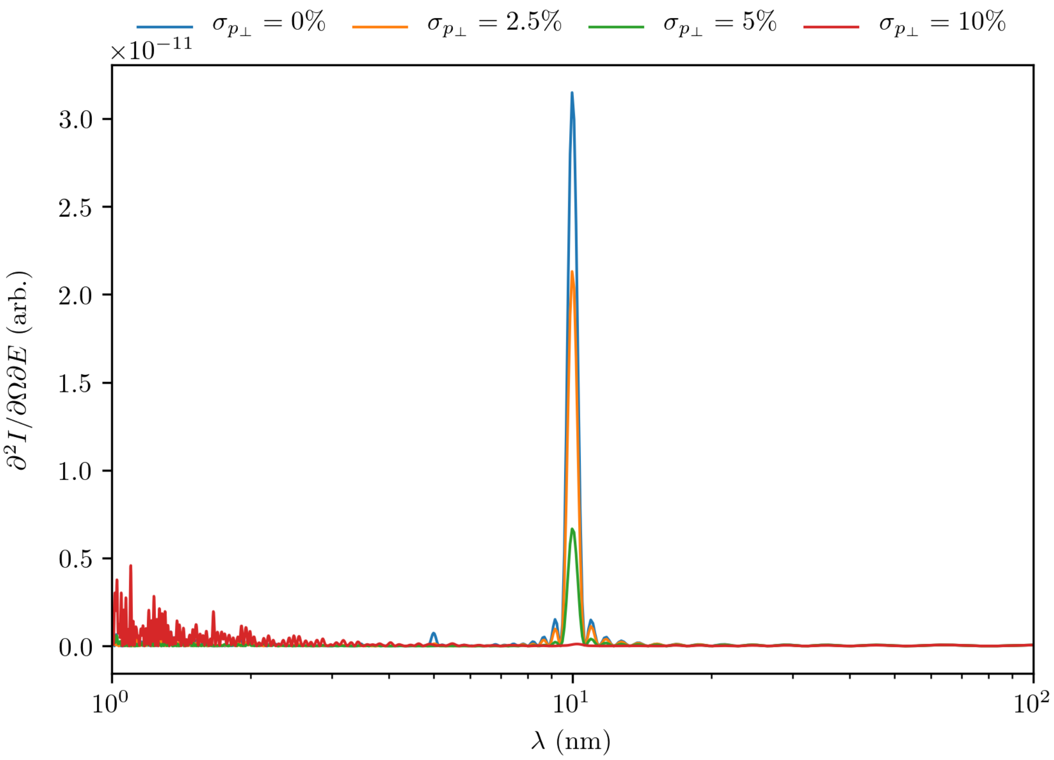

Figure 5.24: Emitted radiation spectrum from a train of 16 bunches with rms length 2 nm spaced at 10 nm intervals and varying transverse momentum spread $\sigma_{p_\perp}$ performing betatron motion in an ideal bubble field with relativistic transverse momentum. Electron motion is numerically computed using the Bubblecalc code and radiation computed using the radt code. All bubble and electron parameters are described in the text.

transverse motion can affect the longitudinal motion, there is therefore neglible change in the longitudinal velocity or oscillation frequency of the electron and the bunch spread and phase do not evolve.

In contrast to this result, figure 5.24 shows that in the case that the transverse motion is relativistic, the radiation coherence is very sensitive to transverse momentum spread. Here we find that just a few percent spread in the transverse momentum is sufficient to severly reduce the coherent enhancement and that a 10% spread completely destroys the coherence. This is consistent with the analytic predictions made in section 5.12.1, which shows that a 5% difference from the 1 μm transverse oscillation amplitude leads to a 2 nm longitudinal position shift at dephasing and a phase shift of a significant fraction of a wavelength.

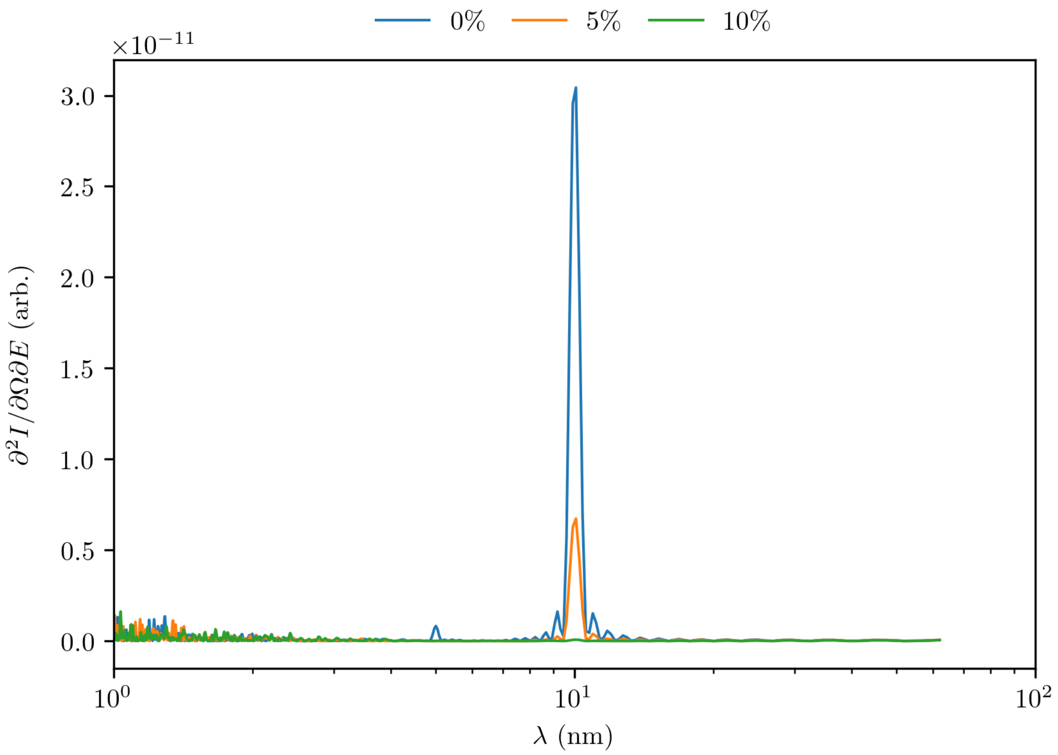

Figure 5.25: Emitted radiation spectrum from a train of 16 bunches with rms length 2 nm spaced at 10 nm intervals and varying longitudinal momentum spread $\sigma_{p_\parallel}$ performing betatron motion in an ideal bubble field with non-relativistic transverse momentum. Electron motion is numerically computed using the Bubblecalc code and radiation computed using the radt code. All bubble and electron parameters are described in the text.

In the case that there is a spread in the longitudinal momentum, shown in figures 5.25 and 5.26, we find that the results are independent of the transverse oscilation amplitude. This is to be expected as the longitudinal momentum behaviour is largely independent of the transverse momentum behaviour. In both cases shown here the resulting coherent enhancement is reduced with energy spread as predicted by the analytic approximation, though it is less sensitive to longitudinal spread than the transverse spread for the chosen parameters. We see from the analytic results that a shift in the initial longitudinal momentum of 10% leads to a position difference at dephasing of 8 nm, therefore a bunch with an initial rms energy spread of 20% and rms length of 2 nm can be expected to spread to a length of $\sim$ 8 nm at dephasing. Expansion to such a bunch length

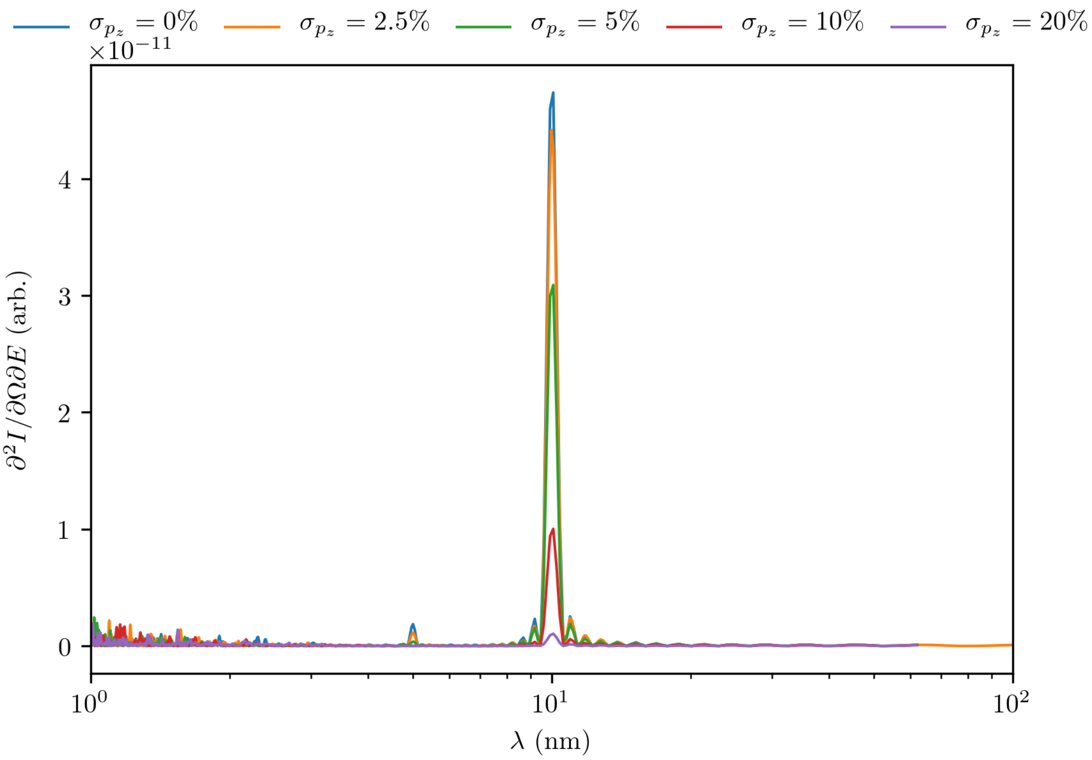

Figure 5.26: Emitted radiation spectrum from a train of 16 bunches with rms length 2 nm spaced at 10 nm intervals and varying longitudinal momentum spread $\sigma_{p_\parallel}$ performing betatron motion in an ideal bubble field with relativistic transverse momentum. Electron motion is numerically computed using the Bubblecalc code and radiation computed using the radt code. All bubble and electron parameters are described in the text.

would almost completely destroy any coherent enhancement effects, as described in section 5.9, and the observed reduction in coherent enhancement in figures 5.25 and 5.26 is consistent with this result.

From these results we find that the use of a train of bunches to drive coherent enhancement of betatron radiation at XUV wavelengths is feasible. However, the effects of bunch momentum spread, in particular for large transverse momenta, can lead to rapid spreading of the bunch and relative dephasing of the electron oscillations, which destroys the coherent enhancement. In order to mitigate this, the transverse and longitudinal momentum spreads must be minimized in order to retain sufficient bunch train structure over the acceleration distance that there is still coherent emission when the bunches have maximum energy close to dephasing.

For bunch and bubble properties consistent with the ALPHA-X accelerator at Strathclyde, these limits are found to be of the order of a few percent for both the transverse and longitudinal momentum spreads.

5.14 Conclusions

The goal of this chapter was to investigate the feasilibty of using modulated electron bunch currents as a means to control the coherence and spectral properties of the emitted radiation. Initially the radiation emitted by single electrons moving in both an ion-channel laser, and undergoing strong acceleration in the LWFA bubble was considered. In both of these cases the strong electrostatic focusing fields of the channel cause the electrons to undergo rapid transverse oscillation and emit XUV and X-ray radiation. In the ion-channel the lack of acceleration means that there is a constant phase difference between subsequent oscillations hence coherent enhancement of radiation at multiples of the fundamental frequency of oscillation. In the LWFA, however, this is not the case and instead the rapid acceleration gives rise to a broadband emission spectrum.

The primary result of this chapter has therefore been demonstrating the use of bunched electron beams to selectively tune narrowband radiation emission from the LFWA. The resulting radiation spectrum is calculated showing that a regularly spaced series of bunches causes coherent enhancement at the spacing wavelength, with interference between the bunches leading to significant radiation only in a small window around the bunch spacing wavelength. The bandwidth scales inversely with the number of bunches in the train, with increasing bunch number leading to increasingly monochromatic radiation. These results have been demonstrated both analytically and numerically. Numerical calculation was performed using a custom particle tracking code developed by the author (Bubblecalc - see appendix C) to calculate the individual electron trajectories within the bubble, and the resulting radiation spectrum calculated using the "radt" code provided by Dr. Enrico Brunetti.

Real electron bunches have a finite distribution in phase-space, and it is therefore necessary to investigate the robustness of this scheme with respect to longitudinal and transverse momentum spread. Due to the statistical nature of the numerical scheme, numerical calculation of these effects requires a prohibitively large number of electrons to be simulated to ensure full coverage of the phase space volume and valid results. Therefore, these effects were investigated analytically using perturbative methods to determine the phase difference and longitudinal bunch spread caused by spreads in the longitudinal and transverse momenta. This resulted in expressions for the evolution of the maximum phase difference and longitudinal spread, which can be compared with the known limits for coherent behaviour (namely a phase difference $\Delta\phi << \pi$ and bunch spread $\Delta S << \lambda_r$). Calculation for typical ALPHA-X parameters demonstrates that such a scheme could viably produce tuned XUV radiation $\lambda \sim 10\,\mathrm{nm}$ with currently achievable beam parameters, subject to the necessary electron bunch spacing being achieved.

Chapter 6

Conclusions

6.1 Controlled Injection

As discussed in the introduction, the key motivation for this work is the need to improve the tunability of LWFA systems to make them useful scientific and industrial tools. This thesis furthers that goal by demonstrating methods for improving the tunability of the LWFA. A scheme for the control of self-injection using plasma density perturbations is outlined and investigated using PIC simulation. The length and charge of the injected bunch can be controlled by changing the shape of the density perturbation in the bulk plasma. Simulations demonstrate the potential for repeatable injection of ultra short electron bunches with lengths down to nm scale. The process is shown to be repeatable multiple times within a short distance, enabling the injection of trains of bunches.

The properties of the injected bunches are very sensitive to the shape of the density perturbation, therefore there is potential for further development of this technique to identify plasma density structures that produce desirable structures in the injected bunch. For example, the identified limitation on the spacing between bunches for a sinusoidal density perturbation may be overcome by having a stepped density distribution so that the bunch does not contract and cause ejection of the injected bunches. Beam loading is also found to be important for the injection of large beam currents. When density gradients well above the injection threshold are used, beam loading effects limit the injection current, leading to longitudinally asymmetric beam current distributions.

Evolution of the laser pulse intensity is also shown to affect self-injection. Sufficiently rapid increases in the intensity, caused by strong relativistic self-focusing, lead to expansion of the bubble and self-injection of electrons, analogous to the effects of density perturbations. For the case where the laser pulse does not self-guide and intensity rapidly reduces, the bubble will shrink and self-injection will be inhibited. This method of causing self-injection is difficult to control reliably, however, due to the non-linear nature of the laser-plasma interaction and laser evolution. Therefore, for density controlled injection the laser pulse must be well matched to the plasma. If this is not the case, variations in bubble size due to the laser evolution can interfere with those caused by the density gradients in the plasma, inhibiting injection or distorting the injected bunch.

The next step in the development of this scheme is experimental verification. The major challenge in this regard is the production of the desired plasma structures. Methods to produce some of these structures are already well developed, and suitable structures can be developed by exploiting careful gas jet nozzle design,[108] supersonic shocks,[128] or by the use of multi-stage gas cells to create suitable plasma density gradients.[129,130]

An appropriate experimental setup would therefore require a gas jet or gas cell with a stable flat top density profile and a matched laser beam with intensity close to, but below the threshold for self-injection. A controlled perturbation with known gradient should then be introduced in the region of constant density. This may be measured by plasma shadography using a suitable probe beam. The length

---

[108] K. Schmid and L. Veisz. *Rev. Sci. Instrum.* **83**, pp. 1–10, 2012.

[128] K. Schmid et al. *Phys. Rev. Spec. Top. Accel Beams* **13**, pp. 1–5, 2010.

[129] M. Vargas et al. *Appl. Phys. Lett.* **104**, p. 174103, 2014.

[130] G. Golovin et al. *Phys. Rev. Spec. Top. Accel Beams* **18**, p. 011301, 2015.

of the bunch can be measured using coherent transition radiation,[131] and the total bunch charge with a Faraday cup, beam transformer or calibrated dosimeters. Varying the magnitude of the density perturbation with reference to theoretical predictions then allows experimental validation of the model described in this thesis.

There are also further theoretical investigations which would enhance the injection scheme investigated in this thesis. In particular, the current method of determining the injection threshold by simulation would benefit from replacement with an analytically determined estimate. Achieving this requires good understanding of the dynamics of the electron sheath at the rear of the bubble. These are known to be highly complex,[21] however, it may be feasible to create a reduced model which reproduces the key behaviours sufficiently to provide a useful estimate of this threshold velocity. Such a model would likely still require the application of numerical methods to solve, but would still produce a result much more rapidly than the current PIC simulation based approach.

The results of simulations have shown that the controlled injection process is highly sensitive to both the plasma structure, and the laser intensity and its evolution. Therefore, to produce the desired stable, repeatable electron beams, the LWFA system components - gas jet or gas cell, and driver beam or laser - must also be highly stable and repeatable. Whilst, historically, this has been problematic, in particular with regard to the stability of laser drivers,[15] continued technological advancements bring ever more precisely controllable systems. These developments, in concert with the continued refinement of LWFA control schemes, promise an exciting new generation of low-cost high energy accelerators for the academic, clinical and industrial communities.

---

[131] J. van Tilborg et al. *Phys. Rev. Lett.* **96**, p. 014801, 2006.

[21] M. R. Islam et al. *New J. Phys.* **17**, p. 093033, 2015.

[15] J. Ferri et al. *Sci. Rep.* **6**, pp. 1–10, 2016.

6.2 Radiation

The second theme of this thesis has been the development of methods to control the betatron radiation produced by the oscillation of injected electron bunches within the LWFA bubble fields. This is again motivated by the need for fine control to take LFWA systems from the laboratory and build compact, turn-key plasma-based radiation sources. Such systems are highly desirable since the plasma-based undulator has a tremendous advantage of scale when compared with a conventional magnet-based FEL wiggler, made feasible by the extreme field strengths within the plasma channel. Whilst XUV and soft X-ray radiation can now routinely be produced from the LWFA,[22] once again, methods for fine control of frequency and bandwidth are required. The work in this thesis supports this by demonstrating the ability to use bunched electron beams, such as those demonstrated in the previous chapter, to select the desired emission frequency and bandwidth. This is shown for both the acceleration-free ion-channel case, and also in the the LWFA. Interference of the radiation emitted by the bunches in the beam causes coherent enhancement at the bunching wavelength, with the bandwith controlled by the number of bunches. Combined with the demonstrated results in the previous chapter this presents the potential to tune the emission of coherent radiation within the $1 - 100\,\mathrm{nm}$ XUV to soft X-ray range, for use in imaging and spectroscopy. Implementation of this method requires bunch spacing on the scale of nanometres, something which the previous results on controlled self-injection have shown to be feasible.

A key requirement for the generation of coherent light from accelerated electrons is good beam quality.[118] This is particularly true for the plasma wiggler, where the transverse oscillation frequency depends on the electron energy, thus a small spread in the bunch energy leads to a rapid loss of coherence. This has

---

[22] A. G. Khachatryan et al. *New J. Phys.* **10**, pp. 1–12, 2008.

[118] B. Ersfeld et al. *New J. Phys.* **16**, p. 093025, 2014.

been investigated analytically using perturbative methods to determine the effect of small energy spread around a reference trajectory on the rate of longitudinal spread and phase shift. From this, beam quality requirements can be found for emission at a desired frequency. For the case of coherent XUV radiation from a typical LWFA, the beam quality requirements are found to require that the energy spread and transverse amplitude spread are constrained to the order of a few percent or less. This ensures that the spread of the bunch length and phase is sufficiently small to avoid strong decoherence of the emitted radiation.

The next step for this work is to perform experimental validation and demonstration of this scheme. The suggested experimental validation for this setup would naturally build on successful demonstration of the previous injection scheme. The laser and plasma parameters should be chosen to ensure that broadband emission of a single bunch has strong emission at the desired frequency. The emitted radiation can then be measured with a suitable spectrometer. Modification of the gas jet or cell design to provide a series of modulations would provide multiple injected bunches with a chosen wavelength. Multiple bunches may then be injected to apply the coherent enhancement effect and the resulting spectrum compared to that for the single bunch.

Attempts to investigate the radiation behaviours by simulation highlighted the difficulties in using Liénard-Wiechert solvers when the phase space occupied by the electron bunch is large, due to the computational time required. It may be worth investigating the possibility of using GPU computing to solve such problems. Modern cards such as the NVIDIA Tesla V100 can achieve performances of 7.5 TFLOPS, compared to CPU performance, which is typically of the order of 10s of GFLOPS for high-end workstation and server hardware. This could potentially provide a two order of magnitude improvement in solver performance, allowing numerical analysis of these scenarios.

6.3 Outlook

The laser wakefield accelerator has already been seen to be a disruptive new technology, the perfection of which promises to vastly reduce the barrier-to-access for electron accelerators and radiation sources. Since the first experimental demonstration in 2004,[11–13] there has been huge technological development in the field of plasma based acceleration. High-energy, beam-driven PWFAs such as the FACET[132] and AWAKE[133] projects, have been built to demonstrate the viability of high energy electron acclerators, driven by existing conventional accelerators. Recent developments in laser technology have also lead to the development of new LWFA facilities such as the Extreme Light Infrastructure (ELI).[134]

At the same time, the cost and compactness of the latest generation of laser systems allows them to be operated by university research labs like the 350 TW SCAPA facility at the University of Strathclyde. These developments, when combined with advancement in tunability and stability such as those demonstrated in this thesis are a path to the democratisation of accelerators and radiation sources. Making these machines accessible and affordable to science, medicine and industry worldwide will open the door to a new era of improved healthcare, advanced materials development and new scientific discovery.

---

[11] S. P. D. Mangles et al. *Nature* **431**, pp. 535–8, 2004.

[12] C. G. R. Geddes et al. *Nature* **431**, pp. 538–541, 2004.

[13] J. Faure et al. *Nature* **431**, pp. 541–544, 2004.

[132] M. Litos et al. *Nature* **515**, pp. 92–95, 2014.

[133] A. Caldwell. *Proc. North Am. Part. Accel. Conf.*, pp. 266–270, 2017.

[134] G. Korn et al. *Proc. Conf. Lasers Electro-Opt.*, JThG2, 2010.

Appendix A

The WKB Approximation

The asymptotic expansion solution for differential equations of the form

$$\frac{\mathrm{d}^2 y}{\mathrm{d}t^2} + \frac{f(t)}{\delta^2} y = 0 \tag{A.1}$$

is variously referred to as the WKB (Wentzel-Kramers-Brillouin), WKBJ (Wentzel-Kramers-Brillouin-Jeffreys), or LG (Liouville-Green) approximation. It has an interesting history, having been rediscovered many times in different fields,[135] most recently by Wentzel, Kramers and Brillouin for solutions to the quantum harmonic oscillator equation[61].

The solution for $y(t)$ is assumed to be expressible as an asymptotic expansion in powers of a small factor δ, such that

$$y(t) = \exp\left[\frac{i}{\delta} S(t)\right] = \exp\left[\frac{i}{\delta} \sum_{n=0}^{\infty} \frac{S_n(t)}{\delta^n}\right] \tag{A.2}$$

and so (A.1) may be rewritten as

$$-\frac{S'^2(t)}{\delta^2} + \frac{iS''(t)}{\delta} + \frac{f(t)}{\delta^2} = 0 \tag{A.3}$$

For $\delta \to 0$ the solution should be well approximated by the first order terms in the expansion of $S(t)$, and so the above may be approximated as

$$\frac{1}{\delta^2}\left[f(t) - S_0'^2(t)\right] + \frac{1}{\delta}\left[iS_0''(t) - 2S_1'(t)S_0'(t)\right] \simeq 0. \tag{A.4}$$

---

[135] R. B. Dingle. *Asymptotic Expansions: Their Derivation and Interpretation*, Academic Press, 1973.

[61] R. Shankar. *Principles of Quantum Mechanics*, Springer US, 1994.

In the limit that $\delta \to 0$ we require that the terms for each power of δ vanish independently, and so the first term in $S(t)$ is given by

$$S_0'(t) = \pm\sqrt{f(t)}S_0(t) = \pm \int_{t_0}^{t} \sqrt{f(t')}\,\mathrm{d}t'. \tag{A.5}$$

We may now continue to find a solution for the second term in $S(t)$ using this solution for $S_0(t)$

$$S_1'(t) = \frac{i}{2}\frac{S_0''(t)}{S_0'(t)} \tag{A.6}$$

which integrates to give.

$$S_1(t) = i \ln \left[S_0(t)^{\frac{1}{2}}\right] + c \tag{A.7}$$

The approximate solution for $y(t)$ to second order in δ is therefore

$$y(t) \simeq y(t_0)\sqrt[4]{\frac{f(t_0)}{f(t)}} \exp\left[\pm\frac{i}{\delta}\int_{t_0}^{t} \sqrt{f(t')}\,\mathrm{d}t'\right], \tag{A.8}$$

however, the process above may be extended to include additional terms of the expansion as required.

Appendix B

SDFTracks: Extracting EPOCH Trajectory Data

SDFTracks is a tool for extracting particle tracks from EPOCH output files, converting them to timeseries data in HDF5 format. Selection critera may be specified to allow extraction of only certain particles. This selection may be bounded to a given time window, but trajectories will be extracted for the whole range of sdf files found. Note that EPOCH must have been run with particle ids and these must be present in the sdf files

B.1 Usage

SDFtracks has no real command line interface, but accepts a single .ini formatted input file which contains all options. This is a deliberate design decision to encourage documentation of analysis steps.

```
user@machine $ sdftracks -h
Usage: sdftracks [-h] <configfile>
Allowed Options:
  -h [ --help ]           Print this help message
    <configfile>            Configuration .ini file
```

B.2 Input File

The configuration file format is .ini, with key = value pairs. The full set of available options is shown in the example below:

```
;; specified values are defaults which will be used if not
   overridden

; epoch species name to consider
species = 'electron'
; minimum gamma particle must achieve (at any point within time
   window)
; to be selected
gamma_min = 10.0

; simulation time during which begin selecting particles for
   trajectory extraction
time_min = 0.0
time_max = 1.79769e+308

; Select at random this fraction of the total particles to output
; (this is useful if there is too much data to handle all selected
   trajectories)
rand_frac = 1.0

; name of output file
output_filename = 'output.h5'

; prefix appended to all epoch sdf files, e.g "sim_" will look for
   files called
; "sim_0000.sdf" and so on. defaults to looking for "0000.sdf" etc.
prefix = ""

; convert units to OSIRIS for input to radiation solver code
```

```
; (this is mostly for use by the Author)
radt_mode = false
```

B.3 HDF5 File Structure

The output file is structured with one group per electron, the subgroups for each electron then contain all available timeseries data.

B.4 Installation

Source code is available from the github repository: https://github.com/ptooley/sdftracks.git

Prerequisites for installation are:

- A C++11 capable compiler (e.g gcc 6 or greater)
- Cmake version 3.6 or later
- Boost version 1.58 or later
- HDF5 (version 1.10 or later recommended)

Installation is then performed by checking out the code, running cmake and then make:

```
user@machine $ git clone https://github.com/ptooley/sdftracks.git
user@machine $ cd sdftracks
user@machine $ cmake .
user@machine $ make
```

Sdftracks can then be found in the ./bin/ directory.

Appendix C

The BubbleCalc Numerical Integrator

BubbleCalc is used to calculate the motion of electrons in an idealised wakefield bubble. Electron bunch and bubble parameters are specified via a configuration file. Output is in hdf5 format with SI units of Orisis units for input to an in-house radiation solver code (radt).

C.1 Usage

Like SDFtracks, BubbleCalc has no real command line interface, but accepts a single .ini formatted input file which contains all options. This is a deliberate design decision to encourage documentation and reproducibility of research.

```
user@machine $ bubblecalc -h
Usage: bubblecalc [-h] <configfile>
Allowed Options:
  -h [ --help ]            Print this help message
    <configfile>             Configuration .ini file
```

C.2 Input File

The configuration file format is .ini, with key = value pairs. The full set of available options is shown in the example below:

```
; Not all fields are required for a valid config, default options are shown where applicable

; Output section contains file handling options
[Output]
; number of timesteps to split trajectory into
nsteps = [no default, integer]

; output filename
filename = [no default, string - must be valid filename]

; make output units compatible with radt (Osiris units - for Author use)
radt_mode = false

; Bubble section contains global physics related parameters
[Bubble]
; laser wavelength providing reference for critical density (units of meters)
lambda0 = [no default, real number]

; plasma density as a fraction of the critical density for given laser wavelength
eta2 = [no default, real number]

; Bunch sections specify properties of individual bunches
; A single file can contain an arbitrary number of bunch sections
; all bunch sections should have a title [Bunch*], e.g
[Bunch1]
```

```
; All units are SI, laser propagation is in the positive x direction
; Input coordinate system is referenced relative to the centre of the bubble
; this means typically bunches will be specified with negative x position

; number of particles in the bunch
npart = [no default, integer]

; total bunch charge, if not set assume each particle represents one electron
q = [no default, integer]

; statistical distributions are set as follows, example of x position:
; ”normal” normal distribution with centre x, standard deviation dx
; ”sin2” sin−squared distribution with centre x and width dx
; ”constant” all values x, dx ignored
; ”linspaced” uniformly spaced over the range x−dx/2 to x+dx/2
; ”” − if unset and dx given, normal distribution, otherwise constant
;xdist = ””

; average x position, defaults to 0
;x = 0.0

; width of x distribution, defaults to 0
;dx = 0.0

; These options are similarly set for the y, z, positions, px, py, pz momentum distributions
; and start time t:

;ydist = ””
```

```
;y = 0.0
;dy = 0.0

;zdist = ""
;z = 0.0
;dz = 0.0

;pxdist = ""
;px = 0.0
;dpx = 0.0

;pydist = ""
;py = 0.0
;dpy = 0.0

;pzdist = ""
;pz = 0.0
;dpz = 0.0

;tdist = ""
;t = 0.0
;dt = 0.0
```

C.3 Output File Structure

The output HDF5 file will contain one group per electron specified in the input file. Each electron group contains time series datasets for the electron motion in either SI units or Osiris units as requested by the user.

C.4 Installation

Source code is available from the github repository: https://github.com/ptooley/bubblecalc.git

Prerequisites for installation are:

- A C++11 capable compiler (e.g gcc 6 or greater)
- Cmake version 3.6 or later
- Boost version 1.58 or later
- HDF5 (version 1.10 or later recommended)

Installation is then performed by checking out the code, running cmake and then make:

```
user@machine $ git clone https://github.com/ptooley/bubblecalc.git
user@machine $ cd bubblecalc
user@machine $ cmake .
user@machine $ make
```

BubbleCalc can then be found in the ./bin/ directory.

Appendix D

Analytic Approximations for Radiation Spectra

A potential strategy for calculating the radiation from an electron performing a single cycle or half cycle of oscillation in an ion channel can be developed beginning from the description for the many cycle radiation given by Esarey *et al.*[121].

Returning to expressions (5.28) to (5.31) for the radiation spectrum, if we do not make the assumption of Esarey *et al.* that interference between terms with $n \neq n'$, we require another strategy to reduce the infinite sums to a calculable expression. We may accomplish this by the following algorithm:

1. Calculate the central harmonic number $n_c(k)$ as

$$n_c = \lfloor \frac{\alpha_0 k}{k_\beta} \rceil, \tag{D.1}$$

   where $\lfloor \ldots \rceil$ indicates rounding to the nearest integer. This gives the summation range in n which is $n_c - \Delta n \leq n \leq n_c + \Delta n$.

2. Calculate initial estimate for the maximum order m_m, p_m, of the Bessel functions $J_n(\alpha_z)$, $J_p(\alpha_x)$. The values used for initial estimates in this work

---

[121] E. Esarey et al. *Phys. Rev. E: Stat., Nonlinear, Soft Matter Phys.* **65**, p. 056505, 2002.

are

$$m_m = \lceil 50 + 2\alpha_z \rceil, \qquad p_m = \lceil 50 + 2\alpha_x \rceil. \tag{D.2}$$

The values of the Bessel functions $J_n(\alpha_z)$, $J_p(\alpha_x)$ over their respective ranges may then be calculated and cached. Convergence checking is performed by confirming that $|J(\alpha)| < \delta_m$ consistently for increasing m and p. If the result does not converge to suitable accuracy the maximum order is increased and the calculation repeated.

The values of m_m, p_m may be cached between calculations for different k and updated as $m_{m,\mathrm{new}} = \lceil m_{m,\mathrm{old}}\, k_{\mathrm{new}}/k_{\mathrm{old}} \rceil$, and similarly for p_m. This allows for tuning to optimise computational time spent against appropriate accuracy.

3. Having calculated the values of the Bessel functions from 0 to the limit in positive order, the values up to the negative order limit can be calculated using the relation $J_{-n}(x) = (-1)^n J_n(x)$. It is also possible to use this relation directly in the calculations in the following step, however, performing them ahead of time reduces the total computational load, as well as greatly simplifying the calculation of I_x, I_z at the cost of a small amount of additional memory. Note that it is also possible for an overestimate of the maximum order to cause calculation underflow, this must also be correctly tested for and handled, and the maximum order of the calculation decreased accordingly.

4. The values of I_x, I_z may now be calculated using the cached values of the Bessel functions. For each n, the calculation range $m_{\mathrm{lo}}(n) \leq m \leq m_{\mathrm{hi}}(n)$ for which there is overlap between the $J_n(\alpha_z)$ and $J_p(\alpha_x)$ is calculated as

$$m_{\mathrm{lo}}(n) = \max\left\{\frac{-n - p_m + 2}{2}, -m_m\right\} \tag{D.3}$$

$$m_{\mathrm{hi}}(n) = \min\left\{\frac{-n + p_m - n - 2}{2}, m_m\right\} \tag{D.4}$$

The values of I_x, I_z are then calculated as

$$\tilde{I}_x = k_\beta r_\beta \sum_{n_c-\Delta n}^{n_c+\Delta n} Q(n,k) \sum_{m_{\mathrm{lo}}(n)}^{m_{\mathrm{hi}}(n)} J_m(\alpha_z)\left[J_{n+2m-1}(\alpha_x) + J_{n+2m+1}(\alpha_x)\right] \tag{D.5}$$

$$\begin{split}\tilde{I}_z = \beta_{z0}\,\mathrm{e}^{i\psi_0} \sum_{n_c-\Delta n}^{n_c+\Delta n} Q(n,k) \sum_{m_{\mathrm{lo}}(n)}^{m_{\mathrm{hi}}(n)} \times \left\{ 2\left(1 - \frac{k_\beta^2 r_\beta^2}{4}\right) J_{n+2m}(\alpha_x) - \right.\\ \left. \frac{k_\beta^2 r_\beta^2}{4}\left[J_{n+2m-2}(\alpha_x) + J_{n+2m+2}(\alpha_x)\right]\right\}.\end{split} \tag{D.6}$$

5. Finally I_x, I_z are used to calculate the components of the spectral energy

$$\frac{\mathrm{d}^2 I_\theta}{\mathrm{d}\omega\,\mathrm{d}\Omega} = \frac{q^2\omega^2}{16\pi^3\varepsilon_0 c}\left|\tilde{I}_x \cos\theta\cos\phi - \tilde{I}_z \sin\theta\right|^2, \tag{5.28 revisited}$$

$$\frac{\mathrm{d}^2 I_\phi}{\mathrm{d}\omega\,\mathrm{d}\Omega} = \frac{q^2\omega^2}{16\pi^3\varepsilon_0 c}\left|\tilde{I}_x \sin\phi\right|^2. \tag{5.29 revisited}$$

which may be summed to give the total spectral energy.

D.0.1 Analytic Approximation of Betatron Radiation

Numerical calculation of betatron radiation requires substantial computational effort to calculate first the electron trajectory and then the radiation. We therefore attempt to approximate the effects of this acceleration, making use of the result for emission by an ion-channel electron over a half-cycle as discussed in section 5.3.3. This approximation should perform well for lower frequency radiation, in particular the incoherent radiation emitted in the XUV and soft x-ray range, however, as we shall see, errors introduced by the approximations in the analytic model cause problems for calculation of potential coherence effects at high frequencies. It is important to perform the summation over the emitted fields rather than simply the intensities, since the phase information encoded within the complex field is crucial for correctly calculating the coherence effects.[136]

Recall from section 3.2.4 that the electron betatron motion may be approximated as relativistic simple harmonic motion in the transverse direction with

---

[136] W. Leemans et al. *IEEE Trans. Plasma Sci.* **33**, pp. 8–22, 2005.

adiabatically increasing total electron energy $\gamma \simeq p_{z\max}(1-\tau^2)$,

$$y(t) = y(t_0)\sqrt[4]{\frac{\gamma_i}{p_{z,\max}(1-\tau^2)}}\cos\left[2\gamma_\phi \arcsin(\tau)\right]. \qquad (3.42 \text{ revisited})$$

The adiabatic nature of the change in γ means that over any small propagation distance, the local portion of the electron trajectory may be reasonably approximated by the ion-channel motion description for an electron with the same momentum and phase.

We have also seen in section 2.7.3 that the majority of the radiation is emitted in the small region around the extrema of the transverse position. Therefore, we may approximate the betatron motion in each of these regions with ion-channel motion. This allows us to write an approximation for the betatron radiation in terms of the analytic results for the acceleration-free case.

For an electron performing betatron motion from time 0 to T and performing with N oscillations, the integral over the motion in the spectral energy calculation (2.93), may be divided into a series of integrals over each oscillation period

$$\begin{aligned}\int_0^T \hat{n}\times[\hat{n}\times\bar{\beta}(t')]\,\mathrm{e}^{ik(ct-\hat{n}\cdot\bar{r}(t'))}\,\mathrm{d}t' = &\int_{T_0}^{T_1} \hat{n}\times[\hat{n}\times\bar{\beta}('t)]\,\mathrm{e}^{ik(ct-\hat{n}\cdot\bar{r}(t'))}\,\mathrm{d}t' + \\ &\int_{T_1}^{T_2} \hat{n}\times[\hat{n}\times\bar{\beta}(t')]\,\mathrm{e}^{ik(ct-\hat{n}\cdot\bar{r}(t'))}\,\mathrm{d}t' + \ldots,\end{aligned} \tag{D.7}$$

where the times T_n are the times of successive z-axis crossings. Each of these integrals may be approximated by the result for an electron performing a half-cycle of ion-channel motion with parameters equal to those of the betatron motion at each extremum of the motion. Therefore, the integral in (2.93) is approximated by

$$\int_0^t \hat{n}\times[\hat{n}\times\bar{\beta}(t')]\,\mathrm{e}^{ik(ct-\hat{n}\cdot\bar{r}(t'))}\,\mathrm{d}t' \simeq \sum_{n=0}^{N}\mathrm{e}^{i\Phi_n}\int_{-Tn/2}^{T_n/2}\hat{n}\times(\hat{n}\times\bar{\beta_n})\,\mathrm{e}^{ik(ct-\hat{n}\cdot\bar{r_n})}\,\mathrm{d}t. \tag{D.8}$$

The position r_n, velocity β_n and time T_n are for a half-cycle of the ion channel motion given by the ion-channel motion equations (5.10) to (5.13), for the electron parameters at the time t_n. The replacement of the true integral over the motion with the discrete sum of solutions for individual oscillations requires an additional phase term $\mathrm{e}^{i\Phi_n}$ in order to correctly model the interference between emissions from sucessive cycles. Because the majority of the radiation occurs at the extrema of the transverse motion, this point is used to calculate the relative phase of each contribution as $\Phi_n = k[ct_n - \hat{n} \cdot \bar{r}(t_n)]$.

Recalling the expressions for the betatron motion derived in section 3.2.4,

$$\gamma(\tau) = \gamma_d(1-\tau^2), \tag{3.41 revisited}$$

$$y(\tau) = Y_0 \sqrt[4]{\frac{1}{1-\tau^2}} \cos\left[2\gamma_\phi \arcsin(\tau) + \phi_0\right], \tag{3.42 revisited}$$

we see that the extrema of the transverse motion occur when the phase term is a multiple of π. Therefore, the values of τ at each extremum are given by

$$\tau = -\sin\left(\frac{m\pi - \phi_0}{2\gamma_\phi}\right), \tag{D.9}$$

for $1 \leq m \leq 2\gamma_\phi$. From the value of τ the energy γ and transverse amplitude $y_\beta(t)$ can then be calculated in order to find the field contribution for the half cycle.

The electron longitudinal position must also be calculated in order to find the correct phase $\Phi_n = k[ct_n - \hat{n} \cdot \bar{r}(t_n)]$ for each contribution. As we saw in section 2.7.4, the resonant frequencies of the coherent radiation are dependent upon the distance the electrons slip back relative to the emitted radiation. The lack of a closed-form analytic expression for $r(t)$ is potentially problematic here, because the phase factor is sensitive to errors in the difference term of order k^{-1}. Therefore, correct calculation of the phase requires the error in the longitudinal position to be smaller than k_β/k and for hard x-ray frequencies this can be a relative error tolerance smaller than 10^{-7}. This can be achieved with high quality numerical integration algorithms such as those implemented in the GSL,[49] which include error estimation and correction strategies.

---

[49] M. Galassi et al. *GNU Scientific Library*, GNU Software Foundation,

There is also the issue of the assumptions in creating the analytic approximation. As is discussed in section 3.2.4, the model is not fully self-consistent and only the zero-order contribution to the longitudinal acceleration is included. Due to the sensitivity of the phase term to the correct calculation of the longitudinal position this may alter the calculated interference behaviour at high frequencies.

Appendix E

PIC Input Files

For completeness and reproducibility the input files used to perform the simulations in this thesis are recorded here. EPOCH simulations were run using EPOCH versions between 4.7 and 4.12, FBPIC simulations were run using version 0.7.1. If attempting to reproduce results it is advisable to rerun with the latest version of the code which may include additional bug fixes and performance improvements.

E.1 Epoch Input Decks

All EPOCH simulations in this thesis were undertaken using the same fundmental input file structure shown below. The constants block at the head of the script contains all relevant variables used for controlling the simulation parameters described in this thesis.

Listing E.1: EPOCH input deck template.

```
# Density Controlled Injection Input Deck #

### Phil Tooley 2016

###### Constants Block ######

#All the most commonly altered properties of the sim can be changed
    here

begin:constant
```

```
### basic laser parameters

  las_lambda = 0.8*micro
  las_t_peak = 25*femto
  las_t_fwhm = 10*femto
  las_spot_size = 20*micron
  las_a0 = 4.0
  las_phase = 0

  # laser derived parameters
  las_intensity = 1.384e18 * las_a0^2 / (las_lambda / micro)^2 #W/cm
     ^2
  las_trans_profile = gauss(y,0,las_spot_size)
  las_t_w = las_t_fwhm / (2*loge(2))
  las_t_prof = gauss(time,las_t_peak,las_t_w)
  las_omega = 2.0*pi*c/las_lambda

### plasma parameters

  plas_n_crit = critical(las_omega)
  plas_ramp_start = 0
  plas_ramp_end = 300*micro
  plas_plat_n = 0.001*plas_n_crit
  plas_osc_amp = 0.0
  spike_half_width = 50*micro
  spike1_x = 500*micro
  spike2_x = 800*micro
  spike3_x = 1100*micro
  plas_spike_n = plas_plat_n * plas_osc_amp

  # this sets the plasma density to be a linear ramp from 0 to
     plas_plat_n, over the range
  # plas_ramp_start to plas_ramp_end

  spikes = plas_spike_n * (sin(pi*(x-spike_half_width)/(2*
     spike_half_width)))^2
  spike1 = if( x gt (spike1_x - spike_half_width), if( x lt (
     spike1_x + spike_half_width), spikes, 0), 0)
  spike2 = if( x gt (spike2_x - spike_half_width), if( x lt (
     spike2_x + spike_half_width), spikes, 0), 0)
  spike3 = if( x gt (spike3_x - spike_half_width), if( x lt (
     spike3_x + spike_half_width), spikes, 0), 0)
  plas_spikes = plas_plat_n + spike1 + spike2 + spike3
  plas_n = if( x lt plas_ramp_start, 0, if(x lt plas_ramp_end,
     plas_plat_n * (x - plas_ramp_start)/(plas_ramp_end -
     plas_ramp_start), plas_spikes ))

### Laser group velocity

  plas_freq_max = sqrt((plas_plat_n * qe^2)/(epsilon0 * me))
  las_vg_min = c * sqrt(1-(plas_freq_max/las_omega)^2)

### Grid Parameters

  # Pseudoparticles per cell
```

```
    # N.B to be trustworthy a simulation should not change its
       result when
    # you change the number of particles per cell, if it does, you
       need more!

  part_per_cell = 16     #somewhere between 12-16 is good for 2D

  # Cell size
  cell_length = 0.04*micro  #be sure to resolve both the plasma
     wavelength and laser wavelength
  cell_width = 0.20*micro    #ditto, be especially careful if your
     laser has large Ey/Ez components
                            # i.e circular polarisation or very
                               short pulses

  # Box size
  half_width = 45*micro      # width from the centre of the box to
     the edge, box width is twice this
  length = 90*micro          # be sure to leave room for the laser to
      slowly drop back in the window

  # Grid offset from origin
  offset_long = 0.0          # these are really here for pedantic
     purposes
  offset_width = 0.0

### End condition

  prop_length = 1500 * micro   # I find it easier to think about the
      literal length of a simulation
  end_time = prop_length /c   # but you can set a temporal length if
      you prefer

### Output parameters
  output_step = 2.1 * micro            # again I tend to think about
     the distance between snapshots
  output_timestep = output_step / c   # rather than the time

end:constant

begin:control

# Most of this is actually set up in the constants block above,
   apart from the restart shapshot

  # restart_snapshot = roll0000.sdf

  dlb_threshold = 0.5

### Should never need to shange things below here.

### Grid parameters

  nx = nint(length / cell_length)
  ny = nint((half_width * 2) / cell_width)
  npart = part_per_cell * nx * ny
```

```
  t_end = end_time

  x_min = offset_long
  x_max = offset_long + length
  y_min = offset_width − half_width
  y_max = offset_width + half_width

  stdout_frequency = 10

  use_random_seed = F

  use_exact_restart = T

end:control

### Output blocks control the output files produced

begin:output

  # There are too many options here to describe, so look at the
     manual for a full picture of
  # all the ueful things you can do here.
  #
  # Currently it is set up to dump information on the EM fields,
     some basic statistical particle
  # information such as mean kinetic energy (ekbar), charge and
     number densities and temperatures,
  # additionally a second, less regular dump outputs the individual
     particle information, (this
  # will be a much bigger file so be careful), and finally a rolling
     restart dump is used so that
  # an interrupted sim can be restarted with minimal CPU time lost.

  name = main

  dt_snapshot = output_timestep

  grid = always
  ex = always
  ey = always
  ez = restart
  bx = always
  by = restart
  bz = always
  jx = restart
  jy = restart
  ekbar = restart
  mass_density = restart
  charge_density = restart
  number_density = always + species + no_sum
  temperature = restart

  distribution_functions = never
  particle_probes = never
```

```
  particles = always
  id = always
  px = always
  py = always
  gamma = always
  particle_weight = always

end:output

#begin:output

#name = restart

#dt_snapshot = output_timestep * 10

#restartable = T

#end:output

#!!!!! Here be dragons !!!!!!

# Beyond here are the nitty gritty details of setting up the
   simulations, with a lot of potential
# for confusing and (cpu time) costly mistakes.  All the possible
   options are detailed in the
# manual, but I have broken out the common things I might want to
   change into the constants block at
# the top to make my life easier.


begin:window

# This controls the moving window, the velocity is set in the
   constants block so you can likely
# just leave this be.  It starts the window moving once the front of
    the laser is ~9/10 of the
# way through the box.  If you find your laser colliding with the
   box edge you can change this

  move_window = T
  window_v_x = las_vg_min
  window_start_time = 0.9 * length / las_vg_min
  bc_x_min_after_move = simple_outflow
end:window

begin:boundaries

# Unlikely you will need to change these, unless you *need* CPML,
   which means no moving window

  bc_x_min = simple_laser
  bc_x_max = simple_outflow
  bc_y_min = simple_outflow
  bc_y_max = simple_outflow

end:boundaries
```

```
begin:species
  # Should never need to change these
  name = electron
  charge = -1.0
  mass = 1.0
  frac = 0.5

  density = plas_n
  temp = 0*ev

  dumpmask = always

end:species

begin:species
  # Should never need to change these
  name = helium
  charge = 1.0
  mass = 1836.0 * 4
  frac = 0.5

  density = plas_n
  temp = 0*ev

  dumpmask = restart

end:species

begin:laser

  #shouldn't need to change much in here
  boundary = x_min
  id = 1
  intensity_w_cm2 = las_intensity
  lambda = las_lambda
  pol_angle = 0.0
  phase = las_phase
  t_profile = las_t_prof
  profile = las_trans_profile
end:laser
```

E.2 FBPIC Setup Files

Similar to the EPOCH simulations, all FBPIC simulations were performed using the same common template file to control the simulation. All relevant parameters may be set in the constants section at the top of the file.

Listing E.2: FBPIC input deck template.

```
"""
This is a typical input script that runs a simulation of
laser-wakefield acceleration using FBPIC.

Usage
-----
- Modify the parameters below to suit your needs
- Type "python -i lwfa_script.py" in a terminal
- When the simulation finishes, the python session will *not* quit.
    Therefore the simulation can be continued by running sim.step()

Help
----
All the structures implemented in FBPIC are internally documented.
Enter "print(fbpic_object.__doc__)" to have access to this
   documentation,
where fbpic_object is any of the objects or function of FBPIC.
"""

# -------
# Imports
# -------
import numpy as np
from scipy.constants import c, e, epsilon_0, m_e
# Import the relevant structures in FBPIC
from fbpic.main import Simulation
from fbpic.lpa_utils.laser import add_laser
from fbpic.openpmd_diag import FieldDiagnostic, ParticleDiagnostic,
   \
     set_periodic_checkpoint, restart_from_checkpoint

# ----------
# Parameters
# ----------

# Whether to use the GPU
use_cuda = True

# The simulation box
Nz = 2000          # Number of gridpoints along z
zmax = 0.e-6     # Right end of the simulation box (meters)
zmin = -60.e-6    # Left end of the simulation box (meters)
Nr = 400           # Number of gridpoints along r
rmax = 60.e-6     # Length of the box along r (meters)
Nm = 2            # Number of modes used

# The simulation timestep
dz = (zmax - zmin)/Nz
dt = dz/c   # Timestep (seconds)
N_step = int(5e-3/dz)     # Number of iterations to perform

# The plasma
eta = 0.001
p_zmin = 0.e-6  # Position of the beginning of the plasma (meters)
p_zmax = 20.e-3  # Position of the end of the plasma (meters)
```

```
p_rmin = 0.      # Minimal radial position of the plasma (meters)
p_rmax = rmax  # Maximal radial position of the plasma (meters)
p_nz = 2         # Number of particles per cell along z
p_nr = 2         # Number of particles per cell along r
p_nt = 4         # Number of particles per cell along theta

# The laser
l_lambda = 800e-9  # Laser wavelength
l_a0 = 3.          # Laser amplitude
l_w0 = 15.e-6      # Laser waist
l_tau = 25.e-15    # Laser duration FWHM
l_z0 = -14.e-6      # Laser centroid
l_zf = l_z0        # Laser focus

# Derived parameters
l_ctau = l_tau * c / np.sqrt(2*np.log(2))
n_c = ( 2 * np.pi * c /(l_lambda * e))**2 * epsilon_0 * m_e
n_e = eta * n_c  # Density (electrons.meters^-3)

# The moving window
v_window = c       # Speed of the window

# The diagnostics and the checkpoints/restarts
diag_period = 100         # Period of the diagnostics in number of
   timesteps
save_checkpoints = True # Whether to write checkpoint files
checkpoint_period = diag_period * (N_step // diag_period)   # Period
    for writing the checkpoints
use_restart = False      # Whether to restart from a previous
   checkpoint
track_electrons = False  # Whether to track and write particle ids

# The density profile
ramp_start = 0.e-6
ramp_length = 150.e-6
bump_width = 50e-6
bump1 = 300e-6
bump2 = 700e-6
alpha = 0.10

def dens_func( z, r ) :
    """Returns relative density at position z and r"""
    # Allocate relative density
    n = np.ones_like(z)
    # Make linear ramp
    n = np.where( z<ramp_start+ramp_length, (z-ramp_start)/
       ramp_length, n )
    # Supress density before the ramp
    n = np.where( z<ramp_start, 0., n )
    # make density bump 1
    n = np.where(np.logical_and(z > bump1-bump_width, z < bump1+
       bump_width),
                 1 + alpha*np.cos(0.5*np.pi*(z-bump1)/bump_width)
                    **2, n)
    # make density bump 2
```

```
    n = np.where(np.logical_and(z > bump2-bump_width, z < bump2+
        bump_width),
                1 + alpha*np.cos(0.5*np.pi*(z-bump2)/bump_width)
                    **2, n)

    return(n)

# -------------------------------
# Carrying out the simulation
# -------------------------------

# NB: The code below is only executed when running the script,
# (`python -i lpa_sim.py`), but not when importing it (`import
    lpa_sim`).
if __name__ == '__main__':

    # Initialize the simulation object
    sim = Simulation( Nz, zmax, Nr, rmax, Nm, dt,
        p_zmin, p_zmax, p_rmin, p_rmax, p_nz, p_nr, p_nt, n_e,
        dens_func=dens_func, zmin=zmin, boundaries='open',
        use_cuda=use_cuda)

    # Load initial fields
    # Add a laser to the fields of the simulation
    add_laser( sim, l_a0, l_w0, l_ctau, l_z0, l_zf, lambda0=l_lambda
        )

    if use_restart is False:
        # Track electrons if required (species 0 correspond to the
            electrons)
        if track_electrons:
            sim.ptcl[0].track( sim.comm )
    else:
        # Load the fields and particles from the latest checkpoint
            file
        restart_from_checkpoint( sim )

    # Configure the moving window
    sim.set_moving_window( v=v_window )

    # Add a field diagnostic
    sim.diags = [ FieldDiagnostic( diag_period, sim.fld, comm=sim.
        comm ),
                ParticleDiagnostic(diag_period, {"electrons" : sim.
                    ptcl[0]},
                                select={"uz" : [1., None ]},
                                    comm=sim.comm)
                ]
    # Add checkpoints
    if save_checkpoints:
        set_periodic_checkpoint( sim, checkpoint_period )

    ### Run the simulation
    sim.step( N_step )
    print('')
```

Additional Acknowledgements

My thanks to Siarhei Khirevich (http://www.khirevich.com/latex/bibliography/) on whose work the biblatex styles in this thesis are based.

[1] M. P. Tooley, B. Ersfeld, S. R. Yoffe, A. Noble, E. Brunetti, Z. M. Sheng, M. R. Islam, and D. A. Jaroszynski. "Towards Attosecond High-Energy Electron Bunches: Controlling Self-Injection in Laser-Wakefield Accelerators Through Plasma-Density Modulation". *Physical Review Letters* 119, p. 044801, 2017. (See pp. ii, 22)

[2] J. D. Cockcroft and E. T. S. Walton. "Artificial Production of Fast Protons". *Nature* 129, p. 242, 1932. (See p. 1)

[3] S. Hanna. *RF linear accelerators for medical and industrial applications.* English. Boston: Artech House, 2013. (See pp. 1, 6)

[4] J. V. Crivello. "UV and electron beam-induced cationic polymerization". *Nuclear Instruments and Methods in Physics Research Section B: Beam Interactions with Materials and Atoms* 151, pp. 8–21, 1999. (See p. 1)

[5] E. O. Lawrence and M. S. Livingston. "The Production of High Speed Light Ions Without the Use of High Voltages". *Physical Review* 40, pp. 19–35, 1932. (See p. 1)

[6] W. E. Parkins. "The Uranium Bomb, the Calutron, and the Space-Charge Problem". *Physics Today* 58, pp. 45–51, 2005. (See p. 2)

[7] T. Tajima and J. M. Dawson. "Laser electron accelerator". *Physical Review Letters* 4, pp. 267–270, 1979. (See p. 3)

[8] P. Chen, J. M. Dawson, R. W. Huff, and T. Katsouleas. "Acceleration of Electrons by the Interaction of a Bunched Electron Beam with a Plasma".

Physical Review Letters 54, pp. 693–696, 1985. arXiv: `arXiv:1011.1669v3`. (See p. 3)

[9] J. B. Rosenzweig, B. Breizman, T. Katsouleas, and J. J. Su. “Acceleration and focusing of electrons in two-dimensional nonlinear plasma wake fields”. *Physical Review A* 44, 1991. (See pp. 4, 46, 47)

[10] A. Pukhov and J. Meyer-ter-Vehn. “Laser wake field acceleration: the highly non-linear broken-wave regime”. *Applied Physics B: Lasers and Optics* 74, pp. 355–361, 2002. (See pp. 4, 46, 47, 80)

[11] S. P. D. Mangles, C. D. Murphy, Z. Najmudin, A. G. R. Thomas, J. L. Collier, A. E. Dangor, E. J. Divall, P. S. Foster, J. G. Gallacher, C. J. Hooker, D. A. Jaroszynski, A. J. Langley, W. B. Mori, P. A. Norreys, F. S. Tsung, R. Viskup, B. R. Walton, and K. Krushelnick. “Monoenergetic beams of relativistic electrons from intense laser-plasma interactions.” *Nature* 431, pp. 535–8, 2004. (See pp. 4, 195)

[12] C. G. R. Geddes, C. Toth, J. van Tilborg, E. Esarey, C. B. Schroeder, D. L. Bruhwiler, C. Nieter, J. Cary, and W. P. Leemans. “High-quality electron beams from a laser wakefield accelerator using plasma-channel guiding”. *Nature* 431, pp. 538–541, 2004. (See pp. 4, 195)

[13] J. Faure, Y. Glinec, A. Pukhov, S. Kiselev, S. Gordienko, E. Lefebvre, J.-P. Rousseau, F. Burgy, and V. Malka. “A laser–plasma accelerator producing monoenergetic electron beams”. *Nature* 431, pp. 541–544, 2004. (See pp. 4, 195)

[14] S. P. Mangles, A. G. Thomas, O. Lundh, F. Lindau, M. C. Kaluza, A. Persson, C. G. Wahlström, K. Krushelnick, and Z. Najmudin. “On the stability of laser wakefield electron accelerators in the monoenergetic regime”. *Physics of Plasmas* 14, 2007. (See p. 4)

[15] J. Ferri, X. Davoine, S. Fourmaux, J. C. Kieffer, S. Corde, K. Ta Phuoc, and A. Lifschitz. "Effect of experimental laser imperfections on laser wakefield acceleration and betatron source". *Scientific Reports* 6, pp. 1–10, 2016. (See pp. 4, 192)

[16] I. Kostyukov, A. Pukhov, and S. Kiselev. "Phenomenological theory of laser-plasma interaction in "bubble" regime". *Physics of Plasmas* 11, p. 5256, 2004. (See pp. 5, 46–48, 51, 80, 118, 173)

[17] S. Y. Kalmykov, A. Beck, S. A. Yi, V. N. Khudik, M. C. Downer, E. Lefebvre, B. A. Shadwick, and D. P. Umstadter. "Electron self-injection into an evolving plasma bubble: Quasi-monoenergetic laser-plasma acceleration in the blowout regime". *Physics of Plasmas* 18, p. 056704, 2011. (See p. 5)

[18] F. Y. Li, Z. M. Sheng, M. Chen, L. L. Yu, J. Meyer-ter-Vehn, W. B. Mori, and J. Zhang. "Radially polarized, half-cycle, attosecond pulses from laser wakefields through coherent synchrotronlike radiation". *Physical Review E: Statistical, Nonlinear, and Soft Matter Physics* 90, p. 043104, 2014. arXiv: `1401.2799`. (See pp. 5, 81)

[19] D. Lu, X.-Y. Zhao, B.-S. Xie, M. Ali Bake, H.-B. Sang, and H.-C. Wu. "Electrons trajectories around a bubble regime in intense laser plasma interaction". *Physics of Plasmas* 20, p. 063104, 2013. (See pp. 5, 62)

[20] A. G. R. Thomas. "Scalings for radiation from plasma bubbles". *Physics of Plasmas* 17, pp. 1–12, 2010. (See pp. 5, 38, 39, 51, 58)

[21] M. R. Islam, E. Brunetti, R. P. Shanks, B. Ersfeld, R. C. Issac, S. Cipiccia, M. P. Anania, G. H. Welsh, S. M. Wiggins, A. Noble, R. A. Cairns, G. Raj, and D A Jaroszynski. "Near-threshold electron injection in the laser–plasma wakefield accelerator leading to femtosecond bunches". *New Journal of Physics* 17, p. 093033, 2015. (See pp. 5, 61, 62, 81, 119, 121, 192)

[22] A. G. Khachatryan, F. A. Van Goor, and K. J. Boller. “Coherent and incoherent radiation from a channel-guided laser wakefield accelerator”. *New Journal of Physics* 10, pp. 1–12, 2008. (See pp. 5, 124, 193)

[23] M. Fuchs, R. Weingartner, A. Popp, Z. Major, S. Becker, J. Osterhoff, I. Cortrie, B. Zeitler, R. Hörlein, G. D. Tsakiris, U. Schramm, T. P. Rowlands-Rees, S. M. Hooker, D. Habs, F. Krausz, S. Karsch, and F. Grüner. “Laser-driven soft-X-ray undulator source”. *Nature Physics* 5, pp. 826–829, 2009. (See pp. 6, 124)

[24] A. Bernhard, V. Afonso Rodríguez, S. Kuschel, M. Leier, P. Peiffer, A. Sävert, M. Schwab, W. Werner, C. Widmann, A. Will, A.-S. Müller, and M. Kaluza. “Progress on experiments towards LWFA-driven transverse gradient undulator-based FELs”. *Nuclear Instruments and Methods in Physics Research Section A: Accelerators, Spectrometers, Detectors and Associated Equipment*, 2017. arXiv: `1712.04740`. (See p. 6)

[25] B. Hidding, J. B. Rosenzweig, Y. Xi, B. O’Shea, G. Andonian, D. Schiller, S. Barber, O. Williams, G. Pretzler, T. Königstein, F. Kleeschulte, M. J. Hogan, M. Litos, S. Corde, W. W. White, P. Muggli, D. L. Bruhwiler, and K. Lotov. “Beyond injection: Trojan horse underdense photocathode plasma wakefield acceleration”. *AIP Conference Proceedings*. **1507**. 2002. Proc. AIP. 2012. Pp. 570–575. (See p. 6)

[26] M. Zeng, M. Chen, L. L. Yu, W. B. Mori, Z. M. Sheng, B. Hidding, D. A. Jaroszynski, and J. Zhang. “Multichromatic Narrow-Energy-Spread Electron Bunches from Laser-Wakefield Acceleration with Dual-Color Lasers”. *Physical Review Letters* 114, p. 084801, 2015. arXiv: `1406.7106`. (See p. 6)

[27] J. Vieira, S. F. Martins, V. B. Pathak, R. A. Fonseca, W. B. Mori, and L. O. Silva. “Magnetic Control of Particle Injection in Plasma Based Accel-

erators". *Physical Review Letters* 106, p. 225001, 2011. arXiv: `1107.4912`. (See p. 6)

[28] J. Kruger and M. Bovyn. "Relativistic motion of a charged particle in a plane electromagnetic wave with arbitrary amplitude". *Journal of Physics A: Mathematical and General* 9, pp. 1841–1846, 1976. (See p. 16)

[29] E. Sarachik and G. Schappert. "Classical Theory of the Scattering of Intense Laser Radiation by Free Electrons". *Physical Review D: Particles and Fields* 1, pp. 2738–2753, 1970. (See p. 16)

[30] J. D. Lindl. "Ponderomotive Force on Laser-Produced Plasmas". *Physics of Fluids* 14, p. 371, 1971. (See p. 17)

[31] D. Bauer, P. Mulser, and W. H. Steeb. "Relativistic Ponderomotive Force, Uphill Acceleration, and Transition to Chaos". *Physical Review Letters* 75, pp. 4622–4625, 1995. (See p. 17)

[32] P. Gibbon. *Short Pulse Laser Interactions with Matter: An Introduction*. Imperial College Press, 2007. (See p. 17)

[33] P. M. Bellan. *Fundamentals of Plasma Physics*. Cambridge: Cambridge University Press, 2006. (See pp. 19, 20)

[34] C. K. Birdsall and A. B. Langdon. *Plasma physics via computer simulation*. McGraw-Hill, 1985. (See pp. 20, 21)

[35] K. S. Yee. "Numerical solution of initial boundary value problems involving maxwell's equations in isotropic media". *IEEE Transactions on Antennas and Propagation* 14, pp. 302–307, 1966. (See pp. 20, 21)

[36] B. M. Cowan, D. L. Bruhwiler, J. R. Cary, E. Cormier-Michel, and C. G. R. Geddes. "Generalized algorithm for control of numerical dispersion in explicit time-domain electromagnetic simulations". *Physical Review Special Topics - Accelerators and Beams* 16, p. 041303, 2013. (See p. 20)

[37] T. D. Arber, K. Bennett, C. S. Brady, A. Lawrence-Douglas, M. G. Ramsay, N. J. Sircombe, P. Gillies, R. G. Evans, H. Schmitz, A. R. Bell, and C. P. Ridgers. “Contemporary particle-in-cell approach to laser-plasma modelling”. *Plasma Physics and Controlled Fusion* 57, p. 113001, 2015. (See pp. 21, 22, 98)

[38] J.-L. Vay, C. Geddes, E. Cormier-Michel, and D. Grote. “Numerical methods for instability mitigation in the modeling of laser wakefield accelerators in a Lorentz-boosted frame”. *Journal of Computational Physics* 230, pp. 5908–5929, 2011. (See p. 21)

[39] R. Lehe, M. Kirchen, I. A. Andriyash, B. B. Godfrey, and J. L. Vay. “A spectral, quasi-cylindrical and dispersion-free Particle-In-Cell algorithm”. *Computer Physics Communications* 203, pp. 66–82, 2015. arXiv: `1507.04790`. (See p. 22)

[40] C. D. Decker, W. B. Mori, K. C. Tzeng, and T. C. Katsouleas. “Modeling single-frequency laser-plasma acceleration using particle-in-cell simulations: The physics of beam breakup”. *IEEE Transactions on Plasma Science* 24, pp. 379–392, 1996. (See p. 22)

[41] K. C. Tzeng and W. B. Mori. “Suppression of electron ponderomotive blowout and relativistic self-focusing by the occurrence of raman scattering and plasma heating”. *Physical Review Letters* 81, pp. 104–107, 1998. (See p. 22)

[42] M. Zeng, M. Chen, Z. M. Sheng, W. B. Mori, and J. Zhang. “Self-truncated ionization injection and consequent monoenergetic electron bunches in laser wakefield acceleration”. *Physics of Plasmas* 21, 2014. arXiv: `1312.5825`. (See p. 22)

[43] J. Jackson. *Classical Electrodynamics*. 3rd ed. Wiley, 1999. (See pp. 24, 28, 31)

[44] M. Kaku. *Quantum Field Theory: A Modern Introduction.* Oxford University Press, 1993. (See p. 24)

[45] J. H. Poynting. “On the Transfer of Energy in the Electromagnetic Field”. *Philosophical Transactions of the Royal Society of London* 175, pp. 343–361, 1884. (See p. 28)

[46] A. Garg. *Classical Electrodynamics in a Nutshell.* Princeton University Press, 2012. (See pp. 28, 31)

[47] K. F. Riley, M. P. Hobson, and S. J. Bence. *Mathematical Methods for Physics and Engineering.* Cambridge University Press, 2006. (See p. 32)

[48] E. Jones, T. Oliphant, P. Peterson, et al. *SciPy: Open source scientific tools for Python* (see p. 38)

[49] M. Galassi, J. Davies, J. Theiler, B. Gough, G. Jungman, P. Alken, M. Booth, F. Rossi, and R. Ulerich. *GNU Scientific Library.* GNU Software Foundation. (See pp. 38, 146, 210)

[50] A. I. Akhiezer and R. V. Polovin. “Theory of Wave Motion of an Electron Plasma”. *Journal of Experimental and Theoretical Physics* 3, pp. 696–705, 1956. (See p. 40)

[51] J. M. Dawson. “Nonlinear Electron Oscillations in a Cold Plasma”. *Physical Review* 113, pp. 383–387, 1959. (See p. 41)

[52] J. M. Dawson and C. Oberman. “Oscillations of a Finite Cold Plasma in a Strong Magnetic Field”. *Physics of Fluids* 2, pp. 103–111, 1959. (See p. 41)

[53] E. Esarey, C. B. Schroeder, and W. P. Leemans. “Physics of laser-driven plasma-based electron accelerators”. *Reviews of Modern Physics* 81, pp. 1229–1285, 2009. (See pp. 47, 73, 74)

[54] W. Lu, C. Huang, M. Zhou, M. Tzoufras, F. S. Tsung, W. B. Mori, and T. Katsouleas. “A nonlinear theory for multidimensional relativistic plasma wave wakefields”. *Physics of Plasmas* 13, p. 056709, 2006. (See p. 47)

[55] S. A. Yi, V. Khudik, C. Siemon, and G. Shvets. “Analytic model of electromagnetic fields around a plasma bubble in the blow-out regime”. *Physics of Plasmas* 20, p. 013108, 2013. (See pp. 47, 48, 62, 118)

[56] W. Lu, C. Huang, M. Zhou, W. B. Mori, and T. Katsouleas. “Nonlinear Theory for Relativistic Plasma Wakefields in the Blowout Regime”. *Physical Review Letters* 96, p. 165002, 2006. (See pp. 48, 62, 81)

[57] I. Kostyukov, E. Nerush, A. Pukhov, and V. Seredov. “A multidimensional theory for electron trapping by a plasma wake generated in the bubble regime”. *New Journal of Physics* 12, p. 045009, 2010. (See pp. 48, 81, 118)

[58] P. Sprangle, E. Esarey, and A. Ting. “Nonlinear theory of intense laser-plasma interactions”. *Physical Review Letters* 64, pp. 2011–2014, 1990. (See pp. 50, 69)

[59] S. Corde, K. T. Phuoc, G. Lambert, R. Fitour, V. Malka, A. Rousse, A. Beck, and E. Lefebvre. “Femtosecond x rays from laser-plasma accelerators”. *Reviews of Modern Physics* 85, pp. 1–48, 2013. (See pp. 51, 54)

[60] H. Goldstein, C. P. Poole, and J. L. Safko. *Classical Mechanics*. Addison-Wesley series in physics. Addison Wesley, 2002. (See pp. 54, 64)

[61] R. Shankar. *Principles of Quantum Mechanics*. Boston, MA: Springer US, 1994. (See pp. 54, 196)

[62] S. M. Hooker. “Developments in laser-driven plasma accelerators”. *Nature Photonics* 7, pp. 775–782, 2013. (See p. 61)

[63] X. Yang, E. Brunetti, D. R. Gil, G. H. Welsh, F. Y. Li, S. Cipiccia, B. Ersfeld, D. W. Grant, P. A. Grant, M. R. Islam, M. P. Tooley, G. Vieux, S. M. Wiggins, Z. M. Sheng, and D. A. Jaroszynski. “Three electron beams

from a laser-plasma wakefield accelerator and the energy apportioning question". *Scientific Reports* 7, pp. 1–10, 2017. (See pp. 62, 121)

[64] X. F. Li, Y. J. Gu, Q. Yu, S. Huang, F. Zhang, Q. Kong, and S. Kawata. "Dependence of electron trapping on bubble geometry in laser-plasma wakefield acceleration". *Physics of Plasmas* 21, p. 73109, 2014. (See pp. 62, 121)

[65] K. Floettmann. "Some basic features of the beam emittance". *Physical Review Special Topics - Accelerators and Beams* 6, pp. 80–86, 2003. (See p. 63)

[66] T. Mehrling, J. Grebenyuk, F. S. Tsung, K. Floettmann, and J. Osterhoff. "Transverse emittance growth in staged laser-wakefield acceleration". *Physical Review Special Topics - Accelerators and Beams* 15, p. 111303, 2012. (See pp. 64, 78)

[67] E. Esarey, P. Sprangle, J. Krall, and A. Ting. "Self-focusing and guiding of short laser pulses in ionizing gases and plasmas". *IEEE Journal of Quantum Electronics* 33, pp. 1879–1914, 1997. (See pp. 67, 69)

[68] H. Hora. "Theory of relativistic self-focusing of laser radiation in plasmas". *Journal of the Optical Society of America* 65, p. 882, 1975. (See pp. 67, 69)

[69] B. Ritchie. "Relativistic self-focusing and channel formation in laser-plasma interactions". *Physical Review E: Statistical, Nonlinear, and Soft Matter Physics* 50, R687–R689, 1994. (See pp. 67, 69)

[70] A. Zigler, Y. Ehrlich, C. Cohen, J. Krall, and P. Sprangle. "Optical guiding of high-intensity laser pulses in a long plasma channel formed by a slow capillary discharge". *Journal of the Optical Society of America B: Optical Physics* 13, p. 68, 1996. (See p. 67)

[71] C. G. Geddes, C. Toth, J. Van Tilborg, E. Esarey, C. B. Schroeder, J. Cary, and W. P. Leemans. "Guiding of relativistic laser pulses by preformed plasma channels". *Physical Review Letters* 95, pp. 1–4, 2005. (See p. 67)

[72] C. Durfee and H. M. Milchberg. "Light Pipe for High Intensity Laser Pulses". *Physical Review Letters* 71, pp. 2409–2412, 1993. (See p. 67)

[73] D. J. Spence and S. M. Hooker. "Investigation of a hydrogen plasma waveguide". *Physical Review E* 63, p. 015401, 2000. (See pp. 67, 68)

[74] T. P. Rowlands-Rees, C. Kamperidis, S. Kneip, A. J. Gonsalves, S. P. D. Mangles, J. G. Gallacher, E. Brunetti, T. Ibbotson, C. D. Murphy, P. S. Foster, M. J. V. Streeter, F. Budde, P. A. Norreys, D. A. Jaroszynski, K. Krushelnick, Z. Najmudin, and S. M. Hooker. "Laser-Driven Acceleration of Electrons in a Partially Ionized Plasma Channel". *Physical Review Letters* 100, p. 105005, 2008. (See p. 67)

[75] C. G. Durfee, J. Lynch, and H. M. Milchberg. "Development of a plasma waveguide for high-intensity laser pulses". *Physical Review E* 51, pp. 2368–2389, 1995. (See p. 68)

[76] A. Butler, D. J. Spence, and S. M. Hooker. "Guiding of High-Intensity Laser Pulses with a Hydrogen-Filled Capillary Discharge Waveguide". *Physical Review Letters* 89, p. 185003, 2002. (See p. 68)

[77] F. Wojda, K. Cassou, G. Genoud, M. Burza, Y. Glinec, O. Lundh, A. Persson, G. Vieux, E. Brunetti, R. P. Shanks, D. Jaroszynski, N. E. Andreev, C.-G. Wahlström, and B. Cros. "Laser-driven plasma waves in capillary tubes". *Physical Review E* 80, p. 066403, 2009. arXiv: `0910.3116`. (See p. 68)

[78] S. Abuazoum, S. M. Wiggins, B. Ersfeld, K. Hart, G. Vieux, X. Yang, G. H. Welsh, R. C. Issac, M. P. Reijnders, D. R. Jones, and D. A. Jaroszynski. "Linearly tapered discharge capillary waveguides as a medium for a laser

plasma wakefield accelerator". *Applied Physics Letters* 100, p. 014106, 2012. (See p. 68)

[79] C. Benedetti, C. B. Schroeder, E. Esarey, and W. P. Leemans. "Quasi-matched propagation of ultra-short, intense laser pulses in plasma channels". *Physics of Plasmas* 19, p. 053101, 2012. (See p. 68)

[80] S. Cipiccia et al. "Gamma-rays from harmonically resonant betatron oscillations in a plasma wake". *Nature Physics* 7, pp. 867–871, 2011. (See p. 68)

[81] A. Ting, E. Esarey, and P. Sprangle. "Nonlinear wake-field generation and relativistic focusing of intense laser pulses in plasmas". *Physics of Fluids B* 2, pp. 1390–1394, 1990. (See pp. 69, 71)

[82] P. Sprangle, C.-M. Tang, and E. Esarey. "Relativistic Self-Focusing of Short-Pulse Radiation Beams in Plasmas". *IEEE Transactions on Plasma Science* 15, pp. 145–153, 1987. (See p. 69)

[83] P. Chessa, P. Mora, and T. M. Antonsen. "Numerical simulation of short laser pulse relativistic self-focusing in underdense plasma". *Physics of Plasmas* 5, pp. 3451–3458, 1998. (See p. 69)

[84] C. D. Decker, W. B. Mori, K. Tzeng, and T. Katsouleas. "The evolution of ultra-intense, short-pulse lasers in underdense plasmas". *Physics of Plasmas* 3, pp. 2047–2056, 1996. (See p. 70)

[85] D. Teychenné, G. Bonnaud, and J.-L. Bobin. "Electrostatic and kinetic energies in the wake wave of a short laser pulse". *Physics of Plasmas* 1, p. 1771, 1994. (See p. 71)

[86] E. Esarey. "Nonlinear Pump Depletion and Electron Dephasing in Laser Wakefield Accelerators". *AIP Conference Proceedings*. **737**. Proc. AIP. AIP, 2004. Pp. 578–584. (See pp. 71, 72)

[87] B. A. Shadwick, C. B. Schroeder, and E. Esarey. “Nonlinear laser energy depletion in laser-plasma accelerators”. *Physics of Plasmas* 16, p. 056704, 2009. (See pp. 71–74)

[88] C. Benedetti, F. Rossi, C. B. Schroeder, E. Esarey, and W. P. Leemans. “Pulse evolution and plasma-wave phase velocity in channel-guided laser-plasma accelerators”. *Physical Review E* 92, p. 023109, 2015. (See p. 71)

[89] S. V. Bulanov, I. N. Inovenkov, V. I. Kirsanov, N. M. Naumova, and A. S. Sakharov. “Nonlinear depletion of ultrashort and relativistically strong laser pulses in an underdense plasma”. *Physics of Fluids* 4, p. 1935, 1992. (See p. 71)

[90] S. C. Wilks, J. M. Dawson, W. B. Mori, T. Katsouleas, and M. E. Jones. “Photon accelerator”. *Physical Review Letters* 62, pp. 2600–2603, 1989. arXiv: `arXiv:1011.1669v3`. (See p. 72)

[91] F. S. Tsung, C. Ren, L. O. Silva, W. B. Mori, and T. Katsouleas. “Generation of ultra-intense single-cycle laser pulses by using photon deceleration”. *Proceedings of the National Academy of Sciences* 99, pp. 29–32, 2002. (See p. 72)

[92] J. Vieira, F. Fiúza, L. O. Silva, M. Tzoufras, and W. B. Mori. “Onset of self-steepening of intense laser pulses in plasmas”. *New Journal of Physics* 12, 2010. (See p. 72)

[93] P. Michel, C. B. Schroeder, B. A. Shadwick, E. Esarey, and W. P. Leemans. “Radiative damping and electron beam dynamics in plasma-based accelerators”. *Physical Review E* 74, p. 026501, 2006. (See p. 79)

[94] J. Marriner. “Stochastic cooling overview”. *Nuclear Instruments and Methods in Physics Research Section A: Accelerators, Spectrometers, Detectors and Associated Equipment* 532, pp. 11–18, 2004. arXiv: `0308044 [physics]`. (See p. 79)

[95] A. Modena, Z. Najmudin, A. E. Dangor, C. E. Clayton, K. A. Marsh, C. Joshi, V. Malka, C. B. Darrow, C. N. Danson, D. Neely, and F. N. Walsh. “Electron acceleration from the breaking of relativistic plasma waves”. *Nature* 377, p. 606, 1995. (See p. 80)

[96] A. Ting, K. Krushelnick, C. I. Moore, H. R. Burris, E. Esarey, J. Krall, and P. Sprangle. “Temporal evolution of self-modulated laser wakefields measured by coherent thomson scattering”. *Physical Review Letters* 77, pp. 5377–5380, 1996. (See p. 80)

[97] E. Esarey, S. P., J. Krall, and A. Ting. “Review of Plasma-Based Accelerator Concepts”. *IEEE Transactions on Plasma Science* 24, p. 252, 1996. (See p. 80)

[98] W. Lu, M. Tzoufras, C. Joshi, F. S. Tsung, W. Mori, J. Vieira, R. A. Fonseca, and L. Silva. “Generating multi-GeV electron bunches using single stage laser wakefield acceleration in a 3D nonlinear regime”. *Physical Review Special Topics - Accelerators and Beams* 10, p. 061301, 2007. (See p. 81)

[99] A. Zhidkov, J. K. Koga, K. Kinoshita, and M. Uesaka. “Effect of self-injection on ultraintense laser wake-field acceleration”. *Physical Review E: Statistical, Nonlinear, and Soft Matter Physics* 69, p. 035401, 2004. (See p. 81)

[100] S. a. Yi, V. Khudik, S. Y. Kalmykov, and G. Shvets. “Hamiltonian analysis of electron self-injection and acceleration into an evolving plasma bubble”. *Plasma Physics and Controlled Fusion* 53, p. 014012, 2011. (See p. 81)

[101] S. Bulanov, N. Naumova, F. Pegoraro, and J. Sakai. “Particle injection into the wave acceleration phase due to nonlinear wake wave breaking”. *Physical Review E* 58, p. 5257, 1998. (See p. 82)

[102] H. Suk, N. Barov, J. B. Rosenzweig, and E. Esarey. "Plasma electron trapping and acceleration in a plasma wake field using a density transition". *Physical Review Letters* 86, pp. 1011–1014, 2001. (See p. 82)

[103] T. Ohkubo, A. Zhidkov, T. Hosokai, K. Kinoshita, and M. Uesaka. "Effects of density gradient on short-bunch injection by wave breaking in the laser wake field acceleration". *Physics of Plasmas* 13, p. 033110, 2006. (See p. 82)

[104] C. G. R. Geddes, K. Nakamura, G. R. Plateau, C. Toth, E. Cormier-Michel, E. Esarey, C. B. Schroeder, J. R. Cary, and W. P. Leemans. "Plasma-Density-Gradient Injection of Low Absolute-Momentum-Spread Electron Bunches". *Physical Review Letters* 100, p. 215004, 2008. (See pp. 82, 166, 179)

[105] W. P. Leemans, E. Esarey, C. G. Geddes, C. Toth, C. B. Schroeder, K. Nakamura, A. J. Gonsalves, D. Panasenko, E. Cormier-Michel, G. R. Plateau, C. Lin, D. L. Bruhwiler, and J. R. Cary. "Progress on laser plasma accelerator development using transversely and longitudinally shaped plasmas". *Comptes Rendus Physique* 10, pp. 130–139, 2009. (See p. 82)

[106] M. Hansson, B. Aurand, X. Davoine, H. Ekerfelt, K. Svensson, A. Persson, C.-G. Wahlström, and O. Lundh. "Down-ramp injection and independently controlled acceleration of electrons in a tailored laser wakefield accelerator". *Physical Review Special Topics - Accelerators and Beams* 18, p. 071303, 2015. (See p. 82)

[107] A. V. Brantov, T. Z. Esirkepov, M. Kando, H. Kotaki, V. Y. Bychenkov, and S. V. Bulanov. "Controlled electron injection into the wake wave using plasma density inhomogeneity". *Physics of Plasmas* 15, p. 073111, 2008. (See p. 82)

[108] K. Schmid and L. Veisz. "Supersonic gas jets for laser-plasma experiments". *Review of Scientific Instruments* 83, pp. 1–10, 2012. (See pp. 92, 96, 191)

[109] *NIST Digital Library of Mathematical Functions.* http://dlmf.nist.gov/ (see pp. 97, 130)

[110] S. Wilks, T. Katsouleas, J. M. Dawson, P. Chen, and J. J. Su. "Beam Loading in Plasma Waves". *IEEE Transactions on Plasma Science* 15, pp. 210–217, 1987. (See p. 102)

[111] M. Tzoufras, W. Lu, F. S. Tsung, C. Huang, W. B. Mori, J. Vieira, R. A. Fonseca, and L. O. Silva. "The physical picture of beam loading in the blowout regime". *2007 IEEE Particle Accelerator Conference (PAC'07).* Proc. Part. Accel. Conf. (PAC'07). IEEE, 2007. Pp. 3061–3063. (See p. 102)

[112] S. P. Mangles, A. G. Thomas, O. Lundh, F. Lindau, M. C. Kaluza, A. Persson, C. G. Wahlström, K. Krushelnick, and Z. Najmudin. "On the stability of laser wakefield electron accelerators in the monoenergetic regime". *Physics of Plasmas* 14, 2007. (See pp. 104, 122)

[113] G. Fubiani, E. Esarey, C. B. Schroeder, and W. P. Leemans. "Improvement of electron beam quality in optical injection schemes using negative plasma density gradients". *Physical Review E: Statistical, Nonlinear, and Soft Matter Physics* 73, p. 026402, 2006. (See p. 104)

[114] T. Katsouleas. "Physical mechanisms in the plasma wake-field accelerator". *Physical Review A* 33, pp. 2056–2064, 1986. (See p. 104)

[115] M. Tzoufras, W. Lu, F. S. Tsung, C. Huang, W. B. Mori, T. Katsouleas, J. Vieira, R. A. Fonseca, and L. O. Silva. "Beam loading by electrons in nonlinear plasma wakes". *Physics of Plasmas* 16, 2009. (See pp. 104, 122)

[116] S. P. Mangles, A. G. Thomas, M. C. Kaluza, O. Lundh, F. Lindau, A. Persson, F. S. Tsung, Z. Najmudin, W. B. Mori, C. G. Wahlström, and K. Krushelnick. "Laser-wakefield acceleration of monoenergetic electron beams in the first plasma-wave period". *Physical Review Letters* 96, pp. 1–4, 2006. (See p. 112)

[117] Z.-C. Shen, J. Luo, T. Yuan, G.-B. Zhang, M. Chen, S.-M. Weng, C. B. Schroeder, L.-L. Yu, E. Esarey, and J.-Y. Yu. "Dynamics of boundary layer electrons around a laser wakefield bubble". *Physics of Plasmas* 23, p. 103112, 2016. (See p. 121)

[118] B. Ersfeld, R. Bonifacio, S. Chen, M. R. Islam, P. W. Smorenburg, and D. A. Jaroszynski. "The ion channel free-electron laser with varying betatron amplitude". *New Journal of Physics* 16, p. 093025, 2014. (See pp. 124, 125, 133, 193)

[119] E. Wallin, A. Gonoskov, and M. Marklund. "Radiation emission from braided electrons in interacting wakefields". *Physics of Plasmas* 24, 2017. arXiv: `1704.07237`. (See p. 124)

[120] P. Luchini and H. Motz. *Undulators and free-electron lasers*. International series of monographs on physics. Oxford: Clarendon Press, 1990. (See p. 124)

[121] E. Esarey, B. A. Shadwick, P. Catravas, and W. P. Leemans. "Synchrotron radiation from electron beams in plasma-focusing channels". *Physical Review E: Statistical, Nonlinear, and Soft Matter Physics* 65, p. 056505, 2002. (See pp. 125, 126, 128, 133, 140, 206)

[122] S. Chen. "FEL Theory in an Ion Channel Wiggler". PhD. Thesis. 2016. (See p. 126)

[123] H. P. Freund, D. C. Nguyen, and B. Carlsten. "Three-dimensional analysis of prebunched electron beams in an x-ray free-electron laser". *Physical Review Special Topics - Accelerators and Beams* 15, pp. 4–7, 2012. (See p. 156)

[124] L. Reid. "TBC". PhD. Thesis. 2018. (See p. 157)

[125] E. Brunetti, R. P. Shanks, G. G. Manahan, M. R. Islam, B. Ersfeld, M. P. Anania, S. Cipiccia, R. C. Issac, G. Raj, G. Vieux, G. H. Welsh, S. M. Wiggins, and D. A. Jaroszynski. "Low Emittance, High Brilliance Relativistic Electron Beams from a Laser-Plasma Accelerator". *Physical Review Letters* 105, p. 215007, 2010. (See pp. 166, 179)

[126] S. M. Wiggins, R. C. Issac, G. H. Welsh, E. Brunetti, R. P. Shanks, M. P. Anania, S. Cipiccia, G. G. Manahan, C. Aniculaesei, B. Ersfeld, M. R. Islam, R. T. L. Burgess, G. Vieux, W. A. Gillespie, A. M. MacLeod, S. B. van der Geer, M. J. de Loos, and D. A. Jaroszynski. "High quality electron beams from a laser wakefield accelerator". *Plasma Physics and Controlled Fusion* 52, p. 124032, 2010. (See pp. 166, 179)

[127] G. H. Welsh, S. M. Wiggins, R. C. Issac, E. Brunetti, G. G. Manahan, M. R. Islam, S. Cipiccia, C. Aniculaesei, B. Ersfeld, and D. A. Jaroszynski. "High resolution electron beam measurements on the ALPHA-X laser-plasma wakefield accelerator". *Journal of Plasma Physics* 78, pp. 393–399, 2012. (See pp. 166, 179, 181)

[128] K. Schmid, A. Buck, C. M. S. Sears, J. M. Mikhailova, R. Tautz, D. Herrmann, M. Geissler, F. Krausz, and L. Veisz. "Density-transition based electron injector for laser driven wakefield accelerators". *Physical Review Special Topics - Accelerators and Beams* 13, pp. 1–5, 2010. (See p. 191)

[129] M. Vargas, W. Schumaker, Z.-H. He, Z. Zhao, K. Behm, V. Chvykov, B. Hou, K. Krushelnick, A. Maksimchuk, V. Yanovsky, and A. G. R. Thomas. "Improvements to laser wakefield accelerated electron beam stability, divergence, and energy spread using three-dimensional printed two-stage gas cell targets". *Applied Physics Letters* 104, p. 174103, 2014. (See p. 191)

[130] G. Golovin, S. Chen, N. Powers, C. Liu, S. Banerjee, J. Zhang, M. Zeng, Z. Sheng, and D. Umstadter. "Tunable monoenergetic electron beams

from independently controllable laser-wakefield acceleration and injection". *Physical Review Special Topics - Accelerators and Beams* 18, p. 011301, 2015. (See p. 191)

[131] J. van Tilborg, C. B. Schroeder, C. V. Filip, C. Tóth, C. G. R. Geddes, G. Fubiani, R. Huber, R. A. Kaindl, E. Esarey, and W. P. Leemans. "Temporal Characterization of Femtosecond Laser-Plasma-Accelerated Electron Bunches Using Terahertz Radiation". *Physical Review Letters* 96, p. 014801, 2006. (See p. 192)

[132] M. Litos et al. "High-efficiency acceleration of an electron beam in a plasma wakefield accelerator". *Nature* 515, pp. 92–95, 2014. (See p. 195)

[133] A. Caldwell. "Awake: A Proton Driven Plasma Wakefield Acceleration Experiment at CERN". *North American Particle Accelerator Conference (NA-PAC'16)*. North American Particle Accelerator Conference 3. Proc. North Am. Part. Accel. Conf. Geneva, Switzerland: JACoW, 2017. Pp. 266–270. (See p. 195)

[134] G. Korn, S. V. Bulanov, J.-P. Chambaret, D. Charambilidis, J. Collier, M. Dunne, K. Ertel, J. Hein, S. Karsch, F. Krausz, G. Mourou, P. Nickles, K. Osvay, B. Rus, W. Sandner, G. Tsakiris, and T. Tajima. "Extreme Light Infrastructure (ELI): Physics and Lasers at the ultra-intense frontier". *Conference on Lasers and Electro-Optics*. Proc. Conf. Lasers Electro-Opt. Washington, D.C.: OSA, 2010. JThG2. (See p. 195)

[135] R. B. Dingle. *Asymptotic Expansions: Their Derivation and Interpretation.* Academic Press, 1973. (See p. 196)

[136] W. Leemans, E. Esarey, J. van Tilborg, P. Michel, C. Schroeder, C. Toth, C. Geddes, and B. Shadwick. "Radiation from laser accelerated electron bunches: coherent terahertz and femtosecond X-rays". *IEEE Transactions on Plasma Science* 33, pp. 8–22, 2005. (See p. 208)